Electron quantum optics in quantum Hall edge channels

Erwann Bocquillon

ÉCOLE NORMALE SUPÉRIEURE

Département de Physique

laboratoire pierre aigrain
électronique et photonique quantiques

THÈSE de DOCTORAT de L'UNIVERSITÉ PARIS VI

Spécialité : Physique Quantique

présentée par

Erwann BOCQUILLON

Pour obtenir le titre de DOCTEUR de l'UNIVERSITÉ PARIS VI

Sujet de la thèse :

Electron quantum optics in quantum Hall edge channels

Soutenue le 30 novembre 2012 devant le jury composé de :

M.	Laurens Molenkamp	Examinateur
Mme.	Janine Splettstösser	Examinateur
M.	Jean-Michel Raimond	Président
M.	François Lefloch	Rapporteur
M.	Christian Schönenberger	Rapporteur
M.	Gwendal Fève	Co-directeur de thèse
M.	Bernard Plaçais	Directeur de thèse

A la mémoire de Jules, Liévin et Gérard.

Remerciements

Je souhaite remercier en premier lieu François Lefloch et Christian Schönenberger d'avoir accepté la charge de rapporteur du présent manuscrit, ainsi que Laurens Molenkamp, Jean-Michel Raimond et Janine Splettstoesser pour avoir constitué le jury. Ce fut un honneur de leur présenter mon travail, je les remercie vivement pour leur présence à ma soutenance, ainsi que pour leur travail en amont.

Cette thèse fut réalisée au sein du Laboratoire Pierre Aigrain, où il fut très agréable de travailler pendant un peu plus de trois années. Cela tient aux compétences scientifiques de ses membres, mais aussi à leurs remarquables qualités humaines. À tout seigneur tout honneur, je remercie d'abord Jean-Marc Berroir d'oeuvrer pour la cohésion du laboratoire : merci pour le foot et la vie sociale du labo, merci de m'avoir accepté en thèse au sein du labo, guidé vers le poste d'agrégé-préparateur et initié aux arcanes de la vie de labo à travers les conseils scientifiques et nos permanentes discussions avec l'équipe de méso. Travailler dans cette équipe fut un réel plaisir, malgré les moments difficiles où la manip piétine... Bernard Plaçais et Gwendal Fève ont encadré mon travail avec sagesse, ambition et bonne humeur et je les en remercie chaleureusement. Gwendal m'a appris la physique méso bien au delà des rudiments, m'a fait confiance et nous a permis d'avancer toujours avec le sourire. Il a donné beaucoup de ses nuits et week-ends et je l'en remercie, ainsi que Delphine qui a du supporter cette contrainte. En dehors de la vie scientifique, j'ai apprécié de pouvoir échanger sur Messi, le stade Rennais ou le LOSC, écouter R.E.M. ou Garbage (un peu moins les Black Eyed Peas), merci chef! Bernard a accompagné ce travail avec enthousiasme, apportant quotidiennement sa touche au cours de nos riches discussions. Il ne fut jamais avare d'une petite blague (toujours subtile) et a contribué par sa jovialité à l'excellente atmosphère de la P13. Même si sa charge de directeur l'a maintenu un peu plus loin du cryostat, merci à Jean-Marc pour son soutien permanent, et pour les transferts d'Hélium pendant les vacances. J'ai aussi eu la chance de faire équipe avec Adrien Mahé, François Parmentier et Vincent Freulon. Je dois énormément à François, qui a consacré de longues heures à me former et à me transmettre son savoir, même s'il a partiellement échoué sur certains points : je reste encore modérément sensible au Camembert Electrique... C'est désormais sur les épaules de Vincent que repose la suite de l'aventure, je lui souhaite bon courage et bonne chance. Christian Glattli a aussi apporté sa pierre à l'édifice, Takis Kontos a souvent apporté un éclairage bienvenu sur nos travaux, avec une touche d'exubérance méditerranéenne, merci à eux pour nos discussions.

Merci aux autres mésoscopistes pour nos aventures, depuis la mezzanine jusqu'aux sommets de la Vanoise, du jus de goyave aux bières belges, toujours dans une excellente ambiance : Andi (pirate in scientist desguise), Emi, Quentin, Sung Ho, Thomas, Chéryl,

Julien, Takis, Audrey, Matt, Jérém, Dora, Subha, Laure, Nico, Manu, Philippe, JD, Ben, François, Mickael, ainsi que Cécile et Clara. Que soient remerciés aussi les autres membres du LPA et du département avec qui les échanges furent toujours enrichissants, autour d'une table optique, d'un ballon de foot, d'un verre, ou au jardin du Luxembourg : Antoine et Ben L. (pour le séminaire "jeunes"), Fabien, Michele, Christophe, Vincenzo, Pierrick, Jean, Kenneth, David, Sukhy, Bruno, Igor, Rémi, Nir, Sylvain et tous les autres. J'ai aussi pu bénéficier du soutien des services du département et du LPA. Je remercie Anne Matignon, Fabienne Rénia, Pascal Morfin, Jules Silembo, Claude Dodray, Anne Denis, Philippe Pace, David Darson, Mickaël Rosticher, José Palomo, François-René Ladan, Thierry Desvignes. Tout particulièrement, Olivier Andrieu nous a fourni de l'hélium malgré les pénuries et les conflits douteux au fin fond de la Sibérie, un immense merci... Pour décompresser, rien de tel que de courir en groupe autour du jardin du Luxembourg. Avec notre vénérable coach Olivier, merci à Andi, François, Matt, Mighty Mike, Nico, Nir, Sukhy, Sylvain et tous les autres coureurs occasionnels de m'avoir initié à ce sport ingrat.

La richesse de ces années revient aussi à la partie enseignement. Je tiens à remercier André, Eric, Nasser, Kenneth, Clément, Florian, Jean-Michel, Rémi, Pierre-François, Jean-Marc, Manu et Frédéric pour les heures de cours/TD partagées ensemble, Stephan, Jean-François, Mascia, Marie, Radya, ainsi que Mr le directeur des lieux Werner Krauth.

Le LPN nous fournit depuis des longues années en échantillons de qualité, dont nous tentons d'extraire la substantifique moëlle (d'aucuns diraient "martyriser") : un très grand merci à Yong Jin et Antonella Cavanna. Les collaborations avec l'ENS Lyon, le CPT Marseille et l'université de Genève ont rendu ce travail encore plus passionnant. Je remercie Pascal Degiovanni (de loin pour éviter les maladies), Charles Grenier, Etienne Thibierge et Dario Ferrarro, Thierry Martin, Thibaut Jonckheere, Jerôme Rech, Denis Chevallier, Claire Wahl, Markus Büttiker, Christian Flindt, et Matthias Albert. Au delà de ces trois équipes, merci à Ulf Gennser, Fredéric Pierre, Carles Altimiras, Patrice Roche, Fabien Portier, Phuong-Anh Huynh, Julie Dubois, Preden Roulleau, Mark-Oliver Goerbig pour nos discussions.

Enfin, je ne serais pas là sans le soutien de la famille et des amis de longue date. Merci aux amis de l'ENS (Baptiste, Joran, et Michał en particulier), aux Faidherbards (Ben, Fab, Fisch, Ch'Gus), ainsi qu'à Paul et Olivier, pour les moments passés ensemble. J'adresse un hommage ému à mes aïeux Liévin, Jules et Gérard pour m'avoir montré le chemin. Je remercie mes grands-parents, parents, beaux-parents, frères et soeur pour leur soutien indéfectible depuis toujours. Enfin, merci à Ramla dont le sourire illumine chacun de mes jours.

Contents

Chapter 1

Introduction

The purpose of this thesis is the study of quantum-coherent electronic transport in mesoscopic structures by implementing analogs of quantum optics experiments. Following the development of nano-fabrication and cryogenic techniques, new mesoscale and nanoscale systems have been investigated, in which conduction properties are governed by quantum mechanics. In particular, high mobility two-dimensional electron gases (2DEG), that exhibit large phase coherence length and elastic mean free path, can be obtained in semi-conductor hetero-junctions. In such structures, several building blocks of optics setups can be recreated, and quantum optics experiments can thus be mimicked. First, the beamsplitter is provided by a set of two voltage-biased metallic gates controlling the transmission of a tunnel barrier in the 2DEG. Then ballistic phase coherent propagation is ensured in chiral one-dimensional edge channels of quantum Hall effect. Major achievements are, for example, the realizations of a double slit experiment [1], a Mach-Zehnder interferometer [2], or a Hanbury-Brown & Twiss intensity correlation experiment [3]. Thus, experimental and theoretical tools of quantum optics can be transposed: ballistic quantum conductors can be used to study electronic transport following the point of view of quantum optics, and coherence theory, in analogy with Glauber's theory of light [4], enables to extract very clear information on electronic properties by the means of current and current correlations. Beside these analogies, electron optics experiments are deeply enriched by Coulomb interactions between electrons, that are in particular responsible for relaxation and decoherence mechanisms that alter the visibility of interference effects. Such electron quantum optics experiments provide benchmark setups to address the problem of interactions.

However, as of yet, these experiments have mostly been performed with DC sources, that emit a continuous flow of electrons without any accurate control on energy and emission times of the charge carriers [5]. Recently developed sources enable to trigger the emission of on-demand single charges [6], paving the way from electron optics toward electron quantum optics. In this manuscript, we present two realizations of such electron quantum optics experiments. The first one is a new implementation of a Hanbury-Brown & Twiss experiment in which single quasiparticles are partitioned one by one on an electronic beamsplitter (chapter 3). The second example is the first realization of a Hong-Ou-Mandel experiment where two (partially) indistinguishable excitations emitted by independent sources are made to interfere on a beamsplitter (chapter 5).

Moreover, these experiments allow to tackle the topic of interactions at a very fundamental level by studying the propagation of a single electron amidst excitations of the Fermi sea. To shed light on such phenomena, we propose in addition a frequency-resolved analysis of capacitive coupling between two edge channels, that enables in particular to observe and characterize a neutral propagation eigenmode (chapter 4).

In this introduction chapter, we present the general framework of electron quantum optics in quantum Hall edge channels, by describing the main building blocks that enable to mimic optical setups. Then, we review milestones of electron optics experiments as well as single charge emitters that enable to study the physics of quantum Hall edge channels at the single charge scale. Finally, we introduce the tool of coherence functions that provides the general theoretical framework of this work and recall the main results obtained so far in the study of interactions between co-propagating edge channels.

1.1 Electron optics in two dimensional electron gases

Several analogies can be drawn between the propagation of electrons in integer quantum Hall edge channels and photons in vacuum. As a consequence, a whole set of experiments realized in quantum Hall devices are directly inspired by their optical equivalents. We here briefly recall the main analogies on which electron quantum optics relies before reviewing major experiments that have been realized in electronic devices.

1.1.1 Building up a quantum optics experiment in a 2DEG

1.1.1.1 Coherence in a 2DEG

The first ingredient to implement a quantum optics experiment is a medium in which ballistic propagation is ensured on a large scale so that phase coherence is conserved over the whole system. In condensed matter, this is provided by two-dimensional electron gases: these semi-conductor hetero-structures (in our case and most frequently GaAs-AlGaAs) are grown by molecular beam epitaxy, which supplies crystalline structures with an extreme degree of purity. Thus mobilities up to about $10 - 30\,10^6$ cm^2/Vs have been reported [7–10], and mean-free path l_e can be on the order of $10 - 20\,\mu$m. These properties enable to pattern samples with e-beam lithography in such a way that the phase coherence of the wavefunction is preserved over the whole structure, thus fulfilling a first requirement to build an electron optics experiment in a condensed matter system. The simplest interference pattern can be produced for example in Young's double-slit experiment (Fig.1.1), which was realized for example by Schuster *et al.* [1]. Defining two paths by electrostatic gates, they can modify the phase difference between paths by tuning the enclosed Aharonov-Bohm flux[1] and observe an interference pattern in the current with a periodicity of h/eS where $S = 0.4\,\mu$m^2 is the surface of the loop.

[1] using moderate fields $B < 20$ mT that do not compare with the ones involved in section 1.1.1.2

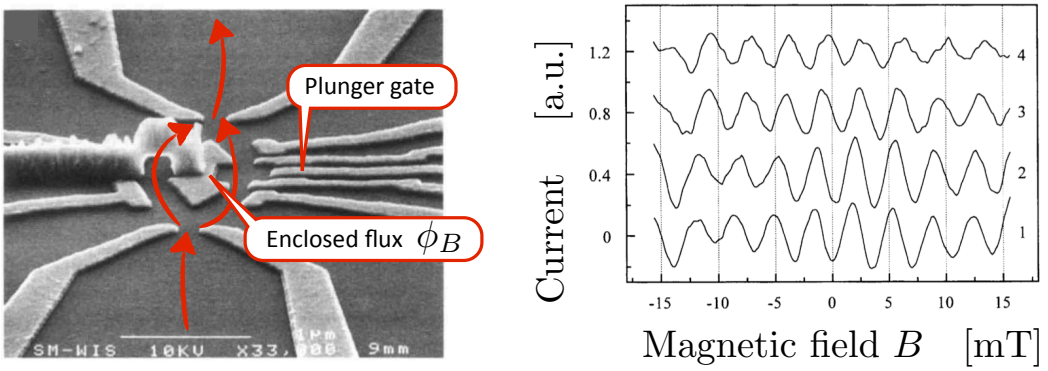

FIGURE 1.1: **Young's double slit experiment** – In GaAs-AlGaAs 2DEG of high mobility $\mu = 1.6\,10^6 \mathrm{cm}^2/\mathrm{Vs}$, two interference paths (red arrows) are defined by electrostatic gates, enclosing a flux $\phi_B = BS$. The phase difference, proportional to ϕ_B being tuned via the field B, interference in the output current is recorded (the graphs correspond to different values of a plunger gate in the right arm that adds an extra contribution to the phase difference). Adapted from [1].

1.1.1.2 Quantum Hall edge channels

Besides, electrons have to be guided from emission and detection through all the optical elements. A powerful implementation of phase coherent quantum rails is provided by (integer) quantum Hall effect. Under a strong perpendicular magnetic field, electronic transport in the 2DEG is governed by chiral one-dimensional conduction channels appearing on the edges while the bulk remains insulating. Then, the conductance of the 2DEG is quantized in units of the inverse of the Klitzing resistance $e^2/h = R_K^{-1} = 1/25.8\,\mathrm{k}\Omega$.

The quantized value of the conductance can be explained by considering the energy spectrum of electrons in the 2DEG: electrons in the bulk are distributed on Landau levels with an energy $E_n = \hbar\omega_c(n+1/2), n \in \mathbb{N}$, where $\omega_c = |eB/m^*|$ is the cyclotron pulsation (the effective mass m^* of electrons in 2DEGs is equal to $0.067m_e$) [11]. These Landau levels are bent near the potential barriers constituting the edges of the sample, see Fig.1.2. Besides, at such high magnetic field, spin-degeneracy in the Landau levels is removed by Zeeman splitting[2] $\hbar\omega_Z$. The finite number of electrons in the 2DEG defines the Fermi energy ϵ_F, which, for an integer number ν filled levels, only crosses the Zeeman-split Landau levels near the edges $x = x_{L,R}$. Thus a finite number of chiral edge channels appear at energy ϵ_F. Importantly, they are chiral: electrons flow with opposite velocities on opposite edges. This number ν, called the filling factor, depends on the magnetic field: as B increases, the Landau levels are shifted upward with respect to the Fermi energy, so that the number of Zeeman-split Landau levels crossing the Fermi

[2] In our samples, typical values are $\hbar\omega_Z/k \simeq 5$ K at $\nu = 2$, while $\hbar\omega_c/k \simeq 60$ K

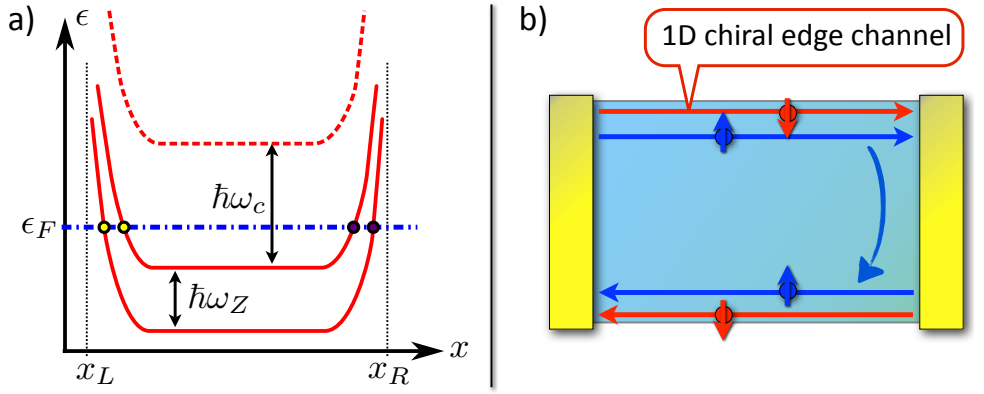

FIGURE 1.2: **Quantum Hall edge channels** – a) *Energy spectrum as a function of position:* in the bulk, Landau levels $E_n = \hbar\omega_c(n+1/2)$ appear. Due to confining potential, levels are bent on the edges ($x = x_{L,R}$). At sufficiently high magnetic fields, spin-degeneracy is lifted by Zeeman splitting $\hbar\omega_Z$ and each level is spin-polarized. When an integer number ν ($\nu = 2$ on this graph) of Landau levels are filled, the Fermi level ϵ_F crosses the energy levels close to the edges, so that transport properties are governed by ν edge channels. b) *Schematic representation of edge channels:* for $\nu = 2$, two spin-polarized chiral edge channels appear on each side. Backscattering mechanism (blue curled arrow), that necessitates to travel from one edge to another due to chirality, is strongly reduced and a ballistic behavior is demonstrated on several hundreds of microns.

level (that is, the number of filled Landau levels, called filling factor ν) decreases. In particular, at filling factor $\nu = 2$ (pictured on Fig.1.1.1.2), electronic transport occurs on two edge channels, which are spin-polarized (the first Landau level is completely filled, spin up and spin down), corresponding to two Zeeman-split levels [11].

Finally, the mean free path of electrons is considerably increased, up to $l_e \sim 100\,\mu$m: the chirality imposed by the magnetic field makes backscattering difficult, as an electron has to scatter from one edge to the counter-propagating one to backscatter, which can only be done when Landau levels are partially filled in the bulk. Beside the absence of backscattering in the edge channels [12], large phase coherence lengths have also been measured ($l_\phi \sim 20\,\mu$m at 20 mK [13]).

In the quantum Hall effect regime, electrons thus propagate along one-dimensional, phase coherent, chiral edge channels without backscattering, that can be used as quantum rails in the realization of electron quantum optics experiments. In this respect, many studies (experimental as well as theoretical) have been performed in order to fully characterize the properties of electronic transport in edge channels. An important result, among others, is the noiseless character of transport in edge channels [14, 15]: a continuous stream of electrons, generated by a bias voltage V appears naturally regularly ordered, with an average time h/eV between charges [5]. The origin of this behavior is Pauli's

exclusion principle, that prevents the presence of two electrons at the same position in the electron beam.

1.1.1.3 Quantum point contact

The electronic analog of a beam splitter can be implemented in a two-dimensional electron gas in the form of a quantum point contact (QPC) which consists of a pair of electrostatic gates deposited on the surface of the sample. The typical geometry of QPC gates is shown in Fig.1.3 a): when a negative gate voltage is applied on the gates, a constriction is created in the 2DEG between the gates because of electrostatic repulsion. This constriction gives rise to a potential barrier (plotted in color scale), the shape of which can be determined from the geometry of the gates [16].

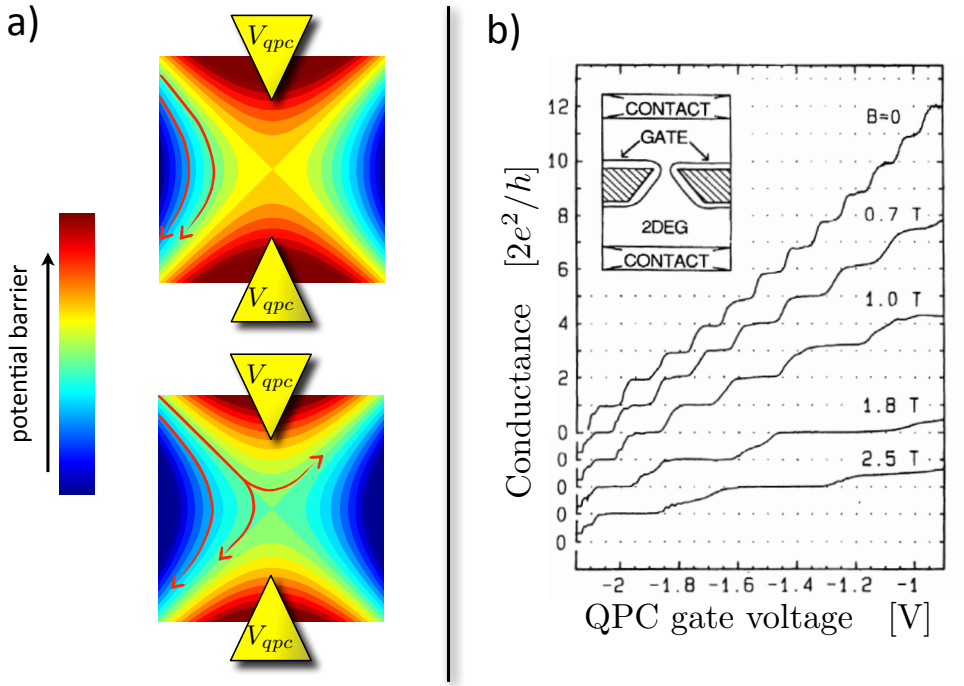

FIGURE 1.3: **Quantum point contact as an electronic beamsplitter** – a) *Geometry of a split gate quantum point contact (QPC):* When polarized with a negative gate voltage V_G, the gates define a tunable potential barrier represented in color scale (negative potentials in red toward zero potentials in blue). In the integer quantum Hall regime, edge channels follow equipotentials and can either be reflected (upper image) or transmitted (outer edge state labeled 1 of lower image). b) *Conductance of a QPC:* the conductance of a QPC is presented as a function of gate voltage and exhibits steps of value $2e^2/h$ corresponding to the progressive transmission of spin-degenerate edge states. As magnetic field B is increased, the number ν of edge states decreases. For high fields, steps at e^2/h starts to appear as the spin-degeneracy of Landau levels is progressively lifted. Data taken from [17].

At high magnetic field, the transmission through the QPC is described in terms of edge channels following equipotential lines, which are reflected one by one as the QPC

gate voltage is swept towards large negative values. This effect was first experimentally demonstrated in [17]: the conductance at magnetic fields below $B = 1$ T presents steps in units of $2e^2/h$ (see Fig.1.3 b). At high magnetic field, the height of the conductance steps is equal to e^2/h, reflecting the removal of spin-degeneracy, while the number of conductance steps n decreases with the magnetic field, and corresponds to the number of edge channels (given by the filling factor ν). Between two conductance plateaus, the conductance G of the QPC is proportional to the transmission probability T: $G = T\frac{e^2}{h}$, and can be generalized for finite number of edge channels ν: $G = \sum_{i=1}^{\nu} T_i \frac{e^2}{h}$, where T_i is the transmission of the i-th edge channel. Fig.1.3 b) therefore demonstrates that one can tune the transmission of a QPC by changing its gate voltage. In particular, when set at the exact half of the opening of the first conductance plateau, the outer edge channel is partially transmitted with a probability $T = 0.5$, while all other edge channels are fully reflected. The quantum point contact therefore acts as a tunable, channel-selective beamsplitter.

1.1.2 Milestones of optics

1.1.2.1 Mach-Zehnder interferometers

Besides double-slit interferences, an other very striking demonstration of the phase coherence in 2DEG is the realization of Mach-Zehnder interferometers implemented this time in the integer quantum Hall regime [2, 13, 18, 19] (Fig. 1.4). Using two quantum point contacts (Fig.1.4 b), Y. Ji *et al.* [2] have defined two paths of different lengths in a geometry that mimics the optical setup (sketched in Fig.1.4 a). Varying the path length by electrostatic influence of an additional gate[3] V_G, they have obtained a sinusoidal interference pattern in the output current of the interferometer. It is important to notice that this experiment probes the wave properties of the source (electronic or light waves), and interference patterns arise from a collection of many single-particle events. For light, classical analysis in terms of wave physics have been proposed during the 17th century (by Hooke, Huyghens and Young) and is associated with first order coherence function $\mathcal{G}^{(1)}(\mathbf{r}, t; \mathbf{r}', t') = \langle E(\mathbf{r}, t) E(\mathbf{r}', t') \rangle$, that encodes the coherence properties of the electric field $E(\mathbf{r}, t)$ at position $\mathbf{r}$ and time t.

[3] as in the double-slit experiment, phase differences can also be controlled by the magnetic flux enclosed in the closed loop of the interferometer.

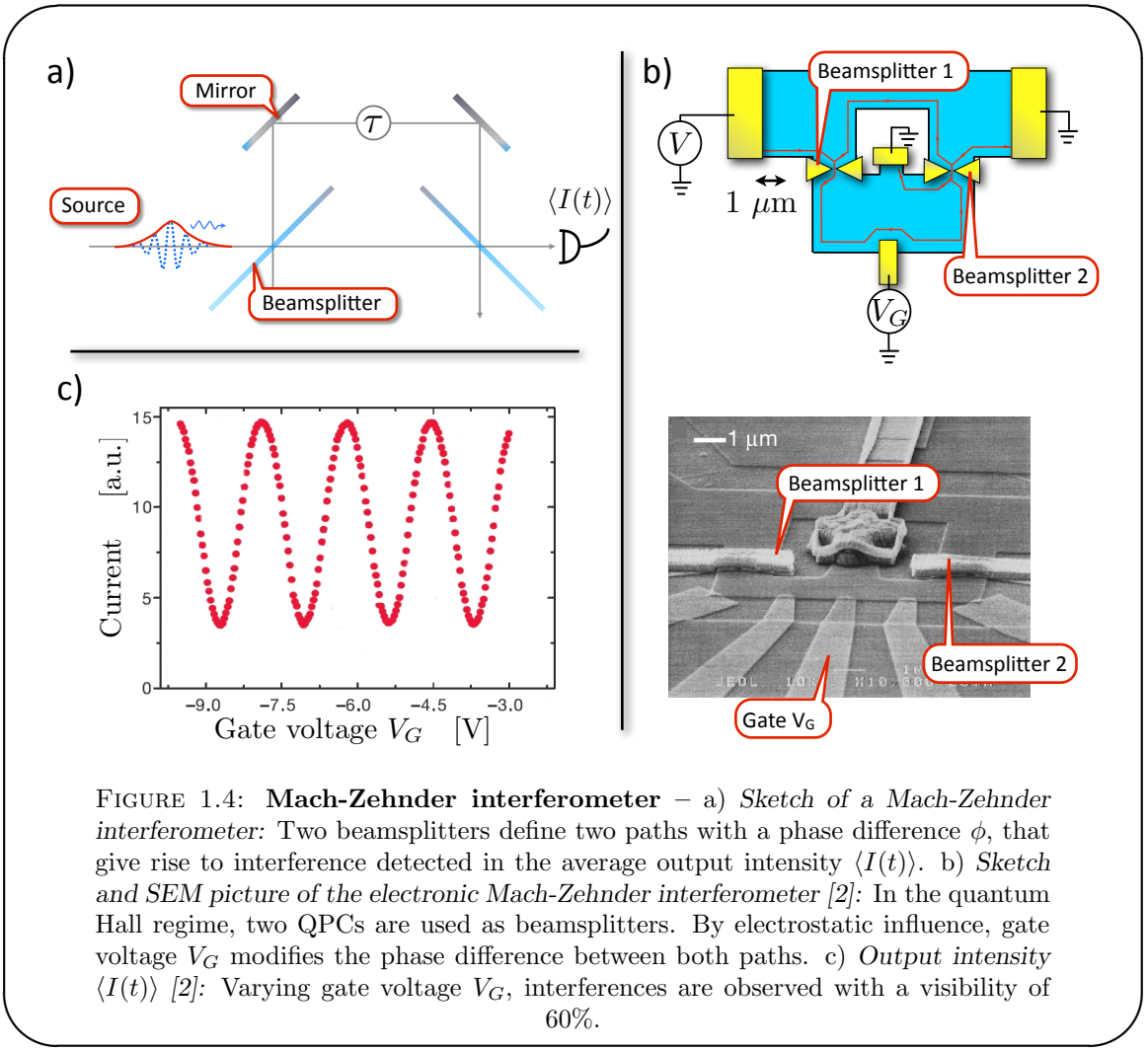

FIGURE 1.4: **Mach-Zehnder interferometer** – a) *Sketch of a Mach-Zehnder interferometer:* Two beamsplitters define two paths with a phase difference ϕ, that give rise to interference detected in the average output intensity $\langle I(t)\rangle$. b) *Sketch and SEM picture of the electronic Mach-Zehnder interferometer [2]:* In the quantum Hall regime, two QPCs are used as beamsplitters. By electrostatic influence, gate voltage V_G modifies the phase difference between both paths. c) *Output intensity $\langle I(t)\rangle$ [2]:* Varying gate voltage V_G, interferences are observed with a visibility of 60%.

1.1.2.2 Hanbury-Brown & Twiss experiments

An other milestone in quantum optics is the implementation of an electronic analog of the Hanbury-Brown & Twiss experiment. In this setup (Fig.1.5), a beam of photons/electrons is partitioned on an optical/electronic beamsplitter and the correlations $\langle I_t(t)I_r(t')\rangle$ between both transmitted $I_t(t)$ and reflected $I_r(t')$ intensities are recorded. The nature of this experiment is quite different from a wave picture, as random partitioning on the beamsplitter is a discrete process at the scale of an individual particle: an electron or a photon is either transmitted or reflected, so that the intensity correlations encodes detailed information on the discrete nature of the involved particles. Once again, a classical model in terms of corpuscles (section 3.1.3) can explain the features observed and give information on the statistics of the source by comparing it with the reference noise of a poissonian process.

In a setup that reproduces the seminal HBT experiment in a 2DEG, Henny *et al.* [3, 20] have demonstrated the relation $\langle \Delta I_t I_r\rangle = -\langle \Delta I_t^2\rangle$ (with $\Delta I_{r,t} = I_{r,t} - \langle I_{r,t}\rangle$). This

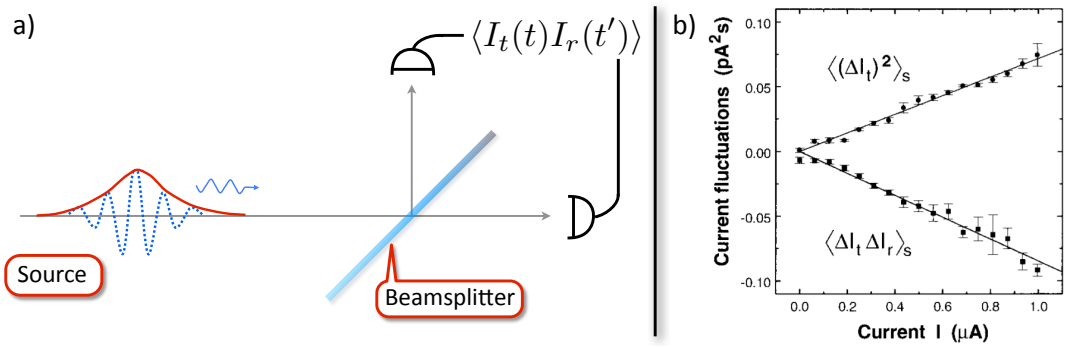

FIGURE 1.5: **Hanbury-Brown experiment** – a) *Sketch of the Hanbury-Brown & Twiss experiment:* A light or electron source is sent on a beamsplitter and correlations between transmitted $I_t(t)$ and reflected $I_t(t')$ intensities are computed, yielding information on the emission statistics of the source. b) *Output correlations:* Perfect anticorrelations are observed between $\langle \Delta I_t I_r \rangle$ and$\langle \Delta I_t^2 \rangle$, reflecting the absence of noise in the electron stream created by a DC-biased contact. This property is enforced by Pauli's exclusion principle. Data taken from [3]

maximal anticorrelation is in fact a signature of the noiseless character of the input source created by a DC voltage source, confirming the results obtained in [14] measuring autocorrelations. It can be interpreted as an antibunching of electrons, also observed for electrons in vacuum [21].

1.1.2.3 Hong-Ou-Mandel effect

As a matter of fact, only few experiments deeply rely on a quantum description that reconciles both wave and particle physics. One important example is given by the Hong-Ou-Mandel effect, named after an experiment carried out in 1987 [22]. In this experiment (sketched in Fig.1.6 a), two particles are sent from two different sources (historically two twin photons emitted simultaneously by a non-linear process in a crystal) in the two inputs of a beamsplitter where they interfere. As a consequence of bosonic/fermionic characters, indistinguishable particles are supposed to give only a limited number of possible outcomes (Fig.1.6 b): two fermions should escape via two different outputs (antibunching), while bosons get out in the same output (bunching) [23, 24]. This two-particle interference [25] relies deeply on quantum indistinguishability and statistics, and consequently neither wave nor particle theories can predict this effect. It is at the heart of this thesis as it plays a key role in the interpretation of both the electronic Hanbury-Brown & Twiss (chapter 3) and Hong-Ou-Mandel (chapter 5) experiments proposed in this manuscript.

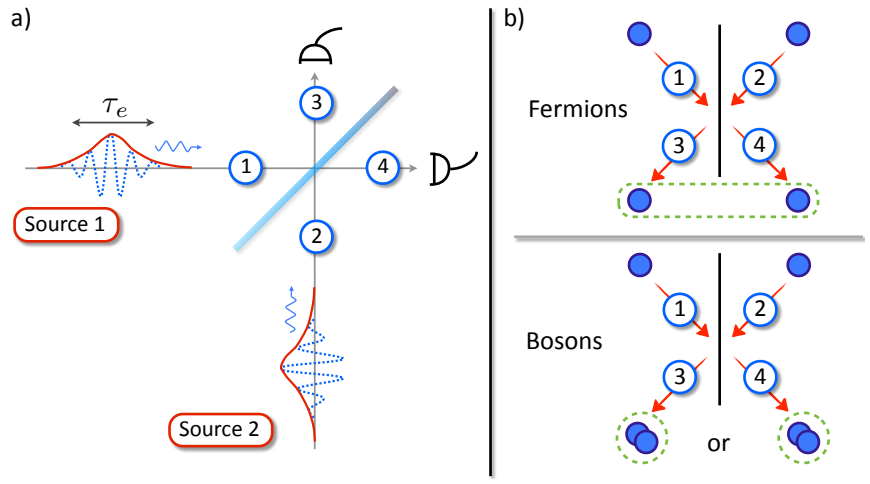

FIGURE 1.6: **Hong-Ou-Mandel effect**– a) *Principles of the Hong-Ou-Mandel experiment:* two synchronized independent wavepackets interfere on a beamsplitter. b) *Possible outcomes of the Hong-Ou-Mandel:* two (indistinguishable) fermions antibunch and come out in different outputs, while two bosons bunch and come out by pair in the same output.

1.2 Electron quantum optics at the single charge scale

1.2.1 Single charge emitters

As of yet, all the mentioned electron optics experiments have been performed with DC sources that continuously emit a large number of electrons and consequently do not offer any precise control either on the energy or emission time of the generated excitations. To operate at a single particle scale, it is crucial to reach ultimate control over a single electron. Several single charge sources have been developed recently, in which an AC signal triggers the emission of mono-electronic excitations, thus paving the way towards electron quantum optics and to a detailed investigation of decoherence and interaction effects at an elementary scale. Here, we briefly introduce several devices realized in 2DEGs that enable the on-demand production of single charges, including the source developed in the Laboratoire Pierre Aigrain that is at the heart of this work.

1.2.1.1 Electrons flying on surface acoustic waves

The piezoelectric properties of the gallium arsenide substrate have been used to generate single charge excitations at GHz repetition rates [28–31]. Applying radio-frequency electric field on a piezo-electric transducer, a surface acoustic wave (SAW) is produced, that in return acts as a trapping potential for electrons in the 2DEG. For sufficiently high amplitudes, this potential creates an array of quantum dots that propagates in the

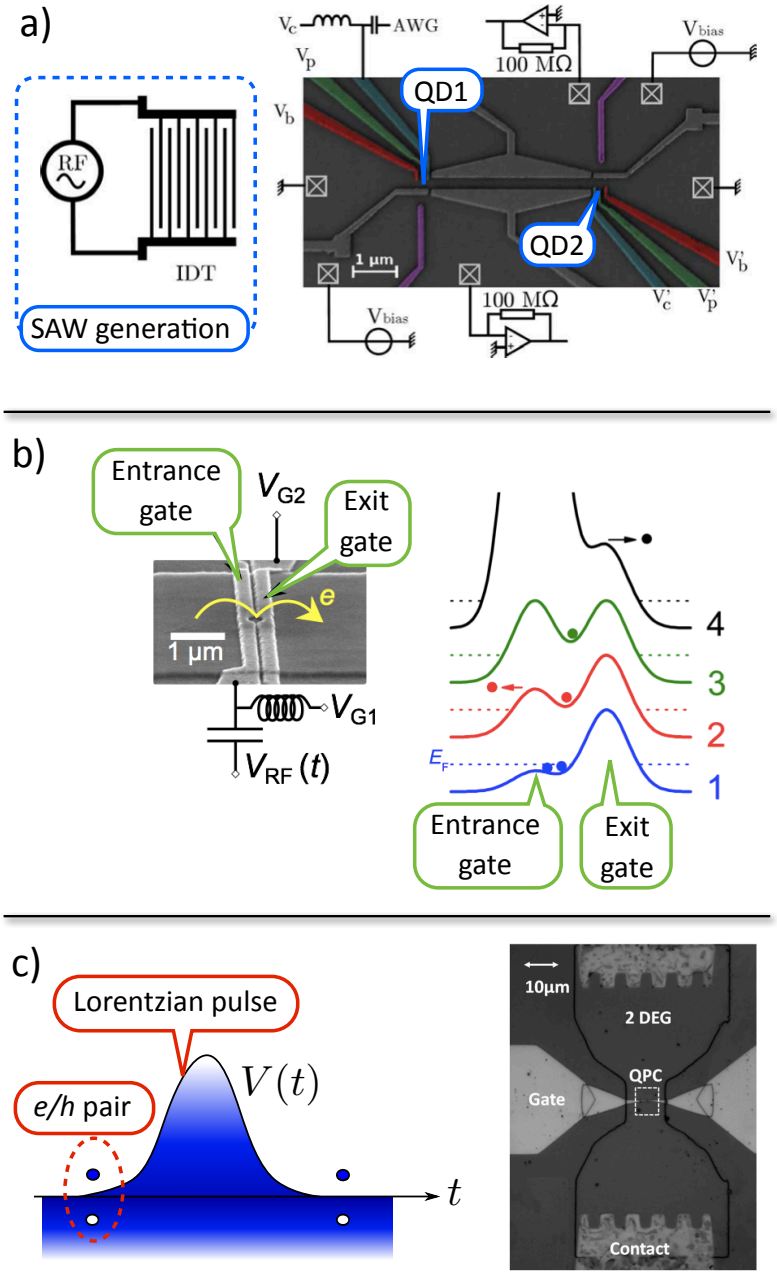

FIGURE 1.7: **Implementations of single charge emitters** – a) *Electrons on surface acoustic waves:* A SAW is generated by a radio-frequency piezo-electric transducer, creating an electric potential that can trap one electron in each minimum. Single charges can then be transported on a few microns, from the electrostatically defined quantum dot 1 to quantum dot 2 (extracted from [26]). b) *Quantum turnstile:* A set of one fast (entrance) and dc (exit) gate are used to create a moving potential (pictured on the right panel) that can trap a single electron coming from the left reservoir before releasing it on the right (extracted from [27]). c) *Lorentzian pulses:* A lorentzian pulse $V(t)$ (pictured on the left) applied on ohmic contact (sample on the right) generates a triggered charge pulse, accompanied with e/h pairs. When $\int dt\, V(t) = h/e$, a quantized charge e is emitted and no addition e/h are created (courtesy of CEA, Saclay).

depleted gas at sound velocity $c \simeq 3\,10^3 \mathrm{m.s}^{-1}$. Each of these quantum dots can trap exactly one electron, so that a quantized DC current $I = ef_{SAW}$ is generated, where f_{SAW} is the frequency of the excited SAW. Recently, two groups [26, 32] have been able to transfer single electrons between distant quantum dots separated by typically 3 to 5 microns (see Fig.1.7, panel a). The challenge is now to implement quantum optics or entanglement protocols in such devices, as quantum information can be stored in the internal states of electrons in dots.

1.2.1.2 Quantum turnstiles and charge pumps

One major challenge to realize a single charge source is the ability to isolate a single charge from the Fermi sea, so that this charge can be quantized. In the previous example, moving quantum dots were created by the SAW potential. On the contrary, two similar techniques, charge pumps [33, 34] and quantum turnstiles [35, 36] allow the controlled capture and release of single charges by the means of a set of fast gates. The latter can be used to create confining potentials modulated at high frequencies, so that a single charge is first trapped, and then released in the 2DEG as presented in Fig.1.7, panel b). DC currents quantized in units of the repetition rate f can then be generated. Recently [27], new designs of the gate drive waveform have enabled to reach an accuracy approaching 0.01 parts per million, so that metrological applications are envisioned, such as a quantum representation of the ampere [37].

1.2.1.3 Lorentzian pulses and modulated contacts

We have already mentioned the DC-biased contact as a source that produces a continuous stream of electrons, pictured as ordered wavepackets (in virtue of Pauli principle) of width h/eV. It however lacks the necessary control over the emission time due to its DC nature. The trigger can be operated by applying a voltage pulse $V(t)$ on an ohmic contact. The charge emitted is then quantized if it verifies the condition $\int dt\, V(t) = h/e$. In general, any pulse shape could be used. However the total number of emitted quasiparticles is not quantized and the emission of additional electron/hole (e/h) pairs is expected, so that quantum electron optics experiments are rendered difficult (see Fig. 1.7, panel c). Nevertheless, it was predicted [38–40] that the application of lorentzian voltage pulses containing one elementary charge e enabled the emission of this single charge without any spurious e/h pair. Such sources are under development in the group of C. Glattli and first demonstrations are expected in a near future.

1.2.1.4 Mesoscopic capacitor as a single electron source

The last implementation described relies on a driven mesoscopic capacitor, that was developed at Laboratoire Pierre Aigrain after proposal from Büttiker *et al.* [41]. It is at the core of the experiments carried out in this PhD work and a complete chapter (chapter 2) will be dedicated to detailing the important properties of this device. Let us briefly sketch how this source can be operated. The source consists of a submicronic quantum dot, that presents a large level spacing Δ coupled to the reservoir through a quantum point contact. The potential in the dot is tuned using a capacitively coupled top-gate deposited at the surface of the sample, controlled by excitation voltage $V_{exc}(t)$. The principle of operation of such a source is depicted in Fig.1.8, panel b): a voltage step is applied to the top gate in order to shift the energy levels upwards with respect to the Fermi energy ϵ_F. If the energy shift is comparable to the level spacing, only one level is promoted above the Fermi energy. The single electron sitting on that level (provided spin degeneracy is lifted) can then be emitted at an energy $\epsilon_+ > \epsilon_F$ in the reservoir through the tunnel barrier formed by the QPC, with an escape time τ_e depending on the transmission of the tunnel barrier D. After emission of the electron, the voltage on the top gate is set back to its original value, so that the level previously promoted above the Fermi energy is shifted back to its position ϵ_- below the Fermi energy. The dot can then absorb an electron from the reservoir, thus emitting a hole at an energy $\epsilon_- < \epsilon_F$ with the same escape time τ_e as the electron (provided that the transmission of the tunnel barrier is independent of energy). On a single cycle, the source therefore emits one single electron, followed by a single hole, both with a controlled energy. This cycle is repeated at GHz rates (typically, $f = 1-2$ GHz), thus generating an AC current composed of alternatively emitted single electrons and single holes [42]. The top gate and the QPC gates allow to tune the energy of the emitted charges and their escape time. The energy and temporal widths of the emitted single-charge wavepackets are respectively given by the width of the levels in the dot and the escape time, both of which only depend on the level spacing Δ and the transmission D. In this respect, the source allows a control over the energy and emission time of the charges close to the quantum limit. A controlled variation of the escape time over several orders of magnitude (< 0.1 ns $\leftrightarrow$ 10 ns) was experimentally demonstrated [42]. The mesoscopic capacitor then appears as a promising candidate to perform single charge emission in electron quantum optics experiments.

1.2.2 Coherence functions

As already mentioned, the propagation of electrons in the quantum Hall edge channels bears strong analogies with the one of photons in vacuum. These analogies have proved

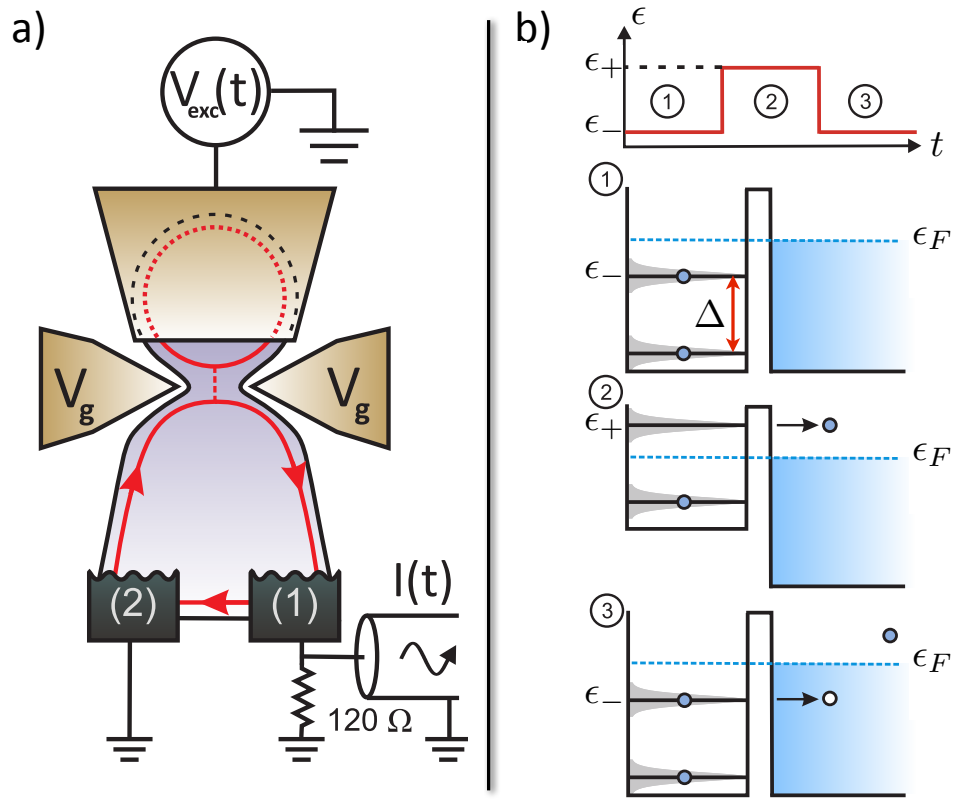

FIGURE 1.8: **Principles of single charge emission** – a) schematic of the mesoscopic capacitor. A quantum dot with a large level spacing is coupled to the reservoir through a QPC (gate voltage V_g). The potential in the dot is tuned using the top gate (voltage V_{exc}, and the emitted current is collected on contact (1). b) principle of single charge emission with the mesoscopic capacitor. The upper graph represents the evolution of the potential of the dot during the emission cycle. ① The dot is at equilibrium, for an initial value of V_{exc}. ② the application of a large voltage step to the dot top-gate shifts the energy levels upwards with respect to the Fermi energy, promoting a single occupied level above the Fermi energy. A single electron is emitted. ③ the excitation voltage is switched back to its original value: the emptied level is shifted back below the Fermi energy, and can absorb an electron from the reservoir. A single hole is emitted. During this cycle, only one level takes part in the emission. The escape time τ_e only depends on the transmission of the QPC.

very useful to shed light on the electronic transport in quantum Hall devices. The latter can be understood in terms of coherence properties of electronic source, so that it seems relevant to adapt, if possible, Glauber's theory of coherence to the case of electrons in 2DEGs.

1.2.2.1 Defining coherence functions in electronic systems

During years 1962-1963, R. J. Glauber developed a general quantum theory of light [4] that has proved very useful to interpret quantum optics experiments. This very general framework relies on the so-called coherence functions $\mathcal{G}$. The first and second order

coherence functions (respectively $\mathcal{G}^{(1)}$ and $\mathcal{G}^{(2)}$) are defined as the following average values [43]:

$$\mathcal{G}^{(1)}(\mathbf{r},t;\mathbf{r}',t') = \langle E^-(\mathbf{r},t)E^+(\mathbf{r}',t')\rangle_\rho \quad (1.1)$$

$$\mathcal{G}^{(2)}(\mathbf{r},t;\mathbf{r}',t') = \langle E^-(\mathbf{r},t)E^-(\mathbf{r}',t')E^+(\mathbf{r}',t')E^+(\mathbf{r},t)\rangle_\rho \quad (1.2)$$

where $\langle \dots \rangle_\rho$ denotes the quantum average over state ρ of the electromagnetic field, and E^-, E^+ respectively the positive and negative frequency part of the field operator. These quantities, that encode field correlations, can be connected quite directly to the signal detected by photon counters, and are as such of great interest in quantum optics.

Grenier *et al.* have developed a similar theory in the case of electrons propagating in quantum Hall edge channels of a 2DEG [44, 45]. Since there are two types of carriers (electrons and holes), we will consider two coherence functions (of the first order), denoted by respectively $\mathcal{G}^{(e)}$ and $\mathcal{G}^{(h)}$, defined by[4]:

$$\mathcal{G}^{(e)}(\mathbf{r},t;\mathbf{r}',t') = \langle \psi^\dagger(\mathbf{r}',t')\psi(\mathbf{r},t)\rangle_\rho \quad (1.3)$$

$$\mathcal{G}^{(h)}(\mathbf{r},t;\mathbf{r}',t') = \langle \psi(\mathbf{r}',t')\psi^\dagger(\mathbf{r},t)\rangle_\rho \quad (1.4)$$

where $\psi(\mathbf{r},t)$ is the field operator, annihilating an electron at position $\mathbf{r}$ and time t while ρ denotes the state of the field upon which the quantum average is calculated. Due to the presence of a complex ground state (a Fermi sea) and two types of charge carriers, several differences arise between photonic and electronic coherence functions. However, we will see that many of our results can be simply interpreted by direct comparison with their photonic equivalent.

1.2.2.2 Generalities on coherence functions

First, in order to simplify the following mathematical expressions, we drop the spatial $\mathbf{r}$-dependence, by assuming a propagation at constant velocity v in quantum Hall edge channels, so that $\psi(r,t) = \psi(r - vt)$:

$$\mathcal{G}^{(e)}(t,t') = \langle \psi^\dagger(t')\psi(t)\rangle_\rho \quad (1.5)$$

$$\mathcal{G}^{(h)}(t,t') = \langle \psi(t')\psi^\dagger(t)\rangle_\rho \quad (1.6)$$

A major difference with optics is the ground state, that now is a Fermi sea $|F_\mu\rangle$ characterized by its chemical potential μ and temperature T, radically different from the

[4] These two functions are closely connected in virtue of commutation relations of fermionic operators. A formulary is presented in Appendix A

vacuum of photons in quantum optics. In full generality, one can decompose coherence functions into a sum of two contributions:

$$\mathcal{G}^{(e/h)}(t,t') = \mathcal{G}_{\mu}^{(e/h)}(t-t') + \Delta\mathcal{G}^{(e/h)}(t,t') \tag{1.7}$$

The first one, denoted $\mathcal{G}_{\mu}^{(e/h)}$, is due to the Fermi sea. Indeed, the coherence functions do not vanish for the ground state $|F_\mu\rangle$ as their photonics counterparts do. One can show that these correlators reduce to:

$$\mathcal{G}_{\mu}^{(e)}(t-t') = \int \frac{d\epsilon}{h} f_\mu(\epsilon) e^{i\epsilon(t'-t)/\hbar} \tag{1.8}$$

$$\mathcal{G}_{\mu}^{(h)}(t-t') = \int \frac{d\epsilon}{h} (1-f_\mu(\epsilon)) e^{i\epsilon(t-t')/\hbar} \tag{1.9}$$

where f_μ is the Fermi-Dirac distribution with chemical potential μ. Please note that since the Fermi sea $|F_\mu\rangle$ is a stationary state, $\mathcal{G}_{\mu}^{(e/h)}$ only depend on the time difference $\tau = t - t'$. The second part $\Delta\mathcal{G}^{(e/h)}$ is the extra contribution representing the single-particle coherence of the electrons and holes emitted in the edge channels by non-equilibrium sources, which depends in full generality on the two times t, t'.

In the following paragraph, we present a simplified model of ideal one-shot emission. Simple analytical formulas will be derived from this model in chapters 2 and 5, providing interesting insights on the underlying physical phenomena.

1.2.2.3 Case of an ideal one-shot single electron source

The quantum state $|\varphi_e\rangle$ is obtained by creating the electron in wavepacket $\varphi_e(t)$ above the Fermi sea, so that the state reads:

$$|\varphi_e\rangle = \int dt\, \varphi_e(t) \psi^\dagger(t) |F_\mu\rangle \tag{1.10}$$

If we consider here the case of the single-shot emission of an electronic excitation at rather high energies, we can assume that the particle is represented by a wavepacket φ_e such that in the energy domain $\varphi_e(\epsilon) = \int dt\, e^{i\epsilon t/\hbar} \varphi_e(t)$ is concentrated around an energy $\epsilon_e \gg kT_{el}$. Thus, the expression of $\mathcal{G}^{(e)}(t,t')$ can be greatly simplified (see Appendix A for details) and the coherence function of an ideal one-shot electron source finally reads:

$$\mathcal{G}^{(e/h)}(t,t') = \mathcal{G}_{\mu}^{(e/h)}(t-t') + \varphi_e^*(t')\varphi_e(t) \tag{1.11}$$

$$\Delta\mathcal{G}^{(e/h)}(t,t') = \varphi_e^*(t')\varphi_e(t) \tag{1.12}$$

This simple example illustrates the idea that the measurement of the single-particle coherence functions provide a direct visualization of the wavepacket in which the particle is emitted. Developing this idea, we will show (section 3.4) that a complete tomography of the quantum state of mono-electronic excitations can be envisioned. In particular, a protocol for measuring $\Delta\mathcal{G}^{(e/h)}$ is described in [46]. It stems from optics where the tomography of an electromagnetic field can be performed by homodyning the studied field with a reference field (called Local Oscillator, LO).

It is important to stress here the difference between the Fermi sea and a mono-electronic wavepacket. Due to the stationary nature of the Fermi sea, $\mathcal{G}_\mu^{(e)}$ depends only on the time difference $\tau = t - t'$. On the other hand, for a mono-electronic wavepacket, $\Delta\mathcal{G}^{(e)}$ depends on both t and t' due to its dynamical character. It reflects the fact that a Fermi sea is a statistical object, entirely described by the populations $\mathcal{G}_\mu^{(e)}(\epsilon) = f_\mu(\epsilon)$ and does not present any coherence. On the contrary, a wavepacket is a quantum object that exhibits both populations and coherences : the two-dimensional Fourier transform $\Delta\mathcal{G}^{(e)}(\epsilon, \epsilon')$ encodes population on the diagonal $\epsilon = \epsilon'$ but also has non-zero off-diagonal components (coherences) for $\epsilon \neq \epsilon'$.

1.2.2.4 Current, current correlations and coherence functions

Like in quantum optics, the coherence functions are very useful as they connect simple theoretical objects to measurable quantities, for example in a Mach-Zehnder interferometer, or in the Hanbury-Brown & Twiss geometry. First, as the average intensity of light is related to $\mathcal{G}^{(1)}$ at coincident times, $\langle\hat{I}(t)\rangle = \mathcal{G}^{(1)}(t,t)$, the average electric current is directly given by $\langle\hat{I}(t)\rangle = e\,\mathcal{G}^{(e)}(t,t)$. We could also define a second order coherence $\mathcal{G}^{(2,e)}$, but (in virtue of Wick's theorem), we will also show that it is possible to calculate current correlations of the form $\langle\hat{I}(t)\hat{I}(t')\rangle$ in terms of $\mathcal{G}^{(e)}$ and $\mathcal{G}^{(h)}$ so that a consistent description of electron quantum optics experiment can be obtained. Moreover, Degiovanni *et al.* [47, 48] and Grenier *et al.* [44, 45] have shown how interactions could be incorporated in this description in simple cases such as voltage pulses or energy resolved excitations.

1.3 Coulomb interactions between electrons

One main difference between electron quantum optics and its photonic equivalent is the presence of many other particles with which electrons interact whereas photons are free from interactions. The difficulty of isolating an electron from the Fermi sea to manipulate it can be circumvented in several manners (section 1.2.1) but the issue

of interactions remains. On one hand, it limits the development of electron quantum optics, as decoherence and relaxation occurs as electrons propagate in the device. On the other hand, these devices supply a very interesting playground to probe these effects at the single charge scale. Here, we briefly review certain aspects of these interactions in quantum Hall edge channels in specific experiments

1.3.1 Interactions in one-dimensional conductors

In one-dimensional quantum conductors such as quantum Hall edge channels, interactions play a major role that do not compare at all with conductors of higher dimensions. For interacting 2D or 3D conductor for examples, the Fermi liquid provides a simple picture of interaction that is very similar to the non-interacting case. In this description, free moving electrons are replaced by dressed electrons (Landau quasiparticles) that are much alike free electrons except that they now have a finite lifetime. On the contrary, strong differences arise in a 1D interacting system. Indeed, the motion of an electron in a straight line strongly modifies the motion of surrounding electrons like toppling dominoes. A reasonable description of a 1D interacting system relies consequently on bosonic collective modes (charge density waves) rather than dressed individual electrons, and constitutes what is known as the Luttinger liquid theory. A large success of this theory is the possibility to take into account interactions in an exact way, by simply renormalizing the velocity of the charge density waves. It will be used in a simple form in chapter 4.

1.3.2 Interactions and electron optics

In chapter 4, we address in particular the case of two chiral co-propagating edge channels at filling factor $\nu = 2$. These two chiral Luttinger liquids are then coupled via Coulomb interactions, allowing for energy exchanges between edge channels. These exchanges have been investigated by Altimiras, le Sueur and co-workers [49–51]. In a sample with variable propagation length and equipped with a quantum dot as an energy filter (Fig. 1.9 a), they have been able to perform a spectroscopy of the excitations in the outermost edge channel and have demonstrated that a non-equilibrium energy distribution injected in the outer channel relaxes towards equilibrium on a scale of a few microns, due to interaction with the inner channel. Moreover, relaxation can be frozen if a gap is created in the excitation spectrum of idler channel in which no energy is injected (by closing the channel on itself) so that energy exchanges are suppressed at low energies [50]. This last result is a strong evidence that coupling between channels is responsible for relaxation. However, though very detailed information can be obtained on the

distribution of energies in the edge channels, it does not provide a direct access to the elementary excitations involved in the energy exchanges.

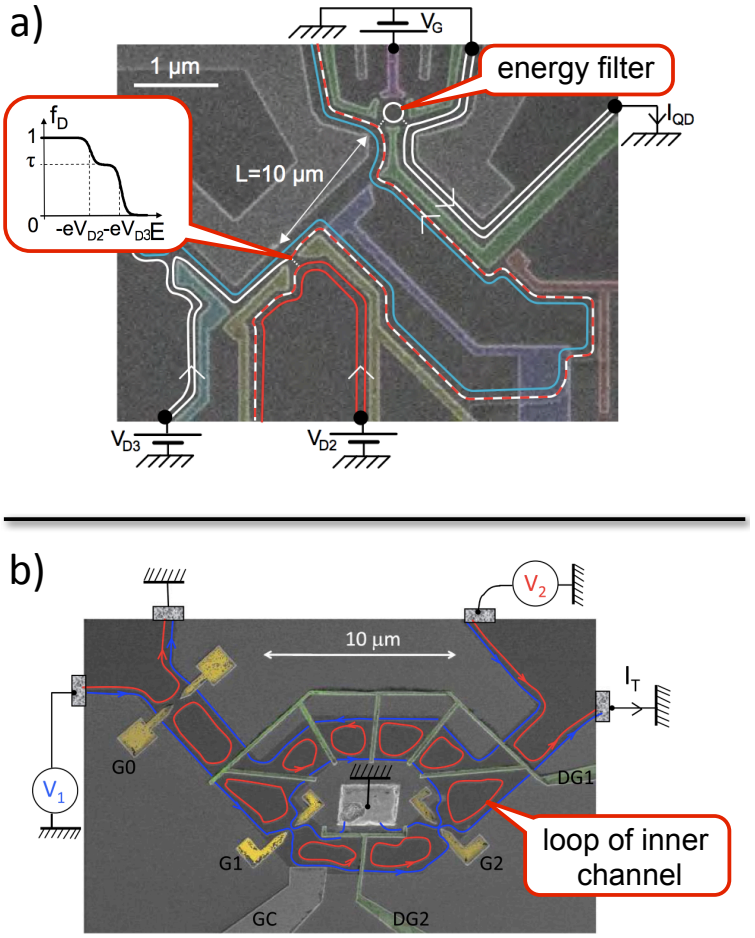

FIGURE 1.9: **Interactions in quantum Hall edge channels** – a) SEM picture of the sample used in [51]. A non-equilibrium energy distribution with a double step feature is created by the mean of a quantum point contact. Using a quantum dot as an energy filter, the energy distribution in the excited edge channel is reconstructed, after variable propagation length (here 10 μm), exhibiting strong energy relaxation (extracted from [51]). b) SEM picture of the Mach-Zehnder interferometer used in [52]. Gates *G1* and *G2* control the two beamsplitters of the interferometer. By changing the voltage applied on *DG1*, loops in the inner edge channel are created, so that charge fluctuations are frozen and coherence length can be doubled (extracted from [52]).

Yet, these elementary excitations can strongly differ from the non-interacting picture of two uncoupled channels. In a strong coupling regime, two eigenmodes are expected to appear at $\nu = 2$: one is fast and carries charge while the other is slow and neutral [53–56]. This mechanism is expected to give rise to decoherence in electron quantum optics devices [57–63]. For example, it gives a very convincing explanation [59] to the unexpected lobe structure in the visibility of Mach-Zehnder interferometers [64, 65]. A

quantum phase transition in the structure of the visibility has in fact been identified [66]. First attempts have been made to tune decoherence via a voltage probe [67], increase the coherence length and freeze decoherence in Mach-Zehnder interferometers [68], by designing closed loops for the idler channel (similarly to [50], see Fig.1.9 b) and a doubling of the coherence has been obtained.

This separation in two very dissimilar eigenmodes bears strong analogies with spin-charge separation in 1D quantum wires. Although this effect has been extensively investigated both experimentally and theoretically in quantum wires [69–71], no direct observation of charge and neutral modes has been reported at $\nu = 2$ yet. As a matter of fact, many experimental works have so far studied charge transport in quantum Hall edge channels and interaction effects between counterpropagating edge states via radio frequency measurements, either in time [72–76] or frequency [77–81] domain, but none directly addressed the separation in charge and neutral modes.

1.4 Outlook

In this manuscript, we address the topic of electron quantum optics in quantum Hall edge channels under two different but complementary approaches. First, we aim at demonstrating the feasibility and relevance of electron optics experiments to study at the single electron scale the propagation of excitations in quantum Hall edge channels. To this end, we singularize one electron (or one hole) amidst the Fermi sea, manipulate it and characterize it via correlations measurements in geometries inspired by photonic quantum optics. As electrons are subject to Coulomb interactions, the natural representation of excitations is then a description in terms of bosonic collective modes in the usual framework of Luttinger liquid theory, that can also be investigated in our devices. The consistence between both aspects is then probed so as to offer a more general understanding of the underlying physics. Experiments presented in this manuscript have been realized in very similar samples. We take advantage of the versatility of the mesoscopic capacitor developed in the lab [6, 82–84] and used as a single electron source (SES), which provides a wonderful and very well-controlled tool to tackle the aforementioned topics.

In the following chapter (chapter 2), we summarize the necessary results of previous works that allow to understand the basic functioning of the SES and its description in terms of Floquet scattering theory and coherence functions. Far from being forsaken, these results constitute the foundations on which the following experiments have been built up. The SES shall be characterized by both its average properties and its fluctuations. First, we discuss the average current that introduce to the general properties of the

SES. Then we turn on to the measurements of short-time correlations that demonstrates how quasi-ideal single charge emission can be achieved.

Then, chapter 3 is dedicated to the realization of a first electron quantum optics experiment by implementing the electronic analog of the Hanbury-Brown & Twiss experiment, where single electrons and holes are individually partitioned on a beamsplitter. We emphasize the difference arising from the AC nature of the partitioned current [85–87] in comparison with previous experiments realized on a continuous flow of electrons. In our case, the HBT correlations give access to the total number of elementary excitations generated by the source [88, 89]. This can not be accessed in the autocorrelations (without partitioning) due to the existence of neutral excitations (electron/hole pairs) that remain undetectable. As a matter of fact, the results we obtained are consistent with the emission of a single electron-hole pair. However, they are deeply modified by the presence of thermal excitations, as antibunching takes place between thermal excitations and the produced quasiparticles. It offers a way to probe the energy spectrum of the triggered excitations, that can be tuned by modifying the operating parameters.

In chapter 4, we propose an experimental investigation of the effects of Coulomb interaction that couples the two co-propagating edge channels at filling factor $\nu = 2$. Then, the mesoscopic capacitor is used not as a SES, but as a way to generate charge density waves selectively in the outer edge channel. Due to capacitive coupling between the two channels, a current is induced in the inner channel that holds details on the interactions. In particular, we have been able to demonstrate and analyze the appearance of two new eigenmodes of propagation in the system of two coupled channels: one is fast and carries charge, while the slow one is neutral.

Finally, chapter 5 presents results on an electronic analog of the Hong-Ou-Mandel experiment: two independent sources generate mono-electronic excitations in each input of a beamsplitter, so that two-particle interference [25] can occur if excitations are indistinguishable and reach simultaneously the beamsplitter. This challenging experiment allows to verify that we can generate independent excitations produced separately that show a certain degree of indistinguishability despite interactions and relaxation.

Chapter 2

Implementation of a single electron/hole source

Introduction to chapter 2

In this chapter, we summarize the major results obtained on the single electron source before the beginning of this work. First, we establish both the general theoretical framework of Floquet scattering theory [90, 91], that will be used throughout this study as a basis for numerical simulations of our results. Then, we concentrate on average current measurement that offer an overall understanding of the behavior of the SES. Both time-resolved and homodyne measurements are broached. The latter are used daily to calibrate the properties and determinate the best set of parameters before turning to noise measurements. Finally, we end up by detailing the results on short-time current autocorrelations. They provide deep insights on the emission dynamics and are used to prove that quasi-ideal single charge emission can be achieved under appropriate operating conditions.

2.1 Theoretical description of the single electron source

In this section, we present a theoretical description of the driven mesoscopic capacitor, that will be used as a single electron/hole source in the following chapters. The mesoscopic capacitor consists of a quantum dot, whose size varies from 0.8 to 1.6 μm, tunnel-coupled to the rest of the 2DEG via a quantum point contact (QPC). The quantum dot is capacitively coupled to a top-gate. When the electric potential of this electrode is driven periodically, charges are periodically pumped in and out of the quantum dot, so that an AC current is generated. The driven mesoscopic capacitor can be described as a time-dependent scatterer, modifying the propagation of the electrons in the nearby channel. This description, known as the Floquet scattering formalism was first introduced by Moskalets and Büttiker in [90, 92]. Equivalent description in time-domain has also been proposed [93], and complementary studies using discrete tight-binding chain has been carried out [94]. In addition to this, electron quantum optics devices can be depicted using the electron coherence functions. Grenier *et al.* have indeed developed a theory of electronic coherence [45] particularly suitable for picturing electron optics experiments, such as the Hanbury-Brown & Twiss one, described in chapter 3 page 62. We present how these coherence functions can be used practically to describe our system, and connect them to the Floquet scattering picture.

2.1.1 Floquet scattering theory

2.1.1.1 Modeling the mesoscopic capacitor

A scheme of the source is presented in Fig.2.1. In the integer quantum Hall regime, electron transport is provided by the quantum Hall edge channels, on the edges of the sample. Working preferably at filling factor $\nu = 2$ (for a perpendicular magnetic field $B \sim 3 - 4$ T [95, 96]), only two edge channels contribute. The quantum dot is tunnel coupled only to the outer edge channel of the reservoir. As a consequence, during the emission process, the inner edge channel does not play any role and will be ignored. Moreover, at this filling factor, edge states are spin-polarized, so that the spin degree of freedom is not taken into account in this description.

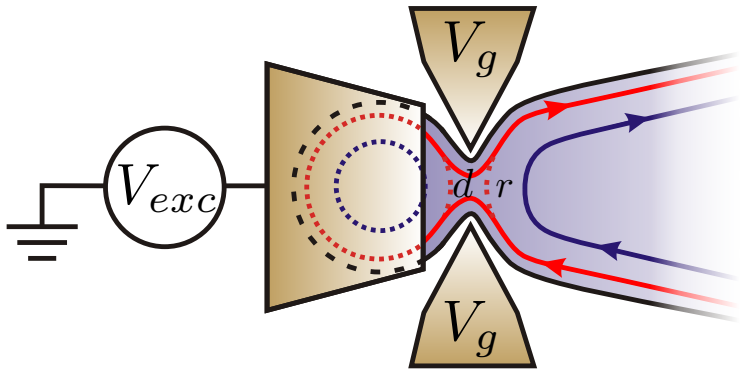

FIGURE 2.1: **Scheme of the mesoscopic capacitor** – A quantum dot is etched in the 2DEG (in blue) and tunnel coupled to the rest of the gas via a QPC, whose transmission is controlled via the gate voltage V_g. An electronic wavepacket in the outer edge channel of $\nu = 2$ (in red) is either transmitted inside the dot with a transmission coefficient d, or reflected with a reflexion coefficient $r = \sqrt{1 - |d|^2}$. A top gate electrode, capacitively coupled to the quantum dot, is driven with a gate voltage V_{exc} at GHz frequencies to induce an AC current in the reservoir.

The quantum point contact then acts as a tunnel barrier of transmission d and reflexion r (in amplitude) for the electronic waves. The quantum dot can thus be seen as a Pérot-Fabry interferometer: an electron wavepacket incoming on the dot can either be reflected with probability $|r|^2$ of tunnel into the dot with probability $|d|^2 = D = 1 - |r|^2$. Inside the dot, the electron performs a certain number of turns, and the wavefunction acquires a phase factor that depends on the electric potential in the dot. Finally the electron escapes the dot. The coherent sum of all the outgoing electronic waves thus constitutes the outgoing wavepacket, related to the incoming wavepacket via the Floquet scattering matrix.

2.1.1.2 Case of a static potential and density of states

These considerations can now be translated in a mathematical language. We assume that the dot, seen as a time-dependent scatterer, is lumped at point $x = 0$, and denote $\hat{a}(t), \hat{b}(t)$ the annihilation operators at time t respectively for the incoming/outgoing modes. Let us consider an electron entering the dot at time t_1, performing $q \in \mathbb{N}$ turns in the dot, each in a finite time τ_0, and escaping at time t_2. If $q = 0$, the electron is in fact directly reflected, so that $t_1 = t_2$. In that case, the phase acquired by the wavepacket is $\phi_0 = 0$, whereas the amplitude of the wavepacket takes a factor r. If $q \neq 0$, $t_2 - t_1 = q\tau_0$, and the phase acquired then depends on the potential inside the dot. The electron, when inside the dot, is indeed submitted to a potential V_0, where V_0 is a DC voltage, used to control the potential inside the dot. The phase after q turns can then be written $\phi_q = \frac{e}{\hbar} V_0 (t_2 - t_1) = \frac{qeV_0\tau_0}{\hbar}$. The amplitude of the wavepacket takes a factor $-d^2 r^{q-1}$. Summing over the number of turns q then yields :

$$\hat{b}(t_2) = r\hat{a}(t_2) - \sum_{q=1}^{\infty} d^2 r^{q-1} e^{-i\phi_q} \hat{a}(t_2 - q\tau_0) \tag{2.1}$$

$$= \int dt_1 \; U(t_2, t_1)\hat{a}(t_1) \tag{2.2}$$

where $U(t_2, t_1)$, relating the incoming state at time t_1 to the outgoing state at time t_2 is the so-called Floquet scattering matrix, written in the time domain:

$$U(t_2, t_1) = r\delta(t_2 - t_1) - d^2 \sum_{q=1}^{\infty} r^{q-1} \delta(t_2 - t_1 - q\tau_0) e^{-i\frac{qeV_0\tau_0}{\hbar}} \tag{2.3}$$

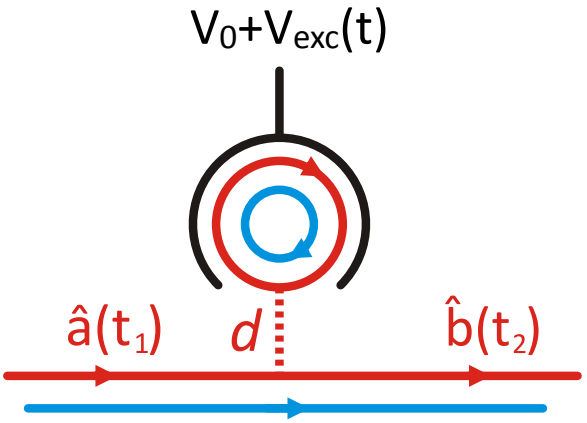

FIGURE 2.2: **Scheme of the mesoscopic capacitor modeled as a time-dependent scatterer** – The electron in input mode $\hat{a}$ enters the dot at time t_1, performs q circles, and escapes in output mode $\hat{b}$ at time t_2. Only the outer edge channel (depicted in red) of the reservoir is coupled to the internal edge channel with a transmission d, while the inner one does not play any role.

Though the interpretation of the previous relation is quite clear, working in the energy domain enables faster and easier numerical computation of the quantities of interest (such as the current generated by the source, or the current correlations in different geometries), that we will derive later in this manuscript. We consequently introduce the expression of the scattering matrix $U(\epsilon, \epsilon')$ defined by the relations :

$$U(\epsilon', \epsilon) = \int dt' dt\, U(t', t) e^{\frac{i}{\hbar}(\epsilon' t' - \epsilon t)} \tag{2.4}$$

$$\hat{b}(\epsilon') = \int d\epsilon\; U(\epsilon', \epsilon) \hat{a}(\epsilon) \tag{2.5}$$

$$\hat{b}(\epsilon) = \int \frac{dt}{\sqrt{h}} e^{i\epsilon t/\hbar} \hat{b}(t) \tag{2.6}$$

In the case of a static potential envisioned in this section, Eq.(2.5) in fact reduces to $\hat{b}(\epsilon) = \mathcal{S}(\epsilon)\hat{a}(\epsilon)$ where $\mathcal{S}(\epsilon)$ is the stationary scattering matrix, given by :

$$\mathcal{S}(\epsilon) = \frac{r - e^{i\tau_0(\epsilon - \epsilon_0)/\hbar}}{1 - re^{i\tau_0(\epsilon - \epsilon_0)/\hbar}} \tag{2.7}$$

where $\epsilon_0 = eV_0$. The density of states in the dot can then be computed from the static scattering matrix $\mathcal{S}$ [97]:

$$\mathcal{N}(\epsilon) = \frac{1}{2\pi i} \mathcal{S}^*(\epsilon) \frac{d\mathcal{S}}{d\epsilon}(\epsilon) \tag{2.8}$$

$$= \frac{1}{\Delta} \frac{1 - r^2}{1 - 2r\cos\left(\frac{2\pi(\epsilon - \epsilon_0)}{\Delta}\right) + r^2} \tag{2.9}$$

For perfect transmission ($r = 0$), the density of states is constant, $\mathcal{N}(\epsilon) = 1/\Delta$ (see Fig.2.3). The quantum dot is completely open, so that no internal structure appears in the density of states. For $r \neq 0$, $\mathcal{N}(\epsilon)$ exhibits a series of equally spaced peaks, corresponding to the discrete levels in the dots. The level spacing $\Delta = \frac{h}{\tau_0}$ is on the order of a few Kelvins. The tunnel coupling (with transmission D) to the electron gas broadens the levels, with a width given by $\hbar\gamma = \frac{D\Delta}{2\pi}$. In the limit $D \to 0$, the peaks are lorentzian:

$$\mathcal{N}(\epsilon) = \sum_n \frac{2}{\pi\hbar\gamma} \frac{1}{1 + \left(\frac{\epsilon - \epsilon_0 - n\Delta}{\hbar\gamma/2}\right)^2} \tag{2.10}$$

The static potential V_0 can then be used to modify the position of the levels at equilibrium, with respect to the Fermi level of the leads ϵ_F, which we will set to zero throughout this manuscript. Introducing the phase shift $\phi_0 = \epsilon_0\tau_0/\hbar$, two configurations are of particular interest. When $\phi_0 = 0$, ($\epsilon_0 = 0$), the Fermi level of the reservoir is at resonance with the highest occupied level in the dot. When $\phi_0 = \pi$, ($\epsilon_0 = \Delta/2$), at equilibrium,

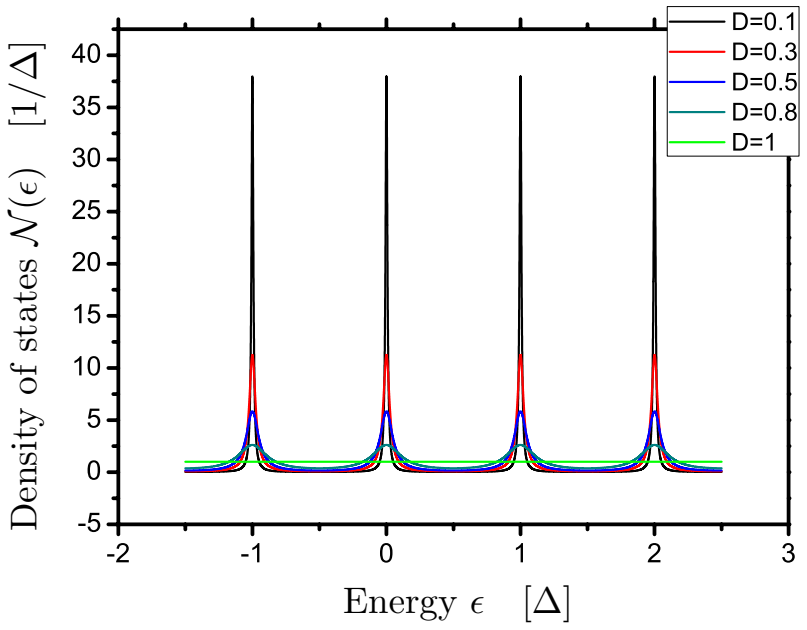

FIGURE 2.3: **Simulations of the density of states $\mathcal{N}(\epsilon)$ in the dot, for different transmissions** D – For low transmissions, $\mathcal{N}(\epsilon)$ exhibits equally spaced lorentzian peaks, with a spacing Δ, and a width $\hbar\gamma = \frac{D\Delta}{2\pi}$. For $D = 1$, $\mathcal{N}(\epsilon) = 1/\Delta$ is constant: no structure appears in the density of states.

the Fermi level of the reservoir lies midway between the highest occupied level and the lowest unoccupied level.

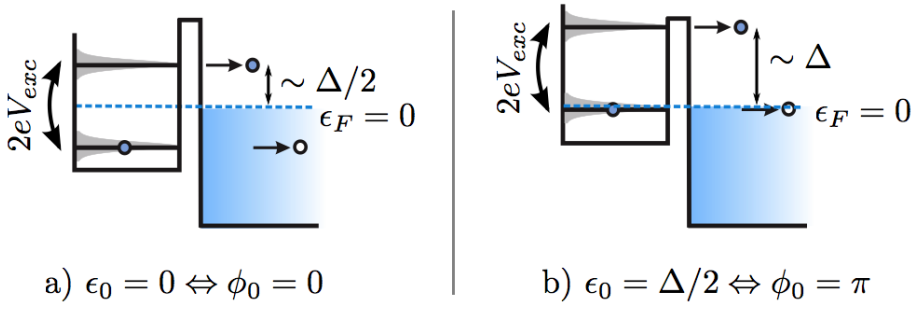

FIGURE 2.4: **Scheme of the position of levels in the dot** – A voltage of amplitude $V_{exc} = \Delta/2e$ is applied on the top-gate, shifting the energy levels. a) For $\phi_0 = 0$, levels are driven far from the Fermi level $\epsilon_F = 0$. b) For $\phi_0 = \pi$, levels come very close to the Fermi level when driven.

We present these two positions in Fig.2.4. Anticipating on the next section, and accordingly with section 1.2.1.4, we examine the motion of the levels when driven with an excitation voltage V_{exc} verifying $2eV_{exc} \sim \Delta$. If $\phi_0 = 0$ (panel a), the level lies at the Fermi level ϵ_F in the absence of drive. When excitation is turned on, the level is driven symmetrically with respect to Fermi level, and at rather high energies (on the order of $\Delta/2$). On the contrary, if $\phi_0 = \pi$ (panel b), two levels contribute: they oscillate between

very high energies ($\pm\Delta$), and energies close to the Fermi level. We will see later that in this situation, the properties of the source are quite sensitive to the characteristics of the Fermi sea and of the excitation signal.

Quantum and geometrical capacitances, issue of interactions

In previous discussion, we have related the density of states to the trajectory of electrons visiting the dot: as this trajectoire is closed, an orbital level spacing arises $\Delta_o = h/\tau_0$. However, we have not taken into account the charging energy $E_c = e^2/C_g$, where C_g is the geometrical capacitance. The sample has been designed to maximise C_g, and G. Fève and F.D. Parmentier have given [6, 84] serious experimental evidence that both contributions are of the same order of magnitude $E_c \simeq \Delta_o \simeq 1$ K for dots of micron perimeters. In this regime of relatively low contribution of interactions (unlike metallic dots), we describe our results by non-interacting models, but simply take into account a renormalization of $\Delta_o \to \Delta = \Delta_o + E_c$. Please note that our calibration of the dot in fact gives direct access to the renormalized level spacing Δ. This approach has been validated by several articles [98, 99]. However, though we do not observe these effects in our case (spin-degeneracy lifted and strong orbital level spacing), interaction-induced effects have been widely investigated [100–105] in similar geometries but with stronger interactions, metallic dots, or spin-degenerated dots.

2.1.1.3 Case of a periodic drive

In order to induce a current in the outgoing edge channel, one can now add an ac component $V_{exc}(t)$ on the top-gate electrode, so as to modulate the potential in the quantum dot and thus trigger the pumping of electrons in and out of the quantum dot. The Floquet scattering theory that we develop in this paragraph deals with any type of modulation as long as it is periodic. We denote by $\Omega = \frac{2\pi}{T} = 2\pi f$ the pulsation of the drive, also defining f the drive frequency and T the period of modulation.

In this manuscript, two cases are envisioned. The first one is the case of a square drive, that appears to be the best choice to produce single electrons and holes at high energies, i.e. well-separated from the thermal excitations already present in the gas. The second case envisioned is the sine drive, that allows analytical treatment in the adiabatic limit $\Omega \to 0$ [24, 90, 92], and provides an harmonic excitation that we will put to good use in the study of interaction between edge channels (chapter 4 page 108).

An electron entering the dot at time t_1, performing q round trips and escaping at time t_2 then acquires an additional phase $\Delta\phi_q = \frac{e}{\hbar}\int_{t_1}^{t_2} V_{exc}(t)dt$. Since the drive V_{exc} is T-periodic, this phase can be expressed in terms of the Fourier coefficients c_n of the function $\xi : t \mapsto \exp(-i\frac{e}{\hbar}\int_0^t V_{exc}(t')dt')$. Here we will specify that the potential V_{exc} is

an even function of time t. This can be obtained by an appropriate choice of the time reference for a square and sine voltage. Under this assumption, the Fourier coefficients c_n are real, and we obtain:

$$\begin{aligned} \xi(t) &= e^{-i\frac{e}{\hbar}\int_0^t V_{exc}(t')dt'} = \sum_n c_n e^{-in\Omega t} \\ e^{-i\Delta\phi_q} &= \sum_{n,n'} c_n c_{n'} e^{-i\Omega(nt_2 - n't_1)} \end{aligned} \tag{2.11}$$

No compact formula was found for the Floquet scattering matrix U in the time domain, but rather in the energy domain. Because of the T-periodicity of the driving excitation, U can be decomposed in the following way:

$$\begin{aligned} U(t',t) &= \left[r\delta(t'-t) - d^2\sum_{q=1}^{\infty} r^{q-1}\delta(t'-t-q\tau_0)\right] e^{-i\frac{e}{\hbar}\int_t^{t'}(V_0+V_{exc}(\tilde{t}))\,d\tilde{t}} \\ &= \sum_m U_m(\tau) e^{-im\Omega\bar{t}} \end{aligned} \tag{2.12}$$

with[1] $\tau = t - t'$, $\bar{t} = \frac{t+t'}{2}$. A double Fourier transform then yields:

$$U(\epsilon',\epsilon) = \sum_m U_m(\epsilon' - \frac{m}{2}\hbar\Omega)\delta(\epsilon' - \epsilon - m\hbar\Omega) \tag{2.13}$$

$$U_m(\epsilon) = \sum_n c_n c_{n+m} \mathcal{S}\big(\epsilon - (n+\frac{p}{2})\hbar\Omega\big) \tag{2.14}$$

$$\hat{b}(\epsilon') = \sum_m U_m(\epsilon' - \frac{m}{2}\hbar\Omega)\hat{a}(\epsilon' - m\hbar\Omega) \tag{2.15}$$

where $\mathcal{S}$ is the static scattering matrix given by Eq.(2.7). Equation (2.15) clearly demonstrates that scattering occurs through the emission or absorption of a certain number m of energy quanta $\hbar\omega$. U_m is indeed the scattering amplitude associated with the transfer (absorption if $m > 0$, emission if $m < 0$) of m energy quanta, from the driving signal to the scattered electron. These relations are consistent with the static case developed in section 2.1.1.2 : when the excitation drive is turned off, we recover $U_m(\epsilon) = \mathcal{S}(\epsilon)$, and only elastic processes occur.

2.1.2 Coherence functions in the Floquet formalism

Floquet scattering theory provides the main framework for analyzing our experimental results. In this paragraph, we express the coherence functions of the single electron/hole

[1] Due to the underlying periodicity of the drive, this type of decomposition will appear for several quantities of interest throughout the manuscript. The notations employed here are detailed in Appendix A and will be thoroughly kept in every calculation

Gauge transformation

In the previous paragraph, the quantum dot is seen as a time-dependent scatterer, whereas the incoming mode $\hat{a}(\epsilon)$ is assumed to be at equilibrium. This derivation of the scattering matrix U [91] is somewhat different from the calculation presented in previous works [6, 83] where the quantum dot was supposed to be at a fixed potential whereas the leads were driven via the excitation voltage $V_{exc}(t)$. These two descriptions are in fact equivalent up to the gauge transformation $\hat{a}(\epsilon) \to \sum_q c_q \hat{a}(\epsilon - q\hbar\Omega)$. However, only the derivation presented previously can be adapted to the case where two (or more) unsynchronized excitation drives are used in the same experiment (see for example the two-particle Hong-Ou-Mandel experiment described in chapter 5 page 146). Consequently, we will concentrate on the gauge adopted in 2.1.1.3. More details can be found in appendix A.3 of reference [84]

source in terms of Floquet scattering matrix, thus connecting the previous paragraphs to Floquet scattering theory.

Following the notation of section 2.1.1, and denoting $\hat{b}$ the mode at the output of the quantum dot, the electronic coherence function at the output of the time dependent scatterer is:

$$\mathcal{G}^{(e)}(t,t') = \langle \hat{b}^\dagger(t')\hat{b}(t)\rangle_\rho \tag{2.16}$$

The main difficulty to compute $\mathcal{G}^{(e/h)}$ lies in the quantum average $\langle \dots \rangle_\rho$ over the non-equilibrium state in mode $\hat{b}$. This difficulty is circumvented by relating $\hat{b}(t)$ to $\hat{a}(t)$ using Eq.(2.1). The quantum average is then calculated on the field operator $\hat{a}$ of the lead (supposed in state $|F_\mu\rangle$), yielding the results:

$$\begin{aligned}\mathcal{G}^{(e)}(t,t') &= \int dt_1 dt_1'\, U^*(t',t_1')U(t,t_1)\langle \hat{a}^\dagger(t_1')\hat{a}(t_1)\rangle_\mu \\ &= \int dt_1 dt_1'\, U(t',t_1')U^*(t,t_1)\mathcal{G}_\mu^{(e)}(t_1-t_1')\end{aligned} \tag{2.17}$$

This formula shows how Floquet scattering matrix acts on the coherence functions to propagate from the state of equilibrium in the lead to the periodically driven state after the quantum dot. Once again, we translate these results in energy domain. As the source is T-periodic, the coherence function is periodic in $\bar{t} = \frac{t+t'}{2}$. Consequently, $\mathcal{G}^{(e)}$ can be written a Fourier transform with respect to $\bar{t}$ and $\tau = t - t'$:

$$\mathcal{G}^{(e)}(t,t') = \sum_n e^{-i\Omega n\bar{t}}\mathcal{G}_n^{(e)}(\tau) \tag{2.18}$$

Each $\mathcal{G}_n^{(e)}(\tau)$ can then be expressed as a Fourier transform:

$$\mathcal{G}_n^{(e)}(\tau) = \int \frac{d\epsilon}{h}\, e^{-i\epsilon\tau/\hbar}\mathcal{G}_n^{(e)}(\epsilon) \tag{2.19}$$

A rather lengthy calculation then yields the following result :

$$\mathcal{G}_n^{(e)}(\epsilon) = \sum_m U_m^*(\epsilon)U_{m+n}(\epsilon + \frac{n}{2}\hbar\Omega)f_\mu(\epsilon - \frac{m}{2}\hbar\Omega)) \tag{2.20}$$

The contribution of the Fermi sea can be easily isolated. It is obtained by taking $U_m(\epsilon) = \delta_{m,0}$, representing the physical situation where no scattering occurs. Then, $\mathcal{G}_n^{(e)}(\epsilon) = f_\mu(\epsilon)\delta_{n,0}$. Using the unitarity relation on Floquet matrix elements (see appendix A), $\mathcal{G}^{(e)}(t,t')$ decomposes as:

$$\mathcal{G}^{(e)}(t,t') = \mathcal{G}_\mu^{(e)}(t-t') + \Delta\mathcal{G}^{(e)}(t,t') \tag{2.21}$$

$$\Delta\mathcal{G}^{(e)}(t,t') = \sum_n e^{-i\Omega n\bar{t}}\Delta\mathcal{G}_n^{(e)}(\tau) \tag{2.22}$$

$$\Delta\mathcal{G}_n^{(e)}(\epsilon) = \sum_m U_m^*(\epsilon)U_{m+n}(\epsilon + \frac{n}{2}\hbar\Omega)\big(f_\mu(\epsilon - \frac{m}{2}\hbar\Omega) - f_\mu(\epsilon)\big) \tag{2.23}$$

To give a clear meaning to the previous formula is not a simple task. Indeed, the coherence function builds up from the sum of an infinite number of contributions, indexed by the integers m, n. The contribution indexed by integers m, n involve processes in which $m+n$ photons are absorbed and m photons emitted. However, these developments facilitate calculations of quantities such as the average current or the current correlations. They can be expressed simply as a function of $\mathcal{G}^{(e/h)}$, with clearer physical interpretation, and then linked to Floquet matrices for numerical computations.

2.2 Average current

The next paragraphs deal with the first quantity of interest, namely the average current. It summarizes some aspects of the work of Julien Gabelli, Gwendal Fève and Adrien Mahé [6, 82, 83]. Besides, it now constitutes the first diagnosis we establish on new samples before setting up new experiments.

2.2.1 Measuring and simulating the average current

2.2.1.1 Theoretical derivation of the average current

In this paragraph, we derive the average AC current measured in contact 1 when the mesoscopic capacitor is driven. This current is the difference between the average current flowing out of the lead and the current flowing from the source towards the lead.

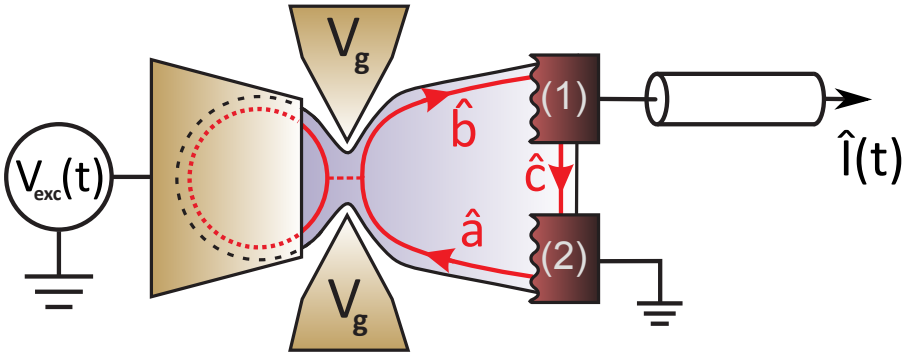

FIGURE 2.5: **Scheme of the source embedded in a 3-terminal geometry**– The input mode is labeled $\hat{a}$, the output mode $\hat{b}$, both modes are related via Floquet scattering matrix. A third mode labeled $\hat{c}$ describes the outer edge channel from contact 1 to 2. Contact 1 is connected to the ground so that $\hat{a}$ is at equilibrium. Contact 2 is connected to the RF amplification and detection scheme (see 4.2.3).

On one hand, the average electric current produced by our single electron source is, as explained in chapter 1:

$$\langle \hat{I}_b(t) \rangle = e\langle \hat{b}^\dagger(t)\hat{b}(t) \rangle \tag{2.24}$$
$$= e\mathcal{G}^{(e)}(t,t) \tag{2.25}$$

On the other hand, since the lead is in state $|F_\mu\rangle$, the equilibrium current flowing out of it reads:

$$\langle \hat{I}_c(t) \rangle = e\langle \hat{c}^\dagger(t)\hat{c}(t) \rangle \tag{2.26}$$
$$= e\mathcal{G}^{(e)}_\mu(t,t) \tag{2.27}$$

The net current in contact 2 is then computed by subtracting the equilibrium contribution, and, as expected, has the same T-periodicity as the drive $V_{exc}(t)$.

$$\langle \hat{I}(t) \rangle = e\big(\langle \hat{b}^\dagger(t)\hat{b}(t) \rangle - \langle \hat{c}^\dagger(t)\hat{c}(t) \rangle\big) \tag{2.28}$$
$$= e\Delta\mathcal{G}^{(e)}(t,t) \tag{2.29}$$

Introducing the harmonics I_k of order k, one can then identify:

$$\langle \hat{I}(t) \rangle = \sum_k I_k e^{-ik\Omega t} \tag{2.30}$$

$$I_k = e\Delta\mathcal{G}_k^{(e)}(0) \tag{2.31}$$

$$= \frac{e}{h}\sum_m \int d\epsilon\, U_m^*(\epsilon) U_{m+k}(\epsilon + \frac{k}{2}\hbar\Omega)\big(f_\mu(\epsilon - \frac{m}{2}\hbar\Omega) - f_\mu(\epsilon)\big) \tag{2.32}$$

In particular, the first harmonic $I_{k=1} = I_\Omega$ is given by:

$$I_\Omega = \frac{e}{h}\sum_m \int d\epsilon\, U_m^*(\epsilon) U_{m+1}(\epsilon + \frac{\hbar\Omega}{2})\big(f_\mu(\epsilon - \frac{m}{2}\hbar\Omega) - f_\mu(\epsilon)\big) \tag{2.33}$$

2.2.1.2 Measuring the average current

Time domain measurements The harmonics of the average current can be computed using Eq.2.32 for example to reconstruct in time domain $\langle \hat{I}(t) \rangle$. It corresponds to a first strategy of measurement of $\langle \hat{I}(t) \rangle$ consisting in the time-resolved acquisition of the current [106]. An ultrafast acquisition card *Acqiris AP240* records the current and averages it over a large number of periods. The results are discussed in 2.2.2.2

Frequency domain measurements Though the results obtained corroborates our theory, the acquisition process takes a lot of time, and an other type of measurement is more commonly used. An homemade/custom GHz homodyne detection enables to measure quickly the first harmonic of the current I_Ω. Both real and imaginary parts are accessed [6, 42]. The setup is quite standard, and will be presented in chapter 4, section 4.2.3 while the results are detailed in section 2.2.3.

2.2.2 Average current in time domain

2.2.2.1 Response to a square drive

When a square voltage is applied, the discrete level in the dot that is promoted above the Fermi level will then relax toward the continuum of states provided by the Fermi sea, during each half-period. This Markovian process gives exponentially decaying probability for the electron to stay in the dot, and consequently exponential average currents. The decay time of this exponential is then necessarily given by the escape time τ_e, itself related to the barrier transmission D: $\tau_e \simeq h/D\Delta$.

This in fact constitutes the asymptotic expression, for low transmissions, of the following formula, demonstrated by Nigg *et al.* [98]:

$$\tau_e = \frac{h}{\Delta}\left(\frac{1}{D} - \frac{1}{2}\right) \tag{2.34}$$

This expression has revealed consistent with numerical simulations and experimental data. In an electronic circuit, this happens to be the classical behavior of an RC circuit. Though we do not detail these developments for the sake of conciseness, the previous results can indeed be understood (in the correct regime of parameter) as the relaxation time $\tau_e = R_q C_q$ of a RC circuit where C_q is the quantum capacitance, and R_q is the series association of the Landauer resistance of the QPC and the interface resistance of a single reservoir:

$$C_q = \frac{e^2}{\Delta} \tag{2.35}$$

$$R_q = \frac{h}{e^2}\frac{1-D}{D} + \frac{h}{2e^2} \tag{2.36}$$

More details can be found in ref. [6, 41, 82, 83, 98, 107].

The interest of time-domain measurements is the possibility to evaluate both transferred charge Q_t and escape time τ_e, by direct comparisons with the following formula, that can be computed in this model of exponentially decaying currents:

$$I_{exp}(t) = \frac{Q_t}{e} e^{-\frac{t}{\tau_e}} \tag{2.37}$$

$$Q_t = e \tanh\left(\frac{1}{4 f \tau_e}\right) \tag{2.38}$$

This can be explicitly unraveled in a time-resolved measurement of the average current, as realized by A. Mahé *et al.* [106] and explained in the following section.

2.2.2.2 Time-domain measurements

In this paragraph is briefly presented the time resolved measurement of the current as realized by A. Mahé *et al.* [106]. An ultrafast acquisition card *Acqiris AP240* records the average current $\langle \hat{I}(t) \rangle$ with a 500 ps resolution. The driving frequency is set to 32 MHz, to reconstruct $\langle \hat{I}(t) \rangle$ with circa 16 harmonics. The recorded signal is averaged in real time over typically 10^8 periods, and corrected for the filtering effects on the measurements. This correction is calculated by measuring the response of the circuit to the parasitic signal, modeled as a pure capacitive coupling.

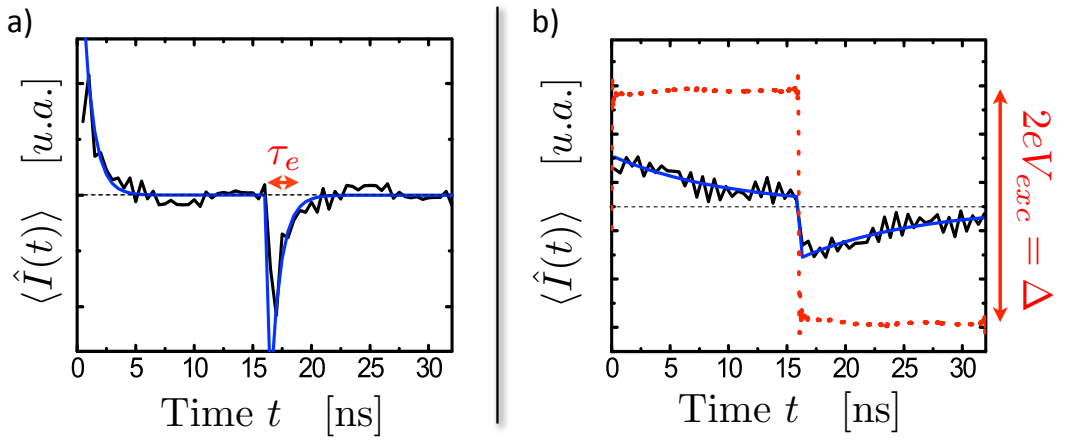

FIGURE 2.6: **Average current in time domain** – In black, experimental data for $\langle \hat{I}(t) \rangle$, compared to an exponential fit (blue line) that yields the transferred charge Q_t and the escape time τ. On panel b), red dots indicates the square excitation signal. The parameters are $f = 32$ MHz, with $D = 0.02$, $\tau = 0.9$ ns, $Q_t = e$ for panel a), and $D = 0.002$, $\tau = 10$ ns, $Q_t = 0.7\,e$ for panel b).

The experimental results are reproduced on Fig.2.6 and corroborate the simple picture developed in 2.2.2.1. In the first panel, the transmission $D = 0.02$ of the QPC is such that the decay time is quite short, and in good agreement with $\tau_e \simeq \frac{h}{D\Delta} \simeq 0.9$ ns. The transferred charge Q_t can be evaluated by integrating the current over half a period, and is close to unity, $Q_t = e$. The mesoscopic capacitor thus works in a regime of single charge emission. In the second panel, the transmission $D = 0.002$ is lowered. Then, the decay time is increased ($\tau_e \simeq 10$ ns) and becomes comparable to the half-period $\frac{T}{2} = 16$ ns. Some electrons/holes are not emitted during the devoted half-period. Consequently, the amplitude of the exponentially decaying current is reduced, as well as evaluated transferred charge $Q_t = 0.7\,e < e$.

Thus, in a regime where the transmission D is sufficiently large so that the escape time τ_e is much smaller than the half-period $T/2$, we verify that the condition $2eV_{exc} = \Delta$ ensures the emission of a quantized charge of $2e$ per period (one electron plus one hole in a period). However, the recording of $\langle \hat{I}(t) \rangle$ is technologically limited to low excitation frequencies and require a long time of averaging. On the opposite, the first harmonic I_Ω of the average current can be measured in a fast and accurate manner using low noise amplifiers and a homodyne detection (detailed in section 4.2.3), giving access to both the real and imaginary part of I_Ω.

2.2.3 Frequency domain measurements

In this section, we present the main results on the measurement I_Ω, used on a daily basis for quick diagnoses of the sample parameters prior to longer noise measurements.

2.2.3.1 First harmonic quantization

The first and most striking feature is the quantization of the first harmonic $|I_\Omega|$ in units of $2ef$. It is the equivalent of the charge quantization discussed in section 2.2.2.2, this in the frequency domain and appears as well when the excitation voltage matches the level spacing $2eV_{exc} = \Delta$. Then, exactly one level is successively promoted above/below the Fermi level of the reservoir, allowing the emission/absorption of exactly one electron per half-period. If the transmission D is large enough so that the escape time is smaller than the half-period, these two charge transfers actually occur and thus give rise to a quantized AC current $|I_\Omega| = 2e/T = 2ef$.

First harmonic quantization as a function of V_{exc} This property is independent of the initial position of the levels in the dot: for $2eV_{exc} = \Delta$, first harmonic quantization is guaranteed regardless of ϕ_0 because the density of states $\mathcal{N}$ is integrated exactly over one of its period Δ.

On the opposite, when $2eV_{exc} \neq \Delta$, quantization of $|I_\Omega|$ crucially depends on ϕ_0. This can be investigated in the following way. As V_g increases, the transmission D increases, and the dwell time of charges in the dot $\tau_e \simeq h/D\Delta$ decreases. However, the gate voltage V_g slightly couples to the gas in the dot and shifts electrostatically the position of the levels ϕ_0. In Fig.2.7 a), measurements for different values of V_g are presented, for which D varies only slightly whereas ϕ_0 describe a variation of π.

Let us concentrate first on the upper panel of Fig.2.7 a), for which the transmission is $D \simeq 0.47$. For $V_g = -334,5$ mV, we have $\phi_0 \simeq 0$. Then the major part of the contribution is integrated for relatively low values of V_{exc} (see Fig.2.7 b). $|I_\Omega|$ rises quickly for small V_{exc} and exhibits a plateau around the quantified value $|I_\Omega| = 2ef$. For $V_g = -335,75$ mV, we have $\phi_0 \simeq \pi$. In that case, the opposite phenomenon occurs (see Fig.2.7 c), so that $|I_\Omega|$ stays constant around 0 for small values of V_{exc}, before rising quickly when $2eV_{exc} \simeq \Delta$. All curves join independently of ϕ for $2eV_{exc} \simeq \Delta$ (that we call the "injection condition") at the value $|I_\Omega| = 2ef$, but a quantization plateau is only observed around $\phi_0 = 0$.

By comparison with lower panel of Fig.2.7 a), for $D \simeq 0.8$, one notices that this quantization gets reinforced when D decreases, as the density of states $\mathcal{N}$ varies more abruptly.

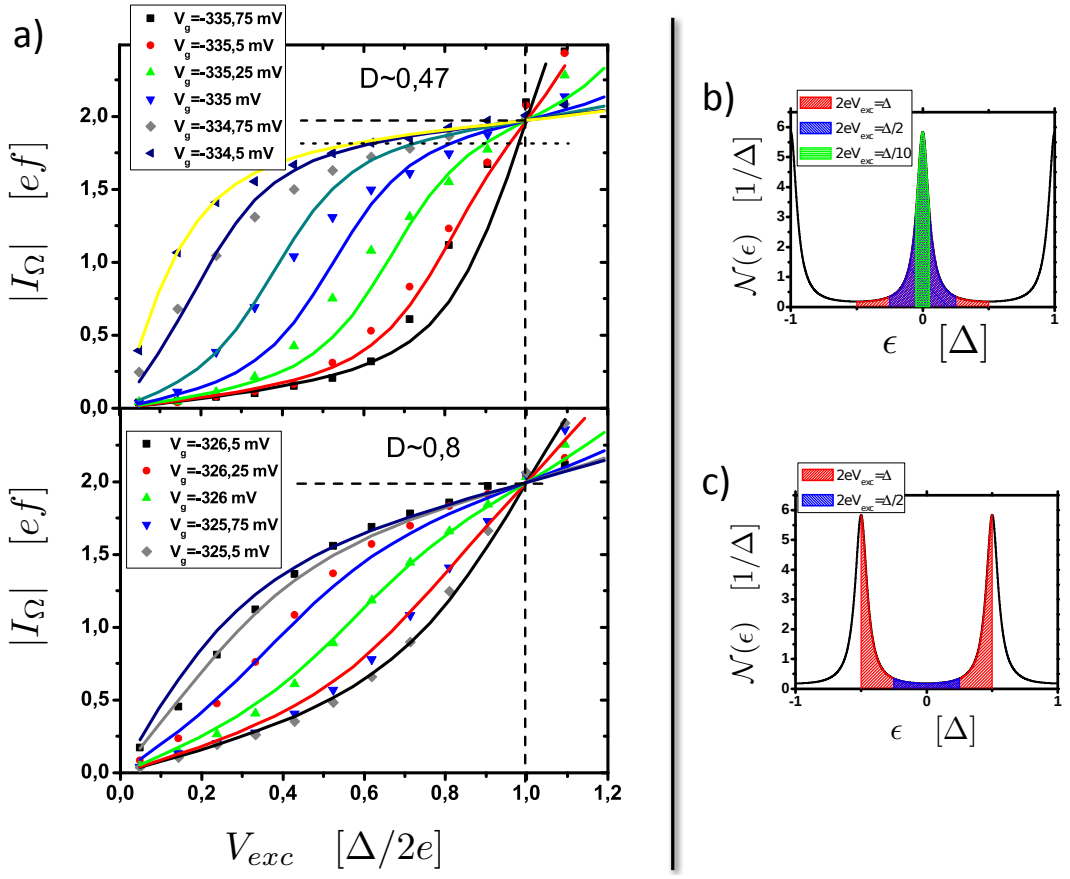

FIGURE 2.7: **Quantization of first harmonic $|I_\Omega|$:** a) For two values of transmission D, first harmonic $|I_\Omega|$ is measured for different gate voltages V_g, that slightly changes the position of levels in the dot ϕ_0. For $\phi_0 = 0$, the last occupied level is at resonance with the Fermi level at equilibrium, and a quantization plateau $|I_\Omega| \simeq 2ef$ is observed for a large range of V_{exc}. Data taken from [84] (for sample $S528$-11 used for the study of autocorrelations, see 2.3). b) For different values of V_{exc}, the checked areas corresponds to the integrated part of the density of states $\mathcal{N}$, for $\phi_0 = 0$. c) Same as b), for $\phi_0 = \pi$.

On the contrary, for $D = 1$, $\mathcal{N}(\epsilon) = \frac{1}{\Delta}$ is constant, and $|I_\Omega|$ varies linearly with V_{exc}, as expected for a pure capacitive coupling between the top gate electrode and the 2DEG.

2D injection plot A complete characterization of the quantization of I_Ω is obtained by representing $|I_\Omega|$ in color scale as a function of both V_g (that varies both D and ϕ_0) and V_{exc}, as in Fig.2.8. The quantization plateaus appear as white diamonds. Two dotted lines symbolize the condition of resonance $\phi_0 = 0$ and anti-resonance $\phi_0 = \pi$ of the levels. When operating on these plateaus, the triggered emission of one electron and one hole per period is achieved on average. The "injection condition" $2eV_{exc} = \Delta$, for which single charge emission is obtained regardless of ϕ_0, is emphasized by the black dashed line. For $V_g < -0.74$ V, $|I_\Omega|$ as the escape time is larger than the half-period

($\tau_e \gg \frac{T}{2}$). For $V_g > -0.72$, diamonds become blurred as the discrete levels in the dot become broader.

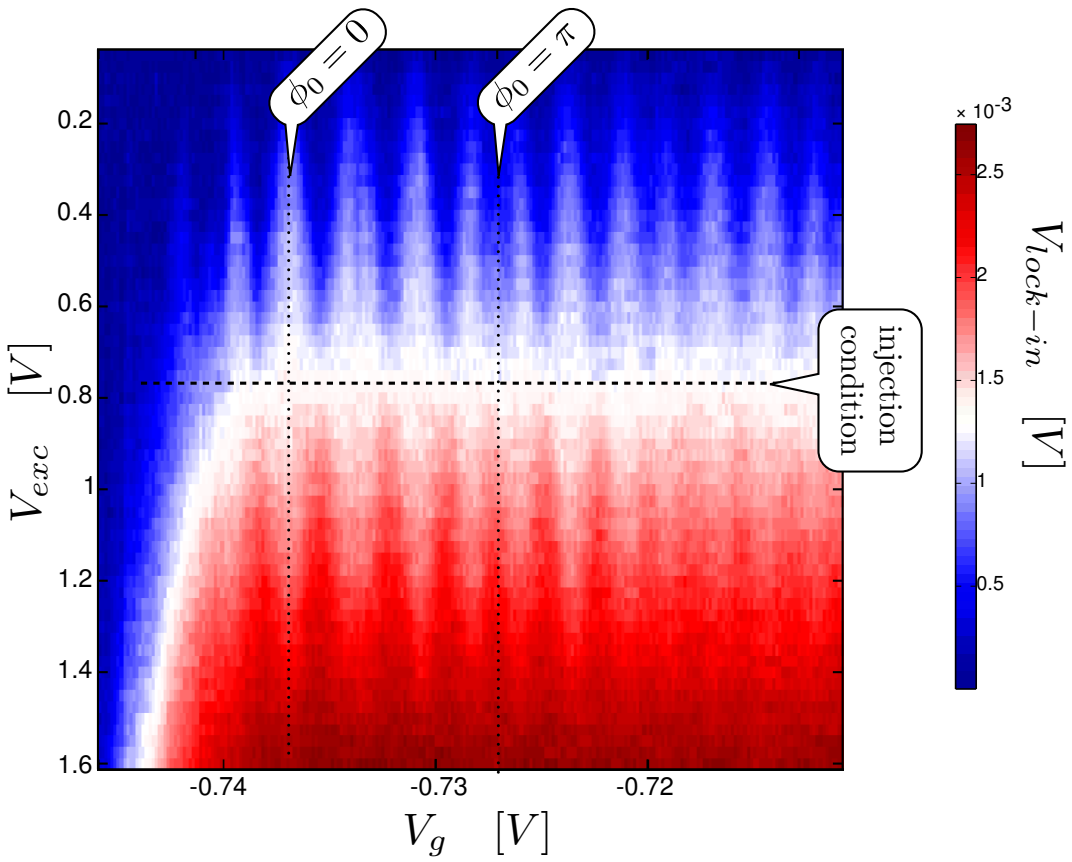

FIGURE 2.8: **2D injection plot** – $|I_\Omega|$ is represented in colorscale as a function of gate voltage V_g and excitation drive V_{exc}, revealing a diamond structure. When on these white diamonds, quantization of the first harmonic $|I_\Omega| = 2ef$ is ensured. (exp. data from sample *S434-C1L25B* used for HBT experiment, see chap. 3).

2.2.3.2 Escape time and average transferred charge

We have seen how to evaluate the escape time τ as well as the average transferred charge when recording $\langle \hat{I}(t) \rangle$ (section 2.2.2.2). These parameters can also be extracted from the measurement of I_Ω. Translating into frequency domain the exponential response of the circuit to a square excitation, one can readily show the following results:

$$\frac{\text{Re } I_\Omega}{\text{Im } I_\Omega} = \Omega\tau_e \tag{2.39}$$

$$Q_t = e \tanh\left(\frac{1}{4f\tau_e}\right) \tag{2.40}$$

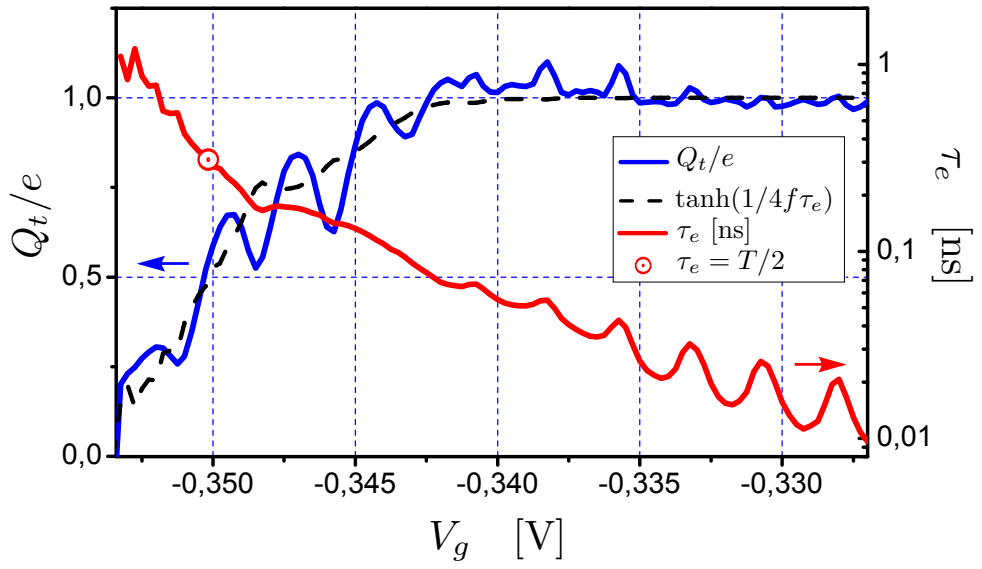

FIGURE 2.9: **Escape time and transferred charge obtained from first harmonic measurement** – Transferred charge Q_t and escape time τ_e can be extracted from average current measurements, via Eqs.(2.39) and (2.40) and presented as a function of gate voltage V_g. Up to small oscillations, the data for Q_t are in good agreement with the expected value $Q_t = e\tanh(1/4f\tau_e)$. Please note that changing the transmission via V_g enables to tune τ_e on two orders of magnitude.

On Fig.2.9 are presented experimental data for Q_t (in blue) and τ_e (in red), extracted as explained from I_Ω. First, we notice that τ_e can be varied on two decades. Then, up to some oscillations, the extracted transferred charge Q_t is in good agreement with prediction of Eq.(2.40) (in black dashed line).

2.3 Current correlations of a single charge emitter

In this section, we present both the theoretical and experimental results obtained concerning the autocorrelations of the current emitted by the single electron/hole source. First, we discuss the usefulness of current autocorrelations to probe irregularities in the emission of single particles. Using the wavepacket model previously discussed, we then derive the fundamental noise of a perfect single charge emitter and compare it with our experimental data, thus proving single charge emission under appropriate operating conditions [95]. Finally, we complete this study by providing two models that describe entirely the observed features of the noise, and in particular establish the universal/non-universal character of the observed fluctuations depending on the parameters.

2.3.1 Limits of average measurements

In the previous section, we have characterized the triggered emission of electrons and holes using average current measurements, either in time or frequency domain and demonstrated that, under appropriate operating conditions, a single electron/hole is emitted on average. The amplitude of the GHz drive has to be chosen to promote exactly one level above the Fermi level of the reservoir, i.e. $2eV_{exc} = \Delta$, and the transmission has to be large enough so that the escape time $\tau_e \simeq \frac{h}{D\Delta}$ is much smaller than the half-period $\frac{T}{2}$. Moreover, placing the level in the dot at resonance when the drive is off ($\phi_0 = 0$) ensures that the quantization is quite insensitive to small inaccuracies in the choice of V_{exc}.

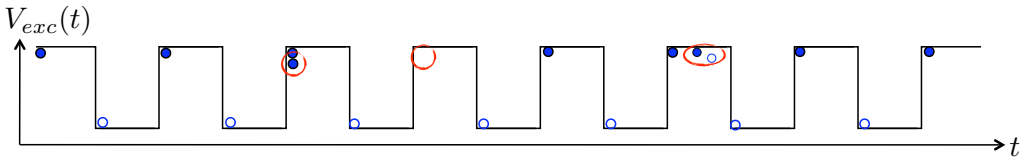

FIGURE 2.10: **Series of emission events** – The excitation signal (black line) triggers the emission of single electron (blue dots) or holes (white dots) in each half period, up to irregularities, circled in red, such as the absence of emission of a particle, or the emission of extra particles or e/h pairs.

Nevertheless, average quantities are not, by nature, sensitive to irregularities in the emission process. Let us consider a series of emission events as a function of time (Fig.2.10). The triggering signal (here a square voltage) is depicted in black lines. On average, during each half-period, an electron (blue dot) or a hole (white dot) is emitted, giving rise to a quantized current $I_\Omega = 2ef$. However, one can imagine some supplementary events (circled in red on Fig.2.10) such as the emission of an extra particle or the absence of emission of a particle, in such a manner that these events do not contribute to the current when averaged on several periods.

Such deviations from perfect single charge emission deteriorate the quality of charge quantization. As demonstrated in a wide variety of systems [108–110], a study of the fluctuations of the current emitted by the source sheds light on these possible discrepancies, as explained in the following sections. In our system, current autocorrelations only reveal at high frequencies due to the AC nature of the source.

2.3.2 Current autocorrelations of a T-periodic emitter

In order to characterize the statistics of the charges generated by the single electron source, it is very relevant to take an interest in the study of the current autocorrelations,

represented by the correlator $\langle \hat{I}(t)\hat{I}(t')\rangle$. From a quantum optics point of view, it bears strong similarities with the second order coherence function for electric fields defined in 1.2.2, from which we can propose a direct interpretation.

2.3.2.1 Coherence functions and fermionic antibunching

In this section, we discuss the general features of the autocorrelations $\langle \hat{I}_b(t')\hat{I}_b(t)\rangle$, viewed under the angle of the previously introduced coherence functions $\mathcal{G}^{(e/h)}$. Making use of Wick's theorem[2] (and Eq.(A.20) in appendix A) we successively find:

$$\begin{aligned}
\langle \hat{I}_b(t')\hat{I}_b(t)\rangle &= \langle \hat{b}^\dagger(t')\hat{b}(t')\hat{b}^\dagger(t)\hat{b}(t)\rangle \\
&= \langle \hat{b}^\dagger(t')\hat{b}(t')\rangle\langle \hat{b}^\dagger(t)\hat{b}(t)\rangle + \langle \hat{b}^\dagger(t')\hat{b}(t)\rangle\langle \hat{b}(t')\hat{b}^\dagger(t)\rangle \\
&= \mathcal{G}^{(e)}(t,t)\mathcal{G}^{(e)}(t',t') + \mathcal{G}^{(e)}(t,t')\mathcal{G}^{(h)}(t,t') \qquad (2.41)\\
&= \mathcal{G}^{(e)}(t,t)\delta(t'-t) + \mathcal{G}^{(e)}(t,t)\mathcal{G}^{(e)}(t',t') - \mathcal{G}^{(e)}(t,t')\mathcal{G}^{(e)}(t',t) \qquad (2.42)
\end{aligned}$$

Even though Eq.(2.42) is not very explicit, an important feature can already be discussed by examining the different contributions [44, 111]. The first one is a poissonian contribution, describing fluctuations proportional to the number of incoming particles, as $\mathcal{G}^{(e)}(t,t) \propto \langle \hat{I}(t)\rangle$. It appears identically in the Shottky formula, and is a reference noise to which the fluctuations are compared.

The second and third terms are corrections to this poissonian noise that encodes the statistics of the emitted electrons. The second term $\mathcal{G}^{(e)}(t,t)\mathcal{G}^{(e)}(t',t')$ is then directly the product of the average currents. The third term comes with a minus sign that stems from the anti-commutation relation of the fermionic operators $\hat{b}/\hat{b}^\dagger$. This sign encodes the anti-bunching of electrons, and would be replaced by a plus sign for photons that naturally exhibit bunching. It contains the correlations between particles and yields information on the emission statistics.

The second part of this formula can actually be written in the following form. We introduce a second-order coherence function (with a normal ordering prescription), which measures the joined probability of measuring two electrons at times t and t':

$$\mathcal{G}^{(2,e)}(t,t') = \langle \hat{b}^\dagger(t')\hat{b}^\dagger(t)\hat{b}(t)\hat{b}(t')\rangle \qquad (2.43)$$

We have then shown that we had:

$$\mathcal{G}^{(2,e)}(t,t') = \mathcal{G}^{(e)}(t,t)\mathcal{G}^{(e)}(t',t') - \mathcal{G}^{(e)}(t,t')\mathcal{G}^{(e)}(t',t) \qquad (2.44)$$

[2] usually holds in general for equilibrium state, but can be demonstrated as well here using Eq.(2.1)

This formula is very interesting as we immediately see that $\mathcal{G}^{(2,e)}(t,t) = 0$: it is not possible to measure two electrons at the same time, in virtue of Pauli principle and fermionic statistics. To prove Eq.(2.44), we have used Wick's theorem, which in general holds only for particular states as equilibrium states, but can also be generalized here using Floquet relations. But in Eq.(2.43), it is clear that any state verifies this statement as $(b^\dagger(t))^2 = 0$ in fermionic algebra. On the contrary, for photons, Wick's theorem leads to:

$$\mathcal{G}^{(2)}(t,t') = \mathcal{G}(t,t)\mathcal{G}(t',t') + \mathcal{G}(t,t')\mathcal{G}(t',t) \tag{2.45}$$

This holds only for a limited number of states such as equilibrium states. In that case, $\mathcal{G}^{(2)}(t,t) = 2$, proving the well-known bunching of photons in thermal light for example. Only non classical light can exhibit $\mathcal{G}^{(2)}(t,t) = 0$, for example in single photon sources, whereas Pauli principle enforces this property in the case of electronic sources.

Revealing the statistics of fermions then requires an access to correlators such as $\langle \hat{I}(t')\hat{I}(t)\rangle$. This is possible through the measurement of current autocorrelations, namely the spectral density of noise $\overline{S}(\omega)$. We give details in the following sections on the link between previous developments and actual measurements.

2.3.2.2 Correlations of a T-periodic current emitter

In the three-terminal geometry depicted in figure 2.5, the central quantity of interest is here the correlator $\langle \delta\hat{I}(t')\delta\hat{I}(t)\rangle$ (with $\delta\hat{I}(t) = \hat{I}(t) - \langle\hat{I}(t)\rangle$). As previously, the current in contact 1 is the difference between $\hat{I}_b$ and $\hat{I}_c$. Since modes $\hat{b}$ and $\hat{c}$ are not correlated it is easy to see that:

$$\langle \delta\hat{I}(t')\delta\hat{I}(t)\rangle = \langle \delta\hat{I}_b(t')\delta\hat{I}_b(t)\rangle + \langle \delta\hat{I}_c(t')\delta\hat{I}_c(t)\rangle \tag{2.46}$$

The second part represents the thermal equilibrium noise in mode $\hat{c}$. It is not related to the properties of the single electron source, and will not be taken into account when measuring the excess noise. We then focus on the first term on the right-hand side, and define :

$$S(t,t') = \langle \delta\hat{I}_b(t')\delta\hat{I}_b(t)\rangle \tag{2.47}$$

Since the emission process is non-stationary (but periodic), usual fluctuating quantities have to be redefined accurately. As the operator $\hat{I}_b(t)$ is itself T-periodic (but non-stationary), the correlator $\langle \delta\hat{I}_b(t')\delta\hat{I}_b(t)\rangle$ depends explicitly on both times t, t' but is also T-periodic. It can thus be decomposed as a Fourier series, and written in the

frequency domain:

$$S(t,t') = \langle \delta\hat{I}_b(t')\delta\hat{I}_b(t)\rangle \quad (2.48)$$
$$= \sum_l S_l(\tau)e^{-il\Omega\bar{t}} \quad (2.49)$$

The experimental setup gives access to the power spectral density of noise, defined as[3]:

$$\overline{S}(\omega) = 2\int d\tau\, \overline{S(t,t')}^{\bar{t}} e^{i\omega\tau} \quad (2.50)$$
$$= 2\int d\tau\, \overline{\langle \delta\hat{I}(t)\delta\hat{I}(t+t')\rangle}^{\bar{t}}\, e^{i\omega\tau} \quad (2.51)$$
$$= 2\int d\tau\, S_0(\tau)e^{i\omega\tau} = 2S_0(\omega) \quad (2.52)$$

where $\overline{\cdots}^{\bar{t}}$ denotes averaging over $\bar{t}$.

So far, we have shown how current autocorrelations could give information on the statistics of electrons/holes emitted by the single electron source by yielding information on $\langle \hat{I}_b(t')\hat{I}_b(t)\rangle$. But this charges are generated among many other electrons and holes that constitute the Fermi sea. The next section is devoted to understanding more in details the Fermi sea contributions and the contributions that provide information our source. This can be achieved using the wavepacket model developed in 1.2.2.3.

2.3.2.3 Effect of the Fermi sea – Wavepacket model

From Eqs.(2.53), and (1.7), it is possible to show that:

$$S(t,t') = e^2\mathcal{G}^{(e)}(t,t')\mathcal{G}^{(h)}(t,t') \quad (2.53)$$
$$= e^2\Big(\mathcal{G}^{(e)}_\mu(t,t)\delta(t'-t) - |\mathcal{G}^{(e)}_\mu(t-t')|^2 + \Delta\mathcal{G}^{(e)}(t,t)\delta(t'-t) - |\Delta\mathcal{G}^{(e)}(t,t')|^2 - \big(\mathcal{G}^{(e)}_\mu(t'-t)\Delta\mathcal{G}^{(e)}(t',t) + \mathcal{G}^{(e)}_\mu(t-t')\Delta\mathcal{G}^{(e)}(t,t')\big)\Big) \quad (2.54)$$

The first two lines of Eq.(2.54) encode the anti-bunching effect described in section 2.3.2.1, but now decomposed over thermal (first line) and excess quasiparticles (second line). The second line encodes the information we are looking for: it contains exclusively the informations on our source, that will be detailed in the next section. These two lines are very similar with what could be obtained with photons, except that we have now two sources of electrons, those generated by the source and the thermal excitations. The

[3]We adopt here and in the rest of the manuscript the "engineering" convention, where a factor 2 is applied to account for both positive and negative frequencies. One can indeed show that the excess noise is symmetric in ω [84].

equilibrium part is of lower interest here and will in fact be subtracted to access the excess noise defined as :

$$\begin{aligned}\Delta S(t,t') &= e^2\Big(\Delta\mathcal{G}^{(e)}(t,t)\delta(t'-t) - |\Delta\mathcal{G}^{(e)}(t,t')|^2 \\ &\quad -\big(\mathcal{G}_\mu^{(e)}(t'-t)\Delta\mathcal{G}^{(e)}(t',t) + \mathcal{G}_\mu^{(e)}(t-t')\Delta\mathcal{G}^{(e)}(t,t')\big)\Big) \end{aligned} \tag{2.55}$$

More interesting are the last two terms (third line of Eq.(2.54)) that have no optical analog since they mix the action of the Fermi sea $|F_\mu\rangle$ with the emitted charges.

The case of a single mono-electronic wavepacket φ_e introduced in 1.2.2.3 gives clear expression of this term and helps to understand the effect of the Fermi sea. Averaging over $\bar{t}$ and performing the integrals, one finds a contribution in $\overline{S}(\omega)$ proportional to:

$$-\int d\epsilon\, f_\mu(\epsilon)|\varphi_e(\epsilon \pm \hbar\omega)|^2 \tag{2.56}$$

For a wavepacket centered on the energy $\Delta/2 \gg kT_{el}$, on can see that these contributions vanish for $|\hbar\omega| < \Delta/2$. Simulations of $\Delta\overline{S}(\omega)$ as a function of the measurement frequency ω then present the general aspect depicted on figure 2.11 (for parameters $\Delta = 2$ K, $T_{el} =$ 50 mK, $\Omega = 2$ GHz, $D = 0.2$). When plotting separately the different components in $\Delta\overline{S}$, one sees that the first two terms control the low-frequency behavior, and especially contain the information about the bunching or anti-bunching of the electrons emitted by the source. This term will consequently be probed in detail by our measurements. The last two term add a frequency cut-off: the presence of the Fermi sea prevents the emission of photons with energies higher than $\Delta/2$. This is related to works from Beenakker *et al.* [112, 113] where they show that the statistics of photons emitted by a DC current impinging on a QPC is modified by the presence of the Fermi sea. They moreover deduce conditions for single photon emission. In our experiments though, the measurement frequency ω is on the order of Ω. We thus probe the regime $\omega \ll \frac{\Delta}{2}$, that enables to concentrate on the time distribution of the charges emitted by the source, since the Fermi sea has no action in this regime.

2.3.2.4 Phase noise

In the regime $\omega \ll \pm\Delta/2$ where the Fermi sea does not play any role, the excess current autocorrelations can be written:

$$\Delta S(t,t') \simeq e^2\big(\Delta\mathcal{G}^{(e)}(t,t)\delta(t'-t) - |\Delta\mathcal{G}^{(e)}(t,t')|^2\big) \tag{2.57}$$

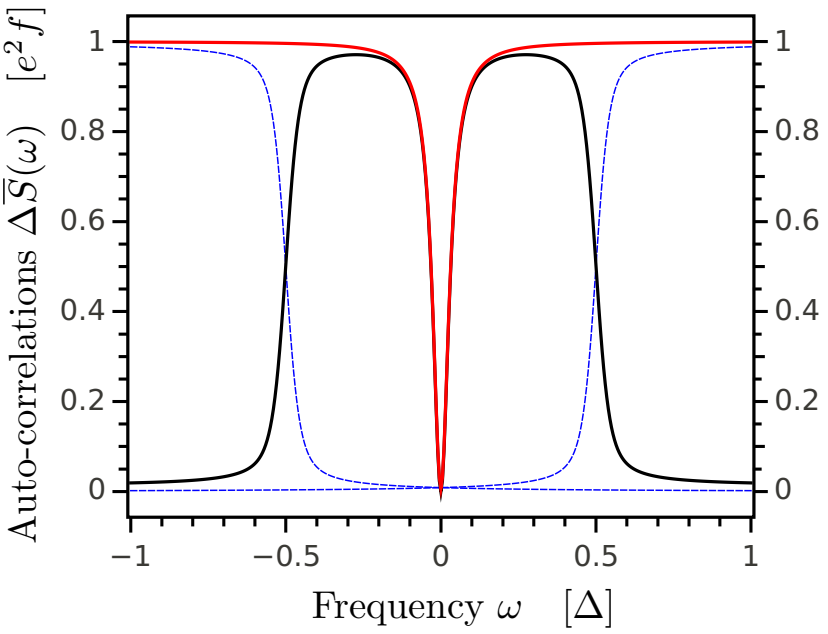

FIGURE 2.11: **General features of autocorrelations as a function of measurement frequency** ω – Excess current autocorrelations $\Delta\overline{S}(\omega)$ are plotted as a function of measurement frequency ω, in black lines. They exhibit a low frequency behavior that describes the antibunching properties of the emitted quasiparticles that are well described by the first line of Eq.2.55 whose contribution is drawn in red line. For frequencies reaching $\omega \simeq \pm\Delta/2$, the presence of the Fermi sea prevents fluctuations at high energies so that $\Delta\overline{S}(\omega) \to 0$. This cut-off frequency is encoded in the last two terms of Eq.2.55, and their contribution is pictured in blue dashed lines: subtracting the blue contribution to the red one gives $\Delta\overline{S}(\omega)$ in black. Parameters are $\Delta = 2$ K, $T_{el} = 50$ mK, $\Omega = 2$ GHz, $D = 0.2$.

In agreement with exponentially decaying currents, we propose to calculate explicitly the different contribution for an exponential wavepacket $\varphi_e(t) = \frac{\theta(t)}{\sqrt{\tau_e}} e^{-\frac{t}{2\tau_e}}$. The average over $\bar{t}$ is done on a period T to simulate a repetition at frequency f of this single shot emission[4]:

$$\begin{aligned}
\Delta\overline{S}(\omega) &= 2e^2 f \left(\int d\epsilon \, |\varphi_e(\epsilon)|^2 - \left| \int d\epsilon \varphi_e(\epsilon) \varphi_e^*(\epsilon + \hbar\omega) \right|^2 \right) \\
&= 2e^2 f \left(1 - \frac{1}{1+\omega^2\tau_e^2}\right) \\
&= 2e^2 f \frac{\omega^2\tau_e^2}{1+\omega^2\tau_e^2}
\end{aligned} \tag{2.58}$$

Moreover, to compare our SES that emits one electron and hole per period (instead of one wavepacket φ_e per period), a factor 2 has to be applied, so that we finally obtain:

$$\Delta\overline{S}_{phase}(\omega) = 4e^2 f \frac{\omega^2\tau_e^2}{1+\omega^2\tau_e^2} \tag{2.59}$$

[4]This implies implicitly that the temporal width τ_e is small: $\tau_e \ll T$.

Several comments can be proposed concerning Eq.(2.59) that is at the core of the following study of the autocorrelations. First, we see that this noise vanishes at zero frequency $\Delta\overline{S}_{phase}(\omega \to 0) \to 0$. This reflects the absence of charge fluctuations at zero frequency/on long times which is a signature of perfect triggered single charge sources: since an excitation signal triggers the emission, there is exactly one wavepacket emitted per emission cycle. As a consequence, information on charge fluctuations can only be obtained by measuring short time autocorrelations, or high-frequency noise.

Second, even for a non-fluctuating number of charges emitted, the emission process is not noiseless. The remaining noise, that we call phase noise, in fact describes the quantum uncertainty on the emission time, related only to one parameter, namely the width of the wavepacket τ_e. It is the hallmark of single charge emission: when one charge is emitted per emission cycle, its noise should fundamentally reduce to this phase noise. This supplies a criterion to establish the ideal single charge emission of a triggered source, and will be the starting point of the next section: by nature, our wavepacket model describes a single particle emitter, whose current correlations will thus be related to fluctuations on the emission time of the particles rather than fluctuations on the number of emitted charges. Consequently, proving that the noise of the SES reduces to the fluctuations of this heuristic model will prove that single charge emission is exactly achieved, and not only on average.

Finally, we can just notice that this noise is ω-dependent, and that proving the ideal single charge emission requires then to vary either ω or τ_e. Varying the frequency ω is very difficult as it requires to develop a detection setup that is both wideband and sensitive. On the opposite, τ_e can be modified easily by changing the transmission of the QPC. This strategy is then followed in our measurements, and the measurement frequency ω is set to $\omega \simeq \Omega$.

2.3.2.5 Noise power spectrum as a function of escape time, in the case $\phi_0 = 0$

Here we present measurements of the autocorrelations $\Delta\overline{S}(\Omega)$ as a function of the escape time τ_e [95]. This experiment was carried out on sample *S528-11*, for which calibrations have yielded a rather high level-spacing of $\Delta = 4.2 \pm 0.2$ K, and an electronic temperature of $T_{el} = 60 \pm 15$ mK. First, we focus on points for which the level is at resonance when $V_{exc} = 0$, situation denoted $\phi_0 = 0$ (see Fig.2.4). Escape times τ_e are obtained independently from average current measurement as detailed in 2.2.3.2, and formula (2.59) is pictured in blue dashes.

The agreement between experimental data measured for $\phi_0 = 0$ and this model is very good in a large transmission regime, for which $\tau_e \ll \frac{T}{2}$, with an agreement of 10%

Experimental setup

The order of magnitude of the current autocorrelations are here given by $e^2 f \simeq 4 \times 10^{-29}\,\mathrm{A^2Hz^{-1}}$. Current fluctuations are converted, via a resistor R_0 into voltage fluctuations and then measured. When measuring high-frequency fluctuations, R_0 is set by the characteristic impedance of RF cables, $R_0 = 50\ \Omega$ so that the conversion factor is small compared to low-frequency measurements where using $R_0 \sim 1 - 10\ \mathrm{k}\Omega$ is frequent. As a consequence, the voltage fluctuations are small and a specific measurement setup was developed by F.D. Parmentier *et al.* [114]. It is mainly based on an impedance matching circuit that enables to choose $R_0 = 120\ \Omega$, and a double-balanced amplifying scheme providing high stability for long measurement times.

consistent with experimental error bars. Under these conditions, the noise spectrum of the driven mesoscopic capacitor is identical to the one of a perfect single particle emitter, that is fundamentally related to the uncertainty on the emission time. This is a very strong and important result, as it is the signature of perfect single charge emission. Thus, the measurement of fluctuations confirms on a solid basis the quantization of the emitted charge, for which average current measurement had already given a glimpse.

However, for larger escape times, $\tau_e \gtrsim T/2$, our model is strongly contradicted by our measurements. This not very surprising, as our model of perfect single charge emitter does not take into account the fact that when $\tau_e \gtrsim T/2$, some charges do not escape from the quantum dot during the devoted emission cycle and fluctuations appear not only on the emission time but also on the number of emitted charge. The transferred charge is then $Q_t < e$ and we in fact recover a shot noise limit (black dashes). Moreover, we have not presented measurements for $\phi_0 = \pi$ (level not in resonance at equilibrium) that would in fact reveal strong discrepancies.

The previous developments have given clear insights about the general physics of fluctuations of periodic sources. A model of perfect single charge emitter has enabled to prove that under certain conditions, quasi-ideal single charge emission could be achieved. However, the description is only partial yet, as several ingredients are still missing: shot noise regime for $\tau_e \gtrsim \frac{T}{2}$, finite temperature $T_{el} \neq 0$. in terms of Floquet matrices, remain largely unclear.

In the next part we present two models that give further insights on current autocorrelations. The first one is an heuristic toy-model that was first introduced by A. Mahé [83], and solved analytically by M. Albert [115]. The analytical results can then be compared with simulations using Floquet scattering framework.

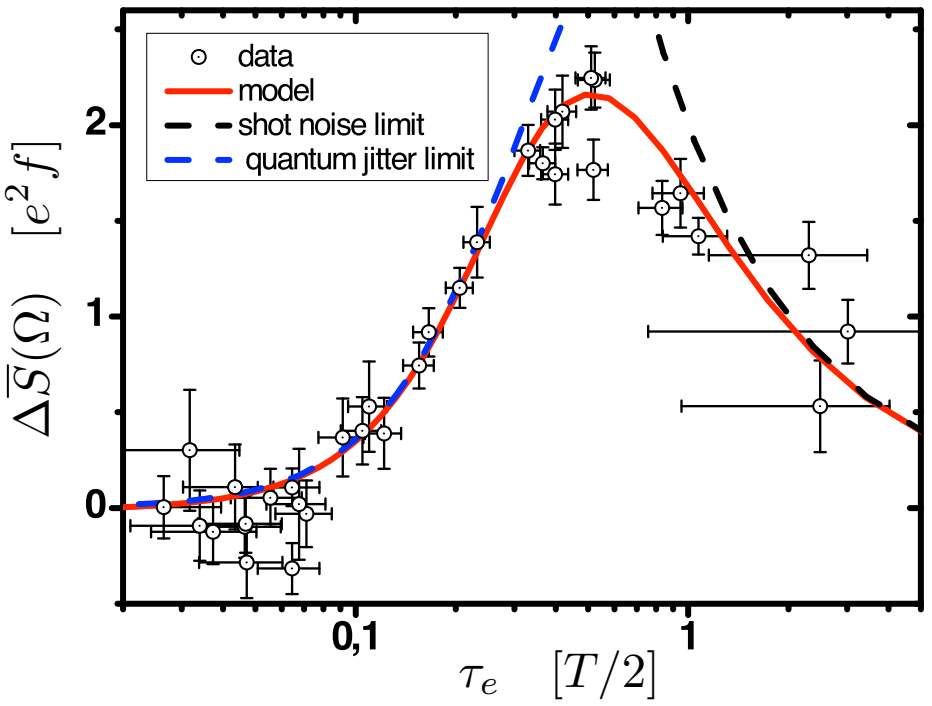

FIGURE 2.12: **Measured noise power spectrum $\Delta\overline{S}(\Omega)$ as a function of escape time τ_e** – Experimental data for $\phi_0 = 0$ are in very good agreement with the phase noise model (Eq. 2.59) in a regime $\tau_e \ll \frac{T}{2}$. Then, single charge emission is achieved. For $\tau_e \gtrsim \frac{T}{2}$, a shot noise regime is recovered. A complete description is provided by both semi-classical and Floquet scattering models (section 2.3.3), in good agreement with experimental data.

2.3.3 Models for current autocorrelations

2.3.3.1 Semi-classical heuristic model

First, we detail the construction of the semi-classical model of the source, based on a few probabilistic rules. As already mentioned, it can be addressed using a master equation approach [115], and yields an analytical formula for the noise of the modeled single charge emitter. But it is also related to the topic of full counting statistics of charges [116, 117]. For conciseness, we then summarize the main results. A detailed review of this model is proposed in Appendix B.

Rules of single particle emission The emitter is described by a few simple rules:

- The charge in the dot can only take two values, 1 or 0, simulating one level only in the dot.

- Inside the dot, the electron performs turns, in a time τ_0, which then naturally appears as the elementary time increment. After each turn, the electron has a probability b to escape.
- Each half-period of the square drive is divided into N turns, $T/2 = N\tau_0$. Emissions of electron can only occur if the charge is 1 in the dot, and only one emission process is permitted during one half-period.
- After the end of the first of the half-period, the second half-period is described with symmetric rules concerning the absorption of electrons: absorptions can only take place if the dot is empty, with a limit of one absorption per half-period.

These simples rules can be simulated easily using pseudo-random number generators. Nonetheless, it is important to understand the limits of this model beforehand, even though most of them are quite obvious. First, this description only applies for a square voltage, for which emission and absorption are clearly triggered by the sudden shifts of potential. Moreover, this incompressible time increment τ_0 renders this model invalid when a time-scale reaches τ_0. This can be the case for $D \to 1$, for which $\tau_e \sim \tau_0$. Last, this model does not take into account the presence of the Fermi sea: no temperature can be simply attributed to the particle reservoir that provides electrons and holes to empty or fill the dot.

Results on average current The successive emission/absorption of holes gives rise to an AC current $I(t)$, pictured on Fig.2.13. A peak (resp. a dip) occurs whenever an electron is emitted (resp. absorbed). The emission rules ensure that every absorption is followed by an emission and vice-versa. Averaging $I(t)$ over a large amount of periods yields the average current $< I(t) >$ and these predictions can then be compared with the experimental results of section 2.2.2.2.

In the domain of validity of the model, we have the following results:

- $< I(t) >$ exhibit exponential decays in each half period, in agreement with experimental results of 2.2.2.2
- The decay time τ_e is in good agreement with the formula $\tau_e = \tau_0(\frac{1}{b} - \frac{1}{2})$ so that using Eq.(2.34) we can identify $b = D, \tau_0 = h/\Delta$.
- The transferred charge per half-period Q_t can also be computed from the previous model and corroborates the formula $Q_t = e \tanh(\frac{1}{4f\tau_e})$.

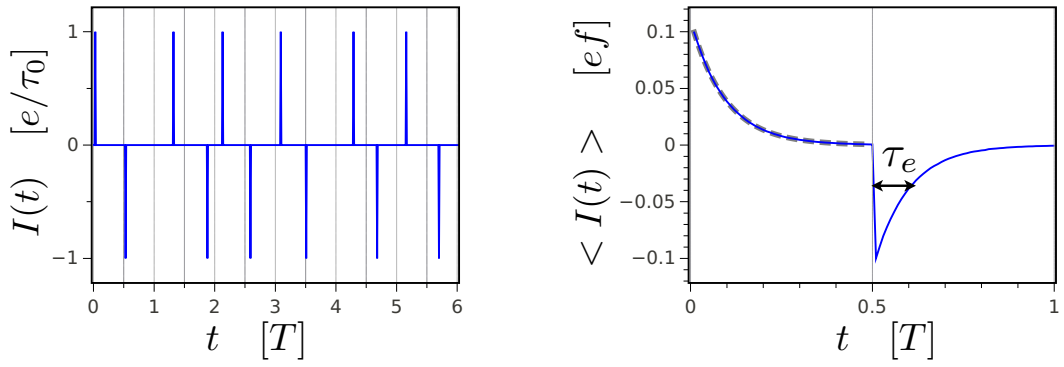

FIGURE 2.13: **Current and average current, computed from the heuristic model** – Instantaneous current (6 periods) and average current (1 period, averaged over 10^6 periods) are presented. In grey dashed line, an exponential fit shows a perfect agreement with simulations. The parameters are: $T = 100\tau_0$, with $b = 0.1$.

Results on current correlations This heuristic model enables to generate sequences of emission/absorption processes, with probabilistic rules that seem to reproduce accurately experimental observation on the average current. Statistical studies of the generated currents $I(t)$ can be pursued beyond average current: we here present the main features of the current correlations of this peculiar single charge emitter.

Two well-defined asymptotic regimes can be clearly identified and are in agreement with the discussion of section 2.3.2.5: phase and shot noise. Analytical calculation is possible in both asymptotic and general regimes from works of A. Mahé *et al.* [83] and M. Albert *et al.* [115].

- *Shot noise regime:* For small escape probabilities, the escape time τ_e becomes comparable or larger than $T/2$, and some emission events do not occur. We obtain the excess noise in this regime

$$\Delta\overline{S}_{shot}(\omega) = \frac{e^2}{\tau_e} = 4e^2 f \times P \tag{2.60}$$

  This expression is similar to the usual shot noise $\overline{S} = 2eI$ with $I = 2ef \times P$.

- *Phase noise regime:* For large probabilities $b = D$ we recover the phase noise limit of a perfect single charge emitter (section 2.3.2.4): if b is large enough so that all charges escape, $P = 1$ and shot noise vanishes. Then, thus average current is written $< I(t) >= e/\tau_e\, e^{-t/\tau_e}$ (in the first half-period). With this expression, $\Delta\overline{S}$ is calculated:

$$\Delta\overline{S}_{phase}(\omega) = 4e^2 f \frac{\omega^2\tau_e^2}{1+\omega^2\tau_e^2} \tag{2.61}$$

This expression is, as expected for a perfect single charge emitter, identical to the one obtain in the wavepacket model 2.3.2.4

- *General case:* M. Albert *et al.* [115] have obtained an analytic formula for the current autocorrelations, valid for all values of $b = D$. One then obtains the noise power spectral density that interpolates between shot noise and phase noise regimes:

$$\begin{aligned}
\overline{S}(\omega) &= 4e^2 f \tanh\Big(\frac{1}{4f\tau_e}\Big)\frac{\omega^2\tau_e^2}{1+\omega^2\tau_e^2} && (2.62)\\
&= \frac{Q_t}{e}\frac{\omega^2\tau_e^2}{1+\omega^2\tau_e^2} && (2.63)\\
&= \frac{1}{4e^2 f}\overline{S}_{shot}(\omega)\overline{S}_{phase}(\omega) && (2.64)
\end{aligned}$$

Finally, the semi-classical model detailed above has enabled to recover both the phase noise and shot noise limits, and has even been completely solved analytically. We now briefly consider a second picture based on the Floquet framework.

2.3.3.2 Autocorrelations in Floquet scattering theory

After the general developments of 2.1.2, current autocorrelations can be readily expressed in the Floquet formalism. Starting from Eq.(2.53), one can easily obtain:

$$\begin{aligned}
\overline{S}(\omega) &= 2S_0(\omega)\\
&= 2e^2\int d\tau \sum_n \mathcal{G}_n^{(e)}(\tau)\mathcal{G}_{-n}^{(h)}(\tau)e^{i\omega\tau}\\
&= \frac{2e^2}{h}\sum_n \int d\epsilon\, \mathcal{G}_n^{(e)}(\epsilon)\mathcal{G}_{-n}^{(h)}(\hbar\omega-\epsilon) && (2.65)
\end{aligned}$$

Knowing how $\mathcal{G}_n^{(e/h)}$ is expressed in terms of Floquet matrix elements U_m (see Eq.(2.20)), we thus get the expression of the autocorrelation [84]:

$$\begin{aligned}
\overline{S}(\omega) &= \frac{2e^2}{h}\sum_p \int d\epsilon \left|\sum_m U_m^*(\epsilon+\frac{m}{2}\hbar\Omega)U_{p-m}(\epsilon+\frac{m}{2}\hbar\Omega-\hbar\omega)\right|^2\\
&\times\ f_\mu(\epsilon)\big(1-f_\mu(\epsilon-\frac{p}{2}\hbar\Omega-\hbar\omega)\big) && (2.66)\\
\Delta\overline{S}(\omega) &= \frac{2e^2}{h}\sum_p \int d\epsilon \left|\sum_m U_m^*(\epsilon+\frac{m}{2}\hbar\Omega)U_{p-m}(\epsilon+\frac{m}{2}\hbar\Omega-\hbar\omega)\right|^2\\
&\times\ \big(f_\mu(\epsilon)-f_\mu(\epsilon-\frac{p}{2}\hbar\Omega-\hbar\omega)\big) && (2.67)
\end{aligned}$$

This last expression is the starting point of numerical simulations that can be compared with both experimental data and semi-classical model.

Now that we have introduced two models to simulate the fluctuations of the current emitted by the source, it is useful to compare both predictions, and confront them to experimental results.

2.3.4 Universal behavior at $\phi_0 = 0$

2.3.4.1 Comparisons between models

Now that we have introduced both models, we present and compare predictions of both Floquet scattering and semi-classical models.

Transmission D/probability amplitude b dependence On Fig.2.14, autocorrelations for $\omega = \Omega$ are plotted as a function of the dot transmission D. The agreement between the two models is excellent and confirms the identification $b = D$. We consequently drop the notation b and only use D in both models.

For small transmissions, $\Delta\overline{S}$ rises linearly with transmission D, and a shot noise regime is observed. Then $\Delta\overline{S}$ reaches a maximum for $Q_t \sim e$ when the uncertainty on the emission time is at its maximum, and then $\tau_e \sim T/2$. As transmission increases, this uncertainty is smaller and smaller, and $\Delta\overline{S} \to 0$. For $D \to 1$, charges systematically escape the dot in each emission cycle, with a very small uncertainty on the emission time (set by $\tau_e \ll T/2$), so that the charges are regularly ordered and the emission process becomes noiseless.

Dependence on the measurement frequency ω We now examine the ω dependence of $\Delta\overline{S}$, as computed from Floquet scattering theory and heuristic model: numerical results are plotted on Fig.2.15. Once again, the agreement between both models is excellent, as the symbols representing scattering model fall exactly on the plain lines from semi-classical simulations (Eq.(2.62)).

First, for a given transmission, we observe a crossover between $\Delta\overline{S}(\omega = 0) = 0$ (due to the triggering of emission) to $\Delta\overline{S}(\omega \to \infty) = \mathrm{C}^{\mathrm{st}}$. Accordingly with Eq.(2.62), the transition between both asymptotic regimes occur for $\omega\tau_e \sim 1$: thus, the smaller the transmission D , the longer the escape time τ_e, the smaller the transition frequency ω.

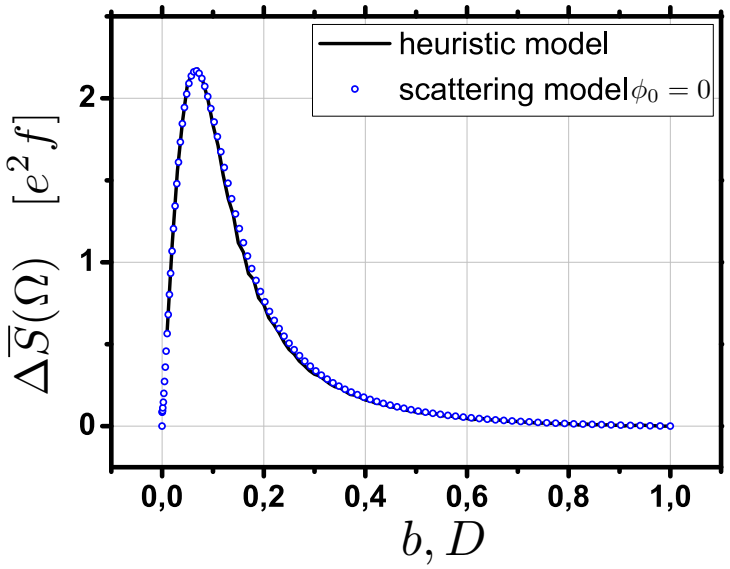

FIGURE 2.14: **Current autocorrelations $\Delta\overline{S}(\Omega)$, predicted by heuristic and Floquet scattering models, as a function of probability b/transmission D** – The excellent agreement between simulations from both models confirms the idenfication b=D. For small D a linear increase of $\Delta\overline{S}$ is observed, signature of shot noise. For $D \simeq 0.06$, a maxima is observed. For larger transmissions, phase noise is observed, tending toward a noiseless emission for $D \to 1$.

Besides, the amplitude of $\Delta\overline{S}(\omega)$ at a fixed ω strongly depends on D, since it reproduces the graph of Fig.2.14.

At higher frequencies (not presented here), we observe in Floquet simulations that $\Delta\overline{S}(\omega)$ drops at $\omega = \Delta/2$, due to the presence of the Fermi and in accordance with section 2.3.2.3. At this point, probabilistic simulations departs from Floquet ones as, the former does not take into account the Fermi sea.

2.3.4.2 Universality of current fluctuations

As demonstrated in 2.3.4.1, both models show a perfect agreement when plotting $\Delta\overline{S}$ as a function of transmission D or measurement frequency ω. Moreover, these simulations are also in good agreement with experimental data, as presented in Fig.2.12 (red plain line). This confirms that the fluctuations of the driven mesoscopic capacitor is only governed by one parameter τ_e, and exhibits some universal behavior independently of microscopic parameters such as the level spacing Δ or electronic temperature T_{el} (that have no meaning in the semi-classical model). In Fig.2.16, one can see that changing the level spacing Δ has no effect on the autocorrelations in the Floquet model. Similar results are obtained when varying T_{el}. This illustrates the universal character of the fluctuations of the source [83, 91, 95]: as long as quasi-particles are emitted well above

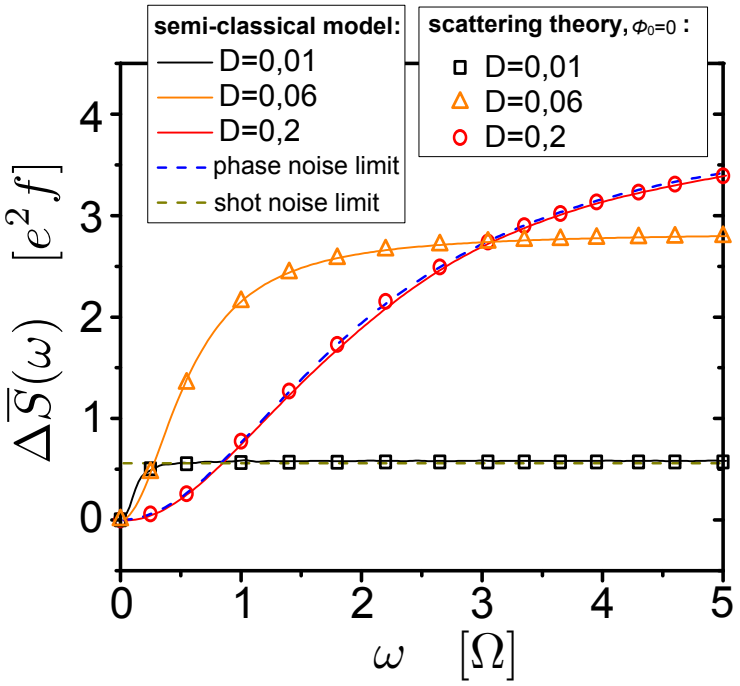

FIGURE 2.15: **Current autocorrelations, predicted by heuristic and Floquet scattering models, as a function of measurement frequency** ω – An excellent agreement is demonstrated between scattering and semi-classical models. For large ω, a white noise (reflecting shot noise) is obtained, whereas $\Delta\overline{S}(\omega) \to 0$ for $\omega \to 0$. The transition occurs for $\omega\tau_e \sim 1$ and thus depends on D.

the Fermi level, i.e. as long as $kT_{el} \ll \Delta$, the effects of the presence of the Fermi sea are negligible, and current correlations only probes the time distribution of the emitted charges.

So far, we have thus proven that a driven mesoscopic capacitor behaves as a single charge emitter in the suitable operating regime, especially under the condition that the upper and lower positions of the driven level lie far from the Fermi level (situation $\phi_0 = 0$). A first prediction from wavepacket model of perfect charge emitter has been enriched by coinciding predictions of a semi-classical probabilistic model and Floquet scattering theory. The global behavior is moreover universal with respect to the escape time τ_e, and as such robust to variations of the experimental parameters. In the next part, we end up the study of the current autocorrelations of the source by comparing the previously developed models with experimental results for $\phi_0 = \pi$.

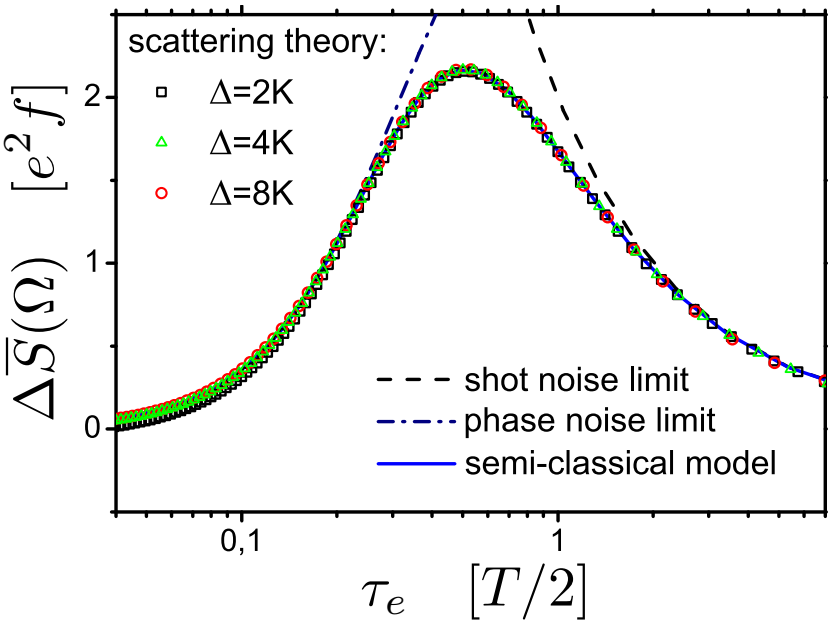

FIGURE 2.16: **Universality of current fluctuations** – Predictions from the semi-classical model (plain line) are compared with Floquet scattering theory computations, for different level spacing Δ. All curves superimpose, and agree with shot noise (dashed line) and phase noise (dash-dotted line) asymptotic regimes. Parameters are $T_{el} = 100$ mK, $2eV_{exc} = \Delta$, with a measurement frequency $\omega \simeq \Omega$.

2.3.5 Non-universal behavior at $\phi_0 = \pi$

2.3.5.1 Noise power spectrum as a function of gate voltage V_g

In this paragraph, we show experimental data for $\Delta\overline{S}(\Omega)$ as a function of gate voltage V_g (Fig.2.17), which controls transmission of the QPC coupling the quantum dot to the rest of the 2DEG. The average transferred charge Q_t as well as the escape time τ_e are deduced from average current measurement, enabling a computation of the noise power spectrum from the semi-classical model. As V_g is swept, the transmission D increases, and in the meantime ϕ_0 varies. A bell-shaped curve is observed, reflecting the same behavior as the one observed in Fig.2.14, since D varies monotonously with V_g. The overall agreement between experimental data and scattering simulations is good. For $V_g < -0.347$ V, the shot noise limit is observed, whereas $V_g > -0.347$ V, the emitter works in a phase noise regime. However, even though experimental points taken at $\phi_0 = 0$ are in very good agreement with simulations, as expected from previous developments, data for $\phi_0 = \pi$ fall systematically above the simulations. We discuss possible reasons in the following section.

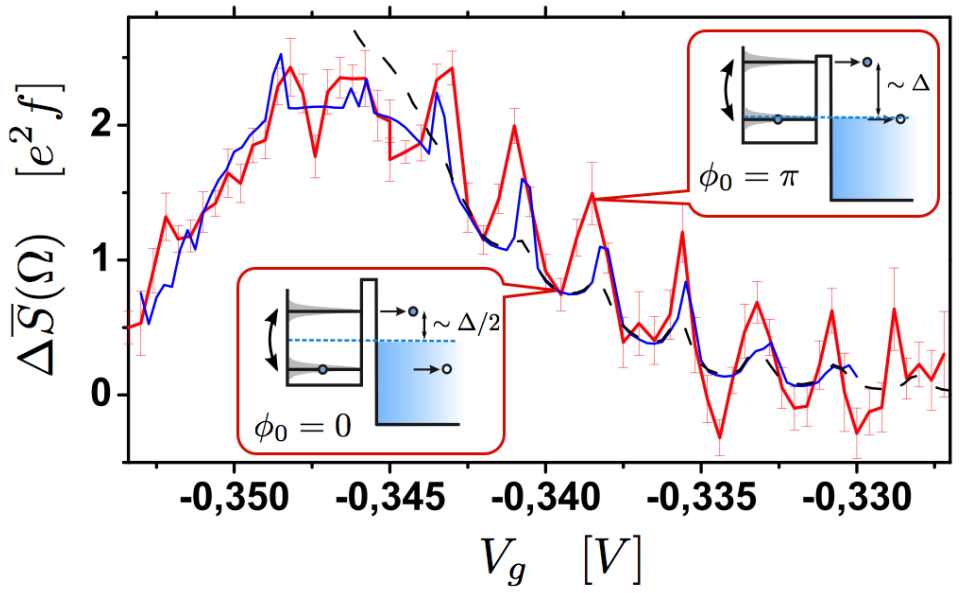

FIGURE 2.17: **Noise power spectrum $\Delta\overline{S}(\Omega)$ as a function of gate voltage** V_g – In plain red line (with error bars) are shown the experimental data. The scattering model (blue line) offers an overall good description of the data, whereas the semi-classical model (here only depicted by the phase noise asymptotic, in black dashes) systematically underestimates the noise power spectrum for $\phi_0 = \pi$

2.3.5.2 Non-universal behavior for $\phi_0 = \pi$

For points where $\phi_0 = \pi$, discrepancies appear between the scattering model and the semi-classical description of the SES. Experimental data systematically fall above the predictions of the heuristic model, and even if the overall agreement is good, deviations are observable between data and Floquet simulations. The most plausible explanation is that for $\phi_0 = \pi$, when driven with a square excitation verifying $2eV_{exc} = \Delta$, levels in the dot come in resonance with the Fermi level of the reservoir. In that situation, additional charge transfer may occur, as schematized in Fig.2.18. In particular, the creation of electron/hole pairs can be enhanced by imperfections in the driving signals (responsible for "shaking" the resonant level in the vicinity of Fermi energy) and electronic temperature in the lead, two parameters that cannot be taken into account in the semi-classical model. In his thesis [83], A. Mahé has demonstrated that, when $\phi_0 = \pi$, Floquet scattering predictions become very sensitive to T_{el} and to the number of harmonics that build up an imperfect square excitation. It is not possible to reach an accurate agreement with experimental data, especially because the precise form of the drive incoming on the top-gate electrode is not known. However, the order of magnitude of the fluctuations of $\Delta\overline{S}$ is totally consistent with the ones observed in our measurements, for a number of 3 odd harmonics.

These considerations assess the necessity to place the level in the configuration $\phi_0 = 0$ to reach a regime of quasi-ideal single charge emission. Otherwise, additional charges are probably emitted as additional noise is detected.

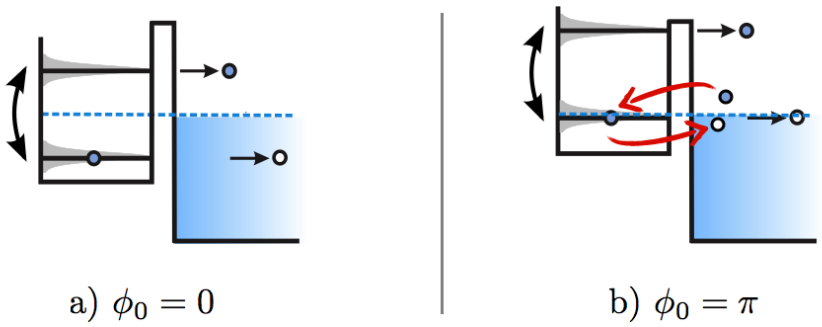

FIGURE 2.18: **Scheme of the two configurations $\phi_0 = 0$ and $\phi_0 = \pi$** – In the case $\phi_0 = \pi$, levels are brought to resonance with the Fermi level of the reservoir, and additional charge transfers may occur, symbolized by the red arrows.

Conclusion to chapter 2

In this chapter, we have introduced and summarized the main results concerning the single electron source before the beginning of this work. In particular, we have shown that the driven mesoscopic capacitor behaves exactly, and not only on average, as a perfect single charge emitter.

First, we have shown that an accurate description of the source could be achieved using Floquet scattering theory and coherence functions. This model takes into account all microscopic parameters, but ignores interactions in the quantum dot. It provides theoretical formulas of average current as well as autocorrelations, that can be easily simulated.

These predictions are then corroborated by experimental measurements of the average current either in time domain of in frequency domain. Especially, the RC-circuit behavior as well as first harmonic quantization are experimentally demonstrated, proving single charge emission on average for an appropriate choice of parameters: $\phi_0 = 0$, $2eV_{exc} = \Delta$ and $\tau_e \leq T/2$.

Beyond average current, current autocorrelations are studied. In addition to Floquet scattering theory, an heuristic model is developed providing deep understanding of the underlying physics. We exhibit a fundamental noise resulting from the uncertainty on the emission time, which constitutes a signature of perfect single charge emission. Finally comparing experimental results, Floquet theory and probabilistic model, we demonstrate

that quasi-perfect single charge emission is achieved. Experimental resolution limits however the bound of $7 - 10\%$ on the error rate. If additional electron and hole were separated by a delay larger than the time resolution of 50 ps of the experiment, they would be detected in short-time autocorrelations and give an extra contribution in the noise, which is not observed, within an accuracy of less than 10%. However, electron-hole pairs separated by less than 50 ps appear as neutral events and remain as such invisible [91, 115, 117].

Indeed, as current autocorrelations only probe charged events, it is impossible to exactly count the number of generated quasi-particles. It is well-known [86, 87, 118, 119] that low-frequency noise can be recovered by partitioning the generated flow of e/h pairs. In the next chapter, we will present the realization of an Hanbury-Brown & Twiss based on this idea and that provides additional information on the number of elementary electron/hole pair generation [88, 89].

Chapter 3

Hanbury-Brown & Twiss experiment with single electrons

Introduction to chapter 3

The new stellar interferometer developed in 1956 by Hanbury-Brown & Twiss [120] has shed light on the possibility to use intensity correlations to gain access to information on the statistics of photons. This technique, confirmed by a second experiment [121], has been extended to other systems such as fermions in 2DEG [3, 122], microwave photons [110, 123], bosons or fermions in cold atom gases [124] or photons interacting in a non-linear medium [125].

In this chapter, we examine an analog of the Hanbury-Brown & Twiss experiment, realized by partitioning mono-electronic excitations on a quantum point contact acting as a beamsplitter [96]. In a geometry that reproduces the seminal optics experiment [121], we show that the correlations of the output currents provide a direct counting of the total number of elementary excitations [88, 89] emitted by the single electron source in the input arm. However, this counting is deeply modified by the presence of thermal excitations in the Fermi sea, as antibunching effects can occur between such excitations and the quasi-particles triggered by the SES. This phenomenon can in fact be used to probe the energy of the latter.

3.1 Principles of the Hanbury-Brown & Twiss experiment

3.1.1 Historical HBT experiment

This work is inspired by an experiment carried out by Hanbury-Brown and Twiss [121] to confirm the interpretation of intensity correlations in astronomical observation [120]. In their setup (Fig.3.1, panel a), a light beam is separated in two via a beamsplitter, and two photomultipliers are placed to record the instant intensity $\hat{I}_k(t)$ in each output $k = 1, 2$. Correlations between the detectors are then calculated to access the correlator $\langle \hat{I}_1(t)\hat{I}_2(t+\tau)\rangle$.

This experiment is considered as a milestone in quantum optics: intensity correlations demonstrate the bunching of classical thermal photons, i.e. their tendency to arrive several at the same time due to bosonic statistics. It relies on a corpuscular interpretation: photons are perceived as discrete particles, partitioned randomly on the beamsplitter. As such, it completely questions the wave picture usually associated with interferometers, that record field correlations rather than intensity correlations. With this experiment, Hanbury-Brown & Twiss have closed the controversy born after their first experiment of 1956 and opened a new field of investigation.

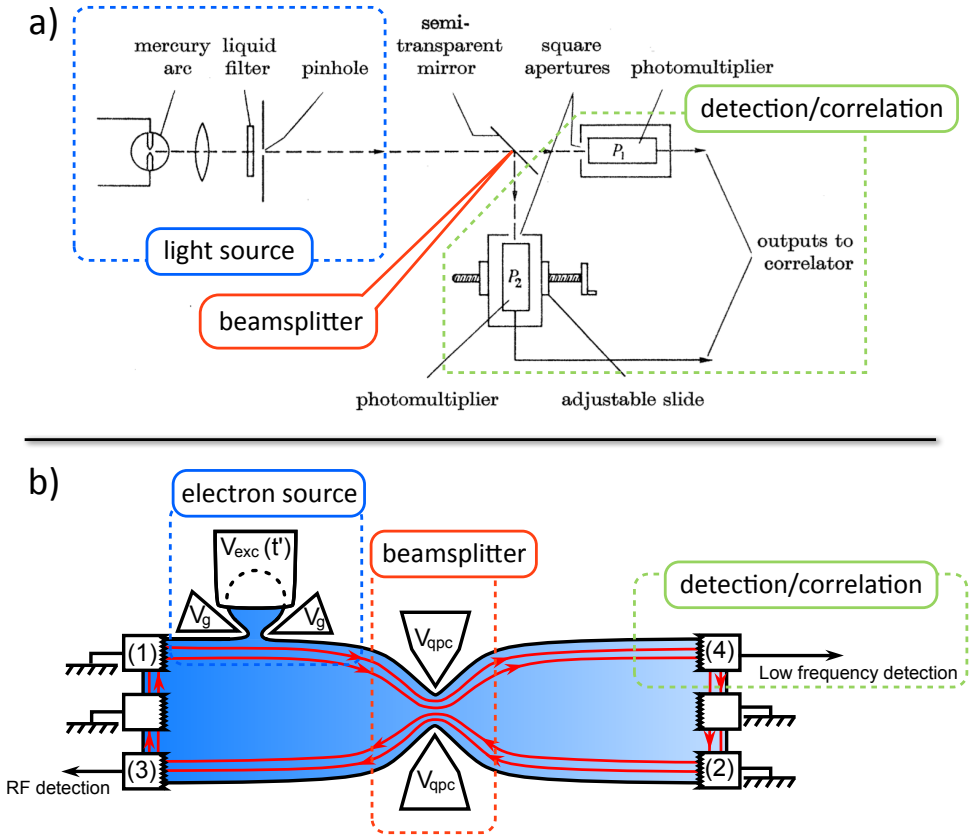

FIGURE 3.1: **Sketches of photonic and electronic versions of the Hanbury-Brown & Twiss experiment**– a) A stream of photons is partitioned on a 50/50 beamsplitter, and the intensity cross-correlations are computed using one detector in each output arm (figure extracted from [121]). b) Similarly, an electron beam is partitioned on a central QPC playing the role of an electronic beamsplitter, and cross-correlations can be calculated from currents emitted in contacts 3 and 4.

Implementing such an experiment has been one of the first goals to open the field of electron optics, which was achieved by Henny *et al.*[3] and Oliver *et al.* [122] using a continuous stream of electrons (see section 1.1.2.2). We here present a more sophisticated experiment where single quasiparticles are partitioned.

3.1.2 Electronic HBT experiment

From the analogies described in section 1.1.1, one can directly imagine an electronic version of this setup, implemented in a quantum Hall device. Such a device is sketched in Fig. 3.1, panel b). The beamsplitter is provided by a quantum point contact, connecting inputs 1 and 2 to outputs 3 and 4. In input 1, the current source can be implemented in several ways. Henny *et al.* [3] and Oliver *et al.* [122] have investigated the case of a DC-biased contact, and demonstrated the noiseless character of the generated electron

beam, property that can also be demonstrated via autocorrelation measurements (see 3.1.3). In this chapter, we study the case of partitioning one by one mono-electronic wavepackets emitted by a SES as sketched in Fig.3.1.

3.1.3 Classical partitioning

In this section we present a classical reasoning that shows how the HBT geometry can be used to gain information on the number of quasiparticles emitted by our single electron/hole source. First we analyse the case of a source that emits only one type of particles. This is for example the case of a photon source, or of a DC-biased contact, in the limit of zero temperature. Then we study the case of an AC source, emitting a succession of electron/hole pairs. We emphasize the differences arising due to the AC nature of the source and demonstrate that one can count the number of quasiparticles emitted using correlations in an Hanbury-Brown & Twiss experiment.

3.1.3.1 Partitioning electrons

Let us consider a stream of electrons described classically as "beads" that are randomly partitioned on a beamsplitter, as shown on figure 3.2, panel a). We assume that during the measurement time T_{meas}, N_e electrons are emitted with probability $P(N_e)$. A DC current $I_1 = \frac{e}{T_{meas}} N_e$ is then produced in input 1. In the meantime, we assume that no particle is emitted from contact 2. The quantity of interest here is the correlator $\langle \delta Q_3 \delta Q_4 \rangle$ where $Q_i = eN_{e,i}$ is the charge transmitted toward contact $i = 3, 4$.

If the transmission of the beamsplitter is set to T, a particle is transmitted in output 4 with probability T and reflected in output 3 with probability $1 - T$, and we have $\langle N_{e,4} \rangle = T \langle N_e \rangle$, and $\langle N_{e,3} \rangle = (1 - T) \langle N_e \rangle$, and thus:

$$\begin{aligned} \langle \delta Q_3 \delta Q_4 \rangle &= e^2 \langle \delta N_{e,3} \delta N_{e,4} \rangle & (3.1) \\ &= e^2 \big(\langle N_{e,3} N_{e,4} \rangle - T(1-T) \langle N_e \rangle^2 \big) & (3.2) \end{aligned}$$

The last unknown $\langle N_{e,3} N_{e,4} \rangle$ can be obtained by computing the probability $P(N_{e,3})$ of having $N_{e,3}$ electrons transmitted toward contact 3, as follows. For a random binomial process of partitioning, one has:

$$P(N_{e,3}) = \sum_{N_e \geq N_{e,3}} P(N_e) \binom{N_e}{N_{e,3}} T^{N_{e,3}} (1-T)^{N_e - N_{e,3}} \quad (3.3)$$

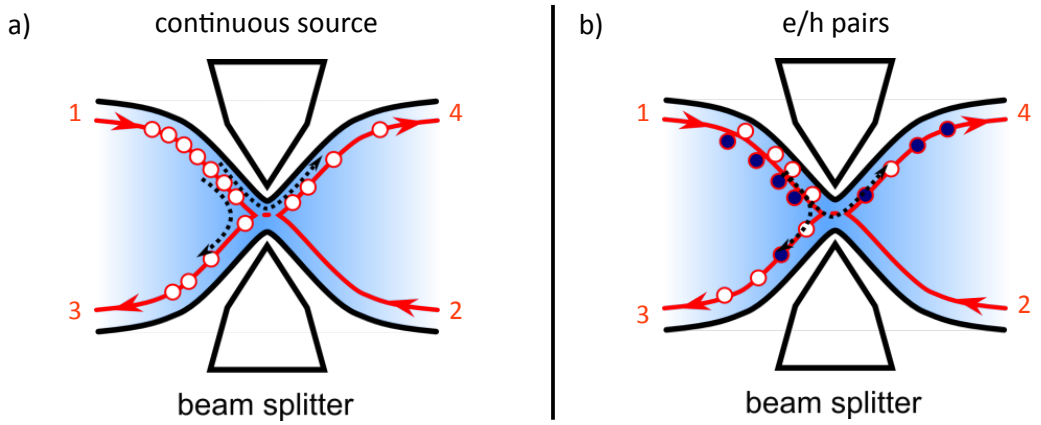

FIGURE 3.2: **Scheme of classical partitioning of electrons and electron/hole pairs** – a) A stream of electrons, as emitted by a DC-biased contact is represented as a succession of classical "beads". It is partitioned on a central quantum point contact acting as a 50/50 beamsplitter. b) Similarly, a succession of electron/hole pairs, as emitted by a purely AC source (such as the driven mesoscopic capacitor) is partitioned on a beamsplitter.

where $\binom{N_e}{N_{e,3}}$ is the binomial factor counting the number of possibilities for $N_{e,3}$ electrons out of N_e to be transmitted. One can consequently calculate the correlator $\langle N_{e,3}N_{e,4}\rangle$:

$$\langle N_{e,3}N_{e,4}\rangle = \sum_{N_{e,3}=0}^{\infty} P(N_{e,3})N_{e,3}\big(N_e - N_{e,3}\big) \tag{3.4}$$

Switching summations then yields the results:

$$\langle Q_3Q_4\rangle = e^2T(1-T)\big(\langle N_e^2\rangle - \langle N_e\rangle\big) \tag{3.5}$$

$$\langle \delta Q_3\delta Q_4\rangle = e^2T(1-T)\big(\langle \delta N_e^2\rangle - \langle N_e\rangle\big) \tag{3.6}$$

Usually, the charge correlations are probed through the measurement of the low frequency correlations $\overline{S}_{3,4}(\omega=0) = \overline{S}_{3,4}$ between the output currents:

$$\overline{S}_{3,4} = 2\int d\tau\ \overline{\langle \delta I_3(t)\delta I_4(t')\rangle}^{\bar{t}} \tag{3.7}$$

where as previously $\overline{\cdots}^{\bar{t}}$ denotes the average on the absolute mean time $\bar{t} = (t+t')/2$ on a long measurement time T_{meas}, and $\tau = t - t'$. $\overline{S}_{3,4}$ is then related to the charge correlations $\langle \delta Q_3\delta Q_4\rangle$ by:

$$\overline{S}_{3,4} = \frac{2}{T_{meas}}\langle \delta Q_3\delta Q_4\rangle \tag{3.8}$$

$$\overline{S}_{3,4} = \frac{2e^2}{T_{meas}}T(1-T)\big(\langle \delta N_e^2\rangle - \langle N_e\rangle\big) \tag{3.9}$$

For a poissonian random source, fluctuations are proportional to the number of incoming carriers: $\langle \delta N_e^2 \rangle = \langle N_e \rangle$. As a consequence, no correlation is expected between outputs 3 and 4. This is the case of laser light in photon optics for example.

When plugging a noiseless source in input 1 for $\langle \delta N_e^2 \rangle = 0$, one gets $\langle \delta Q_3 \delta Q_4 \rangle = -e^2 T(1-T)\langle N_e \rangle$. This is the case for a DC-biased contact; where Pauli principle forces electrons to be regularly ordered. Thus, $\overline{S}_{3,4}$ reduces to:

$$\overline{S}_{3,4} = -\frac{2e^2}{T_{meas}} T(1-T)\langle N_e \rangle \quad (3.10)$$

$$= -2eI_1 T(1-T) \quad (3.11)$$

Follwing the same reasoning, one can show that in this case $\overline{S}_{4,4} = -\overline{S}_{3,4}$: this maximal anti-correlation between cross and auto-correlation only holds for a noiseless source. This result was demonstrated in [3] using a DC-biased contact. A key point here is the minus sign: it characterizes the behavior of electrons, that antibunch in virtue of Fermi-Dirac statistics. These results can be compared with the ones predicted for photons: contrary to thermal electrons that are naturally ordered, photons emitted by a thermal source of light have a tendency to bunch due to their bosonic nature. In that case, one has the following super-poissonian correlations between the number $N_{p,k}, k = 3, 4$ of photons in output k:

$$\langle \delta N_p^2 \rangle = 2\langle N_p \rangle \quad (3.12)$$

$$\langle \delta N_{p,3} \delta N_{p,4} \rangle = T(1-T)\langle N_p \rangle \quad (3.13)$$

As such, we see that the HBT geometry gives access to the fluctuations $\langle \delta N_e^2 \rangle$ and yields results on the statistics of the incoming carriers. However, this information can also be obtained from current auto-correlations, as $\langle \delta I_1^2 \rangle \propto \langle \delta N_e^2 \rangle$. In the next section, we study the case of a purely AC-source, for which these results are strongly modified.

3.1.3.2 Partitioning electron/hole pairs

We now consider an AC current source connected to input 1 emitting e/h pairs [85, 87]. In the measurement time T_{meas}, N electron/hole pairs are emitted with a probability $P(N)$. The number of electrons N_e equals the number of holes N_h so that no DC current $I_1 = \frac{e}{T_{meas}}(N_e - N_h) = 0$ and no low frequency noise $S_{1,1} = 0$ are produced by the source before partitioning according to the study of autocorrelations in section 2.3.2.4. We emphasize the fact that, for an AC source, low-frequency auto-correlations do not give any information either on the charge fluctuations or on the number of

emitted quasiparticles. We then adapt the preceding reasoning to the case of this purely AC source.

We assume that no particle is incident on input 2. The N_e electrons and N_h holes are partitioned independently following a binomial law. The correlations $\langle \delta Q_3 \delta Q_4 \rangle$ between the charges $Q_i = e(N_{e,i} - N_{h,i})$ $(i = 3, 4)$ transmitted at the outputs are given by the following expression:

$$\langle \delta Q_3 \delta Q_4 \rangle = e^2 \Big(\langle \delta N_{e,3} \delta N_{e,4} \rangle + \langle \delta N_{h,3} \delta N_{h,4} \rangle - \langle \delta N_{h,3} \delta N_{e,4} \rangle - \langle \delta N_{e,3} \delta N_{h,4} \rangle \Big) \tag{3.14}$$

It can be evaluated using the probability $P(N_{e,3}, N_{h,4})$ that $N_{e,3}$ electrons are transmitted in output 3 and $N_{h,4}$ holes are reflected in output 4 given by:

$$\begin{aligned} P(N_{e,3}, N_{h,4}) = \sum_{N \geq \max(N_{e,3}, N_{h,4})} P(N) \times \frac{N!}{N_{e,3}!(N - N_{e,3})!} \, T^{N_{e,3}} \, (1-T)^{N - N_{e,3}} \\ \times \frac{N!}{N_{h,4}!(N - N_{h,4})!} \, T^{N - N_{h,4}} \, (1-T)^{N_{h,4}} \end{aligned} \tag{3.15}$$

from which we deduce:

$$\langle \delta Q_3 \delta Q_4 \rangle = -T(1-T) e^2 \Big[\langle N_e \rangle + \langle N_h \rangle \Big] \tag{3.16}$$

Remarkably, for an AC source, the correlations $\langle \delta Q_3 \delta Q_4 \rangle$ between the charges transmitted at the outputs do not provide any information on the fluctuations of the number of electrons and holes. Nevertheless, they provide a direct determination of the average number of electron-hole pairs generated by the source, as we indeed immediately get:

$$\overline{S}_{3,4} = \frac{2}{T_{meas}} \langle \delta Q_3 \delta Q_4 \rangle \tag{3.17}$$

$$\overline{S}_{3,4} = -\frac{2e^2}{T_{meas}} T(1-T) \Big[\langle N_e \rangle + \langle N_h \rangle \Big] \tag{3.18}$$

Identifying the measurement time with the period $1/f$ of the voltage drive applied to the source and $\langle N_e \rangle$, $\langle N_h \rangle$ with the average number of electrons and holes emitted by the source in one period, we finally obtain:

$$\overline{S}_{3,4} = -2e^2 f T(1-T) \big(\langle N_e \rangle + \langle N_h \rangle \big) \tag{3.19}$$

$$= -4e^2 f T(1-T) \delta N_{HBT} \tag{3.20}$$

$$\delta N_{HBT} = \frac{\langle N_e \rangle + \langle N_h \rangle}{2} \tag{3.21}$$

3.1.3.3 Counting quasiparticles through Hanbury-Brown & Twiss correlations

This classical calculation already holds a lot of information. As mentioned earlier, high-frequency current autocorrelations give access to the statistics of charge transfer. But due to the existence of two types of carriers, of opposite charges, neutral events can occur that can not be probed. The previous formula shows that partitioning the electron beam on a beam splitter creates zero-frequency correlations, that directly encodes the total number of emitted quasiparticles. Whereas autocorrelations detect charges and their fluctuations, HBT correlations directly counts the total number of incoming particles $\langle N_e \rangle + \langle N_h \rangle = 2\,\delta N_{HBT}$.

This reasoning is at the core of the following study. One expects to measure the possible additional electron-hole pairs that could be emitted in a non-controlled manner during some of the emission cycles, atop the triggered charges. With the normalization adopted, it is clear so far that a lower bound can be set: the total number of quasiparticles counted via HBT correlations is necessarily larger than the number of charges emitted by the source, i.e. $\delta N_{HBT} \geq Q_t$. The figure of merit of a single electron-hole source would be $\delta N_{HBT} = Q_t = 1$, corresponding to a quantized charge without any additional e/h pair generated. However, some elements are lacking in this classical description, and especially, the Fermi sea is not described. We will see that it is a very important ingredient in the problem, as quantum interferences appear between the triggered quasiparticles emitted by the SES and thermal excitations of the reservoir.

The next section is then naturally devoted to developing a quantum description of the Hanbury-Brown & Twiss experiment, to take into account Fermi-Dirac statistics, thermal excitations and all relevant parameters.

3.1.4 Quantum theory : effect of thermal excitations

We rely once again on the coherence functions formalism, to give a simple picture of the main physical effects before calculating and simulating results obtained from Floquet scattering theory. We recall that interactions can not be taken into account in this particular framework.

3.1.4.1 Partition noise

Description of the electronic beamsplitter First of all we briefly describe the effect of the beamsplitter on incoming modes. The input field operators $\hat{a}, \hat{b}$ are related

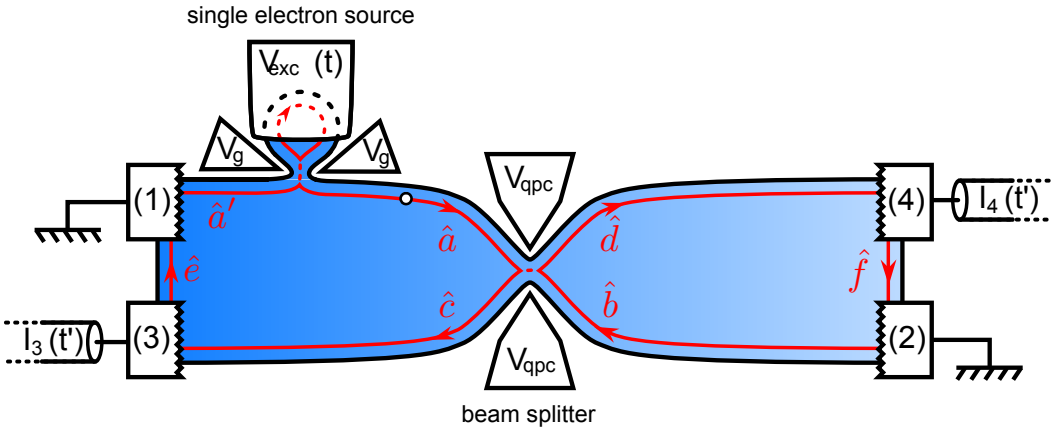

FIGURE 3.3: **Scheme of the sample and notations used** – In the geometry that mimics the HBT experiment described in Fig. 3.1, incoming (resp. outgoing) modes on the splitter are labeled $\hat{a}, \hat{b}$ (resp. $\hat{c}, \hat{d}$). These modes are related by Eq.3.22. The mode $\hat{a}$ exiting the source is related to $\hat{a}'$ at equilibrium by Floquet scattering relation 2.15. Modes $\hat{e}$ and $\hat{f}$ that only contribute to the Hanbury-Brown correlations via a subtracted thermal noise background, will be ignored in the following study.

to the output fields $\hat{c}, \hat{d}$ via the following scattering matrix

$$\begin{pmatrix} \hat{c} \\ \hat{d} \end{pmatrix} = \begin{pmatrix} \sqrt{1-T} & i\sqrt{T} \\ i\sqrt{T} & \sqrt{1-T} \end{pmatrix} \begin{pmatrix} \hat{a} \\ \hat{b} \end{pmatrix} . \tag{3.22}$$

This formula is identical to the description of an optical beamsplitter, acting on modes of the electromagnetic field.

Thus, current operators in output 3 and 4 are given by:

$$\begin{aligned} \hat{I}_3 &= e\,\hat{c}^\dagger\hat{c} \\ &= (1-T)\hat{I}_1 + T\hat{I}_2 + ie\sqrt{T(1-T)}(\hat{a}^\dagger\hat{b} - \hat{a}\hat{b}^\dagger) \qquad (3.23) \\ \hat{I}_4 &= e\,\hat{d}^\dagger\hat{d} \\ &= T\hat{I}_1 + (1-T)\hat{I}_2 - ie\sqrt{T(1-T)}(\hat{a}^\dagger\hat{b} - \hat{a}\hat{b}^\dagger) \qquad (3.24) \end{aligned}$$

One immediately notices an interference effect between both inputs (in the third term of right-hand side), that is not present in the classical theory. It reflects the fact that the beamsplitter acts on field operators, and not current operators. It will clearly appear in the following developments.

Fluctuations and HBT effect From previous developments, one can calculate the current-current correlations, computed between different output contacts $i, j = 3, 4$. Using Eqs.(3.23) and (3.24), the current-current correlations $S_{i,j}(t,t') = \langle \delta\hat{I}_i \delta\hat{I}_j \rangle$ can be

written in the following way[1]:

$$S_{3,4}(t,t') = T(1-T)\big(S_{1,1}(t,t') + S_{2,2}(t,t') - Q(t,t')\big) \quad (3.25)$$

$$S_{4,4}(t,t') = T^2 S_{1,1}(t,t') + (1-T)^2 S_{2,2}(t,t') + T(1-T)Q(t,t') \quad (3.26)$$

where we identify $S_{1,1} = \langle \delta\hat{I}_1 \delta\hat{I}_1 \rangle$ and $S_{2,2} = \langle \delta\hat{I}_2 \delta\hat{I}_2 \rangle$ as current-current autocorrelations in the input channels, as studied in 2.3. Besides, a new term $Q(t,t')$ also arises from quantum interference effects, and will be at the heart of our study [45]:

$$Q(t,t') = e^2\big(\mathcal{G}_1^{(e)}(t,t')\mathcal{G}_2^{(h)}(t,t') + \mathcal{G}_1^{(h)}(t,t')\mathcal{G}_2^{(e)}(t,t')\big) \quad (3.27)$$

This term will be studied in details in the next section, but let us first operate some useful simplifications.

Measuring HBT correlations First, our setup (detailed in section 3.2) does not give access directly to the cross-correlations $\overline{S}_{3,4}$ but to the auto-correlations after partitioning. However, one has the following results. First, at zero-frequency, the auto-correlations $\overline{S}_{1,1}$ and $\overline{S}_{2,2}$ are reduced to equilibrium noise, that is subtracted in our measurement protocol. Namely, $\Delta\overline{S}_{1,1} = \Delta\overline{S}_{2,2} = 0$. Second, from Eqs.(3.25) and (3.26), one gets[2]:

$$\overline{S}_{3,4} = -T(1-T)\Delta\overline{Q} = -\Delta\overline{S}_{4,4} \quad (3.28)$$

Finally, we see that recording the auto-correlations after partitioning on the beamsplitter is enough to gain access to the quantum interference term $\Delta\overline{Q}$. This technique enables to keep output 3 for RF homodyne detection of the average current, necessary to establish an accurate diagnosis of the operating parameters of the source, as explained in section 2.2.

3.1.4.2 Coherence theory of the Hanbury-Brown & Twiss experiment

In this section, we analyze the term ΔQ that encodes interferences between channels 1 and 2. Let us mention that this term is very different from what we observed in the classical partitioning model (even if incoming particles were added in input 2). Indeed, in a sense, classical partitioning is a matter of partitioning currents rather than field operators whereas in a quantum theory, field operators of channels 1 and 2 interfere, and new phenomena are unveiled.

[1] disregarding thermal noises from modes $\hat{e}, \hat{f}$ at equilibrium

[2] $\overline{S}_{3,4}$ does not contain any equilibrium term, as a specific feature of cross-correlations in the HBT geometry.

Hanbury-Brown & Twiss correlations In this experiment, the second output is at equilibrium, at chemical potential $\mu = 0$ and temperature T_{el}, so that $\mathcal{G}_2^{(e/h)}$ reduces to equilibrium coherence functions $\mathcal{G}_2^{(e/h)} = \mathcal{G}_{\mu=0}^{(e/h)}$. In particular, the excess contribution $\Delta\mathcal{G}_2^{(e/h)} = 0$, so that we can write from Eq.(3.27) the excess contribution ΔQ as :

$$\Delta Q(t,t') = e^2\big(\Delta\mathcal{G}_1^{(e)}(t,t')\mathcal{G}_{\mu=0}^{(h)}(t-t') + \Delta\mathcal{G}_1^{(h)}(t,t')\mathcal{G}_{\mu=0}^{(e)}(t-t')\big) \tag{3.29}$$

The zero-frequency part is then written:

$$\begin{aligned}
\Delta\overline{Q} &= 2e^2\int d\tau\ \sum_n \overline{\big(\Delta\mathcal{G}_{1,n}^{(e)}(\tau)\mathcal{G}_{\mu=0}^{(h)}(\tau) + \Delta\mathcal{G}_{1,n}^{(h)}(\tau)\mathcal{G}_{\mu=0}^{(e)}(\tau)\big)e^{-in\Omega\bar{t}}}^{\bar{t}} \\
&= 2e^2\int d\tau\ \big(\Delta\mathcal{G}_{1,0}^{(e)}(\tau)\mathcal{G}_{\mu=0}^{(h)}(\tau) + \Delta\mathcal{G}_{1,0}^{(h)}(\tau)\mathcal{G}_{\mu=0}^{(e)}(\tau)\big) \\
&= \frac{2e^2}{h}\int d\epsilon\big(\Delta\mathcal{G}_{1,0}^{(e)}(\epsilon)\mathcal{G}_{\mu=0}^{(h)}(-\epsilon) + \Delta\mathcal{G}_{1,0}^{(h)}(-\epsilon)\mathcal{G}_{\mu=0}^{(e)}(\epsilon)\big)
\end{aligned} \tag{3.30}$$

Eqs.(1.8) and (1.9) then give the equilibrium population $\mathcal{G}_{\mu=0}^{(e)}(\epsilon) = f_{\mu=0}(\epsilon)$, and $\mathcal{G}_{\mu=0}^{(h)}(\epsilon) = 1 - f_{\mu=0}(-\epsilon)$. As explained in 1.2.2.3, the harmonic $n = 0$ of the coherence function of the source in input 1, $\mathcal{G}_{1,0}^{(e/h)}(\epsilon)$, encodes the number of quasi-particles at a given energy ϵ. Consequently, we introduce the excess energy distribution of electrons and holes $\delta n_{e/h}$ generated by the SES:

$$\Delta\mathcal{G}_{1,0}^{(e)}(\epsilon) = \delta n_e(\epsilon) \tag{3.31}$$

$$\Delta\mathcal{G}_{1,0}^{(h)}(\epsilon) = \delta n_h(\epsilon) \tag{3.32}$$

With these notations, $\delta n_e/\delta n_h$ are respectively the excess population of electrons/holes at energy ϵ (with respect to the Fermi sea $f_\mu(\epsilon)$) Then, one gets a very clear expression of $\Delta\overline{Q}$:

$$\begin{aligned}
\Delta\overline{Q} &= 4e^2 f\,\delta N_{HBT} \\
\delta N_{HBT} &= \frac{1}{2}\int_0^\infty d\epsilon\ \big(1 - 2f_{\mu=0}(\epsilon)\big)\big(\delta n_e(\epsilon) + \delta n_h(\epsilon)\big) \qquad (3.33) \\
&= \frac{\langle N_e\rangle + \langle N_h\rangle}{2} - \int_0^\infty d\epsilon\ \big(\delta n_e(\epsilon) + \delta n_h(\epsilon)\big) f_{\mu=0}(\epsilon) \qquad (3.34)
\end{aligned}$$

where $\langle N_{e/h}\rangle = \int_0^\infty d\epsilon\ \delta n_{e/h}(\epsilon)$ is the excess number of quasiparticles (electron or hole) emitted by the source. Eq.(3.34) then has a very simple interpretation. The first part of δN_{HBT} is the classical term: the HBT correlations count the number of quasiparticles emitted by the source, as demonstrated in section 3.1.3.2. This contribution is then corrected by the second term $-\int_0^\infty d\epsilon\ \big(\delta n_e(\epsilon)+\delta n_h(\epsilon)\big) f_{\mu=0}(\epsilon)$, that measures the overlap between the energy distribution of the electrons/holes emitted by the source and the Fermi distribution encoding the population of thermal excitations in the reservoir.

Antibunching with thermal excitations Consequently, the partition noise is reduced due to the presence of thermal excitations. This can be understood as a Hong-Ou-Mandel two-particle interference (section 1.1.2.3, [22]) as detailed on Fig.3.4: when a quasiparticle of energy ϵ emitted in input 1 finds a symmetric partner in input 2 with same energy impinging on the QPC at the same time, their contribution to the noise is canceled as they have to come out in different outputs to obey Fermi-Dirac statistics. Thus, as pictured on Fig.3.4 the probability $P_{1,1}$ of having one electron in each output is $P_{1,1} = 1$, whereas $P_{2,0} = P_{0,2} = 0$. Contact 1 is populated with electrons and holes with distribution $\delta n_{e/h}(\epsilon)$, whereas contact 2 is at thermal equilibrium with distribution $f_{\mu=0}(\epsilon)$, hence the form of Eq.(3.34). This term is not totally surprising. Indeed, the partition noise of a DC-biased contact can be written as the integral of $f_\mu(\epsilon - eV)\big(1 - f_\mu(\epsilon)\big)$ where the first factor refers to the first input contact 1 and the second to the input 2, and the same interpretation can be given, by simply replacing non-equilibrium distribution created by our SES $\delta n_e + \delta n_h$ by the thermal distribution $f_\mu(\epsilon - eV)$ in input 1.

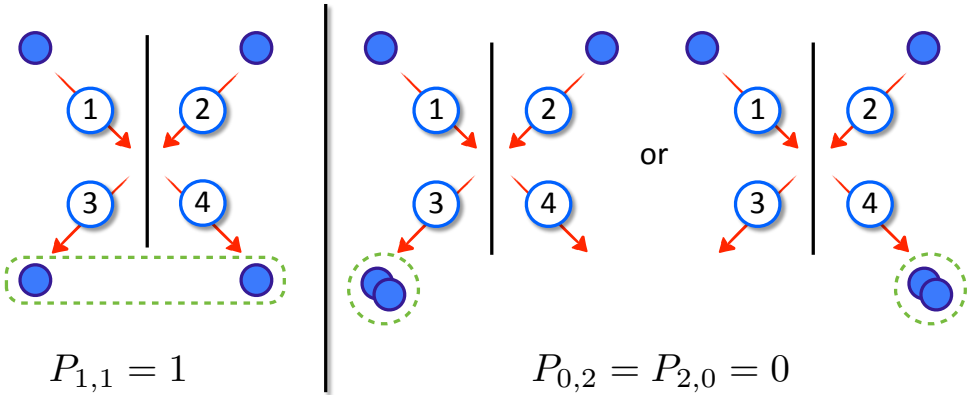

FIGURE 3.4: **Hong-Ou-Mandel effect and antibunching with thermal excitations** – A reduction of the HBT correlations is expected due to Hong-Ou-Mandel effect responsible for anti-bunching with thermal excitations: when a quasiparticle emitted in input 1 finds an indistinguishable partner in input 2 reaching the QPC at the same time, they have to come out on different outputs to obey the Fermi-Dirac statistics. Thus this only possible outcome (left panel) has unit probability ($P_{1,1} = 1$), whereas the two other possibilities (right panel) are forbidden ($P_{2,0} = P_{0,2} = 0$).

3.1.4.3 Floquet scattering theory

Using the Floquet model developed in section 2.1.1, we can obtain the expression of the HBT correlations δN_{HBT} in terms of the Floquet matrix. In fact, it is also simple to calculate directly the energy distribution of the quasiparticles emitted by the source.

From Eqs.(2.20) and (2.23), one gets:

$$n_e(\epsilon) = \langle \hat{b}^\dagger(\epsilon)\hat{b}(\epsilon)\rangle = \sum_k \left|U_k(\epsilon)\right|^2 f_0(\epsilon - \frac{k}{2}\hbar\Omega) \tag{3.35}$$

$$n_h(\epsilon) = \langle \hat{b}(\epsilon)\hat{b}^\dagger(\epsilon)\rangle = \sum_k \left|U_k(\epsilon)\right|^2 \big(1 - f_0(\epsilon - \frac{k}{2}\hbar\Omega)\big) \tag{3.36}$$

$$\delta n_e(\epsilon) = -\delta n_h(-\epsilon) = \sum_k \left|U_k(\epsilon)\right|^2 \big(f_0(\epsilon - \frac{k}{2}\hbar\Omega) - f_0(\epsilon)\big) \tag{3.37}$$

This finally yields:

$$\delta N_{HBT} = \sum_k \int d\epsilon \, \left|U_k(\epsilon)\right|^2 \big(f_0(\epsilon - \frac{k}{2}\hbar\Omega) - f_0(\epsilon)\big)\big(1 - 2f_0(\epsilon)\big) \tag{3.38}$$

As was similarly done for the average current I_Ω (section 2.2) and the autocorrelation $\Delta\overline{S}$ (section 2.3), this expression can be numerically simulated using Matlab programs, offering a way to forecast and analyze quantitatively our experimental results.

In this section, we have provided insights concerning current correlations measured in the Hanbury-Brown & Twiss geometry. A classical reasoning shows that the HBT correlations can be used to count the total number of quasiparticles emitted by the SES. However, in addition, a quantum theory predicts that the HBT signal is corrected by a factor accounting for antibunching effects between triggered quasiparticles and thermal excitations in the gas. The next section details the setup and calibration steps that were developed to measure these fluctuations.

3.2 Experimental implementation

In the first paragraph, we explain the sample design and how several experimental parameters (magnetic field B, QPC gate voltage V_{qpc}) were chosen. Then the low-frequency noise detection is described, as well as its calibration.

3.2.1 Description of the sample and choice of parameters

3.2.1.1 Sample description

On Fig.3.5 is presented a modified SEM picture of the sample used in this experiment. A strong magnetic field $B = 3.2$ T is applied perpendicularly to the sample so as to enter the integer quantum Hall regime with a filling factor $\nu = 2$. The accurate choice of B

must fulfil several technical constraints, and is discussed hereafter. The sample consists of a single electron source of the type described in the preceding chapter. The size of the quantum dot is around 1 μm, and the level spacing has been calibrated to the value of $\Delta = 2.1 \pm 0.2$ K. In input 1, only the outermost of the two copropagating channels

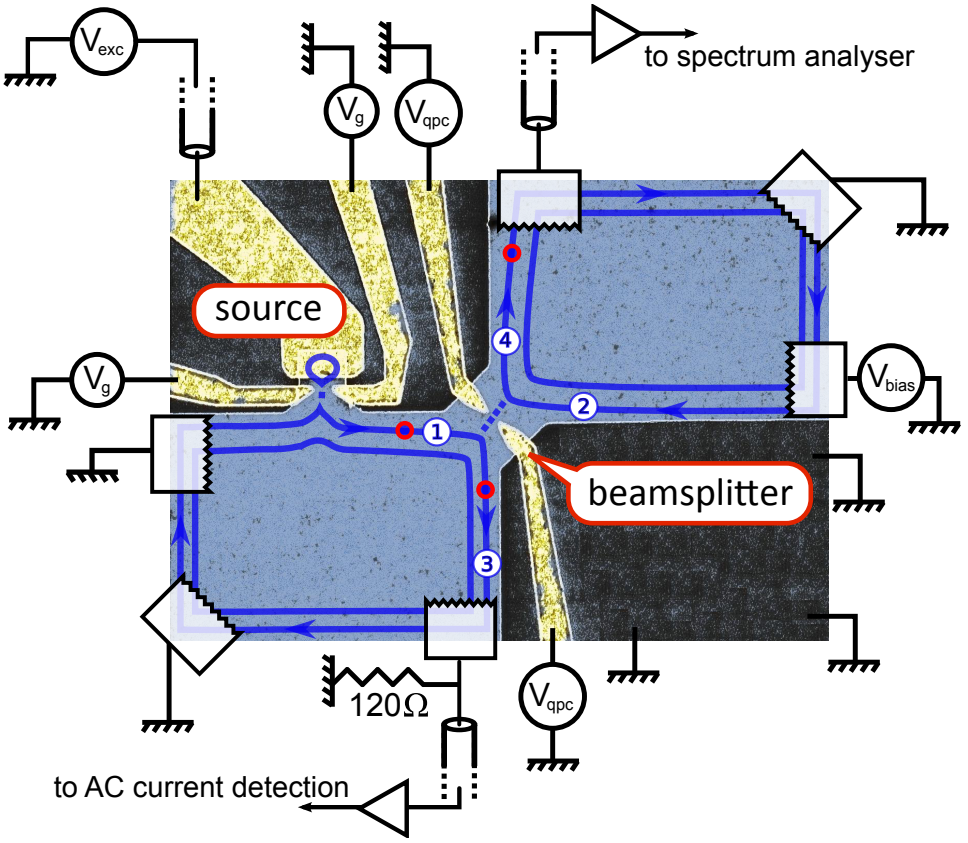

FIGURE 3.5: **Modified SEM picture of the sample used in the Hanbury-Brown & Twiss experiment** – A driven mesoscopic capacitor, used as a single electron/hole source injects quasiparticles in the first input (labeled 1) of a QPC, acting as beamsplitter and controlled via gate voltage V_{qpc}. Input 2 is connected to a biased contact with voltage V_{bias}. This bias is used for calibration purpose but set to $V_{bias} = 0$ when measuring HBT correlations. Output 3 is dedicated to RF average current measurements and cabled toward the GHz homodyne detection. On the opposite side, low-frequency HBT autocorrelations are recorded in output 4, connected to the noise detection scheme presented in section 3.2.2.

of $\nu = 2$ is tunnel coupled to the dot, via the QPC of the mesoscopic capacitor (gate voltage V_g). Consequently, up to interaction processes (discussed in chapter 4), charges are situated only in this edge state, and only the physical phenomena in this channel will be examined throughout this chapter. Input 2 is connected to a low-frequency generator that delivers a voltage V_{bias}. During the measurement of HBT correlations, it is set to $V_{bias} = 0$, but it is used in the calibration of the central QPC and in the choice of the magnetic field, as explained in the following paragraphs.

Roughly 3 μm after the dot, a second QPC (called "central QPC") has been lithographied to recreate the beamsplitter of the HBT geometry. Its transmission T can be tuned via gate voltage V_{qpc}, and enables to split the outer edge channel into a reflected and a transmitted electron/hole beam, so as to mimic the HBT geometry sketched in Fig.3.1.

Second source

Please note that a second source is situated symmetrically from the first one with respect to the central QPC. As it was not working properly on this sample, and is of no use in this experiment, it was blackened for clarity on the SEM picture of Fig.3.5. However a sample with both sources operating is used in Chapter 5.

One of the output (labeled 3) is wired to the RF homodyne detection, in order to measure the first harmonic of the average current I_Ω. Thus, good operating parameters of the dot can be found to reach proximity with perfect single-charge emission: gate voltages for which $\phi_0 = 0$, excitation voltage such that $2eV_{exc} = \Delta$. The second output (labeled 4) connects to either a spectrum analyser for noise measurement (see 3.2.2) or to a low-frequency homodyne detection. This setup is used to perform DC measurement of the transmission of the central QPC, as a function of gate voltage V_{qpc}. Consequently, the spectrum analyzer gives access to the excess autocorrelations $\Delta\overline{S}_{4,4}$, and not directly to cross-correlations $\overline{S}_{3,4}$. However, as shown in 3.1.4.1, current conservation law ensures that $\Delta\overline{S}_{4,4} = -\overline{S}_{3,4}$ at low frequency.

3.2.1.2 Choosing the magnetic field

The choice of the magnetic field $B = 3.2$ T is in fact more complex than simply working anywhere on the quantized plateau of $\nu = 2$. One of the main reason lies in the fact that the electron density in the 2DEG is not homogeneous over the whole sample. In particular, it differs between the bulk and the neighborhood of the central QPC and the quantum dot. Both densities can in fact be probed via DC measurements, in order to find the most favourable configuration.

Density in the bulk – Output 4 can also be used as an input to gain access to the impedance of the 2DEG. In that case, current is injected in the ohmic contact 4, and the impedance between contact 4 and the contact next to it (connected to the ground) is measured, according to Fig.3.6 a).

As a function of the field B, we observe plateaus of quantized Hall resistance (Fig. 3.7), hallmark of the quantum Hall regime. We clearly distinguish $\nu = 2$ to $\nu = 6$ before

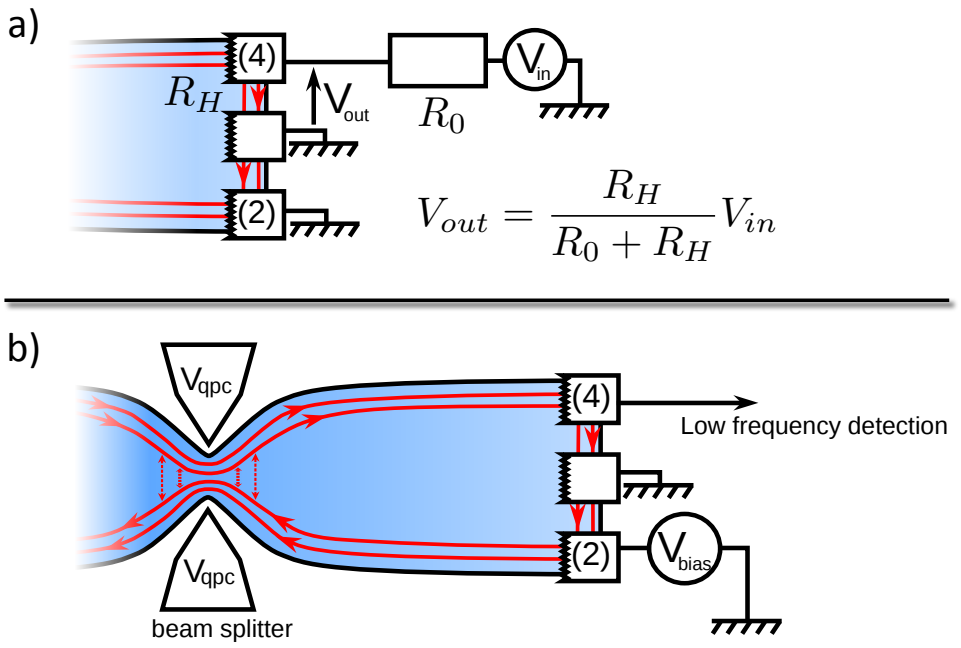

FIGURE 3.6: **Setup for measuring the impedance of the 2DEG** – a) *Configuration for measuring the impedance of the 2DEG:* via a bias V_{in} current is injected in a reverse configuration in contact 4. The voltage V_{out} that develops is directly proportional to the Hall resistance of the 2DEG R_H. Its measurement yields an accurate determination of the filling factor in the bulk. b) *Configuration for measuring backscattering:* current is injected from biased contact 2, as the QPC is completely opened. The backscattering signal (in non-calibrated units) is recorded in output 4 that is connected to a low-frequency homodyne detection. We assume that backscattering mainly occurs near the QPC (symbolized by red dashed arrows), so that this measurement gives access to the filling factor near the QPC.

measurements become less accurate. We can then choose to work on the plateau to reach a filling factor $\nu = 2$.

Density near the QPC – Measuring the impedance of the gas near the QPC is not possible in our experiment, but we can get an insight of the filling factor around the QPC by measuring the "backscattering" as a function of the field B. When $V_{bias} \neq 0$, a net current flows from input 2, that can be detected in 4 (Fig.3.6 b), using the LF homodyne detection, depending on the transmission of the central QPC. When this transmission is set to $T = 1$ (usually for $V_{qpc} \sim 0 - 0.1$ V), all the injected current is transmitted towards contact 3 so that no current should be detected in 4. However, this reasoning only holds if there is no backscattering in the edge channels, i.e. when electrons can not be backscattered from one edge to the other. It is only valid for an integer value[3] of the filling factor ν. When $\nu \notin \mathbb{N}$, backscattering occurs and a small but

[3] or any special fraction giving rise to fractional quantum Hall effect

measurable fraction of the injected current can be measured in 4. This scattering from one edge to the counter-propagating one is more likely to occur near the QPC where counter-propagating edge channels are brought close to one another. Thus we attribute the filling factor deduced from this measurements to the area that neighbours the QPC and the quantum dot.

An example of backscattered signal is presented on Fig.3.7. Minima are clearly visible with a backscattered signal close to 0. According to our analysis, we interpret the suppression of backscattering signal as an evidence of an integer filling factor near the QPC.

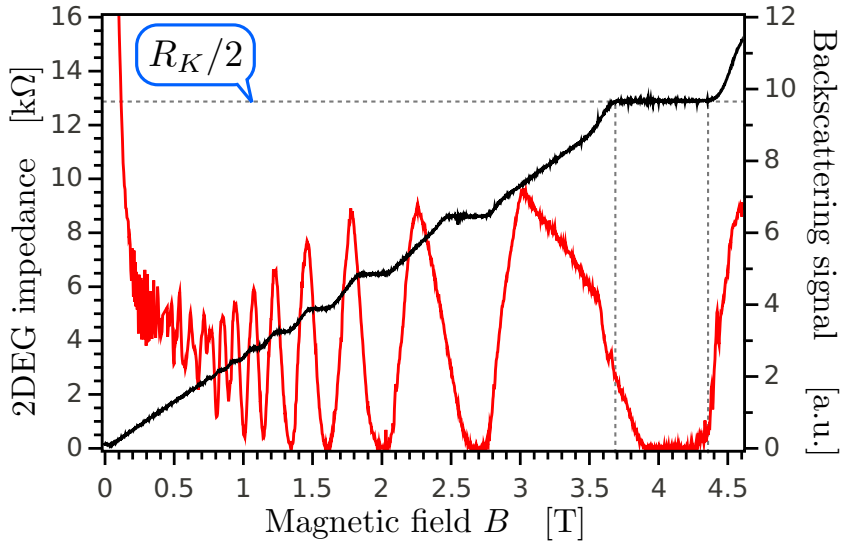

FIGURE 3.7: **Measurements of the impedance of the 2DEG and backscattering near the QPC** – In black line, the impedance of the gas is plotted, clearly exhibiting the typical plateaus of quantum Hall effect. Filling factor $\nu = 2$ in the bulk is identified by a resistance of $R_K/2$ (horizontal grey dashes). In red solid line, the backscattering signal goes to zero for integer filling factor near the QPC. A small discrepancy (vertical grey dashes) is observed between both measurements attributed to inhomogeneities in the density. Data correspond to sample *S434-C16L25A* used in chapter 5

To approach a filling factor $\nu = 2$ in the bulk as well as in the vicinity of the QPC and the source, we can then set the magnetic field in a region where:

- the impedance of the 2DEG is around the quantized value $R_K/2 = 12.8$ kΩ
- backscattering is suppressed.

For the sample presented in Fig.3.7 (used for the Hong-Ou-Mandel experiment, chapter 5), these two rules would consequently lead to set $B \simeq 4$ T. For sample *S434-C16L25A* used in this chapter, we found[4] $B = 3.65$ T.

However, a third ingredient has to be considered when choosing B: the QPC itself deviates from a linear behavior (as a function of bias voltage) when the magnetic field becomes larger. We discuss these features in the following paragraph, as they constitute a crucial point in this experiment.

3.2.1.3 Study of the central QPC

In this paragraph, we examine the central QPC in details. DC measurement can be performed easily and allow an accurate diagnosis of the best working points. In the meantime, it addresses a few problems that arose during the preparation of the experiment.

Transmission and effect of the magnetic field The first study that has to be carried out is the measurement of the transmission of the central QPC, as a function of the corresponding gate voltage V_{qpc}. We here present measurements of this transmission for a large range of magnetic fields. The measurement idea is rather obvious and the setup is identical to the one used to measure backscattering (see Fig.3.6): a DC bias V_{bias} is set on input 2, and the reflected current is measured in output 4, as a function of V_{qpc} and B. the results are presented in Fig.3.8, for the sample used in this chapter.

On this graph, nice conductance quantization steps are observed. The different filling factors can be identified, and when looking at $V_{qpc} = 0$, one recovers the measurements presented in section 3.2.1.2. However, the transition between plateaus is not monotonous for all samples and configurations: for fields above $B = 2.5$ T (corresponding to $\nu < 2$), the opening of the outermost channel sometimes present a rather complex structure, and may exhibit resonance in the conductance of the QPC. In these regions, we have not been able to calibrate or measure correctly current correlations (see section 3.2.3) with values up to 10 times the expected noise. We have attributed this unexpected result to a non-linear behavior of the transmission of the QPC. To find the best working points, we have then examined these features by measuring the dependence of the QPC conductance on the energy of the incoming electrons, by the use of the differential conductance.

[4] After an electrostatic shock due to power shortage in the lab, the density of 2DEG was modified and measurements were finally done at $B = 3.2$ T.

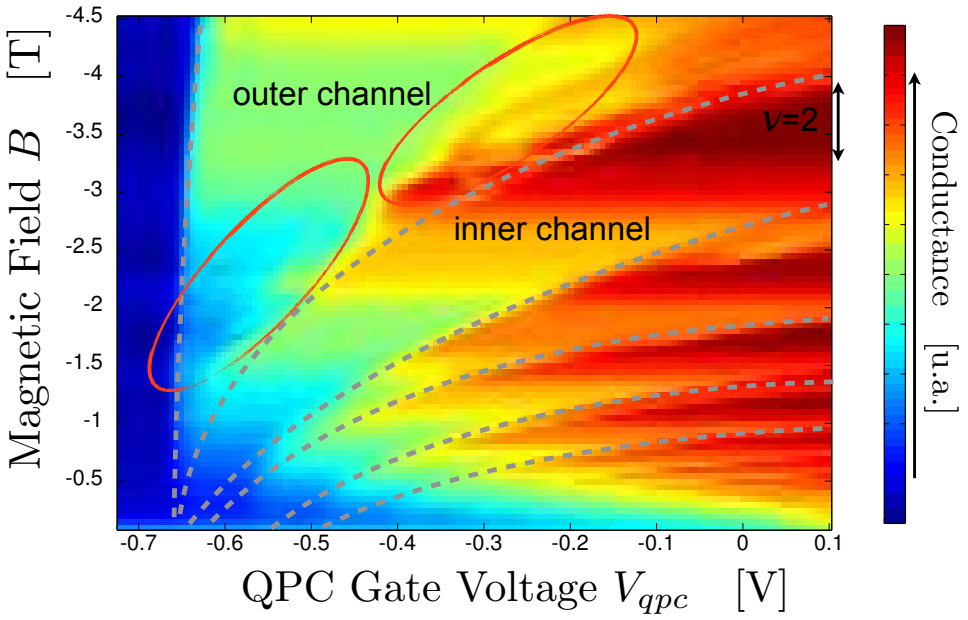

FIGURE 3.8: **2D plot of the transmission of central QPC, as a function of B and V_{qpc}** – The conductance of the central quantum point contact is presented in color scale (conductance increasing from blue to red), as a function of magnetic field B and gate voltage V_{qpc}. The progressive disappearance of the edge channels as B increases (grey dashes) allows for a clear identification of edge channels and filling factor ν. The area $\nu = 2$ labels a range of magnetic fields B where exactly two edge channels are transmitted when the QPC is opened. However non-motoneous behavior of the conductance (red line) necessitates a study of the differential conductance, either on outer or inner edge channels.

Differential conductance The idea of this series of measurement is to probe the behavior of the central QPC at a tunable and relatively well-defined energy. For this purpose, we study the differential conductance of the QPC. Prior to this study, V_{bias} was an AC signal (sine or square, but with no DC component) whose amplitude was arbitrary chosen. The only constraint was to obtain a measurable signal. Thus, the incoming electrons had energies ranging from typically $-V_{bias}$ to V_{bias}. Using typically $V_{bias} \simeq 90\,\mu$V, (corresponding to a temperature of 1 K) no information could be inferred on the energy dependence of the transmission of the QPC. In this study, we have decided to set the AC part V_{bias} to the lowest measurable value (typically 1.5 μV, less than 20 mK) and to vary the DC component V^0_{bias}. The results obtained are strongly sample dependent, but with a major tendency to worsen when the magnetic field B increases. Two different configurations are presented on Fig.3.9. In the first panel (a) are presented results obtained in a unfavorable situation (inner channel at $\nu = 2$, for the sample used in the HBT experiment). The transmission of the quantum point contact strongly depends on the DC bias V^0_{bias}, and exhibits resonances as the gate voltage V_{qpc} is changed. In this situation, the noise measurements can not be realized, as unexpected variations (on

a scale of a factor 10 to 50) are observed and not understood. This situation inevitably appears on the innermost channel for $\nu < 3$, but this channel is not relevant here, so that this problem is circumvented. More disturbingly, it sometimes also occurs when transmitting the outer edge channel, so that it cannot be ignored in the study. In the second panel (b), corresponding to the outer channel of $\nu = 2$, for $B = 3.65$ T, the transmission of the QPC is almost completely independent from the DC bias V^0_{bias}. With this type of behavior, we have been able to calibrate the setup and measure HBT correlations. These configurations are observed for filling factors around $\nu = 3$ for all samples, and up to $\nu = 2$ in certain cases.

This analysis has revealed in fact very important for our measurements. In most cases (though not always), the QPC behaves quite linearly for energies ranging from typically -100 to 100 μV. On one hand, this can be sufficient for an experiment using a DC-biased contact, where the bias is often set to values larger but comparable to the electronic temperature. On the other hand, our source is expected to emit quasiparticles at typical energies up to $\Delta \sim 2$ K ~ 160 μeV. The energy distribution is also expected to depend quite importantly with the choice of the operating parameters (D for example). A linear behavior of the QPC is then necessary in a broad range of energies. The choice of the magnetic field B is then a trade-off between the criteria defined in section 3.2.1.2 and the constraint imposed by a good behavior of the quantum point contact. Luckily, for this experiment, both criteria were fulfilled for filling factor $\nu = 2$, and the magnetic field was then set to[5] $B = 3.65$ T. In chapter 5, we resolved to work at $\nu = 3$ as we were unable to find a linear behavior of the QPC at $\nu = 2$.

3.2.2 Low-frequency noise detection

In this part, we describe the low-frequency noise detection and analyze its performance. We also present two independent calibrations of the gain of the whole detection scheme. The first one is an absolute calibration obtained by varying the temperature of the mixing-chamber of the dilution fridge. The second one relies on the measurement of low-frequency partition noise of a DC-biased contact. Both yield similar results, giving good confidence in the quality of the measurements performed.

3.2.2.1 Noise detection setup

The measurement of current correlations at low-frequency has required the development of a new detection setup, totally independent from the high-frequency noise setup used

[5] and finally brought to 3.2 T after, as already mentioned, a change in the density of the 2DEG.

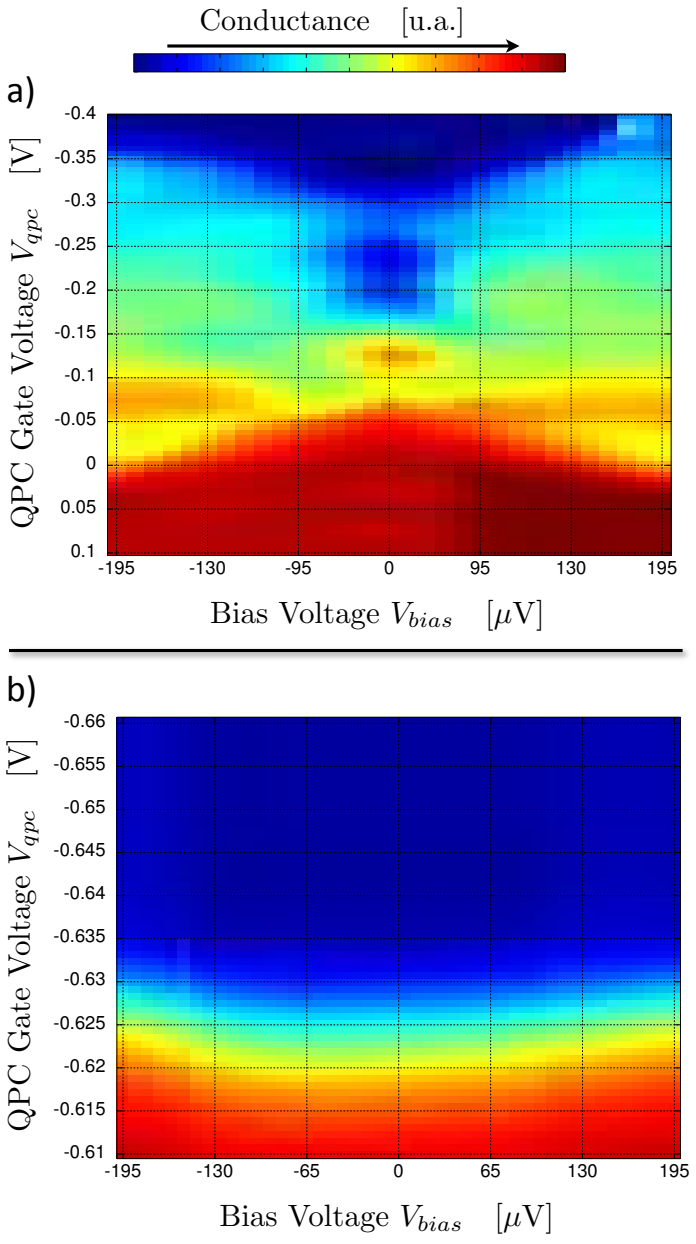

FIGURE 3.9: **Differential conductance of the central QPC in two different configurations** – (a) QPC transition that presents a highly non-linear conductance: $B = 3.65$ T, $\nu = 2$, inner edge channel. (b) QPC transition that presents a favorable linear conductance: $B = 3.65$ T, $\nu = 2$, outer edge channel. This configuration was the one conserved for the HBT correlation measurement, presented in this chapter.

for the study of high-frequency autocorrelations (discussed in 2.3, [83, 95]). First attempts to build up a robust and accurate setup were done during the PhD of F.D. Parmentier and are presented in his thesis [114]. Here is detailed the improved setup that was used to obtain the results presented in section 3.3.

The noise detection setup is presented on Fig.3.11. First, the current fluctuations at low-frequency are converted into voltage fluctuations by the use of a very stable resistor. It

Origins of the resonances in the QPC

The features observed in the study of the central QPC are in fact widely spread and can be observed in QPC conductances reported in [52]. Though it has not been scrutinized, it is very likely that the origin of the observed resonances is the existence of localized states trapped between the two metallic split gates. This has been studied in detail in [126]. As this phenomenon has annoying consequences, we will in the future try to slightly modify the gates design to reduce it.

Coupling between gate voltages

Throughout the manuscript, the different gate voltages are assumed to be completely independent. In fact, due to their proximity, V_g and V_{qpc} are coupled, but in a relatively weak way. For example, a variation of the dot gate voltage ΔV_g induces a variation $\Delta V_{qpc} \simeq 0.02\,\Delta V_g$ of the QPC gate voltage. But as V_{qpc} is varied on a wide span of circa 1 V, it is necessary to correct the dot gate voltage V_g for this parasitic coupling. On Fig.3.10, we reported the variations in gate voltage V_{qpc} of three different values of the QPC transmission T when V_g is changed. We observe that the coupling is linear which enables to correct V_g by simple linear corrections.

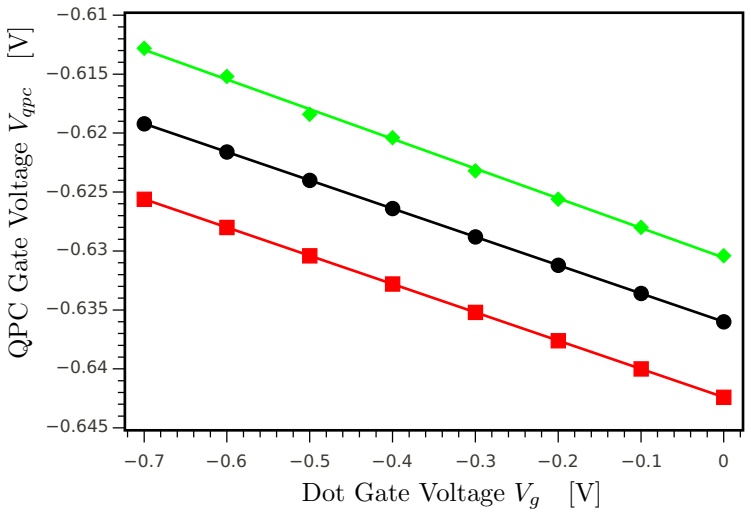

FIGURE 3.10: **Couplings between gates** V_g/V_{qpc} – By measuring the evolution of the gate voltages V_{qpc} for which $T = 0.25, 0.45$ and 0.81 for different values of V_g between -0.7 and 0 V, we observe a linear coupling from V_g on V_{qpc}. Similarly, the action of V_{qpc} on V_g is linear. This enables a simple but efficient correction of the static couplings between gates.

is supplied by the impedance of the 2DEG itself in the quantum Hall regime. Working at $\nu = 2$, this conversion resistor is then $R_0 = R_K/2 = 12.9\ \mathrm{k}\Omega$. The quantized value of this resistor is very robust, as it does not change with temperature, or with the applied RF or

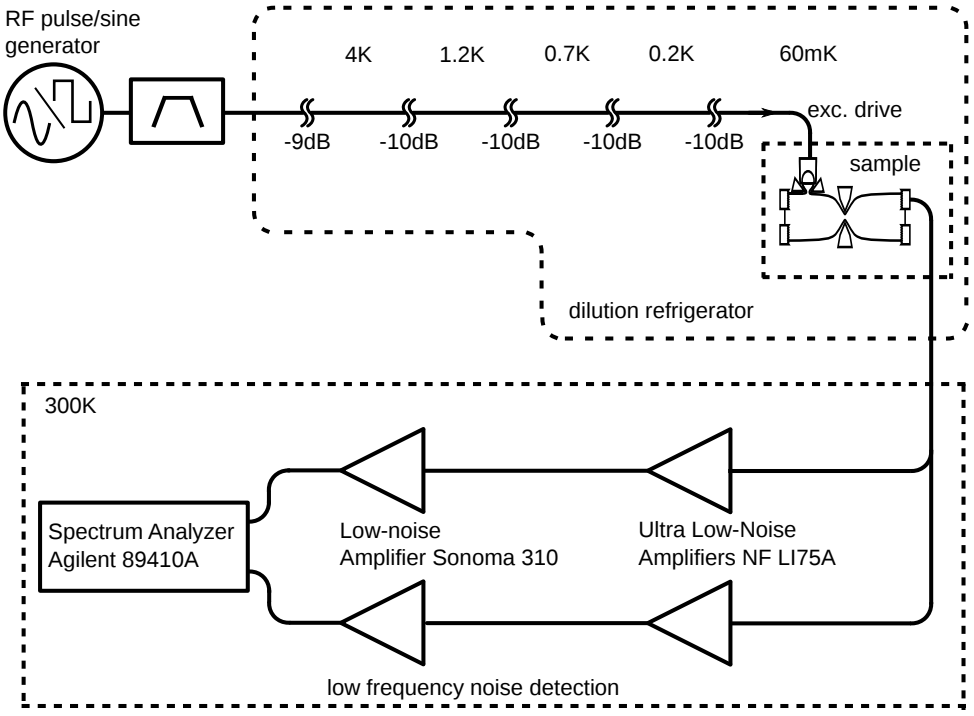

FIGURE 3.11: **Low-frequency noise detection setup** – Ultra-low noise room temperature amplification is provided by *NF LI75A* amplifiers, while the second stage of amplification is made of *Sonoma 310*. Both arms are cabled to the two input of an *Agilent 89410A* spectrum analyzer that computes averaged power in band in the range $35 - 98.125$ kHz.

DC voltages. It thus guarantees that the impedance seen from the detection line (and consequently from the amplifiers) is constant, and enhances the stability of the noise measurements. The voltage fluctuations are then transmitted via a coaxial RF cable from the sample to room temperature, where the signal is split using a T-connector, and connected to two different *NF LI-75A* amplifiers. After a second stage of amplification using *Sonoma 310* amplifiers, both signals are connected to a spectrum analyser (*Agilent 89410A*) where the spectrum of the cross-correlation is computed and averaged (between 200 to 500 times). Finally, the total power in band, in the range 35 to 98.125 kHz is computed by the spectrum analyzer and transmitted to a computer. This measurement is then repeated during approximately ten hours, to reach a resolution of $2\,10^{-30}\mathrm{A}^2\mathrm{Hz}^{-1}$. This method presents several experimental advantages that are presented in the next paragraph.

3.2.2.2 Expected performances of the noise measurement setup

In this paragraph, we analyze the performance of the noise detection scheme, and discuss other possible configurations, by examining an electrical model of the noise detection.

Assets and drawbacks of the choice of RF cables for collecting low-frequency noise

The choice of coaxial RF cables to collect the DC noise can be surprising at first sight. It indeed has assets and drawbacks. On the one hand, it enables the measurement of average current using room-temperature amplification. It is especially used for cross-checking results obtained from the usual RF measurement lines, that are equipped with cryo-amplifiers, but the wide bandwidth of the RF cables is also a strong asset to access frequencies out of the range of the cryo-amps. This will be used in chapter 4. On the other hand, it is quite difficult to thermalize this line (especially the core), that then brings heat from the room-temperature environement to the sample. This is responsible for an unusually high electronic temperature $T_{el} = 150$ mK in this experiment. It has nevertheless been improved to $T_{el} = 90$ mK for the measurements presented in chapter 5.

It follows a first developed by F.D. Parmentier in his thesis [84], and has been pursued under our supervision by V. Freulon.

Model of the noise detection setup In Fig.3.12, an outline of the noise detection setup is presented in panel a) while its model is pictured in panel b). The noise of the sample, that contains the HBT correlation and the thermal noise of the sample, is pictured as a current noise generator i_N with $< i_N >= 0$ and $< i_N^2 > \neq 0$, where $< \cdots >$ is the ensemble average. It is converted into voltage by virtue of the quantized Hall resistance $R_0 = R_K/2$.

As usually done, noisy amplifiers are modeled as perfect amplifiers with, on the input, fluctuating voltage e_k and intensity i_k generators of zero-mean value ($k = 1, 2$). Besides, we also introduce the total integrated capacitance C of the coaxial cable that will in the end limit the bandwidth. It is given by the linear capacitance of 100 pF/m multiplied by the length (roughly 2 m) of coaxial line, so that $C \simeq 0.2$ pF.

At point T where a T-splitter is placed, the voltage v_T can be computed and:

$$v_T = Z(i_1 + i_2 + i_N) \quad \text{with } Z(\omega) = \frac{R_0}{1 - iR_0C\omega} \tag{3.39}$$

As the voltage in outputs 1 and 2 is given by $v_k = e_k + v_T$, we may readily show that, for $k = 1, 2$:

$$< v_k^2 > = < e_k^2 > + |Z|^2 \big(< i_1^2 > + < i_2^2 > + < i_N^2 > \big) \tag{3.40}$$

$$< v_1 v_2 > = |Z|^2 \big(< i_1^2 > + < i_2^2 > + < i_N^2 > \big) \tag{3.41}$$

We immediately see one advantage of our scheme: the computation of cross-correlations $< v_1 v_2 >$ between two independent amplifiers (instead of auto-correlations $< v_k^2 >$ using

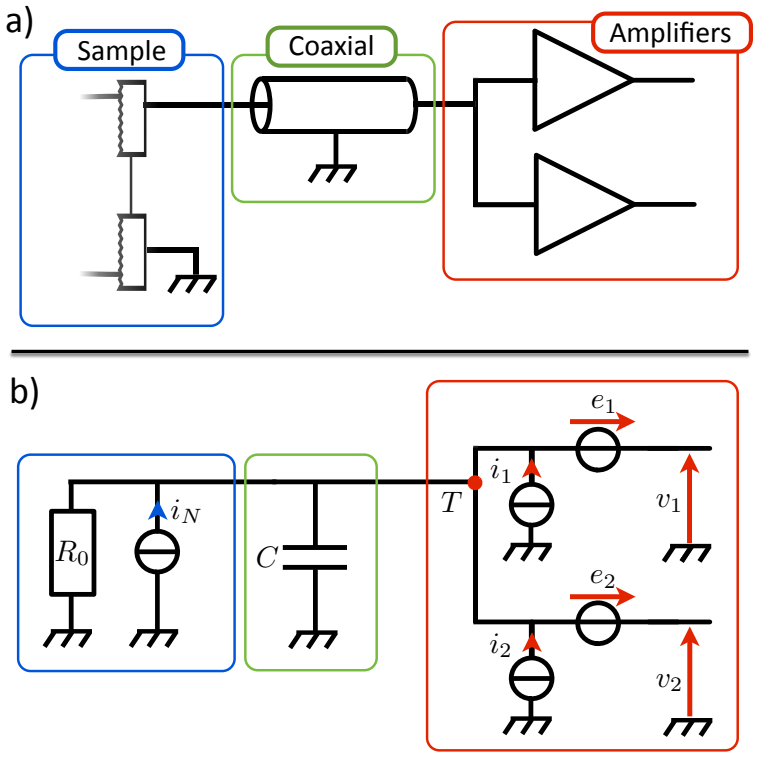

FIGURE 3.12: **Model of the noise detection setup** – a) The noise detection performances is governed by the properties of the sample (seen at $\nu = 2$ as a resistor of impedance $R_0 = R_K/2$), framed in blue, the coaxial cable (framed in green), and the first stage of amplification (*NF LI75A*, in a red frame). b) These different parts are modeled as an electrical circuit, a description that is valid at low frequencies. The noise of the sample (resp. the amplifier $k = 1, 2$) is described as a fluctuating generator delivering a current i_N (resp. $i_k, k = 1, 2$), while the coaxial is modeled as a parallel capacitance C. The performances of the noise detection can then be evaluated, by calculating the time τ necessary to reach a defined SNR.

one amplifier only) enables to get rid of the voltage noise $< e_k^2 >$ of the amplifiers. This is very interesting as this voltage noise acts as a background that can fluctuate or drift on long time-scales during the measurements.

Prediction of the measurement time The signal we want to measure is the current noise $\overline{S}_{4,4}$, converted in voltage noise $|Z|^2 S_{4,4}$ and is encoded in the cross-correlation $S_{v_1 v_2}$. For a measurement time $T_m \to \infty$, the Wiener-Khintchine theorem then gives $S_{v_1 v_2} = \lim_{T_m \to \infty} \frac{1}{T_m} < v_1 v_2 >$. When repeating N times the acquisition of $S_{v_1 v_2}$, the signal-to-noise ratio SNR is then given by:

$$\text{SNR} = \frac{|Z|^2 \overline{S}_{4,4}}{\Delta S_{v_1 v_2}} \sqrt{N} \tag{3.42}$$

$$\text{with } \Delta S_{v_1 v_2} = \lim_{T_m \to \infty} \frac{1}{T_m} \sqrt{< v_1^2 v_2^2 > - < v_1 v_2 >^2} \tag{3.43}$$

We assume for simplicity that both amplifiers are identical (which is approximately true using two *NF LI75A*), and we can obtain

$$\begin{aligned}\Delta S^2_{v_1v_2} &= \lim_{T_m\to\infty}\frac{1}{T_m^2}\Big[3|Z|^2\Big(2<i_2^2>^2+<i_N^2>^2\Big)\\ &+ <e_1^2>\Big(<e_1^2>+2|Z|^2\big(2<i_2^2>^2+<i_N^2>^2\big)\Big)\Big] \qquad (3.44)\end{aligned}$$

In our setup as in most cases, the signal is much smaller than the noise of the amplifiers and moreover, the noise of the amplifiers is here governed by the voltage noise of the amplifiers. Indeed, *LI75A* nominal specifications are:

$$S_v = \lim_{T_m\to\infty}<|e_k|^2>\simeq(1.8\,\mathrm{nV}/\sqrt{\mathrm{Hz}})^2 \qquad (3.45)$$

$$S_i = \lim_{T_m\to\infty}<|i_k|^2>\simeq(15\,\mathrm{fA}/\sqrt{\mathrm{Hz}})^2 \qquad (3.46)$$

One can then verify that, with $|Z|\sim R_0$ and $\overline{S}_{4,4}\sim\Delta\overline{Q}\sim e^2f$, $\Delta S_{v_1v_2}\simeq S_v\simeq(1.8\mathrm{nV}/\sqrt{\mathrm{Hz}})^2$. For a given SNR, the number of measurements N in a time τ_{meas} is then evaluated [83] using the integration bandwidth of the spectrum analyzer $\Delta f = 78.125$ kHz, yielding:

$$N = \Delta f\tau_{meas} \qquad (3.47)$$

$$\tau_{meas} = \frac{SNR^2}{\Delta f}\left(\frac{S_v}{|Z|^2\overline{S}_{4,4}}\right)^2 \qquad (3.48)$$

A crucial point here is the bandwidth Δf over which the signal is integrated, as compared to the corner frequency of the coaxial line $f_c = 1/R_0C$. With $|Z|^2 = \frac{R_0^2}{1+R_0^2C^2\omega^2}$, it appears that the noise of the source is efficiently collected at frequencies much smaller than f_c while the white voltage noise of the amplifier is not affected by this factor, and integrated over the full bandwidth Δf.

Finally, the upper bound of the bandwidth is set to 98.125 kHz as the signal is nearly non-existent above such frequencies much bigger than f_c. The lower bound is unfortunately fixed to 30 kHz due to vibrations in the 1K pot of the dilution fridge, responsible for noisy spectra below 30 kHz. Taking into account that subtracting a background multiplies the measurement time by a factor 2 and the standard deviation by $\sqrt{2}$, we can evaluate the total measurement time to $\tau_{meas}\simeq 8$ hours per point (for $SNR\simeq 7$), which is not very far but slightly underestimates the real measurement time, of about 10 hours.

3.2.3 Calibration of the noise detection scheme

In this section, two independent calibration of the low-frequency correlations are presented. The results obtained are compatible, within a 10% error rate.

3.2.3.1 Absolute calibration by noise thermometry

The first method is to record the variations of the equilibrium noise (background noise usually subtracted in the measurements) as the temperature of the mixing chamber T_{mc} is varied. We observe (see results on Fig.3.13) a variation of the absolute HBT correlation $\overline{S}_{4,4}$ with T_{mc}, that we can fit using the Johnson-Nyquist function $G\overline{S}_{4,4} = 4G\frac{2}{R_K}T_{eff}$, where G is the gain of the detection scheme (with $\overline{S}_{4,4}$ expressed in $\mathrm{A^2Hz^{-1}}$, and $G\overline{S}_{4,4}$ measured in $\mathrm{V^{-2}}$), and where $T_{eff} = \sqrt{T_{el}^2 + T_{mc}^2}$ is an effective temperature, T_{el} being as previously the residual electronic temperature, when the dilution fridge lies at its base temperature. The conductance $2/R_K$ corresponds here to a filling factor $\nu = 2$. From this measurement, we get $T_{el} = 150 \pm 10$ mK. From the linear extrapolation as well as the previous non-linear fit, we also get $G = 1.3\,10^{19}\,\mathrm{V^2/A^2Hz^{-1}}$.

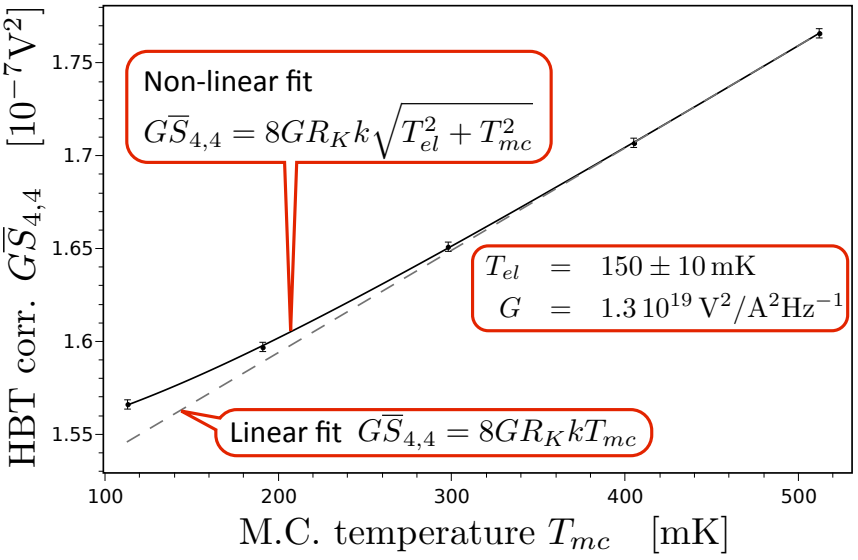

FIGURE 3.13: **Absolute calibration using noise thermometry** – The (absolute) equilibrium Johnson-Nyquist noise of the sample is measured as a function of T_{mc}, temperature of the mixing chamber of the fridge. A fit $\overline{S}_{4,4} = 4G\frac{2}{R_K}\sqrt{T_{el}^2 + T_{mc}^2}$ then sets the calibration of the electronic temperature $T_{el} = 150$ mK and of the gain $G = 1.3\,10^{19}\,\mathrm{V^2/A^2Hz^{-1}}$

3.2.3.2 Relative calibration by partition noise of a DC source

The second calibration method relies on the partition noise obtained when a DC current is impinging upon the central quantum point contact. This current is created by biasing contact 2 (see Fig.3.5) using V_{bias}. Unlike in the previous calibration, only the excess contribution is recorded, and the background noise is subtracted. Using $G = 1.3\,10^{19}\,\mathrm{V^2/A^2Hz^{-1}}$ and $T_{el} = 150$ mK obtained earlier, the data (Fig.3.13) are in

excellent agreement with the theoretical predictions (black plain line):

$$\overline{S}_{4,4} = 2\frac{e^2}{h}T(1-T)eV_{bias}\left[\text{cotanh}\left(\frac{eV_{bias}}{2kT_{el}}\right) - \frac{2kT_{el}}{eV_{bias}}\right] \tag{3.49}$$

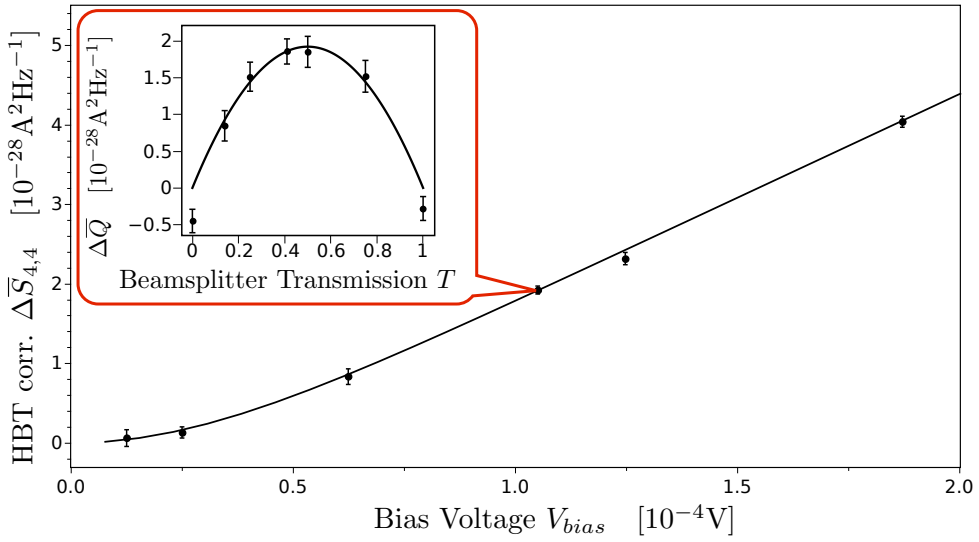

FIGURE 3.14: **Relative calibration using partition noise of a DC-biased contact** – Current created by biasing contact 2 (with voltage V_{bias}) is partitioned and the resulting excess noise $\Delta\overline{S}_{4,4}$ is recorded. The data is in excellent agreement with the theoretical prediction of the scattering model (Eq.(3.49)), where the gain G and electronic temperature T_{el} are settled by the absolute noise thermometry calibration described in paragraph 3.2.3.1

Although this calibration was mostly performed at a transmission $T = 1/2$, one point of this calibration has been obtained by verifying the $T(1-T)$ dependence. The graph obtained is presented as an inset, and the fit with a parabola $\alpha T(1-T)$ of arbitrary amplitude α then yields the point reported on the graph. This second calibration thus confirms both the evaluation of T_{el} and G, and demonstrates the correct behavior of the electronic beamsplitter when it comes to noise measurements.

The development of a robust and accurate noise detection has been examined in this section. Two different calibrations have been proposed, that yield similar results and thus give a good confidence in the quality of the acquired data. In the next section, we examine the results obtained when partitioning the quasiparticles emitted on demand by our single electron source.

3.3 Results

As explained in section 3.1, the Hanbury-Brown & Twiss correlations provide a direct counting of the total number of quasiparticles emitted by the single electron source, and helps to probe the energy distribution of the emitted wavepackets by direct comparison with the Fermi distribution.

First, we examine the effect of the beamsplitter transmission T on the HBT signal recorded. We establish the expected $T(1-T)$ dependence of the correlations (see Eq.(3.28)) in three different configurations, which demonstrates that the signal measured is partition noise, with no visible unexpected parasitic contribution. Then, the amplitude of the HBT correlation is carefully analyzed in these three situations: a phenomenological understanding of the underlying physics is first presented, before using Floquet scattering theory to confirm the claims. Finally, we scan a portion of the phase space by changing the transmission of the dot D, for two types of excitation drives (sine and square), and examine the variation of the correlations, that are found to be in good agreement with Floquet scattering theory, and tend to prove that an engineering of the emitted wavepackets can be achieved.

3.3.1 HBT partition noise as a function of the beamsplitter transmission T

We first investigate the T-dependence of the HBT correlations, for three choices of typical operating conditions. The data is presented in Fig.3.15, where parameters are summarized in a table. The three graphs are well adjusted with fits of the expected form $\Delta\overline{S}_{4,4} = T(1-T)\Delta\overline{Q}$ (in plain lines). In particular, no extra noise is recorded at $T = 1$ or $T = 0$: this demonstrates that the source in itself is not giving low-frequency noise, and that the subtraction of background noise is not a source of problems. The amplitude of the fits then enables to access $\delta N_{HBT} = \Delta\overline{Q}/4e^2 f$, which is reported in the table of Fig.3.15.

Case of a sine drive In black plain line and triangles, the parameters chosen are a sine excitation, the dot being opened, and completely coupled to the reservoir ($D = 1$). In that case, no discrete level appear in the dot (the density of states is constant, $\mathcal{N}(\epsilon) = 1/\Delta$), and the escape time τ_e is much shorter than the half-period $T/2$. The average transmitted charge $Q_t = 1.27 > 1$ (deduced from homodyne current measurement) show that the emitted charge is not accurately quantized in this regime. On the opposite, the HBT signal gives $\delta N_{HBT} = 0.51$. The number of particles counted with HBT

correlations is then smaller (by 60%!) than the number of charges counted via the current. Since $\delta N_{HBT} < Q_t$, no extra electron/hole pairs are then clearly visible in that case. Indeed, in a naive picture, the number of quasiparticles counted through HBT correlations can only be larger than the total charge transferred charge. This is a first evidence that the correcting factor coming from antibunching with thermal excitations plays an important role in the explanation of this experiment.

In red line and dots, we report results for a sine wave with a dot transmission of $D \simeq 0.3$. Then, the density of states in the dot has a structure of well-defined equidistant quantized levels, and τ_e is larger than in the previous case. The transferred charge is then close to unity $Q_t = 0.93$ and in the meantime we find $\delta N_{HBT} = 0.63$. As compared to previous case, δN_{HBT} has increased but remains smaller that Q_t, which has decreased.

Case of a square drive In the third situation (green line and squares), we use a square wave, with $D \simeq 0.4$. This is the generic case of quasi-perfect single charge emission, that was demonstrated in section 2.3. Indeed, we record the transfer of a charge unity $Q_t = 1$. In that case, the transferred charge is comparable to the one emitted with a sine wave at $D = 0.3$, but δN_{HBT} is increased up to 80% of Q_t. Still no extra particles are detected.

In a nutshell, we see that in all cases, $\delta N_{HBT} < Q_t$. As classical partitioning (Eq.(3.19)) predicts a lower bound of $\delta N_{HBT} \geq Q_t$, we clearly see that our results can only be explained by the quantum theory that takes into account an antibunching effect with thermal excitations in the reservoir. This effect, totally encoded in the second term of Eq.(3.34), appears as an important feature to understand our results. In fact, it also offers a way to probe the energy distribution of the emitted quasiparticles. Indeed, as appears in Eq.(3.34), the two-particle interference with thermal excitations strongly depends on the energy distribution $\delta n_{e/h}$ and is in particular reinforced for quasiparticles emitted at low energies.

The next section is then dedicated to explain why quasiparticles are emitted preferably at low or high energies depending on the parameters. Qualitative arguments will first be given, thus establishing an intuitive picture of the results described in this section. Then, the energy distribution $\delta n_{e/h}$ will be computed via Floquet scattering theory and will confirm these findings.

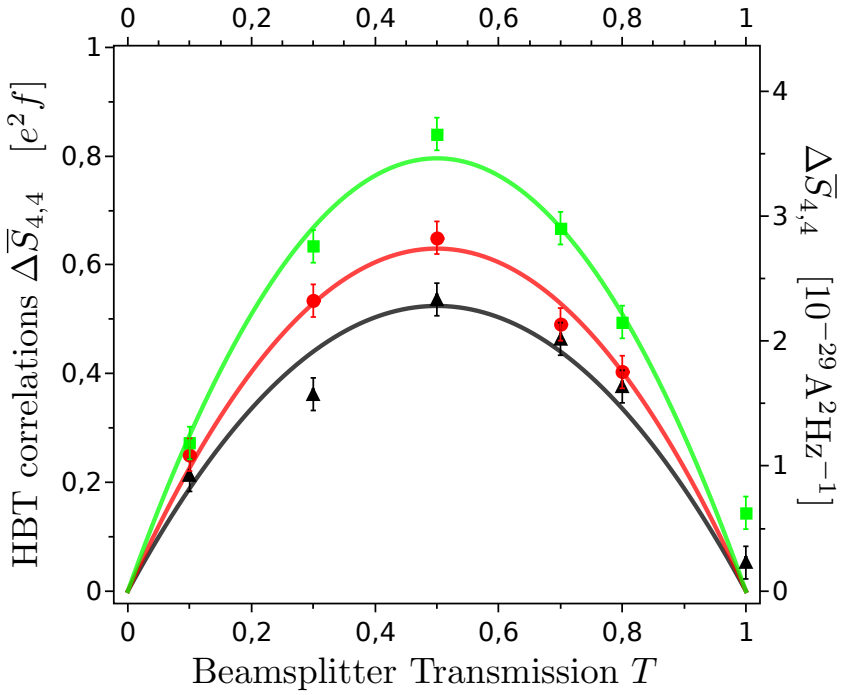

Color	Parameters	Q_t	δN_{HBT}
— ▲	Sine, $D = 1$	1.27	0.51
— ●	Sine, $D = 0.3$	0.93	0.63
— ■	Square, $D = 0.4$	1	0.80

FIGURE 3.15: **Hanbury-Brown & Twiss partition noise as a function of the beamsplitter transmission T, in three different cases** – In all cases, $\Delta\overline{S}_{4,4} \propto T(1-T)$, proving that the term $\Delta\overline{Q}$ is effectively captured. The amplitude of these parabola yields δN_{HBT}. The value of δN_{HBT} strongly depends on the shape of the drive and on the transmission of the dot D, and we observe values violating the classical bound $\delta N_{HBT} < Q_t$. These features are attributed to the quantum interference between thermal excitations and quasiparticles emitted by our source (Eq.(3.34)), effect which strongly varies depending on the energy distribution of the emitted quasi-particles.

3.3.2 Analysis of the results

3.3.2.1 Qualitative model

Simple and intuitive explanations can be given to understand the antibunching effect with thermally excited electron/hole pairs. They explain remarkably well the influence of the choice of the excitation (sine or square) and of the transmission D on the dramatic decrease of the HBT signal. All the explanations are summarized in figure Fig.3.16, that we comment hereafter.

In Fig.3.16, we picture qualitatively the energy $\epsilon(t)$ (in red) of the highest occupied level of the dot as a function of time. When the injection condition $2eV_{exc} = \Delta$ is satisfied, $\epsilon(t)$ (depicted in red) moves between $-\Delta/2$ and $+\Delta/2$ and reproduces the variations of V_{exc}. The discretization of the emission time in units of $\tau_0 = h/\Delta$ (duration of a turn in the dot) is schematized.

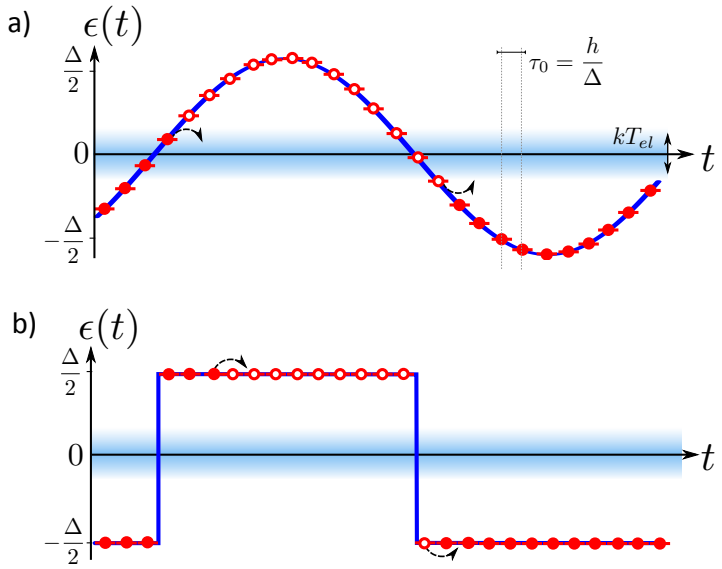

FIGURE 3.16: **Sketch of the emission process** – The position $\epsilon(t)$ of the highest occupied level in the dot is depicted as a function of time t, for the two types of drive (sine and square) used in this experiment. The time axis is discretized in units of $\tau_0 = h/\Delta$, and emission events are symbolized by black dashed arrows. a) *Sine drive:* When a sine drive is used, the highest occupied level level crosses smoothly the Fermi level of the reservoir. Consequently, for sufficiently large transmissions D, emission occurs at low energies that are comparable with the energy of thermal excitations, depicted as a blue blur of energy width kT_{el}. b) *Square drive:* When a square drive is used, the highest occupied level level is shifted rapidly. Consequently, emission occurs for energies around $\pm\Delta/2$. The quasiparticles are then well separated from thermal excitations.

Case of a sine drive When using a sine wave, $\epsilon(t)$ varies smoothly in time, and consequently the crossing of the highest occupied level and the Fermi level of the reservoir (lying at $\epsilon_F = 0$) is also smooth. When the transmission is large ($D = 1$), τ_e is very short (with respect to $T/2$) and the quasiparticles are mostly emitted in a very short-time interval around the crossing $\epsilon(t) = \epsilon_F = 0$ (pictured as black curved arrows). Consequently, most of the quasiparticles are likely to lie at low energies, that can be comparable to kT_{el}, so that the antibunching effect is expected to be quite large. The energy distribution $\delta n_{e/h}$ is then expected to give mainly a peak around $\epsilon = 0$

When the transmission is set to a lower value ($D = 0.3$), the emission can be delayed by several τ_0 with respect to the instant at which the crossing $\epsilon(t) = \epsilon_F = 0$ occurs. In that

case, the quasiparticles are emitted at higher energies as $\epsilon(t)$ is significantly different from $\epsilon_F = 0$ when the tunneling event takes place. This corresponds to a widely spread energy distribution $\delta n_{e/h}$ around $\epsilon_F = 0$, with a width that can be much larger than kT_{el} so that we understand that the two-particle thermal interferences should be indeed reduced, and δN_{HBT} enhanced.

Case of a square drive This reasoning can be revisited for the use of a square drive. For an ideal square, one can imagine that $\epsilon(t)$ is periodically abruptly shifted between positions $\pm\Delta/2$. Even for large transmission / short emission time ($D \simeq 1$ / $\tau_e \ll T/2$), quasiparticles are injected in the reservoir with an energy neighbouring $\pm\Delta/2$. As a consequence, thermal antibunching is greatly reduced with this set of parameters.

These considerations explain qualitatively the behavior observed previously. To summarize, the observed variation of the antibunching effect with thermal electron/hole pairs of the reservoir is attributed to a modification of the energy distribution $\delta n_{e/h}$, that can be explained qualitatively to a great extent. On the one hand, a sine drive has a tendency to produce low-energy quasiparticles, but the energy distribution seems to be greatly modified when reducing the transmission D of the SES. On the other hand, the HBT signal given by an ideal square drive is only poorly affected by thermal excitations, as quasiparticles are much likely to be emitted at energies around $\pm\Delta/2$. We also expect the effect of D to be less pronounced. However, one must keep in mind that the production of an ideal square voltage can not be achieved experimentally, due to limited bandwidths of generators as well as RF excitation lines.

3.3.2.2 Energy distribution $\delta n_{e/h}$ from Floquet scattering theory

In this paragraph, we present numerical simulations of the energy distribution $\delta n_{e/h}$, in all of the forementioned cases, that support the discussion of the previous section. In Fig.3.17, distributions $\delta n_{e/h}$ are drawn as a function of energy ϵ as obtained from Eq.(3.37). According to notations adopted in section 3.1.4.3, energies are counted positively for both electrons and holes and are scaled in units of level-spacing Δ. The electronic temperature is set to $T_{el} = 0$ in this computation. Recalling the HBT correlation calculated from the quantum model (Eq.(3.33)),

$$\delta N_{HBT} = \frac{1}{2}\int_0^\infty d\epsilon \, \big(1 - 2f_{\mu=0}(\epsilon)\big)\big(\delta n_e(\epsilon) + \delta n_h(\epsilon)\big) \tag{3.50}$$

it appears relevant to plot the counting factor $1-2f_{\mu=0}(\epsilon)$ that encodes the antibunching effect with thermal excitations coming from the Fermi sea at the residual electronic temperature $T_{el} = 150$ mK (in grey dashed line): quasiparticles lying at low energies

are weighted with a reduced counting factor, and thus do not fully participate to the Hanbury-Brown & Twiss correlation as could be expected from a classical binomial partitioning process.

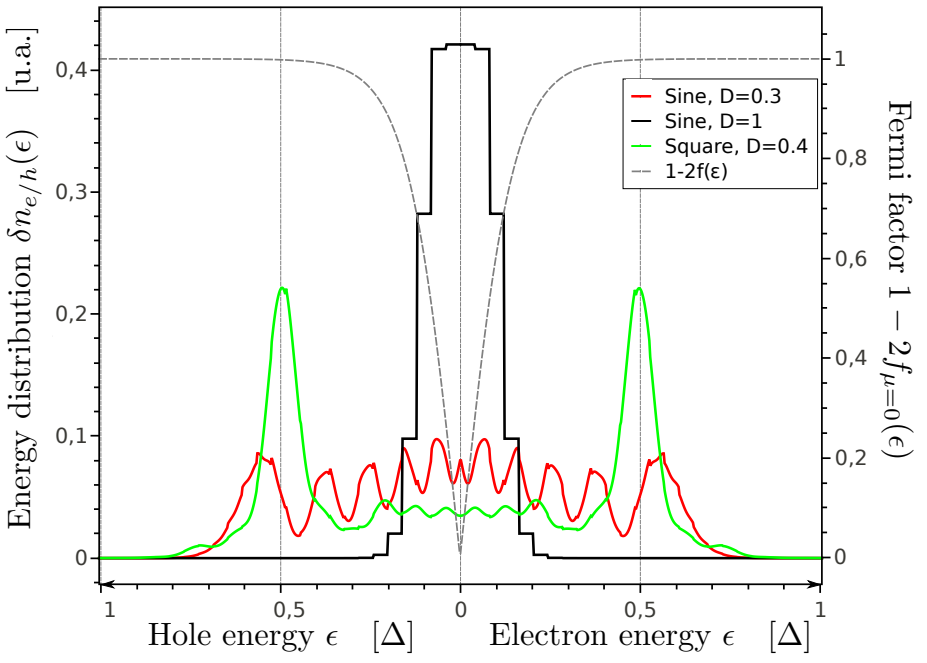

FIGURE 3.17: **Energy distribution of emitted quasiparticles, computed via Floquet scattering theory** – In grey dashes is drawn the counting factor $1-2f_{\mu=0}$ that can be compared with energy distributions calculated in the three cases studied here. In black, a source at $D = 1$ and driven by sine waves produces excitations of low energies, highly affected by anti-bunching. In red, when driven by a sine wave at $D = 0.3$, the energy distribution $\delta n_e(\epsilon)$ spreads over a large range of energies $[-\Delta/2, \Delta/2]$ and is less sensitive to the presence of thermal excitations. In green, a square wave at $D = 0.4$ emits quasi-ideal energy-resolved excitations around $\pm\Delta/2$ only slightly affected by the electronic temperature.

Case of a sine drive Represented in black line, the energy distribution $\delta n_{e/h}$ obtained for a sine drive with opened dot $D = 1$ consists of a single peak around the Fermi energy $\epsilon_F = 0$. The step structure of the peak, with periodicity $\hbar\Omega$, arises from the multi-photon absorption/emission processes. As such, the overlap between $\delta n_{e/h}$ and the factor $1 - 2f_{\mu=0}$ is very large, as they both have the same typical energy width.

When the transmission is set to $D \simeq 0.3$ (red line), $\delta n_{e/h}$ is broadened on the full energy range $[-\Delta/2, \Delta/2]$. The step structure is not visible anymore as tunneling in and out of the quantum dot is responsible for complex non-linear mechanisms. On the opposite, new regularly spaced peaks appear. They in fact remarkably confirm our simple reasoning of the previous section. Numerical investigations have indeed shown that they stem from the finite time τ_0 to perform a turn in the dot, that favours emission

events at certain instants separated in time by τ_0. As the energy $\epsilon(t)$ of the level in the dot is following a sine variation, these enhanced emission instants correspond to different energies. Consequently, the number of peaks n_{peaks} in $\delta n_{e/h}$ is globally governed by the number of τ_0 in half a period $T/2$: $n_{peaks} \simeq \frac{T/2}{\tau_0} \simeq \frac{\Delta}{2\hbar\Omega} \simeq 11$ (for $\Omega \simeq 90$ mK and $\Delta \simeq 2$ K) as observed on Fig.3.17. The increased HBT signal recorded in that case can then be reasonably attributed to the broadening of $\delta n_{e/h}$.

Case of a square drive Finally, for a square excitation at $D = 0.4$ (green line), we observe mainly two peaks at $\epsilon = \pm\Delta/2$, confirming the idea of energy-resolved quasiparticles, flying above the Fermi sea. Consequently, HBT correlations are less affected by the presence of the Fermi sea. However, in this simulation, a finite number of harmonics (3 odd harmonics) have been kept in the square voltage. This choice seems reasonable when evaluating the bandwidths of the RF lines and has been corroborated undirectly by noise measurement presented in section 2.3.5.2. This imperfection is responsible for a residual weight around $\epsilon = 0$ in the energy distribution. This residual contribution is highly sensitive to thermal excitations and thus reduces the HBT signal to 80% of the expected value.

In this section, we have studied the amplitude of the HBT correlations in three typical cases. After having demonstrated the validity of our measurements by capturing the $T(1-T)$ dependence in the beamsplitter transmission, we have shown that the amplitude of the recorded signal could be attributed to the antibunching of the quasiparticles emitted with thermal excitations already present in the reservoir. In good agreement with predictions from Floquet scattering theory, this phenomenon tends to prove that the wavepackets of electrons and holes emitted by the SES can be engineered by the choice of the parameters such as the dot transmission D or the type of excitation (sine/square). In the next section, we investigate the HBT correlation as a function of D, in order to get further evidence of a possible tuning of the wavepacket.

3.3.3 Wavepacket engineering

The idea is here to scan a portion of the phase space, by changing the transmission of the dot D for the two types of excitation (sine or square), still keeping the condition of non-resonance $\phi_0 = 0$.

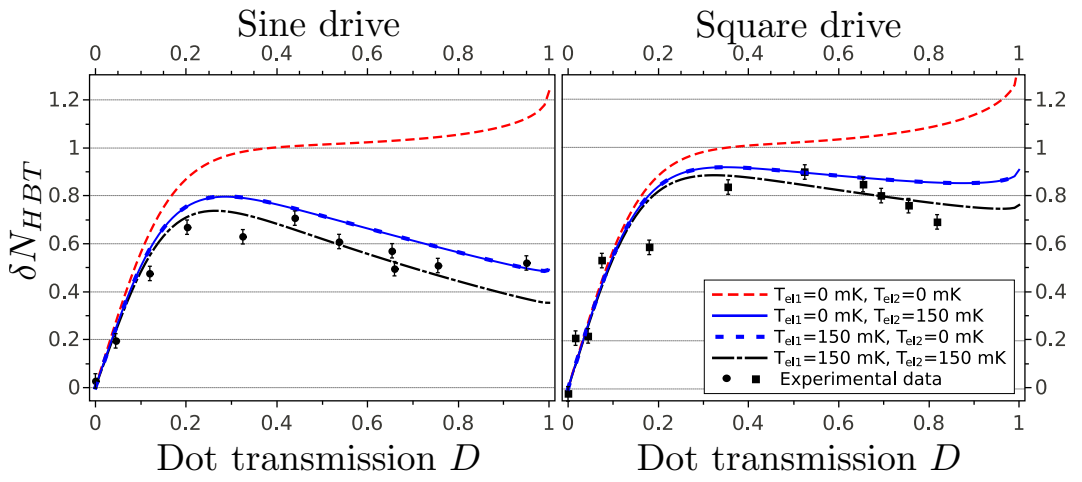

FIGURE 3.18: **Hanbury-Brown & Twiss partition noise as a function of the dot transmission D for excitation signals sine or square** – HBT correlations are in good agreement with Floquet simulations at $T_{el} = 150$ mK (black dashed-dotted line), but not at $T_{el} = 0$ mK (red dashes), confirming the primordial role of thermal excitations. In the low transmission regime $D < 0.2$, the anti-bunching effected is almost undetectable as quasiparticles are emitted at rather high energies, for both square and sine drives. However some emission events are missed in this regime, so that we have $Q_t < 1$ and $\delta N_{HBT} < 1$. In the high transmission $D > 0.2$, the anti-bunching is much more pronounced, especially in the case of sine excitation, that tends to produce quasiparticles at low energies, as compared with the square excitation. In blue line and dashes, simulations demonstrate the equivalent role of temperatures in contacts 1 and 2.

3.3.3.1 Description of the results

The data is presented in Fig.3.18. A first interpretation can be proposed, before turning to the detailed analysis of the effect of temperature via Floquet scattering theory. For this we focus on the experimental points and on two (out of four proposed) numerical simulations: the red dashed line is the simulation of δN_{HBT} (Eq.(3.33)) for $T_{el} = 0$ in all the contacts of the reservoir, while the black dashed-dotted lines shows the same quantity calculated for the calibrated $T_{el} = 150$ mK.

General features Globally, we identify (both on simulations and data) two regimes in each graph, regardless of the type of excitation. For $D < 0.2$, the low transmission regime takes place, governed by the non-unit emission probability. Since τ_e is large, some quasiparticles are not emitted during the dedicated half-period. It corresponds to the shot noise regime already observed in the average current (section 2.2) or the autocorrelations (section 2.3). For $D > 0.2$, the high transmission is characterized by a unit emission probability: all quasiparticles are emitted, but we expect strong variations of their wavefunctions, depending on the choice of D and type of drives.

Low transmission regime For $D < 0.2$ we observe that both simulations give similar results that are in rather good agreement with our data. The effect of temperature seems rather small in this regime, which can be understood in the following manner: since τ_e is large, the SES quasiparticles are likely to be emitted at rather high energies as explained in 3.3.2.1, and are consequently less sensitive to the presence of thermal excitations. As a consequence, simulations and data at finite temperature resemble the zero temperature limit. For the very same reason, the difference between the sine and square drive is less prominent. In this regime, we approach the limit of classical partitioning, and $\delta N_{HBT} \simeq Q_t$.

High transmission regime For $D > 0.2$, the SES quasiparticles are emitted with unit probability during each emission cycle. We first observe that the effect of temperature is quite important in simulations, and that the data (for both sine and square drives) are in good agreement with finite temperature simulations. In both panels, the simulation at zero temperature exhibits a plateau around $\delta N_{HBT} = 1$. In this regime, the HBT signal reaches the limit of classical partitioning of single quasiparticles. On the other hand, the simulation at $T_{el} = 150$ mK gives δN_{HBT} reduced by 20 to 60% as compared with classical results, due to the quantum antibunching effect with thermal electron/hole pairs.

The data and simulations in this domain of transmission strongly depends on the choice of drive type. For a sine wave, the HBT contribution at $T_{el} \neq 0$ is much smaller than for the square drive, whereas predictions are identical for $T_{el} = 0$ mK. This confirms once again that the overall tendency to produce low energy excitations when using a sine drive, as compared to high energy excitations using a square drive. This interpretation is also corroborated with the D-dependence in itself. Whereas the HBT signal only slightly decreases when $D \to 1$ for a square, it drops more strikingly with a sine. According to the discussion of 3.3.2.1, the effect of D should indeed be more pronounced in the latter case.

3.3.3.2 Detailed study of the effect of temperature

In this section, we investigate a peculiar phenomenon. So far, our explanations refer implicitly to an antibunching effect with particles coming from contact 2, that are incident on the central beamsplitter. They are responsible for the correction term $1 - 2f_\mu$ in the formula (3.33). But from Eq.(3.37), we see that $\delta n_{e/h}$ itself is also affected by the effect of temperature, but this time in contact 1. This has driven us to investigate numerically the separate influence of temperature in these contacts, labeled $T_{el,1}$ and

$T_{el,2}$. We have then observed that both contacts played the same role in the decrease of the HBT signal: the two blue dashed curves of Fig.3.18 are perfectly superposed.

This can be understood in the following manner. Temperature can be seen as an additional fluctuating V_T voltage bias on the contact, with $< V_T^2 > /R_K \sim kT_{el}$. By a translation of potentials, one can then transfer the fluctuating voltage from contact 2 to contact 1, 3, 4 and top-gate (see Fig.3.5 page 74 for notations). By virtue of chirality, fluctuations in contact 3 and 4 do not play any role in the study. Fluctuations on the top-gate of the dot do not play any role either due to a large impedance mismatch between the capacitance and the channel $\omega R_K C_q \ll 1$ at low frequencies, so that in the end temperature on contact 1 and 2 have the same influence on the HBT correlation. We have checked this reasoning by showing that same simulations were obtained for $T_{el,1} = T_{el,2} = T_{el} \neq 0$ (same finite temperature in both contacts) than for $T_{el,1} = 0$ and $T_{el,2} = \sqrt{2}T_{el}$.

This section has been dedicated to the detailed analysis of our experimental results concerning current autocorrelations in an Hanbury-Brown & Twiss geometry. The two-particle interference between mono-electronic wavepackets emitted by the on-demand SES and thermal excitations appears as a major effect that has to be taken into account to understand the measured correlations. Besides, it gives a way of probing the wavepacket of the single on-demand quasiparticles by direct comparison with the Fermi distribution. In the next section, we show how this idea can be generalized to reconstruct the complete energy distribution (spectroscopy) or even the complete wavepacket (tomography).

3.4 Towards spectroscopy and tomography of mono-electronic wavepackets

In the Hanbury-Brown & Twiss geometry, the anti-bunching effect between quasiparticles emitted by any source and thermal excitations in the neighbouring contacts can be used to have access to information on the energy distribution of the excitations delivered by the source, by measuring the overlap with the Fermi-distribution. But the Fermi distribution of the contact, though very robust due to its thermodynamic equilibrium properties, only yields partial information. To go beyond this point, one could think of changing the temperature of the contact. But as T_{el} is increased, the thermal smearing increases and information become quite inaccurate. Moreover, in our setup, it is not possible to reach the necessary stability to perform the measurements during several hours (cf. section 3.2.2). However, a complete tomography can be developed in a much

more efficient manner, paving the way towards more advanced electron quantum optics experiment: it was developed by Grenier *et al.* in collaboration with our group [46].

Alternatively, we here mention a complementary study by Haack *et al.* [127] that enables to reconstruct the same information by placing a source in the input of a Mach-Zehnder interferometer and measuring the current at the output the interferometer. This protocol offers the possibility to access information directly via currents (and not current correlations), but requires a more sophisticated setup and is subject to decoherence in the arms of the interferometer (see section 3.4.2).

3.4.1 Principles of spectroscopy and tomography

The idea behind spectroscopy and tomography is to modulate the two-particle quantum interference between the unknown source under study and different reference sources. As these interferences basically measure the overlap of the emitted wavepacket with the reference states, one can gain information on the source and reconstruct the energy distribution or the wave-function of the emitted quasiparticles.

3.4.1.1 Spectroscopy of mono-electronic excitations

Principle of spectroscopy Naturally, if changing the temperature of the Fermi sea is not very convenient, one can easily envision to tune the electro-chemical potential of the contact facing the source (contact 2). On this simple principle is based a spectroscopy protocol described in Grenier *et al.* [46].

Indeed, if we start from Eq.(3.33), and simply modify it to take into account a shift of the chemical potential by an energy eV_{bias}, we simply get:

$$\Delta\overline{S}_{4,4}(eV_{bias}) = 2e^2 fT(1-T)\int d\epsilon \left(1-2f_{\mu=eV_{bias}}(\epsilon)\right)\left(\delta n_e(\epsilon)+\delta n_h(\epsilon)\right) \quad (3.51)$$

$$= 2e^2 fT(1-T)\int d\epsilon \left(1-2f_0(\epsilon-eV_{bias})\right)\left(\delta n_e(\epsilon)+\delta n_h(\epsilon)\right) \quad (3.52)$$

so that, by taking the derivative of $\Delta\overline{Q}$ with respect to eV_{bias}, we finally obtain (taking $T = 1/2$ for simplicity):

$$\frac{\partial\Delta\overline{Q}}{\partial eV_{bias}} = e^2 f\frac{\partial f_0(\epsilon)}{\partial\epsilon}\left(\delta n_e(\epsilon)+\delta n_h(\epsilon)\right)\Big|_{\epsilon=eV_{bias}} \quad (3.53)$$

In the limit of zero-temperature, $\frac{\partial f_0(\epsilon)}{\partial\epsilon} = -\delta(\epsilon)$:

$$\frac{\partial\Delta\overline{Q}}{\partial eV_{bias}} = e^2 f\left(\delta n_e(eV_{bias})+\delta n_h(eV_{bias})\right) \quad (3.54)$$

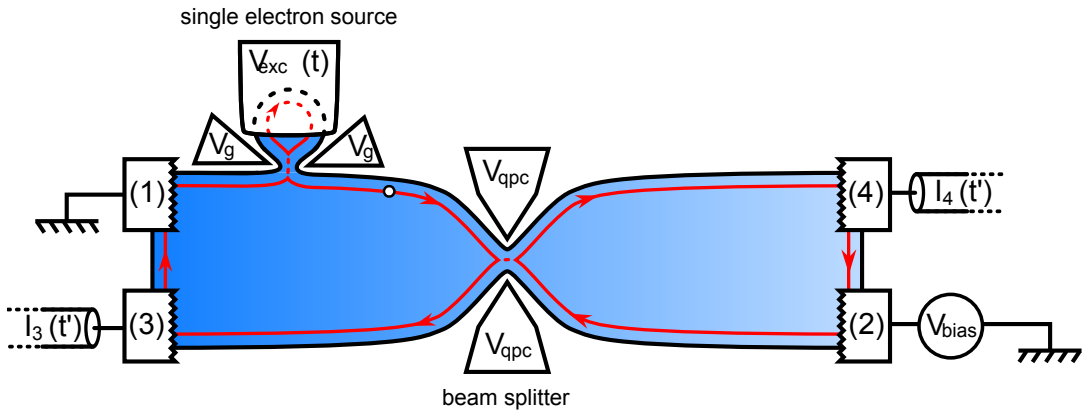

FIGURE 3.19: **Sample design for spectroscopy and tomography protocols** – The sample geometry to realize spectroscopy and tomography of mono-electronic wavepackets is very similar to the one used in the Hanbury-Brown & Twiss experiment, but contact 2 is now connected to a controllable voltage source delivering a bias voltage V_{bias}. Tuning V_{bias} enables to modulate the anti-bunching effect between inputs 1 and 2. By scanning DC biases ($V_{bias} = V_0$) or DC+AC biases ($V_{bias} = V_0 + V_n \cos(n\Omega t + \phi), n \in \mathbb{N}$), one can reconstruct the energy distribution (spectroscopy) or even the complete wavefunction (tomography).

Consequently, in the limit of zero-temperature, scanning the electro-chemical potential of contact 2 using a bias voltage V_{bias} offers the possibility to access directly the energy distribution of the quasiparticles emitted by a source. Temperature limits the accuracy of the protocol, as a thermal smearing appears for $T_{el} \neq 0$. It is important to recall here that such a spectroscopy can be in principle applied to different types of sources such as lorentzian Levitov pulses [38, 39], currently under study at CEA Saclay.

Intuitive understanding An intuitive picture of the principle of spectroscopy can be given, based on the same kind of reasoning as for the HBT experiment: it mainly relies on the two-particle interference between the wavepacket emitted by a source and the particles coming from the DC-biased contact (2). A sketch supporting this discussion is presented in Fig.3.20. The anti-bunching effect can only occur between undistinguishable particles. As a consequence, an electron with a well-defined energy ϵ can only anti-bunch if a symmetric partner exist in input 2. In the limit $T_{el} = 0$, this imposes the constraint $\epsilon < eV_{bias}$. Under this constraint, the anti-bunching effect occurs with unit probability, otherwise, no antibunching is possible. While the HBT experiment counts the number of electrons above $\epsilon_F = 0$, this spectroscopy protocol aims at counting the number of electron situated above a tunable threshold of eV_{bias}, in order to reconstruct the energy distribution $\delta n_{e/h}$. A finite temperature $T_{el} \neq 0$ in the reservoir then loosen the threshold constraint: antibunching occurs with non-unit probability, in a range $\epsilon \simeq eV_{bias} \pm kT_{el}$. It consequently limits the energy resolution of this spectroscopy protocol to kT_{el}.

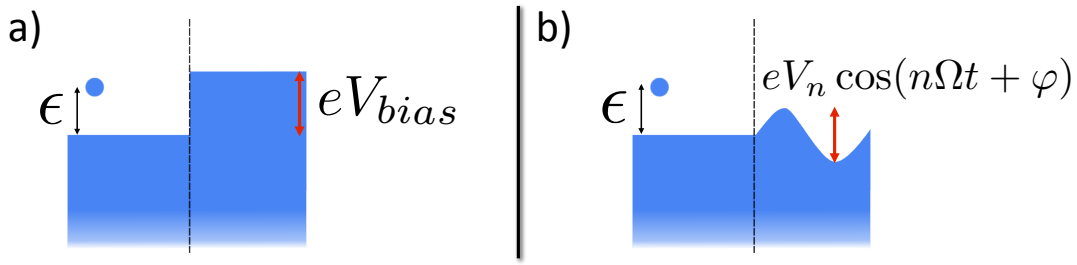

FIGURE 3.20: **Sketch of the principles of spectroscopy and tomography** – The idea behind spectroscopy and tomography is to modulate in a controlled way the two-particle quantum interference between the unknown source under study and a reference source. a) *Spectroscopy:* A scan of DC bias voltage V_{bias} on contact 2 enables to reconstruct the energy distribution $\delta n_{e/h}$ of the quasiparticles emitted by the source. Indeed, an energy resolved electron with energy ϵ only interfere with excitations coming from contact 2 if $\epsilon < eV_{bias}$. b) *Tomography:* Using AC bias (at pulsation $\Omega_n = n\Omega$ multiple of the trigger frequency of the source, and by tuning the phase ϕ) enables to reconstruct the n-th harmonic of the coherence function $\mathcal{G}_n^{(e/h)}$. It yields a way of imaging the complete wavefunction.

3.4.1.2 Tomography of mono-electronic excitations

So far, contact 2 has been DC-biased to obtain information: this enables to access the 0-th harmonic $\mathcal{G}_0^{(e/h)}$ of the coherence function, namely the excess population of quasiparticles $\delta n_{e/h}$. To go beyond this point and access $\mathcal{G}_n^{(e/h)}, n \neq 0$, it seems natural to try to use time-dependent signals to picture the wavepacket. A reasonable idea is to perform some Fourier-like analysis by applying sinusoidal gate voltages on contact 2 as detailed in [44, 46].

This protocol is in fact greatly inspired by similar techniques in quantum optics, denominated optical homodyne tomography. The homodyning with a reference laser is operated on an optical beamsplitter, and can be used to reconstruct the Wigner distribution of the optical field. First results were obtained by Smithey *et al.* [128] on vacuum and squeezed states of light. It has now become a standard technique to detect for example non-classicality of exotic quantum states of light (as Fock number states [129, 130]), and has also been recently extended to microwave fields in superconducting resonators and waveguides [131–133].

In the electronic case, calculations are very similar to the ones performed previously but the tomography protocol is a bit too technical to be discussed in this manuscript. Nevertheless we briefly present the main results, that provides a graphical representation of the emitted wavepackets.

Quadrants in the complex planes The simplest representation of the coherence function $\Delta\mathcal{G}^{(e)}$ is a two-dimensional plot of harmonics $\Delta\mathcal{G}_n^{(e)}(\epsilon)$ as a function of both n and ϵ, as pictured on Fig.3.22. It can be seen as the 2D Fourier transform, as n is Fourier conjugate to $\bar{t}$ and ϵ to τ (Eqs.(2.18) and (2.19)). First, let us recall that the harmonic $n = 0$ play a particular role as it contains the occupation number $\delta n_{e/h}$. This very part is obtained via spectroscopy.

Then, four quadrants can be identified. The right quadrant encodes the electron density operator: a purely electronic state that lies above the Fermi sea (such as the model wavepacket φ_e) exhibits coherences only in this quadrant. Similarly, the left panel is the hole density operator. Finally, upper and lower panel contain the coherences between holes and electrons: in general, the appearance of such coherences is associated with the presence of coherent superposition of electron/hole pairs [44]. This case can be encountered in the low transmission regime $D \ll 1$. In that case, the Fermi sea can remain at equilibrium in state $|F_\mu\rangle$ or an electron φ_e followed by a hole φ_h in the following half-period (or later) can be emitted creating a state schematized as:

$$\frac{1}{\sqrt{2}}\big(|F_\mu\rangle + \psi[\varphi_h]\psi^\dagger[\varphi_e]|F_\mu\rangle\big) \tag{3.55}$$

Typically, the correlation between the emission of electrons and holes generates coherences in this low-transmission regime.

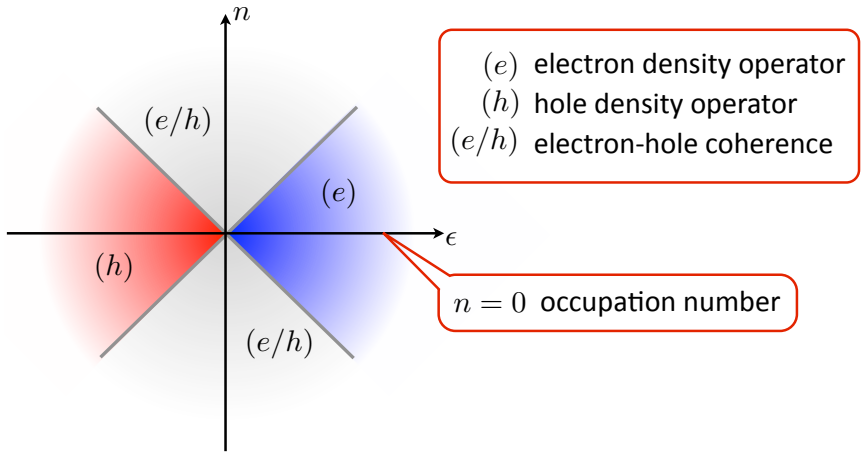

FIGURE 3.21: **Quadrant representation of the coherence function** – A tomography protocol, described in [46] gives access to the complete coherence function $\Delta\mathcal{G}^{(e)}$. In the Fourier complex plane where $\Delta\mathcal{G}_n^{(e)}$ are presented, one can identify four quadrants. Left (red) and right (blue) are respectively the electron and hole quadrants, whereas upper and lower quadrants (light grey) encodes the electron hole coherences.

Tomography of wavepackets Simulations using Floquet scattering theory can be performed. For a perfect square excitation, we have selected three different set of parameters for which we briefly discuss the key features. For clarity, odd and even harmonics of $\Delta\mathcal{G}^{(e)}$ are plotted on separate graphs as they have different parity with respect to ϵ: $\Delta\mathcal{G}^{(e)}_{2p}$ is odd while $\Delta\mathcal{G}^{(e)}_{2p+1}$ is even. First, we clearly see on these graphs the four quadrants identified in the previous paragraph. Several other comments are proposed, starting from $D = 1$ toward $D = 0$.

- $D = 1$ – Excitations lie mostly at low energy, and no correlation are recorded between electrons and holes: the two emission events are decorrelated, showing that electrons and holes are emitted during each of the emission cycles.
- $D = 0.4$ – Around the optimal transmission for single charge emission, excitations are highly energy-resolved, around energies $\pm\Delta/2$, but only weak e/h coherences are detected as the emission probability is very close to one.
- $D = 0.1$ – Strong e/h coherences appear as the emission probability is much smaller than 1. Production of holes and electrons are correlated as the emission of an electron is subject to the emission of the preceding hole, which does not take place in each cycle.

Realizing the tomography of the emitted wavepackets then reveals very interesting details on the generated wavepackets. Moreover, we show in the following section that it is even more interesting to study the effects of interactions on the generated excitations.

3.4.2 On the interest of spectroscopy (and tomography)

The major interest of spectroscopy and tomography is the possibility to access very fundamental quantities such as energy distributions or density matrices of the generated quantum states. As already demonstrated with photons [134], they encode information on decoherence mechanisms, entailed by coupling to other degrees of freedom, such as other co-propagating edge channels in our case [47, 59]. One can then imagine that interactions have a dramatic effect for quasiparticles at high energies. Indeed, Degiovanni *et al.* [47] have shown that the capacitive coupling between edge channels was responsible for a strong modification of the energy spectrum of an energy-resolved quasiparticle.

The graphs of Fig.3.23 present results adapted from [44, 47]. An energy resolved excitation, whose initial energy distribution is pictured as a Dirac function around energy ϵ_0 (blue line), is notably affected by interactions. After a certain length l, the quasiparticle peak sees its amplitude reduced to $Z(\epsilon) < 1$, while a relaxation tail $\delta n_e^{(t)}(\epsilon)$ develops

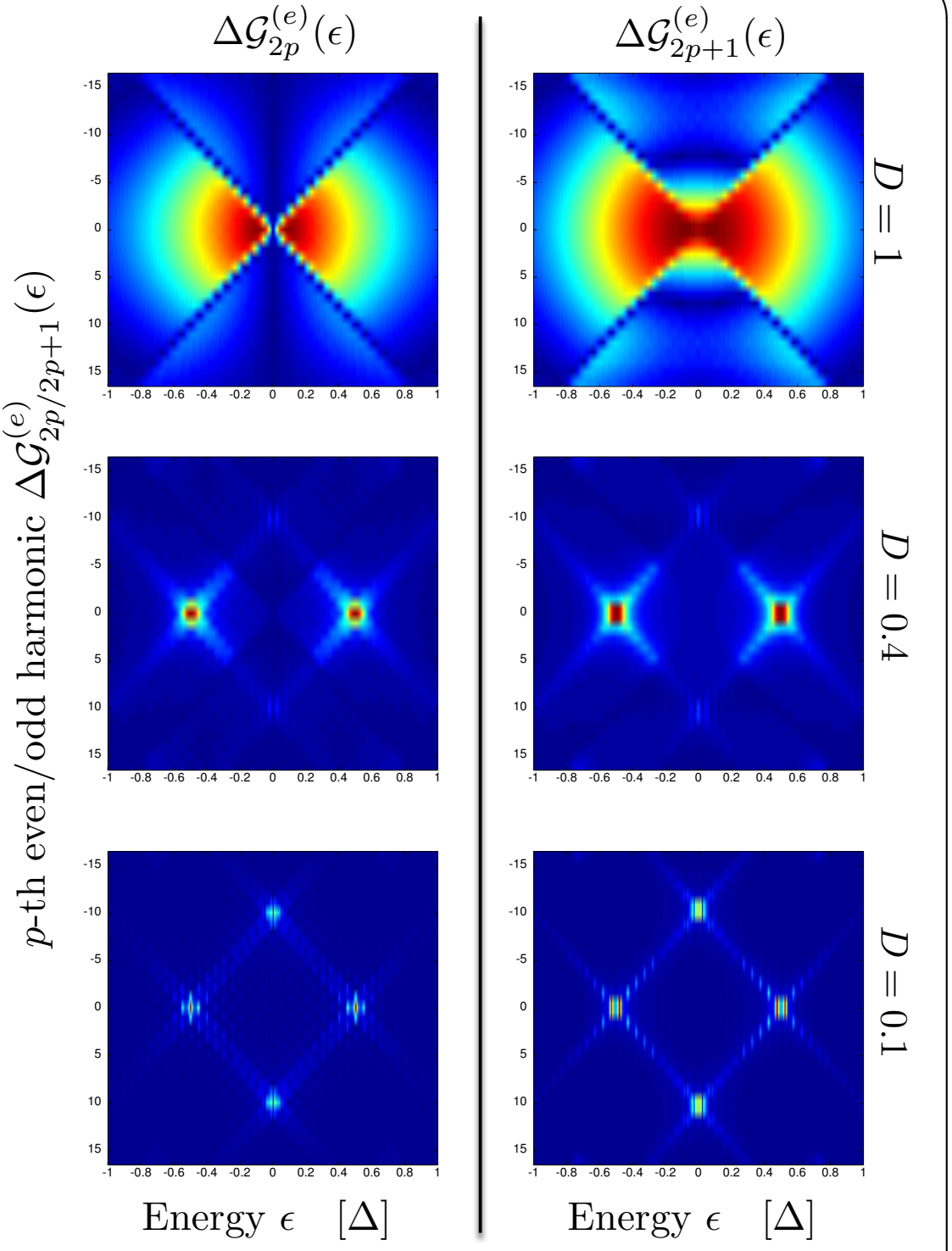

FIGURE 3.22: **Examples of coherence function in the complex plane** – For transmissions $D = 1$, $D = 0.4$, $D = 0.1$, odd and even harmonics of coherence functions $\Delta\mathcal{G}^{(e)}$ are plotted as a function of energy in a 2D plots. In contrast with the case $D = 1$, excitations are energy resolved at rather high energies $\pm\Delta/2$ for $D = 0.4$ and $D = 0.1$. When emission probability drops (for $D = 0.1$), emission of holes and electrons are correlated as the generation of an electron is subject to the generation of the preceding hole

and a non negligible part of the spectral weight $\delta n_e^{(r)}(\epsilon)$ relaxes toward lower energies. Though the general behavior of $Z(\epsilon)$, as a function of the propagation length l, is known (see Fig.3.23, panel b), a certain uncertainty remains on the scale over which this relaxation occurs, and it is not very clear how this model describing energy-resolved excitations can be extended to periodically emitted wavepackets. The achievement of such a spectroscopy experiment would then offer a quantitative way to evaluate the effects of relaxation due to Coulomb interaction, and to test the validity of the aforementioned work.

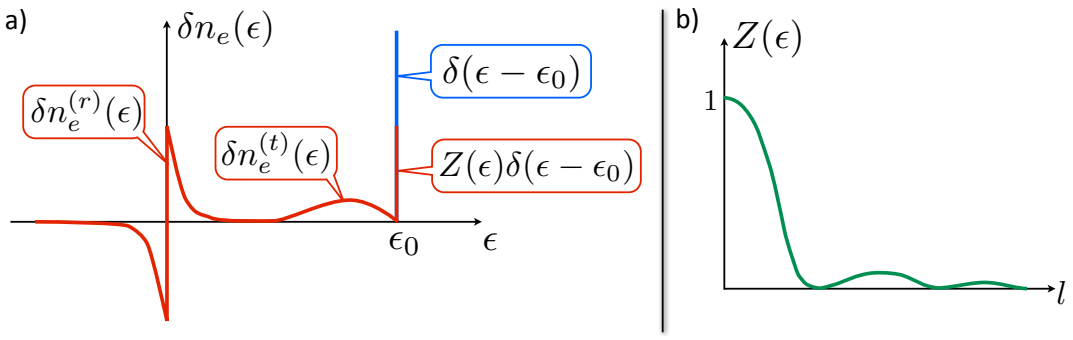

FIGURE 3.23: **Modification of the energy spectrum of an energy-resolved quasiparticle due to interactions between edge channels** – a) *Relaxation of an energy-resolved excitation:* An energy resolved excitation, initially with an energy distribution $\delta n_e(\epsilon) = \delta(n - n_e)$ (blue line) relaxes due to Coulomb interactions: the amplitude of the quasiparticle peak $Z(\epsilon) < 1$ is reduced, a relaxation tail $\delta n_e^{(t)}(\epsilon)$ and spectral weight at low energies $\delta n_e^{(r)}(\epsilon)$ appear, above and below the Fermi level (red line). b) *Amplitude of the quasiparticle peak:* The overall behavior of $Z(\epsilon)$ as a function of the length of propagation l in the interacting region is known and pictured in green line, but the typical scale over which it occurs is still uncertain.

Conclusion to chapter 3

In this chapter, we have seen how an analog of the Hanbury-Brown & Twiss experiment could be realized in quantum Hall devices. Contrary to the usual case of photon quantum optics, electron quantum optics is enriched by the existence of two types of carriers. One important consequence lies in the fact that neutral events (such as the emission of an additional e/h pair) remain invisible in charge or current autocorrelations but are unveiled in the HBT correlations. An other key point is the presence of a Fermi sea replacing photons' vacuum. Inevitably, two-particle interferences between triggered quasiparticles emitted by a single electron source and symmetric thermal counterparts appear and affect the Hanbury-Brown & Twiss signal, reducing its amplitude.

By a careful analysis, and taking advantage of this anti-bunching effect, we have in fact been able to probe the energy distribution of the emitted quasiparticles and bring to light evidence that we can modify in a controlled manner the shape of the wavepacket of the emitted quasiparticles. By tuning the thickness of the tunnel barrier of the quantum dot, and modifying the type of excitation, the excitations can be produced either at low energies comparable to the energy range kT_{el} and or at high energies, typically $\Delta/2 \gg kT_{el}$. Our interpretation relies on an intuitive picture corroborated by Floquet simulations, as developed in section 2.1.1.

Following the analogy with quantum optics, spectroscopy and tomography protocols have been proposed. These simple principles would enable the measurements of new quantities such as energy distribution of the quasiparticles emitted by any source, or the complete image of the wavefunction.

So far, our experimental data are in good agreement with Floquet scattering theory, that takes into account all the parameters of the source but completely ignores interactions between co-propagating edge channels of $\nu = 2$ in the 2DEG. The capacitive coupling between both channels remains surprisingly invisible in this experiment, whereas strong effects have been recorded in edge channel spectroscopy experiments, realized by Altimiras *et al.* [49–51]. This astonishing robustness of the HBT correlations could be due to the fact that the HBT correlations are only sensitive to partial information (namely the integral δN_{HBT}, see Eq.(3.33)) that remains more or less conserved in the presence of inter-channel interaction.

One important source of motivation for the spectroscopy experiment then lies in the fact that it would allow a measurement of the energy spectrum of initially energy-resolved excitations, after a controlled length of interactions. As explained in 3.4, this quantities could be significantly altered along the propagation and direct spectroscopy could offer a quantitative comparison with existing models. But other directions can also be explored to gather information about coupling between channels more directly, and are detailed in the following chapter.

Chapter 4

Interactions between edge channels at $\nu = 2$

Introduction to chapter 4

In one-dimensional systems such as chiral edge states of the integer Quantum Hall effect, Coulomb interactions play a major role in the nature of elementary excitations. The paradigm of Landau quasiparticles, relevant in two or three dimensions, is replaced by a picture of collective excitations called here edge magneto-plasmon (EMP). When working at filling factor $\nu \geq 2$, edge magneto-plasmons in the ν edge channels are coupled and new eigenmodes of the propagation appear with different velocities.

In this section, we investigate the case of $\nu = 2$ that is particularly enlightening: in a limit of strong coupling the two new eigenmodes are particularly dissimilar as one is fast and carries the charge while the other is much slower and neutral [53–55, 59, 63]. Via radio-frequency measurements, we investigate the appearance of these two new eigenmodes. In particular, we extract the dispersion relation of the slow mode and establish its neutrality.

4.1 Probing interactions at $\nu = 2$

4.1.1 Heuristics of interactions in quantum Hall edge channels

In this section, we provide simple heuristics of the interactions in the quantum Hall edge channels. As mentioned earlier, the nature of elementary excitations is considerably modified by the presence of Coulomb interactions. When interacting particles are moving in a one dimensional geometry, the motion of one particle strongly affects the motion of surrounding particles. Consequently, the reasonable representation of excitations relies on a picture of collective modes (rather than Landau quasiparticles in superior dimensions). These collective excitations, called edge magnetoplasmons, are bosonic modes, and can be described via a bosonic field, from which can be derived the current, the charge density and all quantities of interest. This procedure will be detailed in section 4.4.1, but let us for now focus on a simpler picture.

When there are several co-propagating edge channels, the charges in different channels interact via Coulomb interaction. In this part we study the simplest case, already rich in information: the filling factor is set to $\nu = 2$ so that two channels co-propagate on each edge. The outer channel is labeled $k = 1$, the inner $k = 2$. In the Fourier space (with respect to time t), currents in channel k, at pulsation ω and position x are $i_k(x, \omega)$. When both inter and intra channel interactions are absent, currents propagate at the

bare Fermi velocity v, $i_k(x,\omega) = e^{i\frac{\omega x}{v}} i_k(0,\omega)$. The modes $i_k, k = 1,2$ thus constitute eigenmodes of the propagation, with a velocity equal[1] to v.

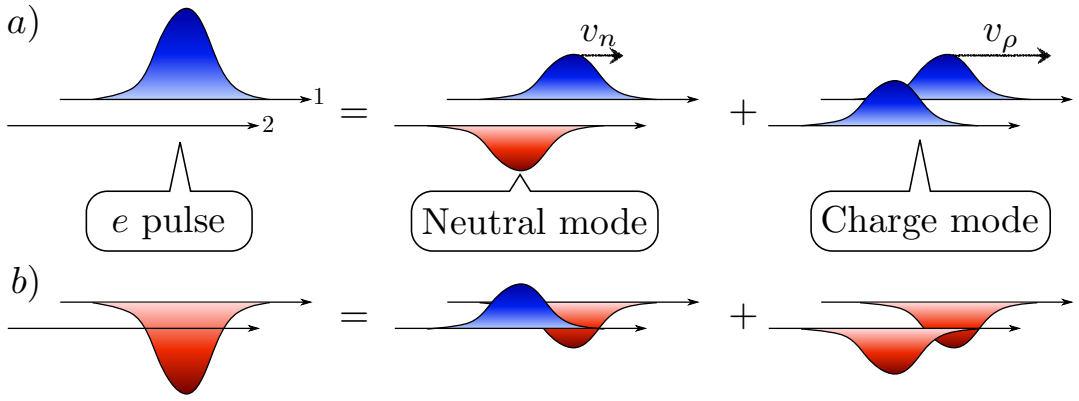

FIGURE 4.1: **Scheme of the decomposition over dipole/charge propagation eigenmodes** – The two chiral edge states are symbolized by black arrows, and positive/negative charge density waves are pictured as blue/red wavepackets. a) An electronic wavepacket is decomposed over a slow dipole mode of velocity v_n and a fast charge mode of velocity v_ρ. b) A hole wavepacket is symmetrically decomposed over a slow dipole mode and a fast charge mode, with inverted signs.

When inter-channel interactions are turned on however, these two modes i_k are coupled and are not eigenmodes of propagation any longer. In the case of strongly coupled channels, the eigenmodes are the symmetric and anti-symmetric combination of the i_k, pictured in Fig.4.1 [53–55]. The symmetric mode denoted $i_\rho = \frac{i_1+i_2}{\sqrt{2}}$ carries charge, at a velocity v_ρ. On the opposite, the antisymmetric combination $i_n = \frac{i_1-i_2}{\sqrt{2}}$ is neutral (but carries spin since both channels are of opposite spins) and has a velocity v_n. This mode is called indifferently neutral or dipole mode. Due to interactions, both modes have very different velocities, leading to spectacular effect in the transport properties of the 2DEG. Let us point out that this decomposition in symmetric/antisymmetric modes is only valid in this strong coupling limit. First, we will provide explanations for our results based on this assumption, before discussing its validity in details in section 4.3.3.

4.1.2 In the time domain: separation of charge and neutral modes

Bringing to light the appearance of two collective modes involving both channels is not straightforward as it requires the ability to excite individually one of the edge channel. Indeed, in most experiments, where DC/AC-biased ohmic contacts are used, both edge channels are driven in the same manner. Thus, only the charge mode is excited so that the dipolar mode doesn't play any role. Let us put aside for now this point (detailed in

[1] We assume here for simplicity that both channels are identical. This hypothesis is discussed in 4.3.3.

section 4.2.1) and assume that one of the edge channel (the outer) can be excited while the other (the inner) remains at equilibrium.

The first idea that comes to mind is to perform a time-resolved experiment [72–74], in which one would induce a charge pulse in one of the channel and measure how it evolves as propagation takes place. As both eigenmodes are excited, a separation between a charge pulse and a neutral pulse is predicted [56, 135]. This can easily be seen for non-dispersive modes of velocity $v_{\rho/n}$. The initial situation where a charge pulse $i_1(x = 0, t)$ is initially created at position $x = 0$ in the outer edge channel, while the inner is not excited $i_2(x = 0, t) = 0$ can be described in the form:

$$\begin{aligned} i_1(x=0,t) &= \frac{i_1(0,t)}{2} + \frac{i_1(0,t)}{2} && (4.1)\\ &= i_{\rho,1}(0,t) + i_{n,1}(0,t) && (4.2)\\ i_2(x=0,t) &= \frac{i_1(0,t)}{2} - \frac{i_1(0,t)}{2} && (4.3)\\ &= i_{\rho,2}(0,t) + i_{n,2}(0,t) && (4.4) \end{aligned}$$

where $i_{\rho/n,k}(0,t), k = 1, 2$ labels the projection of mode ρ/n in channel k, at position $x = 0$. After propagation on a length l, the current $i_k(x = l, t)$ measured is then:

$$\begin{aligned} i_k(x=l,t) &= i_{\rho,k}(l,t) + i_{n,k}(l,t) && (4.5)\\ &= i_{\rho,k}(0,t-l/v_\rho) + i_{n,k}(0,t-l/v_n) && (4.6)\\ &= \frac{i_1(0,t-l/v_\rho)}{2} \pm \frac{i_1(0,t-l/v_n)}{2} && (4.7) \end{aligned}$$

As pictured in Fig.4.2, a detection scheme measuring the current selectively in one edge k will thus record two distinct current pulses separated by a time-delay $\tau_{del} = l(\frac{1}{v_n} - \frac{1}{v_\rho})$. Their amplitude is the half of the amplitude of the initial current pulse $i_1(0, t)$ and they correspond to the currents transported by the fast charge mode and the slow neutral mode.

Though this experiment is appealing, it remains technically challenging with our sample. Indeed, observing distinctly the charge and neutral pulses requires a time delay larger than the temporal width τ_{width} of the initial pulse $i_1(x = 0, t)$. The typical width of these pulses is either determined by the sampling rate of the pulse generator or in our case by the minimal width of a wavepacket set by the escape time τ_e, and is typically on the order of $\tau_{width} \simeq 100$ ps. With the assumption $v_\rho \gg v_n \sim 5\,10^4 \mathrm{m.s}^{-1}$, the condition $\tau_{del} \geq 2\tau_{width}$ finally gives $l \geq 10\,\mu$m, when our samples usually offer $l \simeq 3 - 5\,\mu$m.

Though this experiment could be implemented in the near future with dedicated samples presenting $l \geq 10\,\mu$m, an other one can be realized with our usual sample.

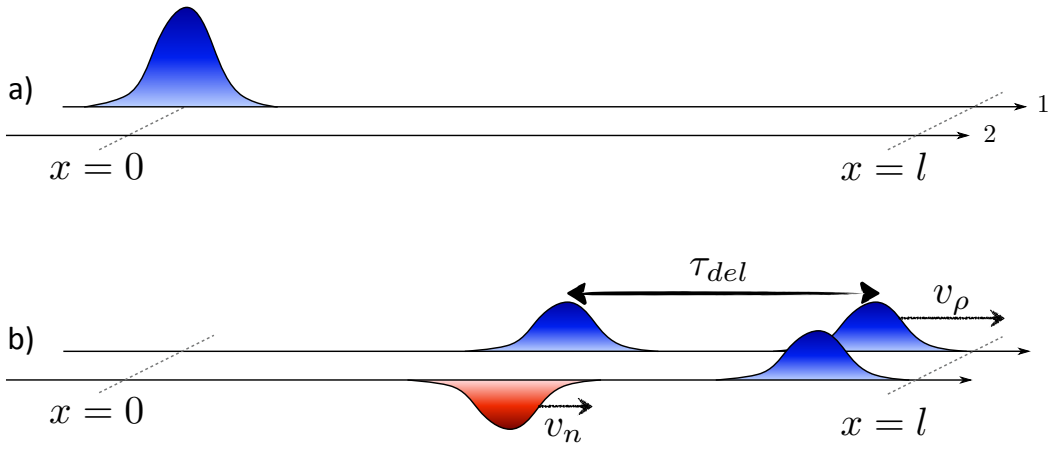

FIGURE 4.2: **Time-resolved experiment : fractionalization of charge pulses** – a) A charge pulse is injected at position $x = 0$ in channel 1 b) After a length of propagation l, the charge pulse has fractionalized and the charge and neutral components are separated by a time-delay $\tau_{del} = l(\frac{1}{v_n} - \frac{1}{v_\rho})$ due to the velocity difference between both eigenmodes

4.1.3 In the frequency domain: charge oscillations between channels

Instead of performing time-resolved experiments that are technically challenging, an other measurement can also be implemented, which is in some way the analog in the frequency domain [77–81]. The idea is no longer to create short wavepackets but then to induce monochromatic charge density waves selectively in one of the edges.

We adopt a scattering approach for plasmonic modes: when currents at pulsation ω $I(x = 0, \omega) = (i_1(x = 0, \omega), i_2(x = 0, \omega))$ in modes $k = 1, 2$ are injected at position $x = 0$, the currents in each channel after a length l are given by

$$I(l,\omega) = \boldsymbol{\mathcal{S}}_{EMP}(\omega, l) I(0,\omega) \tag{4.8}$$

$$= \begin{pmatrix} S_{11}(\omega,l) & S_{12}(\omega,l) \\ S_{21}(\omega,l) & S_{22}(\omega,l) \end{pmatrix} I(0,\omega) \tag{4.9}$$

where $\boldsymbol{\mathcal{S}}_{EMP}(\omega, l)$ is a 2×2 unitary scattering matrix for EMPs. In the strong coupling regime (see section 4.3.3), one has $S_{11} \simeq S_{22}$, and $S_{12} = S_{21}$. This matrix is not diagonal, contrary to the case of non-coupled channel, but is diagonalized in the eigenbasis of modes ρ/n. The propagation of these modes then reduces to a phase factor $S_{\rho/n} = e^{i\frac{\omega l}{v_{\rho/n}}}$, with :

$$S_\rho = S_{11} + S_{21} = e^{i\frac{\omega l}{v_\rho}} \tag{4.10}$$

$$S_n = S_{11} - S_{21} = e^{i\frac{\omega l}{v_n}} \tag{4.11}$$

In the rest of this chapter, we assume that the charge mode has a much larger velocity than the dipole mode: $v_n \ll v_\rho$, such that $\frac{\omega l}{v_\rho} \ll 1$. This assumption will be justified a posteriori by our experimental results. From Eqs.(4.10) and (4.11), one directly gets :

$$S_{11} = \frac{e^{i\frac{\omega l}{v_\rho}} + e^{i\frac{\omega l}{v_n}}}{2} \simeq \frac{1 + e^{i\frac{\omega l}{v_n}}}{2} \tag{4.12}$$

$$S_{21} = \frac{e^{i\frac{\omega l}{v_\rho}} - e^{i\frac{\omega l}{v_n}}}{2} \simeq \frac{1 - e^{i\frac{\omega l}{v_n}}}{2} \tag{4.13}$$

Equation (4.13) demonstrates in this model that the phase shift between both eigenmodes along propagation is responsible for charge oscillations between edge channels: if charges are injected injected in channel 1, they are totally transferred to channel 2 after a length l such that $S_{21} = 1$:

$$\omega l\Big(\frac{1}{v_n} - \frac{1}{v_\rho}\Big) \simeq \frac{\omega l}{v_n} = (2k+1)\pi,\ k \in \mathbb{Z} \tag{4.14}$$

This can be understood in a simple manner. Let us picture the sinusoidal EMP as a succession of electron (e) and hole (h) charge pulses, initially injected in channel 1. After a certain propagation length, the fast mode of a e-charge pulse will catch up the slow neutral mode of the preceding h-charge pulse. When recombining these pulses, one recovers an electronic wavepacket in channel 2, as cartooned in Fig.4.3. The same reasoning holds for the fast h-charge pulse, so that in fact the charge distribution initially created at $x = 0$ in channel 1 is now reconstituted in channel 2.

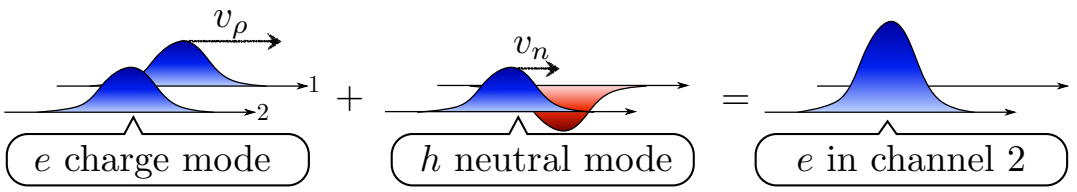

FIGURE 4.3: **Scheme of the recombination** – For a purely AC-current seen as a succession of electron and hole wave-packets, charge oscillations between channels can be understood as the in-phase recombination of the fast charge mode of an electron with the slow neutral mode of the preceding hole.

Moreover, we see from Eq.(4.13) that the propagation length l and the pulsation ω play the very same role. This feature can be understood easily on Fig.4.3, where changing the frequency is equivalent to emitting wavepackets closer to one another. While it is experimentally very tedious to vary the propagation length, the pulsation of the induced EMP is easily tunable. This is one of the key point of our experiment, detailed in section 4.2.1. Once again, let us point out that charge transfer is total only for antisymmetric/symmetric eigenmodes, as proved in 4.3.3.

4.1.4 Predictions for the frequency-resolved experiment

This simple model yields interesting predictions that we briefly analyse in this section before turning on to the realisation of our experiment.

4.1.4.1 Low-frequency behavior

For low frequencies, one obtains:

$$S_{21}(l,\omega) \simeq -i\omega\tilde{\tau}(1+i\omega\tilde{\tau}), \quad \tilde{\tau} = \frac{l}{2v_n} \tag{4.15}$$

In this regime, S_{21} is mainly imaginary (with $\mathrm{Im}\, S_{21} < 0$). To give a clear physical picture of this formula, one can in fact imagine an electrical circuit of discrete elements, with a conductance $G_{21}(\omega) = \frac{S_{21}}{R_K}$. Then, Eq.(4.15) can be associated with an RC circuit presented in Fig.4.4, for which one has:

$$S_{21}(l,\omega) = \frac{-i\omega\tilde{\tau}}{1-i\omega\tilde{\tau}} \tag{4.16}$$

$$\simeq -i\omega\tilde{\tau}(1+i\omega\tilde{\tau}) \tag{4.17}$$

This low-frequency behavior has already been observed and established [78]. The capacitance is then the electrochemical capacitance C_μ given by the series association of a quantum capacitance $C_q = \frac{l}{R_K v_F}$ for each channel and the geometrical capacitance between channels C, while the resistor is R_K, the series combination of a charge relaxation resistance $R_K/2$ for each channel. Our models, detailed in section 4.3 confirm these results.

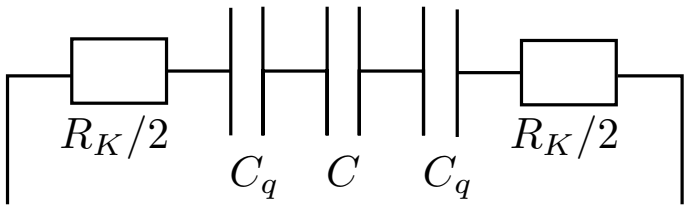

FIGURE 4.4: **Equivalent RC-circuit at low frequencies** – The low-frequency behavior of S_{21} can be mimicked by an RC circuit of conductance $G_{21}(\omega) = \frac{S_{21}}{R_K}$. The electrochemical capacitance C_μ is given by the series combination of a quantum capacitance $C_q = \frac{l}{R_K v_F}$ for each channel and the coupling capacitance between channels C. The resistor R_K stems from the series association of a charge relaxation resistance $R_K/2$ for each channel

4.1.4.2 Charge oscillations

As mentioned earlier, charge oscillations are expected as a result of the progressive phase shift between charge and neutral modes. From Eq.(4.13), one sees that S_{21} draws a circle of radius 1/2, centered on the point of coordinates (1/2,0) with an angle $\Phi(\omega) = \omega l/v_n(\omega) - \pi$. The principal configurations of interest are presented in Fig.4.5. At low frequencies, $S_{21}(\omega = 0) \simeq 0$, as charges injected in channel 1 remain as a majority in 1, and is mainly imaginary as expected for a capacitive coupling. For increasing frequencies, coupling effects become all the more significant and $|S_{21}|$ increases. Due to propagation effects, S_{21} departs from its low-frequency RC-circuit asymptotics. It then follows a circular trajectory and finally reaches $S_{21} = 1$. At this point, the charge injected in the outer channel is totally and coherently transferred to the inner one, for a pulsation ω such that $\omega l/v_n = \pi$. For higher frequencies, charges are coherently transferred back to the first channel, and the initial situation is recovered for $\omega l/v_n = 2\pi$. Consequently, we expect coherent charge oscillations as a function of pulsation ω (or

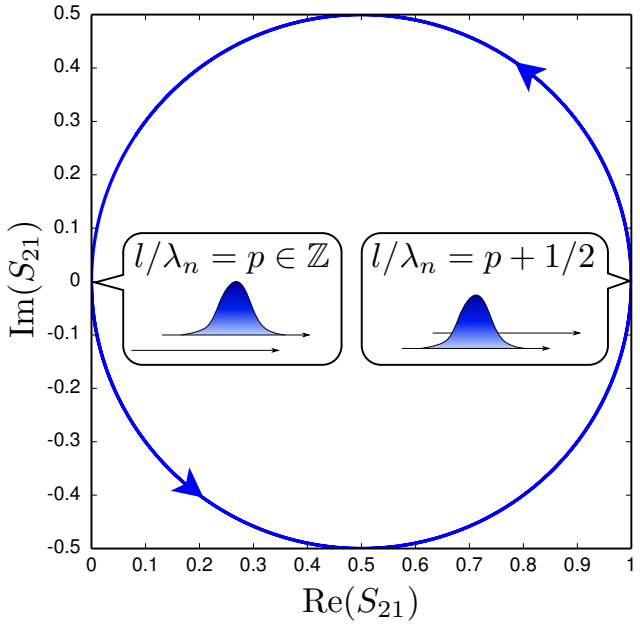

FIGURE 4.5: **Predicted behavior of S_{21} in the complex planes, and main configurations of interest** – Starting from $S_{21}(\omega = 0) = 0$ (no charge transferred in channel 2 at $\omega = 0$), $S_{21}(\omega)$ draws a circle of radius 1/2 and centered on point (0,1/2). The two principal configurations of interest are recalled. When $l/\lambda_n = n \in \mathbb{Z}$, charge injected in channel 1 is recovered in 1 whereas a total and coherent charge transfer towards channel 2 occurs for $l/\lambda_n = n + 1/2$.

equivalently length l). However, for a propagation length of a few microns such as ours, and an estimation of $v_n = 5\,10^4$ m.s^{-1}, a very wide range of frequency (up to 10 GHz) is required to observe this direct manifestation of mode separation. These estimations

will be confirmed in section 4.3 and show why a very wide bandwidth is required, hence the custom homodyne detection detailed in 4.2.3.

4.1.4.3 Dispersion relation of the neutral mode

So far, no assumption was made concerning the ω-dependence of the velocity v_n. These considerations bring to light the remarkable robustness of the Nyquist diagram presented on Fig.4.5. Inter-edge oscillations show up in the circular trajectory of S_{21} around the center of coordinates $(1/2, 0)$. Noticeably this point corresponds to an equal repartition of the EMP. This feature does not depend on the details of the interaction. As a matter of fact, the interaction characteristics are encoded in the ω-dependence of the velocity $v_n(\omega)$ or equivalently in the dispersion relation $k_n(\omega) = \frac{\omega}{v_n(\omega)}$, relating the wave vector $k_n(\omega)$ to ω. This dispersion relation will be consequently extracted from our experimental results presented in section4.3 and gives access to interesting details on the interaction characteristics.

4.2 Experimental implementation

4.2.1 Principles of the experiment

As mentioned earlier, the study of interactions at $\nu = 2$ requires the ability to address individually each edge channel in order to excite both neutral and charge modes. This can be achieved via the use of the single electron source (for the "excitation" part) and a QPC (for the "readout" part): the idea here is to take advantage of the mesoscopic capacitor to induce capacitively an edge-magnetoplasmon at pulsation ω in the outer edge channel only. A selective readout of the current in each edge channel can then be operated by changing the transmission of the quantum point contact.

The sample, presented in Fig.4.6, is identical to the one used for the Hanbury-Brown & Twiss experiment. It is placed in a magnetic field $B = 3.85$ T, to work at a filling factor $\nu = 2$ in the bulk. The mesoscopic capacitor is set at a transmission $D = 1$: the outer edge channel then enters completely the quantum dot, whereas the inner edge channel is totally reflected. Thus, no current is produced in the inner edge channel. On the opposite, a pure sinusoidal charge density wave is capacitively induced in the inner edge channel, at the position $x = 0$ corresponding to the output of the quantum dot. It is important to notice that no charge tunneling from the dot to the outer edge state is involved in the process of inducing current, since the transmission is $D = 1$. The

source then behaves as a linear component, and the EMP generated is a pure sine wave of pulsation ω.

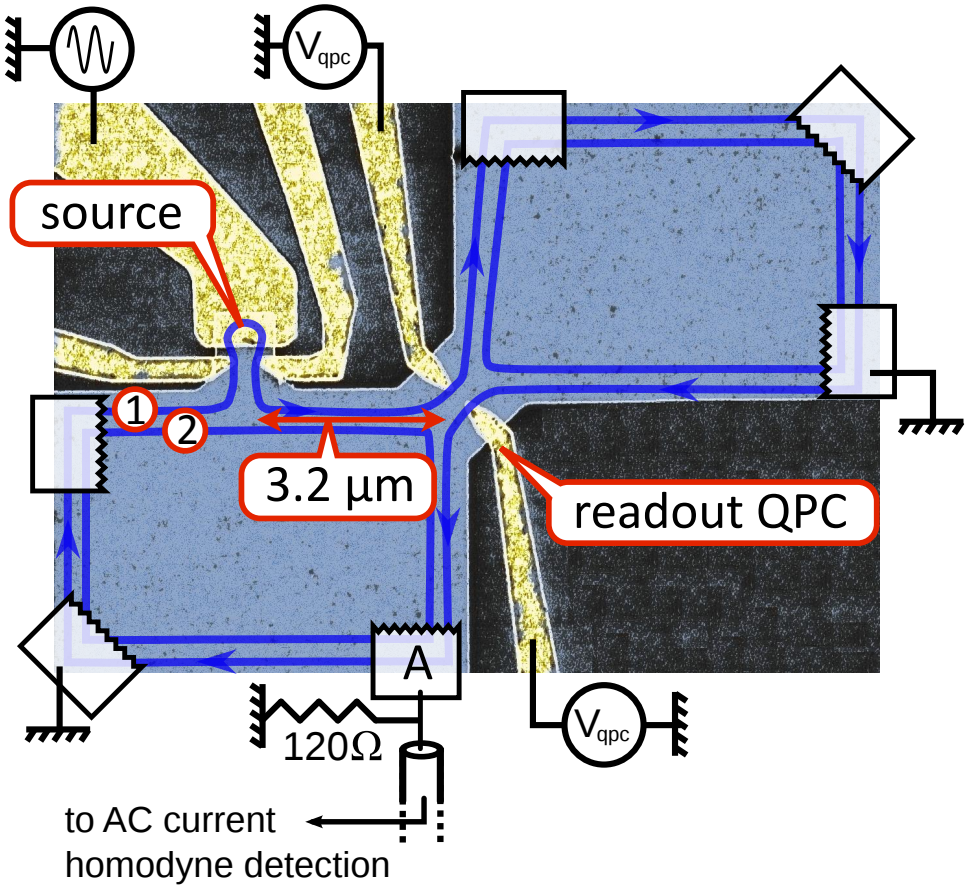

FIGURE 4.6: **Modified SEM picture of the sample** – The sample is placed in perpendicular magnetic field of $B = 3.85$ T to reach a filling factor $\nu = 2$. The edge states are symbolized by blue plain lines, gates in gold, and the 2DEG is in light blue. The transmission of the source is set to $D = 1$: the outer edge channel thus enters completely the dot, in which an EMP is capacitively induced in the channel, whereas the inner channel totally reflected and remains at equilibrium. After the dot, both channels co-propagate on a length $l = 3.2$ μm before reaching the central QPC. Average currents are measured in the reflected path (ohmic contact A).

The EMP generated at position $x = 0$ then propagates over a length l before reaching the central QPC in the HBT geometry. The length l can be evaluated from SEM pictures, with a relatively good precision: $l = 3.2 \pm 0.4\,\mu$m. The gate voltage of the QPC can then be tuned to work in several configurations. In configuration 1, channel 1 is reflected and channel 2 is transmitted. The current in channel 2 resulting from the interaction, denoted $i_2(l,\omega)$, can then be measured, with $i_2(l,\omega) = S_{21}(l,\omega)i_1(0,\omega)$. When the QPC is closed (configuration 2), both channels are reflected so that the total collected current in contact A is $i_1(l,\omega)+i_2(l,\omega) = \big(S_{11}(l,\omega)+S_{21}(l,\omega)\big)i_1(0,\omega)$. Consequently, the ratio

of the currents collected in these two configurations yields the complex quantity

$$\mathcal{R}(\omega) = \frac{S_{21}(l,\omega)}{S_{11}(l,\omega)+S_{21}(l,\omega)} \tag{4.18}$$

which encodes the effect of Coulomb interaction on the propagation along the edge states.

At this point, it is important to emphasize two points. First, $S_{11}(l,\omega)+S_{21}(l,\omega) \simeq 1$ according to previous assumption so that $\mathcal{R}(\omega) = S_{21}(l,\omega)$. The complex ratio we measure directly reflects the coupling coefficient S_{21}. Then, Eq.(4.10) proves that propagation between the QPC and the ohmic contact (on a length $L \simeq 60\,\mu$m) has no influence on the current collected, up to a global phase factor $e^{i\omega L/v_\rho}$ so that it will be neglected throughout this study.

In the next section, we present data that demonstrates the validity of the principles of the proposed experiment. We focus especially on the behavior of the QPC and on the extraction of ratio $\mathcal{R}$ from raw data.

4.2.2 Testing principles of the experiment

4.2.2.1 Raw data as function of gate voltage V_{qpc}

In this section, we comment on raw data measured as a function of the QPC for a fixed frequency of $f = 1.3$ GHz . When the drive is on, a parasitic contribution in the current is observed even when the transmission of the dot is set to $D = 0$. It comes from direct coupling between the top-gate electrode and the gas or the contacts. This parasitic current does not depend on the properties of the source and no control is possible on it. Consequently, we are to assume that it does not depend on D, measure it for $D = 0$ and subtract it. This strategy has always given excellent results in the study of the average current [6, 83], and has thus been conserved in this study.

We present in Fig.4.7 the average current collected (with parasitic contribution subtracted) as a function of V_{qpc} in the complex plane. We observe that I_Ω basically follows two straight lines. This has a simple explanation. When currents i_k channels $k = 1, 2$ are reflected with reflexion coefficients R_k, the total current collected $I_c(R_1, R_2, \omega)$ is then:

$$I_c(R_1,R_2,\omega) = R_1 i_1(l,\omega) + R_2 i_2(l,\omega) \tag{4.19}$$

$$= \big(R_1 S_{11}(l,\omega) + R_2 S_{21}(l,\omega)\big) i_1(0,\omega) \tag{4.20}$$

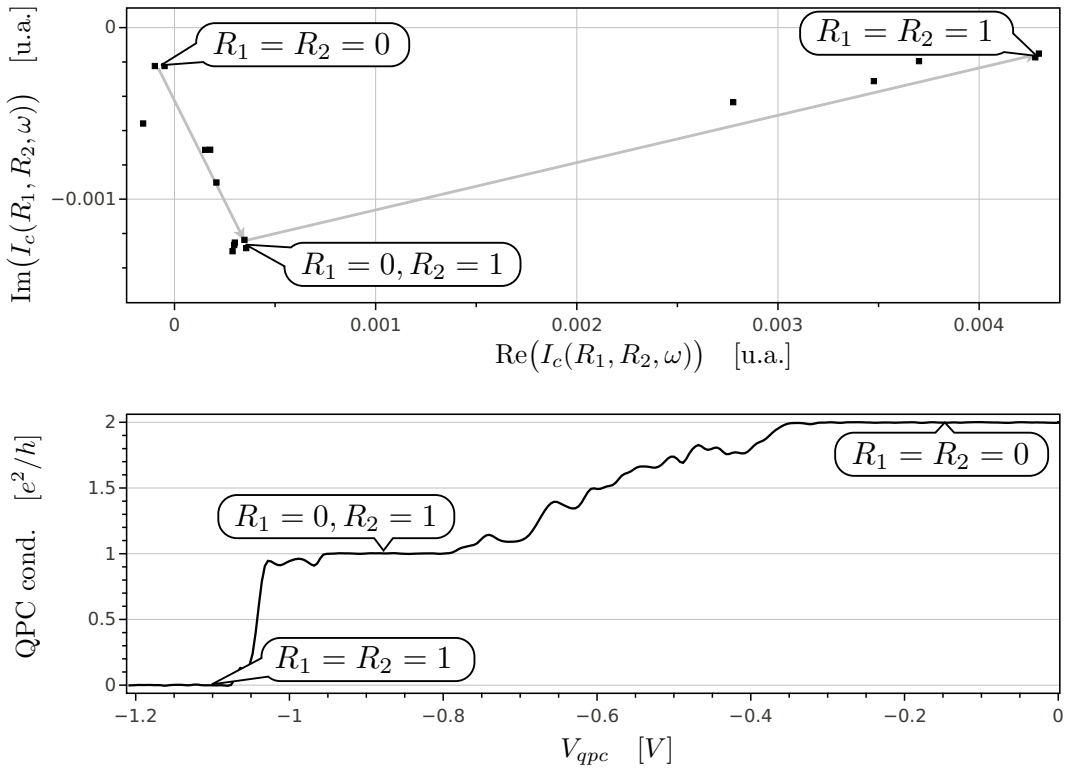

FIGURE 4.7: **Current collected $I_c(R_1, R_2, \omega)$ as a function of V_{qpc}** – (upper panel) *$I_c(R_1, R_2, \omega)$ in the complex plane:* As V_{qpc} is swept from $V_{qpc} = 0$ toward pinch-off at $V_{qpc} = -1.2$ V, $I_c(R_1, R_2, \omega)$ draws two straight lines, emphasized by a grey arrow. For $R_1 = R_2 = 0$, $I_c \simeq 0$ up to parasitic contribution. For $R_1 = 0, R_2 = 1$, $I_c \propto S_{21}$. For $R_1 = R_2 = 0$, $I_c \propto i_1(0, \omega)$, total current injected initially. (lower panel) *DC measurement of the QPC conductance:* Quantized steps in the conductance are recorded, corresponding to the transmission of one or two edge channels. Important configurations of interest here are recalled.

When the QPC is opened, both channels are transmitted, $R_1 = R_2 = 0$ and $I_c(0, 0, \omega) \simeq 0$. When V_{qpc} is increased, the inner channel is progressively reflected, $R_2 \to 1, R_1 = 0$, and $I_c(0, R_2, \omega) = R_2 S_{21}(l, \omega) i_1(0, \omega)$ follows a straight line as R_2 is varied. Then the inner channel is completely reflected and $I_c(0, 1, \omega) = S_{21}(l, \omega) i_1(0, \omega)$ as expected. Then the reflexion of the outer channel is progressively increased ($R_1 \to 1, R_2 = 1$) and a second straight line is observed: $I_c(R_1, 1, \omega) = \big(R_1 S_{11}(l, \omega) + S_{21}(l, \omega)\big) i_1(0, \omega)$. Globally this simple model explains the features of Fig.4.7 and confirms our strategy of measurement of $\mathcal{R}$. However, a parasitic contribution is sometimes observed for $R_1 = R_2 = 0$, for which a non-zero current I_c is measured. We mention that a correction was applied to take into account coupling between V_{qpc} and V_g.

4.2.2.2 Measurement of $\mathcal{R}$

In Fig.4.8, we present refined data giving an overview of the actual measurement technique. As mentioned in previous discussion, collecting the current $I_c(0,1,\omega)$ in ohmic contact 1 for $R_1 = 0, R_2 = 1$ (configuration 1) and normalizing it by $I_c(1,1,\omega)$ (configuration 2, $R_1 = R_2 = 1$) yields $\mathcal{R}$ in the complex plane. After testing our measurement technique as explained in 4.2.2.1, we focus on the measurement of the two configurations 1 and 2. The results obtained for frequency $f = 1.3$ and 5.5 GHz are presented in Fig.4.8 respectively in black dots and red squares. After proper normalization, the grey arrow directly represents $\mathcal{R}$ in the complex plane. Thus both real and imaginary parts, or more conveniently argument and modulus are obtained.

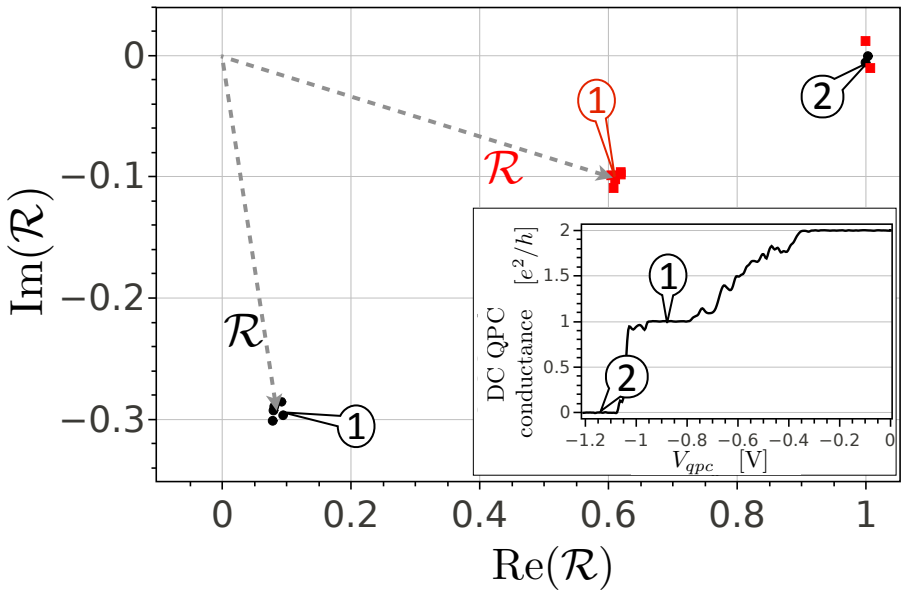

FIGURE 4.8: **Example of measurement of $\mathcal{R}$ for two frequencies** – For $f = 1.3$ GHz (black dots), $\mathcal{R}$, symbolized by a grey arrow is mainly imaginary, whereas for $f = 5.5$ GHz (red squares), $\mathcal{R}$ has a large real part. (inset) DC conductance of the QPC, recalling configurations 1 and 2 of the QPC.

One of the main advantage of measuring the ratio $\mathcal{R}$ lies in its independence regarding the gain of the amplifying scheme. Indeed, the amplification factor varies considerably with frequency, especially since we combine different RF components depending on the frequency range under measurement, as explained in the following section.

4.2.3 Ultra-wideband homodyne detection

Here we describe the realization of a low-noise custom homodyne detection, enabling to measure the current collected in ohmic contact A in a wide range of frequency, covering

0.7 to 11 GHz.

4.2.3.1 General principles

Homodyne detection setups rely on a main principle: when mixing the signal at GHz frequencies (denoted RF) with a synchronized reference signal (LO, for local oscillator), a DC signal is recovered (usually called IF for intermediate frequency), whose amplitude is directly connected to the amplitude of the sought signal RF. This technique is widespread as it has several advantages: it enables a rapid and accurate measurement of the first harmonic of a signal at GHz frequency that is difficult to access even with fast digital oscilloscopes. However, most RF components work in a frequency range of an octave. Consequently, a unique setup for the 0.7-11 GHz range remains unrealistic. We have developed a versatile setup, where several low-noise amplifiers, mixers, filters and modulators are combined to cover the widest possible frequency range. This homodyne detection is operated at room temperature since it requires to replace components. The performance are however good enough to measure average currents up to 11 GHz.

The general setup is presented in Fig.4.10, and is similar to the one presented in [6, 83]. The excitation signal consist in a GHz sine (obtained either by filtering the square voltage of an *Anritsu MT1810A* Pulse generator or by using an *Anritsu 3692C* Sine generator) modulated at kHz frequency (usually 2.7 kHz) using a +1/-1 RF modulator before entering the cryostat. The RF current collected in ohmic contact 1 is amplified by ultra-low-noise room-temperature amplifiers. An hybrid coupler then separates this signal in two components of equal amplitude. One of the component is phase-shifted by $\pi/2$. Then both components are mixed with a reference and filtered, and the output signal in each arm are then proportional to the real and imaginary parts of I_Ω, and modulated at kHz frequency. This signals are then sent on two lock-in synchronized with the kHz frequency.

4.2.3.2 Specificities and specifications of our setup

Though our setup follows the standard setup of homodyne detection, the will to access the widest possible bandwidth brings some difficulties and specificities that are presented here. We point out that a table summarizing all configurations is presented in appendix D.

Parasitic third harmonic The first concern is the presence of higher harmonics in the detection signal, and especially the third one. Indeed, the reference clock LO as

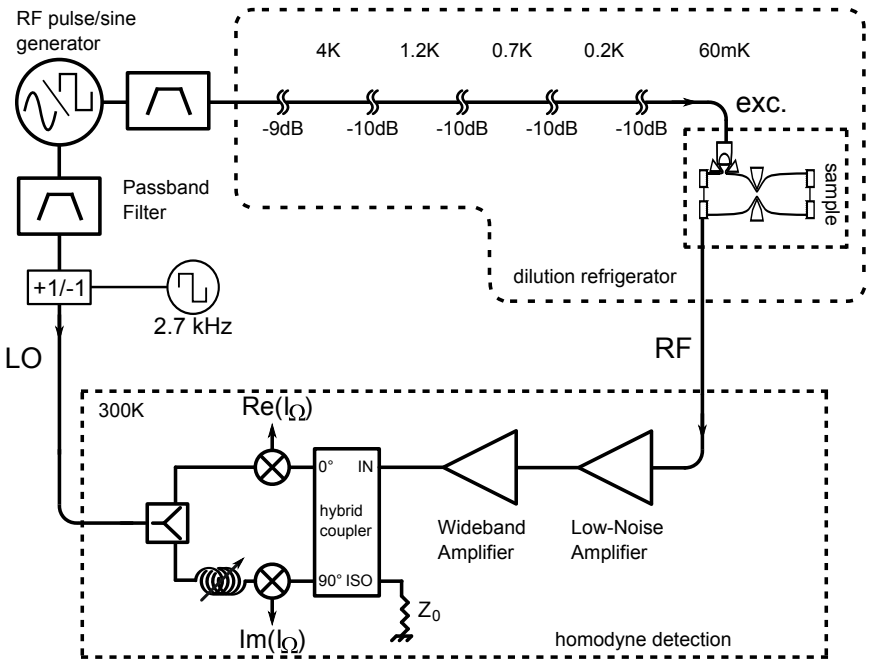

FIGURE 4.9: **Scheme of the ultra-wideband homodyne detection** – The GHz pulse/sine generator supplies both local oscillator (LO) and excitation towards sample. LO is itself modulated at 2.7 kHz using a +1/-1 modulator. The measured signal (RF) is splitted in two components phase-shifted of $\pi/2$. When mixing these components with LO, low-frequency signals (2.7 kHz) are recovered, whose amplitudes are proportional to the real and imaginary part of first harmonic I_Ω.

Phase calibration

The accurate tuning of phases are essential in this setup. First, the two components $\mathrm{Re}(I_\Omega)/\mathrm{Im}(I_\Omega)$ must bear precisely a phase shift of $\pi/2$. This can be ensured by tuning the length between the LO splitter and both mixers and maximize contrast between these quadratures., using a commercial phase shifter. Secondly, in order to measure $\mathrm{Re}(I_\Omega)/\mathrm{Im}(I_\Omega)$ and not any couple of quadratures, a global phase tuning must be realized. It is detailed in [6, 83, 114]

well as the excitation signal at frequency f are sometimes (for $f < 6$ GHz) generated from a square pulse generator (*Anritsu MT1810A*) with odd harmonics at frequencies $f_n = (2n+1)f, n \in \mathbb{Z}$. Since the bandwidth of the hybrid coupler is 2-18 GHz, residual parasitic contribution of higher harmonics can be observed for $f < 6$ GHz, for which f_1 or $f_2 < 18$ GHz. This occurs surprisingly even if the amplification is reduced for harmonics due to a smaller bandwidth for amplifiers for example. We thus particularly pay attention to supply a strong filtering of higher frequencies so as to remove these contributions. In the range where both the square pulse and sine generators can be used, the results obtained with both sources are identical.

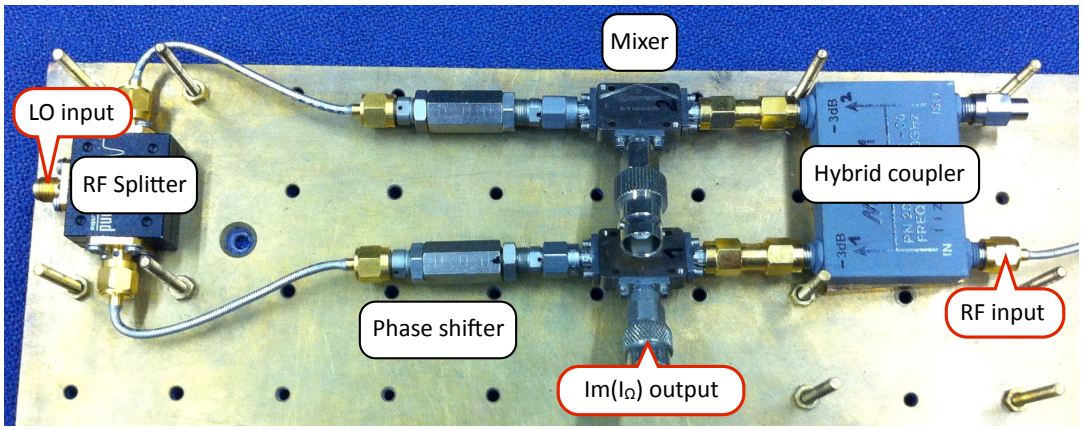

FIGURE 4.10: **Picture of the ultra-wideband homodyne detection** – The homodyning is operated by the two mixers, between the reference signal LO entering on the left and the amplified signal, entering on the right. All components are placed at room temperature, on a gold-plated copper stand. A wide range of frequency is accessed via the replacement of microwave components (such as the mixers or hybrid coupler visible on the picture).

Synchronizing excitation and reference signals Homodyne detection necessitates two accurately synchronized RF signals, one for the excitation, the other one as the reference local oscillator. The *Anritsu MT1810A* pulse generator provides two sources of independent amplitude synchronized on the same clock. Though it requires a proper filtering to produce a sine wave, this situation is quite comfortable, but only operates up to the maximum frequency of the generator (6 GHz). On the opposite, the *Anritsu 3692C* sine generator only has one output. We have tried to synchronize this output with one channel of the pulse generator, via an atomic clock (lent by the Quantum Electronics group, LPA), but the results were surprisingly not sufficient. Consequently, we decided to use an RF splitter to split the output in two channels, one for the reference and the other for excitation, with suitable attenuation.

Limitations in the bandwidth In fine, our setup should be operational up to frequencies around 18 GHz. However, as shown in section 4.3, we have managed to run the experiment only up to about 11 GHz. Indeed, for frequencies above this threshold, difficulties were encountered: a general decrease of the signal-to-noise ratio was observed with paradoxically some strong resonances for some frequencies.

We attribute these limitations to two major phenomena, that occur frequently in RF setups. The reason for the general decrease of the signal is without any doubt due to the increasing attenuation of coaxial cables guiding microwaves from generators to sample and then to detection. As frequency increases, skin effect takes place, reducing

the thickness of conductor carrying effectively the current, thus increasing the overall resistance of the cable.

However, this factor is not really limiting the bandwidth, contrary to the resonances. We attribute this phenomena to the fact that the lines and especially the sample-holder itself were not in the first place designed for such high frequencies. Consequently, parasitic reflexions probably occur in the lines, responsible for Pérot-Fabry like behavior, and thus exhibiting huge resonances. These peaks appear when $f > 10$ GHz, and become all the more intense as f rises.

4.3 Experimental results

4.3.1 Nyquist diagram of $\mathcal{R}$ and dissipation

Experimental data for the ratio $\mathcal{R}$ in the complex plane are presented in Fig.4.11. As explained previously, $\mathcal{R}$ is expected to draw a circle in the complex plane when pulsation ω is varied. It directly stems from the progressive phase shift between dipole and charge eigenmodes of the propagation.

In the low frequency regime, we observe that, as expected, $\mathcal{R}(\omega)$ is mainly imaginary, with a negative imaginary part. It is compatible with the asymptotic RC-circuit regime discussed in 4.1.4.1: $\mathcal{R}(\omega) \simeq S_{21}(\omega) \simeq -i\omega\tilde{\tau}$. However, as frequency information is lacking in this two-dimensional representation, the linear ω-dependence of $\mathcal{R}$ cannot be clearly established.

Globally, $\mathcal{R}$ indeed winds around the point (1/2,0), confirming at first glance the simple heuristics developed in 4.1.1. However, data for $\mathcal{R}$ do not reproduce the anticipated circle (black line), but rather exhibit a spiral toward the point (1/2,0). These coordinates correspond to a state where charges are evenly distributed in each channel. This behavior indicates that a dissipative mechanism occurs during propagation and interaction, that shows up as an imaginary part in the wave-vector $k_n(\omega)$ and is responsible for damping of the coherent charge oscillations. This unexpected dissipation is not naturally present in our heuristic model, but can be included in the model developed in the next part 4.4.

The data reported in this part demonstrate unambiguously the existence of two coupled modes, that resemble the charge and neutral mode, though neutrality is not clearly established yet. We now investigate the extracted dispersion relation $\omega \mapsto k_n(\omega)$. Indeed, contrary to the main features of the Nyquist diagram, the dispersion relation holds informations about the characteristic parameters governing Coulomb interactions.

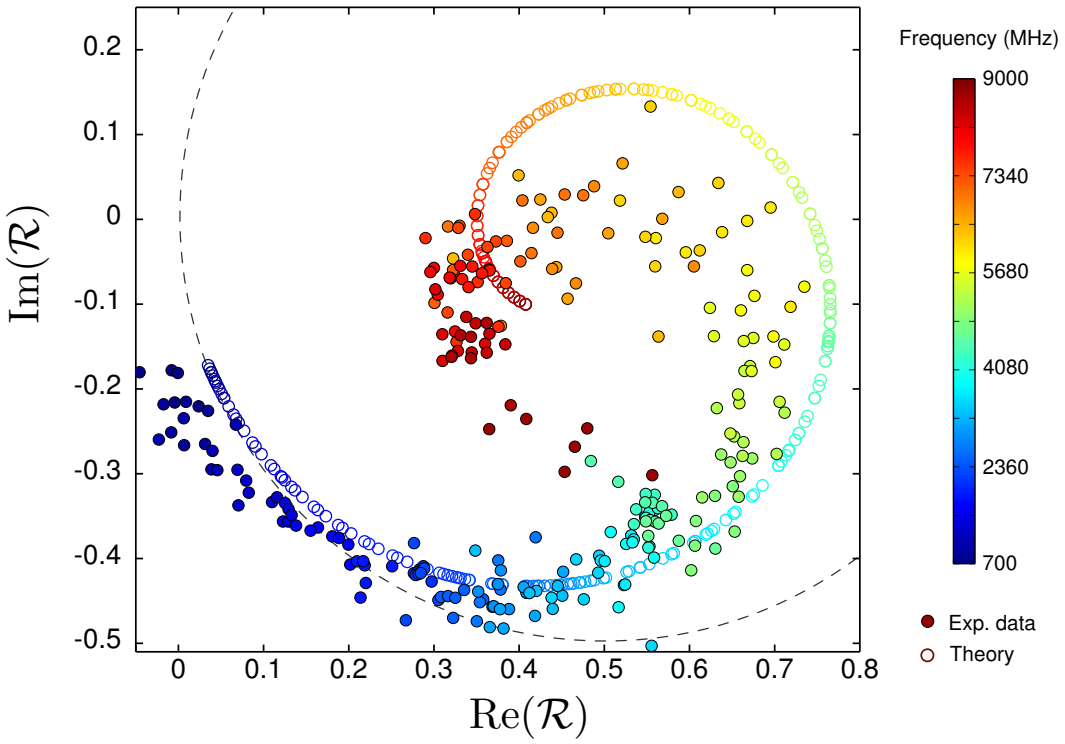

FIGURE 4.11: **Experimental data for $\mathcal{R}$ in the complex plane** – Experimental data for $\mathcal{R}$ are presented as colored dots, the colormap giving insights on the measurement frequency. For $\omega \simeq 0$, $\mathcal{R}$ is mainly imaginary, and follows quite correctly the circle of radius 1/2 centered on (1/2,0). For higher frequencies, data depart from this circle, suggesting that dissipation may occur in channels.

4.3.2 Dispersion relation of the neutral mode

Here are shown the experimental data for the dispersion relation, extracted from the formula:

$$\mathcal{R}(\omega) \simeq S_{21}(\omega) = \frac{1 - e^{ik_n(\omega)l}}{2} \tag{4.21}$$

The results obtained are remarkably clear. The graph $\omega \mapsto \mathrm{Re}\big(k_n(\omega)\big)$ exhibits two non-dispersive regimes for which the dispersion relation is linear with frequency. For low frequencies, a linear fit of the data yields a velocity $v_n(0) = 4.6\ 10^4$ m.s^{-1}. A blunt shift in $\mathrm{Re}\big(k_n(\omega)\big)$ occurs around $f = 6.5$ GHz, and a second non-dispersive dispersion relation reveals for $f > 7$ GHz, with a velocity $v_n(\infty) = 2.3\ 10^4$ m.s^{-1}. The behavior of $\omega \mapsto \mathrm{Im}\big(k_n(\omega)\big)$ is less intuitive. The abrupt shift of $\mathrm{Re}\big(k_n(\omega)\big)$ is accompanied by a peak in $\mathrm{Im}\big(k_n(\omega)\big)$, but the measured values are otherwise relatively low and are globally linearly increasing with frequency. Though we are not able to predict microscopically this dissipation effect, we propose a heuristic approach in section 4.4.1.

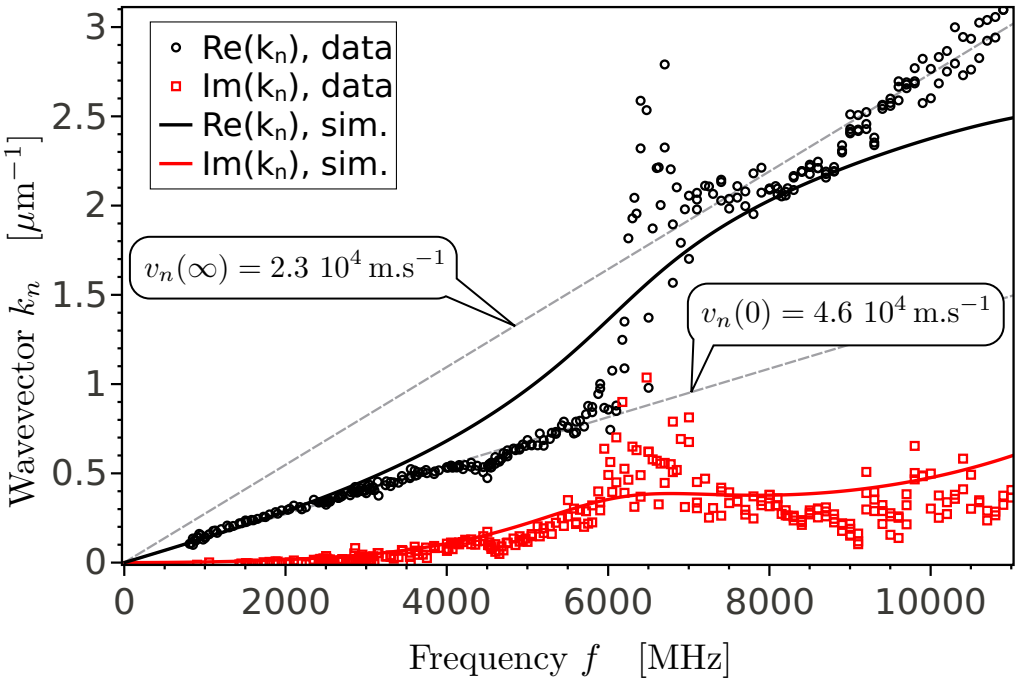

FIGURE 4.12: **Dispersion relation $\omega \mapsto k_n(\omega)$ of the spin mode** – In red circles and black squares are represented respectively the real and imaginary parts of the wavevector k_n as a function of frequency f. $\mathrm{Re}(k_n)$ exhibits two non-dispersive regimes: linear fits (in grey dashes) yields the velocities $v_n(0) = 4.6\,10^4$ m.s^{-1} for low frequencies, whereas $v_n(\infty) = 2.3\,10^4$ m.s^{-1} at high frequencies. An abrupt crossover between both domains occurs around 6 GHz. The existence of two different velocities is attributed to the existence of a finite non-zero range of the interactions. The non-zero imaginary part $\mathrm{Im}(k_n)$ presents an overall linear increase, with in addition a peak at the cross-over frequency between the two non-dispersive domains.

An interpretation can already be given to understand the physical meaning of the appearance of two different velocities in the dispersion relation of the neutral mode.

At low frequency, the wavelength of the EMP is very large: an order of magnitude is $\lambda_n = \frac{2\pi v_n(0)}{f} \simeq 300\,\mu$m. In comparison, the range of the interaction is probably on the order of 10 microns, as they are probably partially screened by the surrounding metallic gates. Consequently we can consider a zero-range limit for the interaction, and a velocity v_n^0 can be predicted in this regime. This simplification is frequently used in chiral edge channels: this zero-range model is described in detail in section 4.4.2.1. Moreover, since there's no characteristic length introduced in this model, the behavior predicted for long wavelength is in fact valid regardless of the wavelength which is in any case much larger than the range of the interactions. Though this is not formally demonstrated yet, we already understand that the absence of range in the interaction is characterized by a non-dispersive dispersion relation, i.e. a constant velocity v_n^0 for the slow neutral mode, that must coincide with $v_n(0)$. This is in strong contradiction with our observations.

We thus attribute the appearance of two non-dispersive regimes to the existence of a finite range in the interactions.

In this section, we have presented our experimental results on the capacitive coupling between edge channels. These results have been analysed on the basis of the simple heuristics presented in section 4.1.1: it only assumes the existence of two eigenmodes, one that is neutral and slow while the other is charged and fast. The phase shift between both modes has been observed, and the dispersion relation exhibits two non-dispersive regimes, feature attributed to the existence of a finite range in the interactions. We now turn to a detailed analysis of our results: first the nature of the eigenmodes is studied and the validity of the hypothesis of antisymmetric/symmetric eigenmodes is demonstrated. Then, both short and long range are discussed in detail.

4.3.3 Discussing the nature of eigenmodes

Our interpretation relies so far on an important hypothesis that needs to be discussed: our model assumes that the eigenmodes are the symmetric charged and antisymmetric neutral modes. We review this point in the following developments, and prove that this decomposition is indeed correct, giving proofs of the neutrality of the slow mode.

4.3.3.1 Eigenmodes in the non-symmetric case

In full generality, one can consider the following eigenmodes, linear combinations[2] of $i_1(x,\omega)$ and $i_2(x,\omega)$:

$$i_+(x,\omega) = \cos\frac{\theta}{2} i_1(x,\omega) + \sin\frac{\theta}{2} i_2(x,\omega) \quad (4.22)$$

$$i_-(x,\omega) = \sin\frac{\theta}{2} i_1(x,\omega) - \cos\frac{\theta}{2} i_2(x,\omega) \quad (4.23)$$

$$i_\pm(l,\omega) = e^{i\frac{\omega l}{v_\pm}} i_\pm(0,\omega) \quad (4.24)$$

The case $\theta = 0$ corresponds to completely independent channels while $\theta = \pi/2$ corresponds to the strong coupling case where the eigenmodes correspond to the charged and neutral modes. Any other intermediate case correspond to partially charged eigenmodes for which we can define the ratio of the total charge carried by modes $-$ and $+$, $z = \frac{\sin\frac{\theta}{2} - \cos\frac{\theta}{2}}{\sin\frac{\theta}{2} + \cos\frac{\theta}{2}}$. In this general case, the expressions for S_{21} and $S_{11} + S_{21}$ and thus for

[2] A microscopic derivation of such eigenmodes will be proposed in section 4.4.1.

the measured quantity $\mathcal{R}$ differ from Eqs.(4.12), and (4.13):

$$S_{21} = \sin\theta \, \frac{e^{i\omega l/v_+} - e^{i\omega l/v_-}}{2} \tag{4.25}$$

$$S_{11} + S_{21} = \frac{e^{i\omega l/v_+} + e^{i\omega l/v_-}}{2} + (\cos\theta + \sin\theta)\frac{e^{i\omega l/v_+} - e^{i\omega l/v_-}}{2} \tag{4.26}$$

$$\mathcal{R} = \frac{\sin\theta \, (1 - e^{i\phi})}{1 + e^{i\phi} + (\cos\theta + \sin\theta) \, (1 - e^{i\phi})} \tag{4.27}$$

$$\phi(\omega) = \frac{\omega l}{v_-} - \frac{\omega l}{v_+} \tag{4.28}$$

From Eq.(4.25), one can immediately see that S_{21} still describes coherent oscillations from the EMP from channel 1 to channel 2, but the amplitude of these oscillations is affected by the factor $\sin\theta$ which only gets to 1 for strong coupling $\theta = \pi/2$. The total current transferred $S_{11} + S_{21}$ is also affected and oscillates (either with frequency f or length l) reflecting the fact that in this general case, the total charge $i_1 + i_2$ is no longer an eigenmode (Eq.(4.26)). As a result, $\mathcal{R}$ still follows a circle in the complex plane but with a θ dependent modulus and center (Eq.(4.27)). From these general expressions and their comparison with our experimental data, one can assess that the eigenmodes are indeed the charge and neutral ones, $i_+ = i_\rho$, $i_- = i_n$ within an accuracy of $z = 0 \pm 0.1$ for the charge ratio between the eigenmodes.

4.3.3.2 Low-frequency behavior

The first argument comes from the low frequency behavior of $\mathcal{R}$ where dissipation can be safely neglected. Both the modulus $|\mathcal{R}|$ and the phase $\arg(\mathcal{R})$ follow a linear ω dependence but with two different θ dependent slopes:

$$|\mathcal{R}| = \sin(\theta)\,\phi(\omega)/2 \tag{4.29}$$

$$\arg(\mathcal{R}) = -\frac{\pi}{2} + \big(\sin(\theta) + \cos(\theta)\big)\,\phi(\omega)/2 \tag{4.30}$$

By measuring the ratio of these slopes, one can directly measure the coupling angle θ. Remarkably, in the strong coupling case, $\theta = \frac{\pi}{2}$, data points for $|\mathcal{R}|$ and $\arg(\mathcal{R}) + \frac{\pi}{2}$ should follow the exact same frequency dependence in the low frequency regime. Data points in the low frequency [0.7, 4.5] GHz range and their linear fits (in the [0.9, 2] GHz range) for $|\mathcal{R}|$ and $\arg(\mathcal{R}) + \frac{\pi}{2}$ are represented on Fig.4.13. As expected in the strong coupling case, $\theta = \pi/2$, both curves exhibit similar ω dependence and can be fitted by very close expressions, $|\mathcal{R}| = 3.8\,10^{-11} \times \omega$, $\arg(\mathcal{R}) + \frac{\pi}{2} = 3.7\,10^{-11} \times \omega$. An estimate of the error is given by the dashed lines. As the slope of $|\mathcal{R}|$ is determined with an accuracy of 10%, one can determine two bounds for the slope of $\arg(\mathcal{R}) + \frac{\pi}{2}$ corresponding to the

condition $\theta 90 \pm 11°$. The dashed lines represent two extremum values of this slope for $\theta = 79°$ and $101°$. We can see that our data points fall within this uncertainty such that we can assess $\theta = 90 \pm 11°$ corresponding to $z = 0 \pm 0.1$.

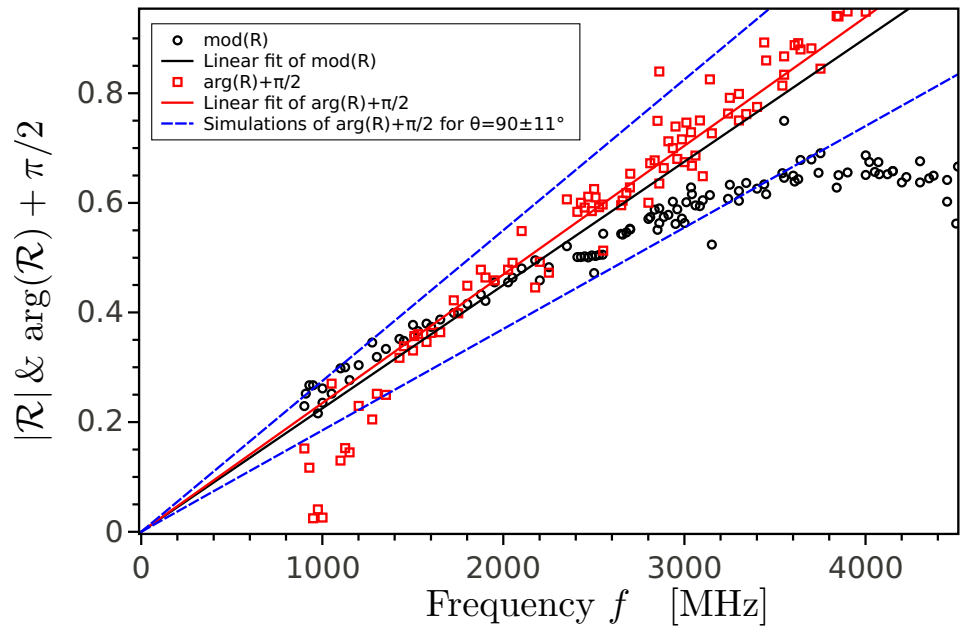

FIGURE 4.13: **Low-frequency test of the neutrality assumption** – Experimental data of $|\mathcal{R}|$ (red circles) and $\arg(\mathcal{R}) + \pi/2$ (black circles) are presented as a function of frequency f. Linear fits (in red and black solid lines) show that they exhibit very similar slopes in the limit $f \to 0$, which gives a first proof of the validity of the neutrality assumption according to Eqs.(4.29) and (4.30). Blue dashes present the slopes expected for $\arg(\mathcal{R}) + \pi/2$ for $\theta = 90 \pm 11°$, $z = 0 \pm 0.1$.

4.3.3.3 Position of the center

An other point that is scrutinized is the position of the center of the circle predicted by Eq.(4.27). The radius r_θ of the circle and the coordinates of the center M_θ are given by:

$$r_\theta = \frac{\sin\theta}{2(\sin\theta + \cos\theta)} \tag{4.31}$$

$$M_\theta = (r_\theta, 0) \tag{4.32}$$

The experimental data for $\mathcal{R}$ enable to find an estimation of M_θ. Due to damping, $\mathcal{R}$ does not follow a trajectory but in fact spirals toward the point M_θ. An evaluation of the admissible M_θ by direct comparison of the data thus gives an admissible range for the coupling angle θ. On Fig.4.14, we compare our data with a range of $\theta = 90 \pm 11°$, corresponding to $z = 0 \pm 0.1$. The corresponding M_θ are pictured by the shaded area, that is situated around the red dot symbolizing $M_{\pi/2} = (1/2, 0)$. Meanwhile, the circle of radius $r_{\pi/2} = 1/2$ and the two circles corresponding to the extreme values of $\theta = 90 \pm 11°$

are pictured respectively in red line and blue dashes. Experimental values of $\mathcal{R}$ have been smoothed over 5 points for the sake of clarity. Though no rigorous criterion can be simply implemented, this range $z = 0 \pm 0.1$ seems to be in good agreement, to the eye, with the experimental data.

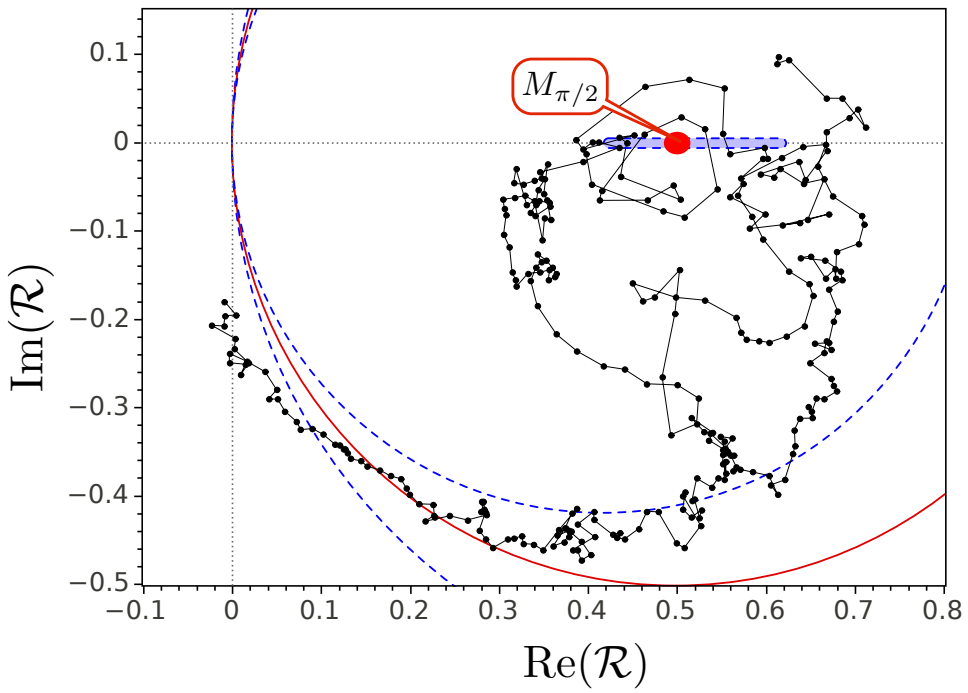

FIGURE 4.14: **Test of the neutrality assumption on the Nyquist diagram** – The shaded area symbolizes the position of the center M_θ of the circular trajectory described by $\mathcal{R}$ for the range $\theta = 90 \pm 11°$, $z = 0 \pm 0.1$ (in the absence of damping). The red dot is placed at $M_{\pi/2} = (1/2, 0)$. The circles for $\theta = 90°$ (in red line) and $\theta = 90 \pm 11°$ (blue dashes) are also drawn. Due to damping, our experimental points seem to converge toward one of the M_θ in the shaded area so that the evaluation $z = 0 \pm 0.1$ is confirmed.

These two tests enable to claim that the slow mode is indeed neutral, carrying less than 10% of the charge carried by the fast mode that is consequently the so-called charge mode. This study confirms a posteriori the validity of the analysis proposed in the previous chapter. In the next section, we introduce elements of theory based on a Luttinger liquid model, that enables to gives a physical meaning to the coupling angle θ in terms of strength of interactions between and inside edge channels.

4.4 Detailed analysis and modeling of interactions

In this section we establish a theoretical basis required to provide a clear interpretation of our experimental results. We follow a Luttinger liquid approach in which the edge

magneto-plasmons are pictured as bosonic fields.

4.4.1 Bosonic description of quantum Hall edge channels

4.4.1.1 Edge channels in the absence of interactions

The peculiarity of one-dimensional systems lies in the fact that interactions strongly influence the nature of elementary excitations. The most adequate representation of excitations relies on a picture of collective bosonic modes, that are consequently described as a bosonic field $\hat{\phi}(x,t)$. We first briefly examine the case of non-interacting edge channels, where we describe the EMP as free bosonic fields. Then, we introduce Coulomb interaction and explain in a simple manner the appearance of two eigenmodes. Complements for the derivation of the following results are provided in Appendix C.

In the integer Quantum Hall regime, an edge magneto-plasmon represented by the bosonic field $\hat{\phi}(x,t)$ can be decomposed as:

$$\hat{\phi}(x,t) = \frac{-i}{\sqrt{4\pi}} \int_0^\infty \frac{d\omega}{\sqrt{\omega}} (\hat{\phi}(x,\omega) e^{i\omega(\frac{x}{v}-t)} - \hat{\phi}^\dagger(x,\omega) e^{-i\omega(\frac{x}{v}-t)}) \tag{4.33}$$

This chiral field propagates at a velocity given by the bare Fermi velocity v, in the absence of both inter and intra channel interactions.

The current $i(x,t)$ and charge density $\rho(x,t)$ in the edge channel can then be defined, and verify the charge conservation equation:

$$i(x,t) = \frac{e}{\sqrt{\pi}} \partial_t \hat{\phi}(x,t) \tag{4.34}$$

$$\rho(x,t) = \frac{-e}{\sqrt{\pi}} \partial_x \hat{\phi}(x,t) \tag{4.35}$$

$$\partial_t \rho + \partial_x i = 0 \tag{4.36}$$

For two non-coupled channels, the eigenmodes of propagation are ϕ_i for $i = 1, 2$, as propagation takes place independently in each channel with possibly different velocities v_i.

4.4.1.2 Interacting edge channels

In the case of a capacitive coupling between channels, $\phi_i(x,\omega)$ are not eigenmodes of the propagation. As in section 4.1.3, an incoming mode at position $x = 0$ is related to an output mode at position $x = l$ via the scattering matrix $\boldsymbol{\mathcal{S}}_{EMP}(\omega, l)$, acting on bosonic

plasmon modes (and not fermionic electronic modes)

$$\Phi(l,\omega) \;=\; \boldsymbol{\mathcal{S}}_{EMP}(\omega,l)\Phi(0,\omega) \tag{4.37}$$

Interactions can be modeled simply in this framework. The fields ϕ_i describing the two edge channels of $\nu = 2$ are labeled $i = 1$ for the outer channel, and $i = 2$ for the inner channel. If $u_i(x,t)$ is the potential in the wire at position x and time t, the equation of motion for ϕ_i reads, in time and Fourier space (see appendix C for details):

$$(\partial_t + v_i\partial_x)\phi_i(x,t) = \frac{e}{\sqrt{\pi}}u_i(x,t) \tag{4.38}$$

$$(-i\omega + v_i\partial_x)\phi_i(x,\omega) = \frac{e}{\sqrt{\pi}}u_i(x,\omega) \tag{4.39}$$

The left-hand side of these equations describe the free motion of fields ϕ_i at velocities v_i (that is here supposed to be channel dependent). Interactions are then encoded in the right-hand side, and in particular in the relation between potentials u_i and fields ϕ_i. We now examine two different cases (zero and finite range couplings). The short range is already known to give an incomplete understanding of our results as it does not describe the observed dispersion relation. However, it provides the basis for a generalization to a finite range model, thus emphasizing the differences between both viewpoints.

4.4.2 Short-range interactions at $\nu = 2$

The most frequently used model to describe interactions in quantum Hall edge channels is the so-called short-range model [55, 56, 79]. Interactions are then assimilated to zero-range density-density interactions. On a theoretical point of view, this assumption is really convenient as interactions are considered as a local phenomenon, simplifying considerably analytical treatment. This has proven to be relevant in several cases such as the study of the lobe structure of visibility in electronic Mach-Zehnder interferometers [64]. Experimentally, this local interaction limit can be approached when large metallic gates efficiently screen interactions on a very short length scale.

4.4.2.1 Zero-range model

Coulomb interactions are then depicted as zero-range density-density interaction, and we introduce the matrix of distributed capacitances $\boldsymbol{\mathcal{C}}$ relating charge densities ρ_i and potentials u_i (see appendix C for details):

$$\begin{pmatrix} \rho_1(x,\omega) \\ \rho_2(x,\omega) \end{pmatrix} \;=\; \begin{pmatrix} \mathcal{C}_1 & -\mathcal{C} \\ -\mathcal{C} & \mathcal{C}_2 \end{pmatrix} \begin{pmatrix} u_1(x,\omega) \\ u_2(x,\omega) \end{pmatrix} \tag{4.40}$$

In this picture, charge densities ρ_i are coupled via capacitance per unit length $\mathcal{C}_{ij}$ (see Fig.4.15 panel a). On the diagonal, $\mathcal{C}_{ii} = \mathcal{C}_i$ thus encodes interactions inside the channels while off-diagonal elements $\mathcal{C}_{12} = \mathcal{C}_{21} = -\mathcal{C}$ describe the coupling between both channels.

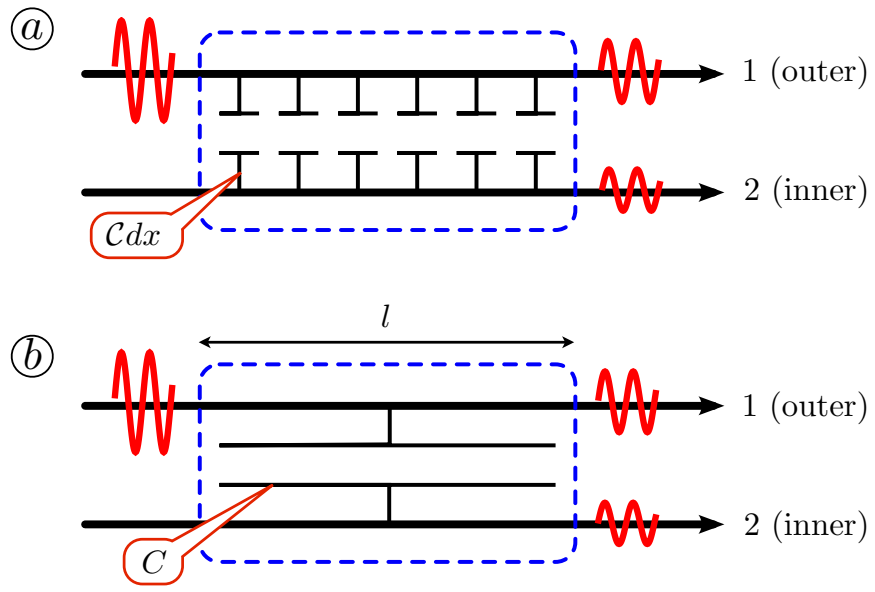

FIGURE 4.15: **Schematics of the coupling between edge channels** – Outer and inner edge channels are pictured by black arrows, with blue dashes symbolization the co-propagation interaction zone. a) In a zero-range picture, channels are coupled via distributed capacitance $\mathcal{C}$. b) In the long-range model, channels are coupled via a discrete capacitance C.

Equations of motion of both fields ϕ_i are then coupled, and one needs to diagonalize the inverse capacitance matrix $\boldsymbol{\mathcal{C}}^{-1}$. If $\Phi = (\phi_1, \phi_2)$, we obtain:

$$\boldsymbol{\mathcal{V}}\partial_x\Phi(x,\omega) = i\omega\Phi(x,\omega) \tag{4.41}$$

$$\mathcal{V}_{ij} = (v_i\delta_{ij} + \frac{e^2}{h}\boldsymbol{\mathcal{C}}^{-1}_{ij}) \tag{4.42}$$

where $\boldsymbol{\mathcal{V}}$ is the velocity matrix. In the absence of inter-channel interactions ($\mathcal{C} = 0$), channels are independent but velocities are renormalized by intra-channel interactions, $\mathcal{V}_i = v_i + \frac{e^2}{h}\mathcal{C}^{-1}_{ii}$.

One can then relate the input mode at position $x = 0$ to an output position $x = l$ via

$$\Phi(l,\omega) = \boldsymbol{\mathcal{S}}_{EMP}(\omega,l)\Phi(0,\omega) \tag{4.43}$$

$$\boldsymbol{\mathcal{S}}_{EMP}(\omega,l) = e^{i\omega l\boldsymbol{\mathcal{V}}^{-1}} \tag{4.44}$$

4.4.2.2 Eigenmodes and scattering matrix elements

Due to coupling between channels, ϕ_1 and ϕ_2 are not eigenmodes for the propagation. Eigenmodes are obtained by diagonalizing either $\mathcal{C}$ or equivalently $\boldsymbol{\mathcal{S}}_{EMP}$. In full generality ($\mathcal{C}_1 \neq \mathcal{C}_2$), two new eigenmodes appear:

$$\phi_+(x,\omega) = \cos\frac{\theta}{2}\,\phi_1(x,\omega) + \sin\frac{\theta}{2}\,\phi_2(x,\omega) \tag{4.45}$$

$$\phi_-(x,\omega) = \sin\frac{\theta}{2}\,\phi_1(x,\omega) - \cos\frac{\theta}{2}\,\phi_2(x,\omega) \tag{4.46}$$

$$\phi_\pm(l,\omega) = e^{i\frac{\omega l}{v_\pm}}\phi_\pm(0,\omega) \tag{4.47}$$

where velocities $v_\pm$ and coupling angle θ are given by:

$$v_\pm = \frac{\mathcal{V}_{11}+\mathcal{V}_{22}}{2} \pm \sqrt{\frac{(\mathcal{V}_{11}-\mathcal{V}_{22})^2}{4} + \mathcal{V}_{12}^2} \tag{4.48}$$

$$\cos\theta = \frac{(\mathcal{V}_{11}-\mathcal{V}_{22})/2}{\sqrt{(\mathcal{V}_{11}-\mathcal{V}_{22})^2/4 + \mathcal{V}_{12}^2}} \in [0,\pi] \tag{4.49}$$

As a consequence from the zero range of the interaction, the velocities $v_\pm$ are ω-independent. Note that the domain $\theta \in [0,\pi/2[$ corresponds to the expected situation where, in the absence of inter channel interaction, the outer edge channel velocity is greater than the inner one, $\mathcal{V}_1 > \mathcal{V}_2$.

The charge ρ and neutral n eigenmodes are recovered for $\theta = \pi/2$ with the identification $+ \to \rho$ and $- \to n$. This case always occurs for identical edge channels, $\mathcal{V}_{11} = \mathcal{V}_{22}$ but also for strong enough inter-channel interaction, $\mathcal{V}_{12} \gg \frac{\mathcal{V}_{11}-\mathcal{V}_{22}}{2}$.

Scattering matrix elements can be calculated easily from Eqs.(4.45), (4.46) and (4.47), and yield the following expressions, used in section 4.3.3:

$$S_{21} = \sin\theta\,\frac{e^{i\omega l/v_+} - e^{i\omega l/v_-}}{2} \tag{4.50}$$

$$S_{11} = \frac{e^{i\omega l/v_+} + e^{i\omega l/v_-}}{2} + \cos\theta\frac{e^{i\omega l/v_+} - e^{i\omega l/v_-}}{2} \tag{4.51}$$

4.4.2.3 Predictions and discussions of the results

As demonstrated in section 4.3.3, the observed experimental situation corresponds to the strong-coupling limit $\theta = \pi/2$. From Eq.(4.48), one gets for the velocities $v_\pm = \overline{v} + \frac{1}{R_K(\overline{\mathcal{C}}\mp\mathcal{C})}$, with $\overline{v} = \frac{v_1+v_2}{2}$ and $\overline{\mathcal{C}} = \frac{\mathcal{C}_{11}+\mathcal{C}_{22}}{2}$. The case $v_\rho \gg v_n$ corresponds to total influence between edge channels, $\overline{\mathcal{C}} \approx \mathcal{C}$ and such that $v_n \approx \overline{v} + \frac{1}{2R_K\mathcal{C}}$. Introducing $C_q = l/R_K\overline{v}$ quantum capacitance and $C = l\mathcal{C}$ the total coupling capacitance, we finally have $v_\rho \to \infty$ and $v_n = v_n^0 = \overline{v}(1 + \frac{C_q}{2C})$.

A key point that has to be discussed is the fact that no characteristic length is introduced in this model, in direct connection with the absence of range in the interactions. Consequently, the velocity $v_n(\omega) = v_n^0$ is independent of the frequency ω, and the angle $\Phi(\omega)$ varies linearly with ω, or in an equivalent way the angular velocity $\frac{d\Phi}{d\omega}$ at which the circle $\omega \mapsto \mathcal{R}(\omega)$ is drawn is constant. Only one parameter governs the short range model, namely $\tilde{\tau}$ (or equivalently $v_n^0 = l/2\tilde{\tau}$) and this parameter is settled by the low-frequency regime. As seen in Fig.4.12, the short-range model is not able to capture properly the dispersion relation.

As such, the short-range model is insufficient to describe accurately our experimental results. This is not surprising as interactions may not be strongly screened as large metallic gates are relatively far away from edges states in our sample. The issue of dissipation was not discussed in the frame of this model, but no satisfying results has been obtained in our attempts to do so. For completeness, this question has been treated in section C.2.1.

A proper description of our results then requires crucially to introduce a finite non-zero range for the interaction. We consequently turn to an other theoretical model proposed to take into account this effect.

4.4.3 Long-range interactions at $\nu = 2$

4.4.3.1 Describing long-range interactions

In this section, we propose a model that takes into account a finite non-zero range for Coulomb interactions between channels. Instead of considering a local coupling between edge channels via distributed capacitances, edge states are coupled using discrete capacitors [136, 137], as pictured on Fig.4.15, panel b). They describe the electrostatic influence between the total charge q_k in the two wires $k = 1, 2$ and the potentials u_k, that are this time assumed to be uniform along the whole length l. The characteristic range for interactions is then naturally given by the propagation length l. Charges can be defined as:

$$q_k(\omega) = \int_0^l dx\, \rho_k(x) dx \tag{4.52}$$

$$= \frac{e}{\sqrt{\pi}} \big(\phi_k(0,\omega) - \phi_k(l,\omega)\big) \tag{4.53}$$

Coulomb interactions are then depicted via the matrix of capacitances $\mathbf{C}$ relating charges q_i and uniform potentials u_i:

$$\begin{pmatrix} q_1(\omega) \\ q_2(\omega) \end{pmatrix} = \begin{pmatrix} C_1 & -C \\ -C & C_2 \end{pmatrix} \begin{pmatrix} u_1(\omega) \\ u_2(\omega) \end{pmatrix} \tag{4.54}$$

Finally, the equation of motion for fields ϕ_k reads:

$$(-i\omega + v_i\partial_x)\phi_k(x,\omega) = \frac{e\sqrt{\pi}}{h}u_i(\omega) \tag{4.55}$$

This equation can be integrated easily since $u_i(\omega)$ is uniform, and yields:

$$\phi_k(x,\omega) = e^{i\frac{\omega x}{v_i}}\phi_k(0,\omega) + \frac{i\sqrt{\pi}}{eR_K\omega}(1 - e^{i\frac{\omega x}{v_i}})u_k(\omega) \tag{4.56}$$

Fixing initial conditions $\phi_1(0,\omega) \neq 0, \phi_2(0,\omega) = 0$, we immediately obtain a conservation equation $\phi_2(l,\omega) = \phi_1(l,\omega) - \phi_1(0,\omega)$. For simplicity, and in agreement with our results (section 4.3.3), we focus now on the strong coupling regime. Simple algebra then yields, with $\tau = R_K C, \tau_q = \frac{l}{v} = R_K C_q$:

$$\phi_1(l,\omega) = \frac{1 + e^{i\omega\tau_q} + \frac{i}{\omega\tau}(1 - e^{i\omega\tau_q})}{2 + \frac{i}{\omega\tau}(1 - e^{i\omega\tau_q})}\phi_1(0,\omega) \tag{4.57}$$

$$\phi_2(l,\omega) = \frac{1 - e^{i\omega\tau_q}}{2 + \frac{i}{\omega\tau}(1 - e^{i\omega\tau_q})}\phi_1(0,\omega) \tag{4.58}$$

The scattering matrix $\boldsymbol{\mathcal{S}}_{EMP}(\omega, l)$ can then be written:

$$\boldsymbol{\mathcal{S}}_{EMP}(\omega,l) = \begin{pmatrix} 1 - S_{21} & S_{21} \\ S_{21} & 1 - S_{21} \end{pmatrix} \tag{4.59}$$

$$S_{21} = \frac{1 - e^{i\omega\tau_q}}{2 + \frac{i}{\omega\tau}(1 - e^{i\omega\tau_q})} \tag{4.60}$$

$$\tau = R_K C, \quad \tau_q = \frac{l}{v} = R_K C_q \tag{4.61}$$

4.4.3.2 Results of the long range model

The eigenmodes are once again the antisymmetric dipole mode n and the symmetric charge mode ρ. We find that $S_\rho = S_{11} + S_{21} = 1$, that can be interpreted as $v_\rho \to \infty$: this infinite value of the charge velocity v_ρ thus ensures current conservation. On the

other hand,

$$\begin{aligned} S_n &= S_{11} - S_{21} && (4.62)\\ &= e^{i\omega\tau_q}\frac{2 - \frac{i}{\omega\tau}(1 - e^{-i\omega\tau_q})}{2 + \frac{i}{\omega\tau}(1 - e^{i\omega\tau_q})} && (4.63)\\ &= e^{i\omega l/v_n} && (4.64) \end{aligned}$$

The velocity v_n thus defined is then frequency dependent, but also depends on the propagation length l. It is not surprising since our description of interactions directly relates the range to this length l. Two asymptotes can be obtained. When $\omega \to 0$, one gets:

$$\begin{aligned} S_n &= 1 - S_{21} && (4.65)\\ &\simeq 1 + 2i\omega\tilde{\tau} \simeq e^{2i\omega\tilde{\tau}} && (4.66) \end{aligned}$$

Thus, we identify $v_n = v_n^0 = \frac{l}{2\tilde{\tau}}$ in the low-frequency limit. This is compatible with the short-range description, as well as with the RC-circuit description. This compatibility is expected, as for $\omega \to 0$ the wavelength of the EMP is very large: at some point, it must indeed become larger that the range of the interactions, which are then correctly described by a short-range model. On the opposite, the high-frequency domain ($\omega\tau \gg 1$) then directly gives $S_n = e^{i\omega\tau_q}$ so that $v_n = v$. This equation will be used to extract the velocity of edge channels in the absence of interactions.

4.4.3.3 Velocities and time scales in the long-range model

As expected, the existence of a finite range in the interaction is responsible for the appearance of two different velocities for the low-frequency and high-frequency domain. This is of great interest in order to obtain a good description of the measured dispersion relation of mode n. Indeed, two time scales are involved in the model, namely τ and τ_q.

In the low frequency regime, these times combine to give the same asymptotic behavior as the short-range model: S_{21} can be written in the form:

$$S_{21}(\omega) = -i\omega\tilde{\tau}(1 + i\omega\tilde{\tau}), \quad \tilde{\tau} = \frac{\tau\tau_q}{2\tau + \tau_q} \tag{4.67}$$

The combination $\tilde{\tau} = \frac{\tau\tau_q}{2\tau+\tau_q}$ exactly corresponds to the characteristic time of the RC-circuit discussed in 4.1.4.1: indeed $\tilde{\tau} = R_K C_\mu = R_K \frac{CC_q}{2C+C_q}$, and allows a proper description of the low-frequency regime.

Now that a long range model has been developed, we proceed to a comparison between predictions of both short range and long range model with our data. Then we propose a way to take into account dissipation in a satisfying heuristic way, though no microscopic derivation is given.

4.4.4 Comparisons between data and models

4.4.4.1 Analysis of $|\mathcal{R}|$ and $\arg(\mathcal{R})$

On Fig.4.16, graphs of $|\mathcal{R}|$ and $\arg(\mathcal{R})$ are presented as a function of frequency $f = \omega/2\pi$. The experimental data are then compared with four different simulated curves: the RC-circuit (green small dashes, following Eq.(4.16)), the short range model (red long dashes), the long range model without dissipation (blue dashed dotted line, Eq.(4.60)) and with dissipation (black plain line, Eq.(4.70)). The different parameters that we extract are then summarized in table 4.1 at the end of this section. We will come back to dissipation in the next section.

Low-frequency regime Let us examine first the low frequency regime. For frequency $f < 3$ GHz, a linear increase of $|\mathcal{R}|$ is observed. In the meantime, $\arg(\mathcal{R})$ also increases linearly starting around $\arg(\mathcal{R}) \simeq -\pi/2$. This behavior is expected, and reflects the RC-circuit asymptotic regime, with $\mathcal{R}$ mainly imaginary.

$$\mathcal{R}(\omega) \simeq S_{21}(\omega) \simeq -i\omega\tilde{\tau}(1 + i\omega\tilde{\tau}) \tag{4.68}$$

From the dispersion relation, we have extracted $v_n(0) = 2.3\,10^4\,\mathrm{m.s}^{-1}$, assimilated to v_n^0 and at the same time $\tilde{\tau} = 35$ ps. Plugging this parameter into our simulations gives a good agreement with experimental data in the low frequency regime.

Higher frequencies For higher frequencies $f > 3$ GHz, we observe that $|\mathcal{R}|$ reaches a maximum $|\mathcal{R}| \gtrsim 0.7$ for $f = 4.5$ GHz, (with $\arg(\mathcal{R}) \simeq -\pi/8$). We interpret this maximum value as a signature of a transfer of around 70% of the injected current (in outer channel) toward inner channel. Due to dissipation, we dot not observe a maximum modulus of $|\mathcal{R}| = 1$ for a phase $\arg(\mathcal{R}) = 0$. Then $|\mathcal{R}|$ decreases to a minimum (around $|\mathcal{R}| = 0.35$) before increasing again while the phase has roughly the same behavior. For very high frequencies ($f > 8$ GHz), we notice that oscillations of $|\mathcal{R}|$ are notably damped, whereas $\arg(\mathcal{R})$ approaches 0.

The RC circuit does not predict charge oscillations and is not in agreement with our results. Moreover the short-range model is also in strong disagreement with our results. This was expected: $\tilde{\tau}$ has been set via the low-frequency regime there is no other free parameter in this model, and the constant velocity v_n^0 of the neutral mode is in contradiction with our results on the dispersion relation.

On the contrary, the long-range model offers the possibility to obtain a good agreement for both low-frequency and oscillation regimes by tuning independently $\tilde{\tau}$ and τ_q. The best fitting is obtained for $\tau_q = 124 \pm 5$ ps, (so that $\tau = 81 \pm 4$ ps in virtue of Eq.(4.67)). This corresponds to a velocity $v = 2.6 \pm 0.2\ 10^4 \mathrm{m.s}^{-1}$, which is consistent with the estimation $v_n(\infty) = 2.3 \pm 0.3\ 10^4 \mathrm{m.s}^{-1}$ obtained from the dispersion relation. This tends to confirm the identification $v_n(\infty) = v$ derived from the long-range model.

	$\tilde{\tau}$ (ps)	τ_q (ps)	τ (ps)	τ_r (ps)	v_n^0 (m.s^{-1})	v (m.s^{-1})
Dispersion relation	35				$4.6\,10^4$	$2.3\,10^4$
Short-range	35				$4.6\,10^4$	
Long-range	35	124 ± 5	81 ± 4	4.1 ± 1	$4.6\,10^4$	$2.6\,10^4$

TABLE 4.1: **Summary of times and velocities extracted from experimental data** – From the dispersion relation (Fig.4.12), we extract the velocities of two non-dispersive regimes, identified with the neutral mode velocity v_n^0 at low frequencies and with the bare Fermi velocity v at high frequencies. Eq.(4.15) then yields $\tilde{\tau}$ that is fixed in the short/long-range fits. In the short range model, there is no other free parameter. On the contrary, the long-range model enables to extract independently τ_q for the period of charge oscillations relaxation constant τ_r. From Eqs.(4.61) and (4.67), τ and v can be extracted and is consistent with the velocity v obtained from the dispersion relation.

The long-range model presented in this manuscript thus gives a reasonable description of our results. At this point, we mention the fact that the velocities extracted in previous developments are relatively small. Though we are not able to obtain the charge velocity v_ρ, it can be compared with measurements reported in [76] for similar samples (densities and filling factor comparable to ours). They indeed obtain $v_\rho \simeq 1.5\,10^6 \mathrm{m.s}^{-1}$, so that $v_\rho \gg v_n$, justifying a posteriori our assumption. However, the damping of the oscillations, which is clearly visible both on the Nyquist diagram (Fig.4.11) and $|\mathcal{R}|$ has not been taken into account yet. We describe the procedure we followed in the next section.

4.4.4.2 Model for dissipation

To take into account dissipation, several possibilities are envisioned. First, one can imagine that a metallic gate, or an additional edge channel is weakly coupled to the two interacting edge states, creating an energy leak in the two-channel system. This method

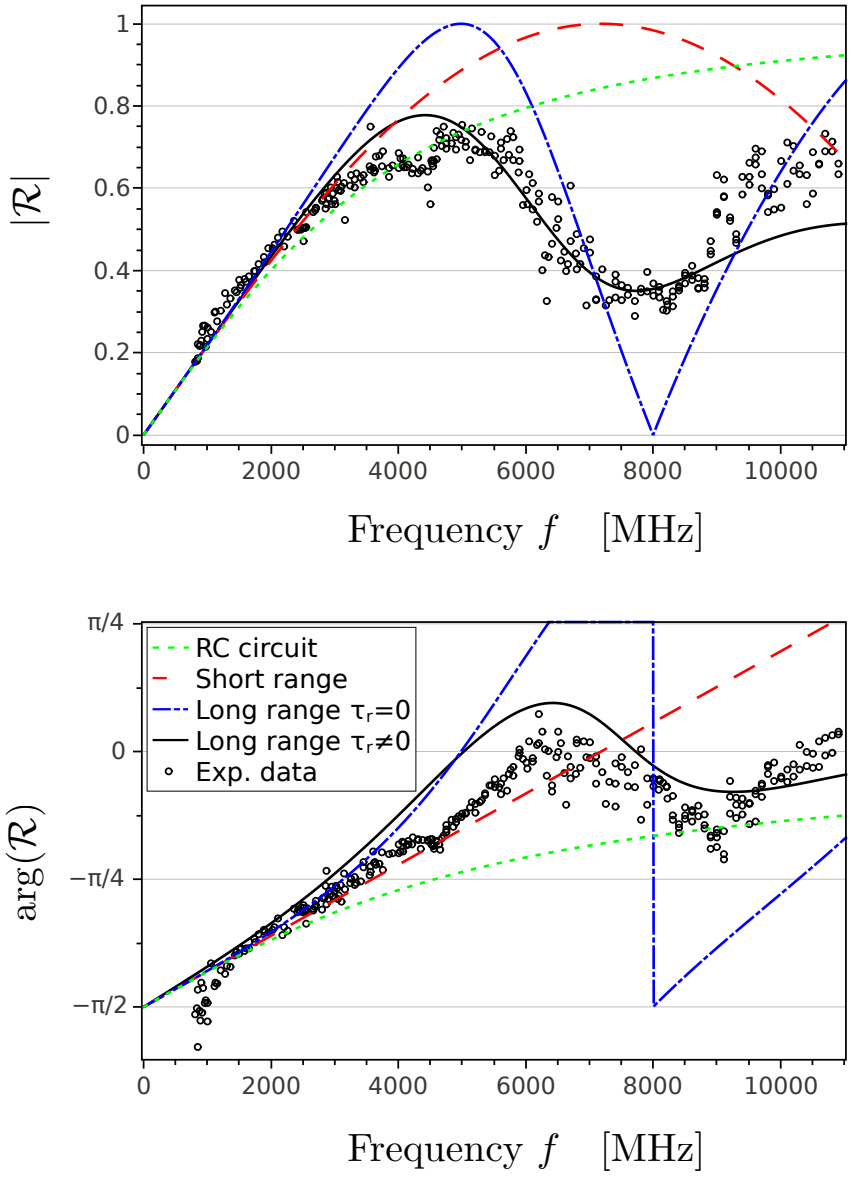

FIGURE 4.16: **Data for $|\mathcal{R}|$ and** $\arg(\mathcal{R})$ – Experimental data for $|\mathcal{R}|$ and $\arg\mathcal{R}$ are presented as a function of frequency f and compared with different models: RC circuit (green small dashes), short range model (red long dashes), long range without dissipation (blue dashed dotted line) and with dissipation (black plain line). With two independent time scales, originating from the finite range of the interaction, the long range model is able to reproduce correctly our data. Dissipation can be added. Fixing $\tilde{\tau} = 35$ ps from the dispersion relation, we find that the best fitting parameters are $\tau_q = 124 \pm 5$ ps, (so that $\tau = 81 \pm 4$ ps) and $\tau_r = 4.1 \pm 1$ ps.

has not proven to be sufficient to explain dissipation. A second method has proven more relevant: we assume that dissipation occurs intrinsically as propagation takes place in the edge channels, which modifies the equation of motions for fields ϕ_k and consequently the resulting scattering parameters S_{21}.

Starting from the equation of motion in the frequency domain, we add a positive term $\gamma(\omega)$, thus substituting $\omega + i\gamma(\omega)$ to ω:

$$\big(-i\omega + \gamma(\omega) + v_F\partial_x\big)\phi_i(x,\omega) = \frac{e\sqrt{\pi}}{h}u_i(x,\omega) \tag{4.69}$$

If $\gamma(\omega) = 0$, channels are not dissipative, otherwise exponentially decaying factors $e^{-\gamma(\omega)\tau_q}$ appear. We obtain, from the very same calculation as previously, the following result:

$$\begin{aligned} S_{21}(\omega) &= \frac{1 - e^{i\omega\tau_q}e^{-\gamma(\omega)\tau_q}}{2 + \frac{i}{(\omega+i\gamma(\omega))\tau}(1 - e^{i\omega\tau_q}e^{-\gamma(\omega)\tau_q})} \\ \tau &= R_K C,\ \tau_q = R_K C_q = \frac{l}{v} \end{aligned} \tag{4.70}$$

Clearly, the ω-dependence of γ will crucially modify the type of dissipation introduced. We have decided to choose $\gamma(\omega) = \omega^2\tau_r$, with τ_r a new parameter governing the amplitude of dissipative effects.

The first reason is that it gives, more or less, an overall linear behavior to $\mathrm{Im}\big(k_n(\omega)\big)$, as basically we have replaced $\omega \to \omega(1 + i\omega\tau_r)$. As such, we thus obtain exponentially decaying factor of the type $e^{-\omega^2\tau_r\tau_q}$. In the limit of high frequencies, $S_{21} \to 1/2, S_{11} \to 1/2$: dissipation in edge channels leads to a relaxation toward a state where currents are equally distributed between inner and outer edge states. Notice that, surprisingly, the conservation equation $S_{21} + S_{11} = 1$ is still guaranteed when dissipation is present. This can be understood in the following manner. Starting from the short-range model, where we would have $S_{21}+S_{11} = e^{i(\omega+i\gamma(\omega))/v_\rho}$ (see Eq.(4.10)), one can see that the phase factor $e^{i(\omega+i\gamma(\omega))/v_\rho}$ decays at a much slower rate than its dipole counterpart $e^{i(\omega+i\gamma(\omega))/v_n}$ since $v_\rho \gg v_n$. In the limit $v_\rho = \infty$, current conservation is still valid even if dissipation occurs. This seems pathological and may question the validity of our description, but it simply tends to prove that, due to its larger velocity, the charge mode is less sensitive to dissipation effects.

Moreover, this choice of γ guarantees compatibility with a circuit of lumped discrete elements at low frequencies. One can easily demonstrate for $\omega \to 0$, to second order in ω the following results:

$$S_{21}(\omega) \simeq -i\omega\tilde{\tau}\big(1 + i\omega(\tilde{\tau} + \tau_r)\big) \tag{4.71}$$

The RC-circuit description is then modified : a resistor of $R_r = \frac{R_K}{2}\frac{\tau_r}{\tilde{\tau}}$ is added in series with the charge relaxation resistor $R_K/2$, as pictured on Fig.4.17.

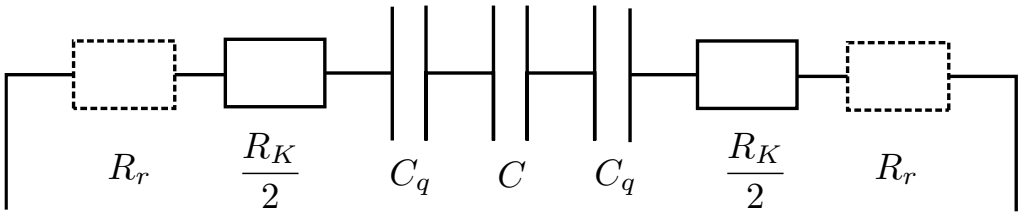

FIGURE 4.17: **Modified RC circuit when taking into account dissipation** – The observed damping of charge oscillations is modeled by dissipative edge channels. The parameter $\gamma(\omega) = \omega^2\tau_r$ is chosen so that the low-frequency equivalent RC is preserved, up to adding resistors $R_r \ll R_K$ (in dashed lines) in series with the charge relaxation resistors. The final lumped elements circuit is then pictured in totality.

With this description of dissipation, a quantitative agreement is found with experimental data: the black plain line is obtained for $\tau_r = 4.1$ ps. This relatively low value proves that the low-frequency regime is only slightly affected by dissipation, as $R_r \ll R_K/2$.

4.4.4.3 Possible origins for dissipation

As of yet, possible origins for dissipation have not been specified. We have mentioned the idea that stray couplings to gates or other edge channels could lead to energy leaks, but our models (based on the same framework as the aforementioned long and short-range models) have not given satisfying results. An other reasonable explanation would be a coupling to internal degrees of freedom, related to the structure of edge channels and especially their finite width [138]. As a consequence, the motion of charged modes couples to neutral acoustic (gapless) modes [139–141] that appear as a source of dissipation in transport experiments.

4.4.5 Effects of interactions on HBT correlations

In this paragraph, we briefly analyse the results of the Hanbury-Brown & Twiss experiment with respect to the issue of interactions, investigated in this chapter. On one-hand the effect of interaction seems indeed quite prominent, and could influence notably the results expected in a non-interacting picture. On the other hand, the experimental data are in good agreement with Floquet scattering theory that offers a thorough analysis but not taking into account Coulomb interaction. How do these results reconcile into a coherent interpretation?

It is difficult to unify both Floquet and EMP theories. From Floquet scattering model, we have obtained the complete electronic (fermionic) N-body state emitted by our SES, with any choice of parameters but neglecting interactions in the dot. The bosonization

formalism then offers the possibility to exactly calculate the corresponding magneto-plasmon (bosonic) state. Unfortunately, the computation of the quantities measured with our detection scheme, such as average current or current correlations remains very difficult, as quantum averages are calculated on the out-of-equilibrium emitted N-body state. On-going efforts lead by our collaborator P. Degiovanni could provide in a near future further interesting results, but a general computation seems out of reach.

Nonetheless, an easy calculation can be performed in the very specific case of the opened dot $D = 1$. It justifies our choice to run the experiment only in this simple case prior to any further investigation for $D < 1$ in the absence of adequate theoretical model.

Case $D = 1$ In the case $D = 1$, one can show [47] that the plasmonic state emitted is a coherent state. It reveals the fact that this state is created by coupling the outer edge channel to a classical voltage source (excitation drive V_{exc}) via a capacitive coupling between the 2DEG and the top-gate electrode. In the monochromatic case (as experimentally examined), the complex amplitude $\alpha(\omega)$ of this coherent state is only affected by the change $\alpha(\omega) \to S_{11}(l,\omega)\alpha(\omega)$ under the effect of interactions. As a consequence, the incident current on the QPC in the outer channel 1, that is partitioned in the HBT experiment is modified by the multipliying factor $I_1(\omega) \to S_{11}(\omega)I_1(\omega)$, and the correlations are then $\langle \hat{I}_1(\omega)\hat{I}_1(\omega)\rangle \to |S_{11}(\omega)|^2\langle \hat{I}_1(\omega)\hat{I}_1(\omega)\rangle$. Using the fact that $\boldsymbol{\mathcal{S}}_{EMP}(\omega, l)$ is unitary (see section 4.1.3), we obtain for $\omega = \Omega \simeq 1.7$ GHz, $|S_{11}(\omega)|^2 = 1 - |S_{21}(\omega)|^2 = 1 - 0.35^2 = 0.88$. This variation of 12% is on the order of magnitude of the experimental error on our measurements. As such, this slight variation is difficult to identify, and to isolate from other effects: uncertainty on the electronic temperature, etc.

Case $D \neq 1$ Though the way of reasoning does not hold for any $D \neq 1$, it seems reasonable to assume that the effects of Coulomb interaction is on the same order of magnitude, and is then almost undetectable. However, in the case $D \neq 1$, the emitted wavepacket is greatly modified. Whereas the quasiparticles emitted at $D = 1$ lie at relatively low energies even when a square voltage is used, the quasiparticles are emitted at energies close to half the level spacing $\Delta/2 \gg kT$ when the dot is closed. As explained in section 3.4.2, such an energy-resolved excitation could collapse dramatically toward the Fermi level, and thus be considerably affected by the anti-bunching with thermal excitations. This behavior is not observed, and though nothing enables to test this idea yet, we can speculate on a possible reason. P. Degiovanni has observed (in numerical simulations) that the periodic repetition could strongly modify the effect of interactions on lorentzian Levitov pulses. When the wavepackets overlap due to a large repetition

rate (as compared to the temporal width of the pulse), the energy distribution is strongly modified and could become less sensitive to interaction. Pauli exclusion principle would indeed block any relaxation toward low-energy levels, as these levels are already occupied. This interpretation is similar to the picture of wavepackets of width h/eV emitted by a DC-biased contact, with a bias V.

Conclusion to chapter 4

In this chapter, we have investigated the effects of Coulomb interaction on the propagation of co-propagating edge channels, in the peculiar case of filling factor $\nu = 2$. Microwave measurements have enabled to study the spectacular effect of charge/neutral mode separation occurring on the 2 coupled co-propagating edge states. Thus the scale at which electronic transport becomes radically modified, given by the criterion $\omega l/v_n \sim 1$, i.e. $f \sim 1 - 10$ GHz for $l \sim 1 - 10$ μm, can be reached.

Using the driven mesoscopic capacitor in the simplest regime (sine excitation, and $D = 1$), we induce sinusoidal charge density waves (EMP) in the outer channel so as to excite both neutral and charge modes. Since these eigenmodes have different velocities, a phase shift progressively appears between the two components, that can be measured. Using a QPC, we are able to measure the (complex) ratio $\mathcal{R}$ of the current in the inner channel that results from the interaction, compared to the total current in both inner and outer channels.

This complex ratio $\mathcal{R}$ directly reflects the phase shift between eigenmodes. We observe damped oscillations of the charge in the inner channel that arise from the phase shift between modes. Contrary to the usual model of short-range interactions, a long-range model gives a quantitative agreement with our experimental data. In particular, we extract the dispersion relation of the spin mode and exhibit the effect of the finite range of interactions. Moreover, we evaluate the bare Fermi velocity ($v = 2.3\,10^4\,\mathrm{m.s}^{-1}$) as well as the velocity of the neutral mode ($v_n = 4.6\,10^4\,\mathrm{m.s}^{-1}$).

A careful analysis of additional data show that parasitic couplings can be ignored up to a 10% error, but the issue of the effect of inter-edge coupling in the Hanbury-Brown & Twiss has to be discussed. Though a general study is far beyond reach, we have envisioned the case of an opened dot $D = 1$ to prove that this question is in fact irrelevant considering the uncertainty of 10% on our noise measurements.

The preceding chapters have thus examined two different topics. Even though we have in this chapter 4 demonstrated the non-negligible effects of Coulomb interaction on

charge density waves as they propagate in quantum Hall edge channels, electron quantum optics is not a born-dead concept. Chapter 3 has indeed proven that the general concepts of quantum optics could still be used to explain quantitatively the interferences observed between triggered quasiparticles emitted by the source and thermal excitations. The previous simple reasoning explains the surprising coherence between these antagonistic ideas. Nevertheless, if interactions do not strongly modify the total amount of charge present in one or the other channel, it should be responsible for modifications of properties of the quasiparticles emitted by our source. The next chapter is then devoted to exploring a new experiment of two particle-interference, that could help to discover more about the aftermath of interactions.

Chapter 5

First results on the Hong-Ou-Mandel experiment

Introduction to chapter 5

The realization of the Hanbury-Brown & Twiss experiment with single electrons (as described in chapter 3) has shed light on the anti-bunching effect between thermal excitations of the Fermi sea and triggered excitations produced on demand by the SES. These two-particle interferences rely on the indistinguishability of two electrons with the same energy, combined with Fermi-Dirac statistics. However, hough very robust, the equilibrium state of the Fermi sea can not be controlled. A new step is then consequently to demonstrate the possibility of generating undistinguishable excitations using two independent and tunable on-demand sources, and study the possible antibunching effect on a beamsplitter, in the same geometry as previously. Besides, such an experiment probes the coherence of the produced wavepackets, which can be altered, in particular in the presence of interactions with neighbouring edge channels, as studied in chapter 4. The visibility of interference effect then gives indications on the importance of decoherence in such a system, and complements the study carried out in chapter 4.

In this chapter, we present the first results obtained by performing the Hong-Ou-Mandel experiment with on-demand electrons, that demonstrate partial indistinguishability of the generated wavepackets. Though our results can be understood via the theoretical tools developed earlier in the manuscript, the finite degree of indistinguishability could be a signature of decoherence mechanisms, that could be attributed to interactions between edge channels.

5.1 Principles of the experiment

5.1.1 Optical realization

5.1.1.1 Experimental realization

The historical experiment by Hong, Ou & Mandel [22] consisted in two-photon interference between twin photons emitted by parametric down-conversion on a non-linear crystal (KDP, potassium dihydrogen phosphate, in their case). When pumped with a UV laser (wavelength $\lambda_0 = \frac{2\pi c}{\omega_0} = 351.1$ nm, see Fig.5.1), a second-order non-linear order produces photon pairs with frequencies ω_1, ω_2 such that $\omega_1 + \omega_2 = \omega_0$ (energy conservation). An adequate filtering enables to select twin photons with frequencies $\omega_1 \simeq \omega_2 \simeq \omega_0/2$, that can interfere on a beamsplitter (BS). The intensity cross-correlation between both outputs is recorded, or more exactly the coincidence counts between both channels N_c.

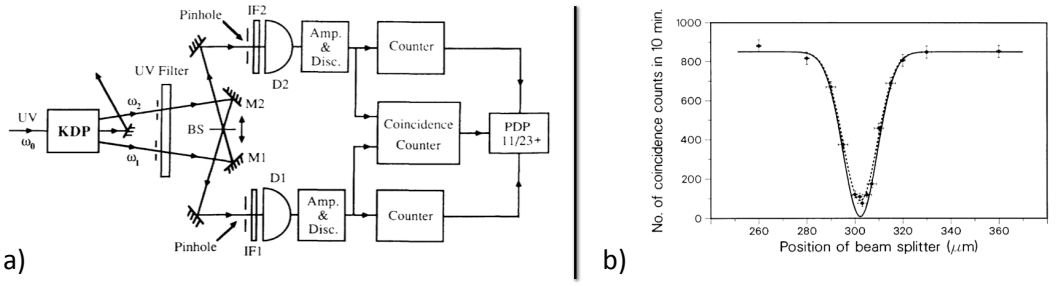

FIGURE 5.1: **Setup and results of the historical Hong-Ou-Mandel experiment** – Figures extracted from [22] a) *Outline of the experimental setup:* Twin photons are prepared by parametric down conversion of a pumped KDP crystal. Made indistinguishable by filtering (IF1 & IF2), they interfere on a beamsplitter BS and coincidence counts between both outputs of the beamsplitter. b) *Coincidence counts:* Recorded coincidence counts N_c (in a 10 minutes time window) as a function of the time delay τ between both output arms, tuned by the position of the beamsplitter. For $\tau = 0$, a dip is observed and attributed to a quasi-perfect (90%-visibility) bunching of indistinguishable twin photons.

When twin photons are sent simultaneously on the BS, they interfere due to bosonic statistics: they bunch together so that they always end up both in the same output 1 or 2. Thus, no coincidence is recorded $N_c = 0$. When a time-delay τ larger than the width of the photon wavepacket is added between both channel, the twin photons do not see each other and do not interfere, and coincidence counts can be recorded when integrating over several minutes. Consequently, the so-called Hong-Ou-Mandel dip observed for $\tau = 0$ on Fig.5.1, panel b) is attributed to a bunching effect between indistinguishable photons.

5.1.1.2 Physical meaning

This experiment is considered as an other milestone in quantum optics. As explained in chapter 1, one-particle interferences that takes place in Mach-Zehnder interferometers can be explained with a wave theory of light, whereas Hanbury-Brown & Twiss experiment that probes the discrete nature and the statistics of the excitations relies on corpuscular models. The Hong-Ou-Mandel experiment can not be explained either by wave or corpuscular models, but only by a purely quantum model. The crucial point here is the quantum indistinguishability between the photons that interfere in virtue of bosonic statistics. The Hong-Ou-Mandel dip is exactly a measure of the resemblance between the two photons that impinge on the beamsplitter: the value for $\tau = 0$ measures in fact the maximal overlap between the two photon states, whereas the width of this dip is then exactly the length of the photon wavepacket, or in an other language, the

coherence time of the source. These features will appear more clearly when examining the electronic Hong-Ou-Mandel experiment in section 5.1.3.

In their article, Hong *et al.* proposed an experiment based on twin photons emitted by pairs, but let us mention that experiments have been performed more recently using two independent sources, for example separate quantum dots [142, 143] or single photons produced by trapped ions [144, 145].

5.1.2 Electron analog

This part is greatly inspired by above work from optics [22]. Moreover electron analogs of this experiment have been investigated, in particular by Fève *et al.* [23], Olkhovskaya *et al.* [24] and more recently Jonckheere *et al.* [146]. The sample used in the implementation of the Hong-Ou-Mandel experiment in a quantum Hall device comes from the same batch as the ones used in chapters 3 and 4, and has consequently the same mobility $\mu = 2.4\,10^6\,\mathrm{cm^2V^{-1}s^{-1}}$. The device is placed in a magnetic field of $B = 2.68$ T to reach the filling factor $\nu = 3$ (due to a non-favourable behavior of the central QPC at higher magnetic fields, see 5.2.1.3). The design is presented in Fig.5.2. For clarity, only the outermost channel of $\nu = 3$ is pictured, and the DC-bias on input 2, used only for calibration has also been removed. First, the electrons to interfere are produced in two identical but totally independent single electron sources. The source labeled $i = 1, 2$ is situated in the corresponding input arm i, and its parameters are respectively gate voltage $V_{g,i}$ and transmission D_i, excitation drive $V_{exc,i}$ and level spacing Δ_i, calibrated to the value $\Delta_1 \simeq \Delta_2 \simeq 1.4 \pm 0.1$ K.

Such a sample design enables in principle to create interference between quasiparticles emitted independently by two emitters situated on each side of the beamsplitter. While photon sources are tuned mainly via their frequency spectra, the indistinguishability between quasiparticles can be tuned via the transparency of the tunnel barrier D_i, as well as the position of the level at equilibrium $\phi_{0,i}$ or the excitation amplitude $V_{exc,i}$. Here we focus on sources in the ideal regime of single-particle emission $\phi_{0,i} = 0$, and $2eV_{exc,i} = \Delta_i$.

To describe the interferences, we first use the wavepacket model and the coherence function theory, and present the main features expected in our experiments. Then, we turn to the Floquet expression of the HOM correlations, as they confirm the previsions of the wavepacket model and enables numerical simulations.

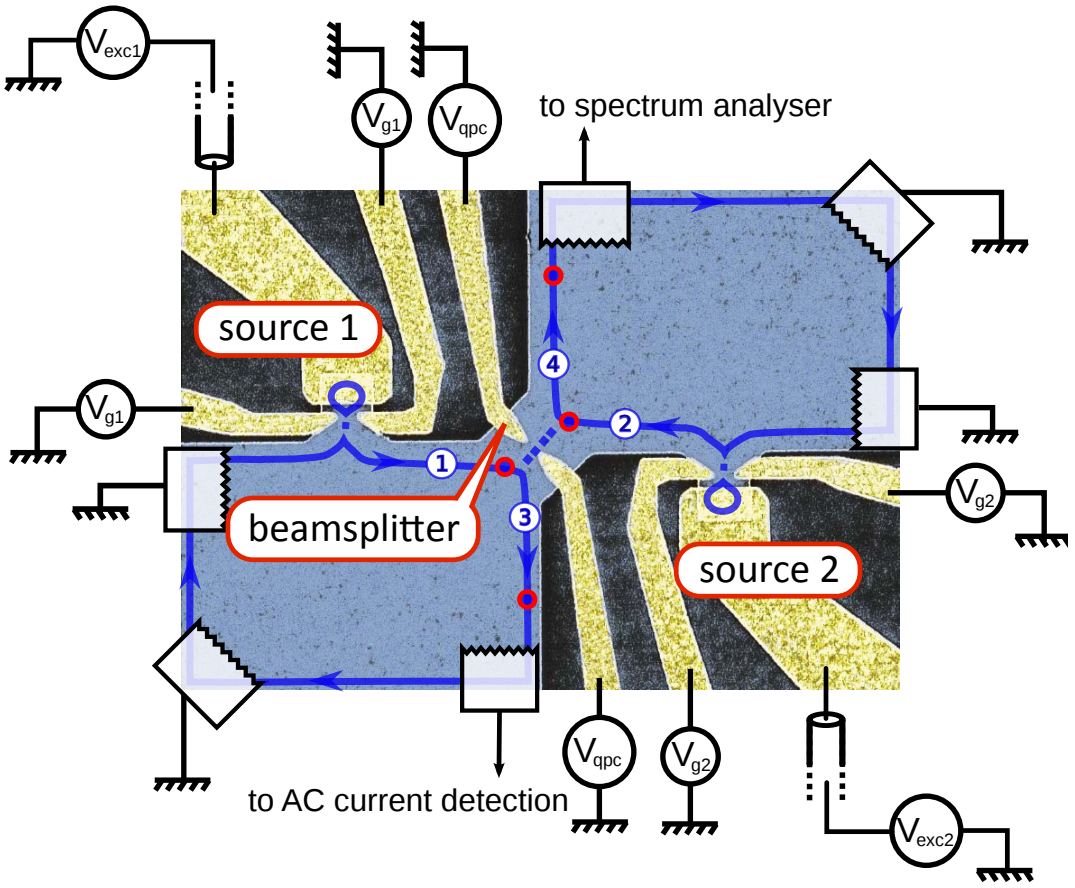

FIGURE 5.2: **SEM picture of the sample for the Hong-Ou-Mandel experiment** – The sample is placed in a magnetic field of $B = 2.68$ T to reach filling factor $\nu = 3$. For clarity, only the outermost edge channel is pictured. Two identical fully independent sources are situated one on each side (input arms 1 and 2) of the central QPC that reproduces the beamsplitter. As in chapter 3, output 3 is equipped with a radio-frequency homodyne detection for average current measurements while output 4 is connected to the noise detection scheme.

5.1.3 Theoretical developments

5.1.3.1 Coherence functions and HOM experiment

HOM correlations can be calculated quite straightforwardly from our previous theoretical developments. Indeed, this new experiment is very similar to the HBT experiment, except that the input 2 is not only connected to leads at equilibrium, but now also contains a second mesoscopic capacitor used as a single electron source. Recalling Eq.(3.27),

$$Q(t,t') = e^2\big(\mathcal{G}_1^{(e)}(t,t')\mathcal{G}_2^{(h)}(t,t') + \mathcal{G}_1^{(h)}(t,t')\mathcal{G}_2^{(e)}(t,t')\big) \tag{5.1}$$

we are in a case where $\mathcal{G}_2^{(e/h)} \neq \mathcal{G}_{\mu=0}^{(e/h)}$, i.e. $\Delta\mathcal{G}_2^{(e/h)} \neq 0$. The excess correlation can then be separated in three different terms:

$$\begin{aligned}
\Delta Q(t,t') &= e^2\big(\Delta\mathcal{G}_1^{(e)}(t,t')\mathcal{G}_{\mu=0}^{(h)}(t,t') + \Delta\mathcal{G}_1^{(h)}(t,t')\mathcal{G}_{\mu=0}^{(e)}(t,t')\big) \\
&+ e^2\big(\mathcal{G}_{\mu=0}^{(e)}(t,t')\Delta\mathcal{G}_2^{(h)}(t,t') + \mathcal{G}_{\mu=0}^{(h)}(t,t')\Delta\mathcal{G}_2^{(e)}(t,t')\big) \\
&+ e^2\big(\Delta\mathcal{G}_1^{(e)}(t,t')\Delta\mathcal{G}_2^{(h)}(t,t') + \Delta\mathcal{G}_1^{(h)}(t,t')\Delta\mathcal{G}_2^{(e)}(t,t')\big) \qquad (5.2) \\
&= \Delta Q_{HBT,1}(t,t') + \Delta Q_{HBT,2}(t,t') + \Delta Q_{HOM}(t,t') \qquad (5.3)
\end{aligned}$$

The first two lines of Eq.(5.2) are similar: they in fact encodes the HBT contributions of both sources 1 and 2, labeled $\Delta Q_{HBT,i}, i = 1, 2$ and are identical to Eq.(3.29). In the first line source 1 is correlated with the opposite input 2 acting as if it was at equilibrium at chemical potential $\mu = 0$, while label 1 and 2 are simply exchanged in the second line. This HBT correlation has been extensively studied in chapter 3, and the separate contributions of both sources are simply added up.

The third line is different and new as it contains the interference ΔQ_{HOM} between the quasiparticles emitted from both sources. In the next section, we investigate this effect in the framework of the wavepacket model.

5.1.3.2 Wavepacket model in the zero-temperature regime

Hong-Ou-Mandel correlations First, we perform a simple analysis of the HOM experiment that relies on the wavepacket picture introduced in 1.2.2.3. This model is very close to the calculations performed by Hong *et al.* [22]. As such, it captures the main features of this experiment though it only holds zero-temperature information. Emitting electronic wavepackets $\varphi_i(t)$ in each input $i = 1, 2$, and recalling $\Delta\mathcal{G}_i^{(e)}(t,t') = \varphi_i^*(t')\varphi_i(t)$, $\Delta\mathcal{G}_i^{(h)}(t,t') = -\varphi_i^*(t)\varphi_i(t')$ (Eq.(1.12)), the HOM correlation are readily expressed as:

$$\begin{aligned}
\Delta\overline{Q}_{HOM} &= -8e^2 f\,\mathrm{Re}\left[\int dtdt'\,\varphi_1(t)\varphi_2^*(t)\varphi_1^*(t')\varphi_2(t')\right] \qquad (5.4) \\
&= -8e^2 f\left|\int dt\,\varphi_1(t)\varphi_2^*(t)\right|^2 \qquad (5.5) \\
&= -8e^2 f\,|\langle\varphi_1|\varphi_2\rangle|^2 \qquad (5.6)
\end{aligned}$$

where $\langle\ldots|\ldots\rangle$ is the usual scalar product[1]. This immediately shows that the HOM correlation stems from the overlap of two wavepackets. This formula can be written as

[1] This somewhat unusual numerical factor 8 can be understood simply. One factor 2 stems from the normalization adopted for correlations, see Eq.(2.51). Then, as done in section 2.3.2.4 for phase noise, we count 2 particles per period and per source, giving in total a factor $2^3 = 8$.

well in the energy domain, using Parseval's theorem:

$$\Delta\overline{Q}_{HOM} = -8e^2 f \left| \int d\epsilon\, \varphi_1(\epsilon)\varphi_2^*(\epsilon) \right|^2 \tag{5.7}$$

The largest two-particle interference is then, as expected, obtained for a large overlap of the wavepackets. This imposes to create identical and synchronized wavepackets (i.e. arriving with a zero time-delay between them on the beamsplitter). One can then compute the total correlation $\Delta\overline{Q}$. In the wavepacket model, exactly one quasiparticle is counted in HBT correlations, as it describes perfect single charge emission in the limit of zero-temperature. We then have

$$\begin{aligned} \delta N_{HBT,i} &= \int |\varphi_i|^2 = 1 \\ \Delta\overline{Q}_{HBT,i} &= 4e^2 f \delta N_{HBT,i} = 4e^2 f \end{aligned} \tag{5.8}$$

Finally summing all contributions of Eq.(5.3) yields the excess noise $\Delta\overline{S}_{4,4}$ in contact 4:

$$\begin{aligned} \Delta\overline{S}_{4,4} &= T(1-T)\Delta\overline{Q} \\ &= 8e^2 f\, T(1-T)\big(1 - |\langle\varphi_1|\varphi_2\rangle|^2\big) \\ &= 2e^2 f \left(1 - |\langle\varphi_1|\varphi_2\rangle|^2\right) \end{aligned} \tag{5.9}$$

for an optimal transmission $T = 1/2$. Thus, this shows that the lower bound $\Delta\overline{Q} \geq 0$ can be reached for identical wavepackets. With respect to the preceding remarks, a practical way of presenting the HOM correlations is to normalize them by the sum of the HBT contributions of both sources (even at finite temperature $T_{el} \neq 0$). For this, we introduce:

$$\Delta\overline{q} = \frac{\Delta\overline{Q}}{\Delta\overline{Q}_{HBT,1} + \Delta\overline{Q}_{HBT,2}} \tag{5.10}$$

$$= 1 - \frac{\Delta\overline{Q}_{HOM}}{\Delta\overline{Q}_{HBT,1} + \Delta\overline{Q}_{HBT,2}} \tag{5.11}$$

For identical wavepackets $\varphi_1 = \varphi_2 = \varphi_e$, emitted with a tunable delay τ, one can then simply write

$$\Delta\overline{q}(\tau) = 1 - \left| \int dt\, \varphi_e(t)\varphi_e^*(t+\tau) \right|^2 \tag{5.12}$$

A clear interpretation of this formula can then be given. When $|\tau| \to \infty$, wavepackets arrive at different times on the beamsplitter, do not feel each other and are independently partitioned. Thus $\Delta\overline{Q}$ is given by the addition of both HBT partition noises: $\Delta\overline{Q} =$

$\Delta\overline{Q}_{HBT,1} + \Delta\overline{Q}_{HBT,2}$, and $\Delta\overline{q} = 1$. On the opposite, for a zero time delay ($\tau = 0$), antibunching between both particles takes place. Since both wavefunctions are identical, this antibunching is total and the noise is totally suppressed $\Delta\overline{q} = 0$. The width of this dip is then related directly to the temporal overlap between $\varphi_e(t)$ and $\varphi_e(t+\tau)$, and consequently gives information about the length of this wavefunction. This will appear more clearly when applying formula (5.12) to typical wave-packets, such as the exponential one. Such a simple model will enable to extract information from our experimental results.

Application to exponential wavepackets Time-resolved measurements (sec. 2.2.2.2) have proven the relevance of picturing the generated wavepackets as exponential waves emitted around energy $\epsilon_0 \simeq \Delta/2$. Such a packet is then written $\varphi_e(t) = \frac{\theta(t)}{\sqrt{\tau_e}} e^{-t/2\tau_e} e^{-i\epsilon_0 t/\hbar}$, where θ is the Heaviside function, while τ_e is as usual the escape time. With these analytical expressions, it is straightforward to show that:

$$\Delta\overline{q}(\tau) \quad = \quad 1 - e^{-|\tau|/\tau_e} \tag{5.13}$$

Thus, it clearly reveals how the measurement of the HOM correlations gives access to the temporal width of the emitted wavepackets.

In this section, we have shown how an electronic analog of the Hong-Ou-Mandel experiment could be implemented with two independent sources, leading to similar interference effects that only occur when two indistinguishable particles are colliding at the same time on the beamsplitter. This requires to manipulate accurately the wavepackets, and in particular to achieve an accurate synchronization of both sources. The correlation detection is on the other hand very similar to the one used in the HBT experiment presented in chapter 3. The next part is devoted to giving details about a few modifications done to improve the setup, and to showing how both sources can be synchronized.

5.2 Experimental realization

5.2.1 Improvements in the noise detection scheme

5.2.1.1 Amplification

In order to be able to measure a little bit more rapidly and accurately the HOM correlations, the noise detection setup presented in section 3.2.2 has been slightly improved. These modifications are briefly reviewed in this section.

The main change consists in replacing the first stage of amplification, initially made of *NF LI75A*. Better performances were obtained by using ultra-low noise amplifiers from Celians and developed in the CNRS center for research on low temperatures of Grenoble (*Celians EPC1-B*). The bandwidth is reduced to DC-130 kHz (for gain $\times 100$) but this is not an issue since our bandwidth is limited to 70 kHz due to the distributed capacitance of coaxial cables. In the meantime, both current and voltage noises are in principle diminished to respectively $4\,\mathrm{fA}/\sqrt{\mathrm{Hz}}$ at 1 Hz, and $0.7\,\mathrm{nV}/\sqrt{\mathrm{Hz}}$. This should in principle offer a strong enhancement of measurement capabilities: the same resolution of $0.05\,e^2 f$ in the Hanbury-Brown & Twiss experiment, obtained after 10 hours of measurements should be in principle accessed in $600/2^4 \simeq 40$ minutes. The measured specifications were slightly above nominal. But these efforts were in fact partially compensated by the fact that the QPC was not satisfying at $\nu = 2$, so that we had to work at a filling factor of $\nu = 3$. Thus, the impedance for the current to voltage conversion was modified from $R_K/2$ to $R_K/3$ and the measurement time (for a given signal-to-noise ratio) was lengthened by a factor $(\frac{R_K/2}{R_K/3})^3 = \frac{27}{9} \simeq 3$.

In the meantime, the strategy of measurement due to the 1K pot issues has been changed. We have not been able to stabilize the 1K pot on very long times (days) to perform our measurements. Consequently, we adopted a more radical method: the 1K pot needle valve as well as the pumping line were completely shut, assuring stability on time lapses on about 100 minutes. This strategy forced us to work on extended hours but the bandwidth was also enlarged downwards to 15 kHz (for a power integrated in the band $15 - 93.125$ kHz). In the end, with all the discussed modifications, the measurement time is about 4-5 hours per point for a signal to noise ratio of approximately $SNR \simeq 8$ as previously.

5.2.1.2 Performances of the modified setup

These modifications of the detection have undoubtedly improved the performances of the noise detection scheme, while the way it is operated and calibrated has remained identical. The calibrations proposed in 3.2.3 have given the following results. First, as mentioned earlier, the electronic temperature is reduced and calibrated at $T_{el} = 90 \pm 10$ mK. Second, in the condition of the experiment ($\nu = 3$), the gain of the detection scheme yields a resolution of $0.05\,e^2 f =$ in about 3 hours, for a driving frequency of $f = 2.1$ GHz.

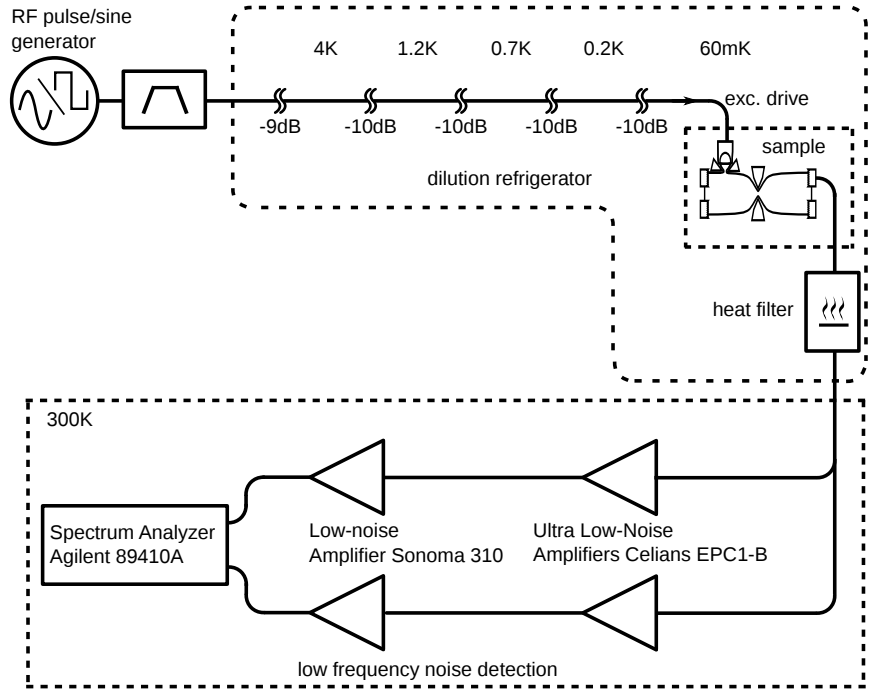

FIGURE 5.3: **Modified noise detection setup used for the Hong-Ou-Mandel experiment** – As compared with the setup of Fig.3.11 used in chapter3, the first stage of amplification is changed (*Celians EPC1-B*) and a heat filter is added, that reduces the electronic temperature from $T_{el} = 150$ mK to 90 mK. The sample is also placed at a filling factor $\nu = 3$, reducing the impedance on which the current fluctuations are read.

5.2.1.3 Working at $\nu = 3$

As mentioned earlier, the central QPC in this experiment was strongly non-linear even for the outer channel at $\nu = 2$. Test measurements of correlations have given very poor results, with signals sometimes 10 times bigger than expected. Finally we resolved to work at $\nu = 3$, where a proper behavior was observed, despite the loss of sensitivity of the correlations measurement setup. Results obtained for the differential conductance (see section 3.2.1.3) on the outer channel are presented in Fig.5.4. A typical non favourable situation, obtained for $\nu = 2$, is shown on the left panel (a), whereas the adopted configuration is described in the right panel (b).

5.2.1.4 Reduction of the electronic temperature

A simple modification of the coaxial lines has enabled to significantly decrease the electronic temperature from $T_{el} = 150$ mK to 90 mK. We found that the residual electronic temperature was in the end limited by the heat transport from outside to inside the cryostat via RF output lines. Indeed, so as to keep the small signals unattenuated, the

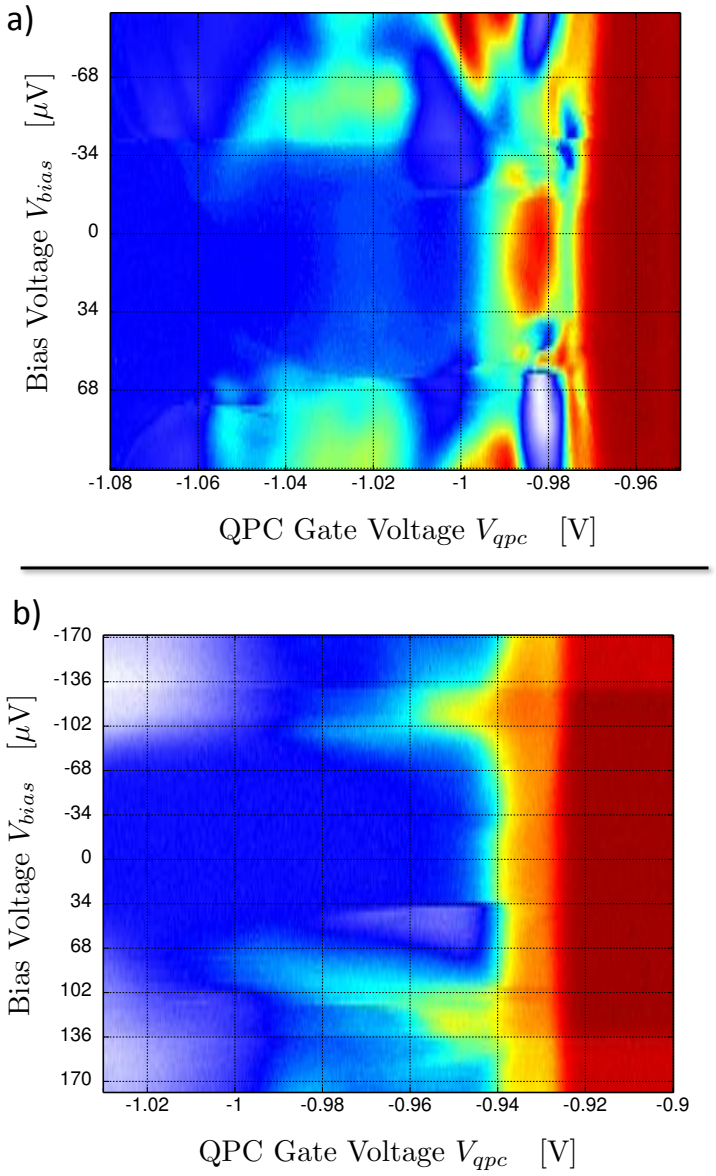

FIGURE 5.4: **Differential conductances for the central QPC of the HOM experiment** – a) 2D plot obtained for $B = 4$ T, $\nu = 2$ exhibit strong non-linear behaviour, that makes the HOM correlation measurements impossible. b) Differential conductance at the magnetic field $B = 2.68$ T, corresponding to $\nu = 3$ and finally adopted in this study.

output line on contact 4 has no attenuator. The anchoring to cold masses thermalizes the grounded shield but not the inner core, that is only coupled via the poorly thermally conducting dielectric.

The idea was to keep the double compatibility with low-frequency (as in chapter 3 and 5) and RF (as in chapter 4) measurements of the output line connected to contact 4 (see Fig.5.2), but to reduce in the meantime the thermal conductivity of the inner core. The adopted trade-off was to design a 50 Ω-matched coplanar waveguide, with a CMS

30 Ω-resistor on the inner part. The waveguide is embedded in a small box of brass to keep a coaxial geometry. Thus, the resistance of the inner core of the coaxial line is augmented from less than 1 Ω to about 30 Ω, and in the meantime the heat conductance is reduced by the same factor. The low and high frequency properties are only slightly diminished.

5.2.2 Synchronization and calibration of the time-delay

5.2.2.1 Generation and synchronization of excitation signals

The excitation are generated and synchronized in a very simple manner using the *Anritsu MT1810A* pulse generator. Two pairs of independent outputs are available, and the phase shift between these pairs can be adjusted. The amplitude of these four channels can be tuned separately. Thus, we devoted one pair to the production of the reference channel for the homodyne detection and the excitation line for source 1, and an output of the other pair for the excitation of source 2. In this configuration, the relative phase-shift between source 1 and 2 can be adjusted on a full 360° span. The synchronization is here supplied on the two pairs by the same GHz clock, and no synchronization issue has been encountered.

5.2.2.2 Calibration of the time-delay between sources

The synchronization of excitation drives is necessary but not sufficient to ensure that both sources are emitting electrons impinging on the beamsplitter at the same time. Indeed the excitation lines are not identical so that a constant time-delay remains even if drives are produced with a zero degree relative phase shift. We can however use RF measurements of the average current to achieve a synchronization with an accuracy of about ±5° of two incoming wavepackets corresponding to an uncertainty ±7 ps on the arrival times for $f = 2.1$ GHz.

Calibration protocol The idea is to superimpose the variation of the RF signal obtained when driving source 1 or 2 and progressively opening the QPC. As explained in section 4.2.2.1, when driving source $k = 1, 2$ and changing the transmission T of the outermost edge channel of the central QPC, the current collected $I_c^{(k)}$ in output 3 (RF homodyne detection) can be written in the following form:

$$I_c^{(1)}(T) = I_p^{(1)} + I_r^{(1)} + (1-T)I_o^{(1)} \quad (5.14)$$

$$I_c^{(2)}(T) = I_p^{(2)} + TI_o^{(2)} \quad (5.15)$$

where $I_p^{(k)}$ is a parasitic current coming from stray couplings, $I_o^{(k)}$ is the current flowing in the outer edge state, which is of interest here. $I_r^{(1)}$ is an extra contribution reflecting the current flowing in the two inner edge channels, and resulting from the interactions between channels. It only appears when exciting source 1 as the two inner channels coupled to source 2 are reflected toward output 4. If we subtract the adequate background, we get:

$$\delta I_c^{(1)}(T) = I_c^{(1)}(T) - I_c^{(1)}(T=1) = (1-T)I_o^{(1)} \quad (5.16)$$

$$\delta I_c^{(2)}(T) = I_c^{(2)}(T) - I_c^{(2)}(T=0) = TI_o^{(2)} \quad (5.17)$$

As both signals are detected in the same contact via the same detection scheme, the complex currents $I_o^{(1)}$ and $I_o^{(2)}$ should have exactly the same phase if the excitations impinge on the beamsplitter with a zero time delay. The graphs $\delta I_c^{(k)}(T)$ should consequently superimpose for synchronized sources: this can be achieved by tuning the relative phase between both excitation signals, as seen in the following paragraph.

Results of the calibration This protocol has given very satisfying results, enabling to synchronize both sources within a ± 7 ps time resolution. On Fig.5.5, we show on a polar plot the complex numbers $\delta I_c^{(1)}(T)$ when T is varied, for different choices of the relative phase between excitations ϕ (colored lines). Source 2 (black bold line) is taken as a reference: the average argument of $\delta I_c^{(2)}(T)$ is set to 0. We see that for the value $\phi = -138.6$, the red line is aligned with the reference black line: in this configuration, a time-delay $\tau = 0$ is expected between the excitations generated by both sources when they reach the beamsplitter.

The accuracy of this calibration is not limited by the choice of ϕ (tunable by increment of $0.18°$), but rather by the overall phase stability of the RF setup: minor modifications of the positions of the coaxial cables, temperature fluctuations (related to the Helium level in the cryostat) are possible reasons for observed fluctuations over a few degrees. Consequently, we assumed error bars of circa $\pm 5°$ (± 7 ps) in the measurements. For the same reasons, this calibration has been repeated every day, confirming fluctuations of a few degrees from one day to the next.

On Fig.5.5, one also see that the bold solid line and red solid line have different length, reflecting a difference in the measured current though both sources are set to emit optimally one electron. This may be a signature of decoherence effects due to interactions with edge channels that are reinforced at $\nu = 3$. To compensate the difference of currents, the excitation voltages have been slightly augmented on source 2 and decreased on source 1 in order to reach a discrepancy of less than 20%. However, so as to manipulate quasi

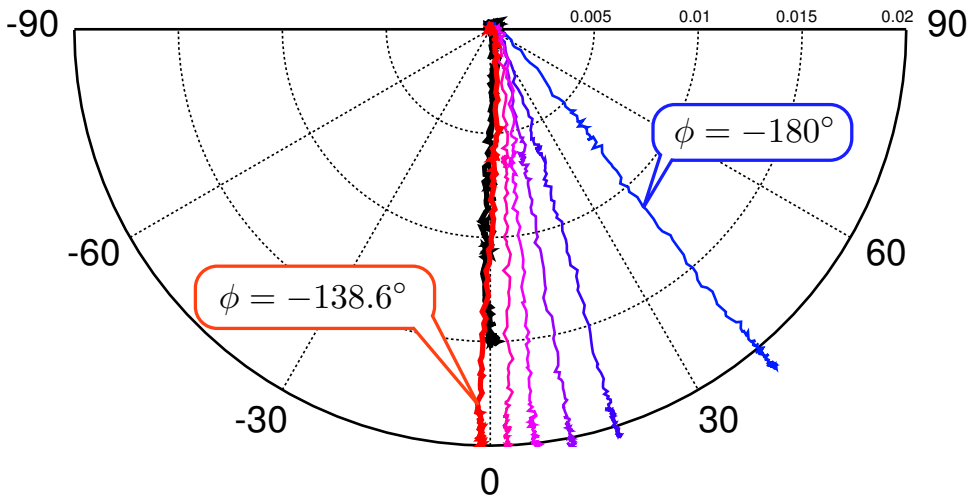

FIGURE 5.5: **Synchronization of sources** – The variation of the collected current in the outer edge channels $\delta I_c^{(k)}(T)$ when varying transmission T and driving source $k = 1, 2$ are presented in a polar plot. $\delta I_c^{(2)}(T)$ is taken as a phase reference (black bold line). $\delta I_c^{(1)}(T)$ (colored lines) is plotted for different values of the relative phase ϕ between excitation of both sources: from blue to red, $\phi = -180; -156.6; -149.4; -144, -141.3; -138.6°$. For the latter, $\delta I_c^{(1)}$ and $\delta I_c^{(2)}$ are aligned, and the synchronization of the quasiparticles emitted by both sources is achieved. The accuracy of the protocol is evaluated to $\pm 5°$.

mono-electronic packets, we paid attention to set the working points on quantization plateaus, with $\phi_{0,i}$, so that the charges in each wavepacket is only slightly modified.

After a few improvements, and an adequate synchronization of both sources, the setup is now ready to perform first measurements of the electronic analog of the Hong-Ou-Mandel experiment. Though they are not detailed in the present manuscript, calibrations and tests of the noise detection scheme have been performed, in a manner similar to what was detailed in section 3.2.3. We now turn to the results obtained in the next section.

5.3 Results and analysis

5.3.1 Experimental results and first analysis

Hong-Ou-Mandel dips and normalization In this first series of experiments, we focus on the most natural case of quasi-ideal single charge emission, where $2eV_{exc\,i} = \Delta_i$ and $\phi_{0,\,i} = 0$, with the additional condition $D_1 = D_2$. Two different configurations are measured: $D_1 = D_2 = 1$ and $D_1 = D_2 \simeq 0.4$, for the full span $\tau \in [-\frac{T}{2}, \frac{T}{2}]$. After

the calibration of the time-delay, we thus expect a maximum two-particle interference around $\tau = 0$.

Experimental data for the HOM correlations are presented in Fig.5.6: in panel a), $D_1 = D_2 = 1$, whereas in panel b) $D_1 = D_2 \simeq 0.4$. The first comment that is to be done is that a dip in the HOM correlations is actually detected in both cases around the expected point of zero-time delay $\tau = 0$, while a plateau appears when $|\tau| \to \frac{T}{2}$.

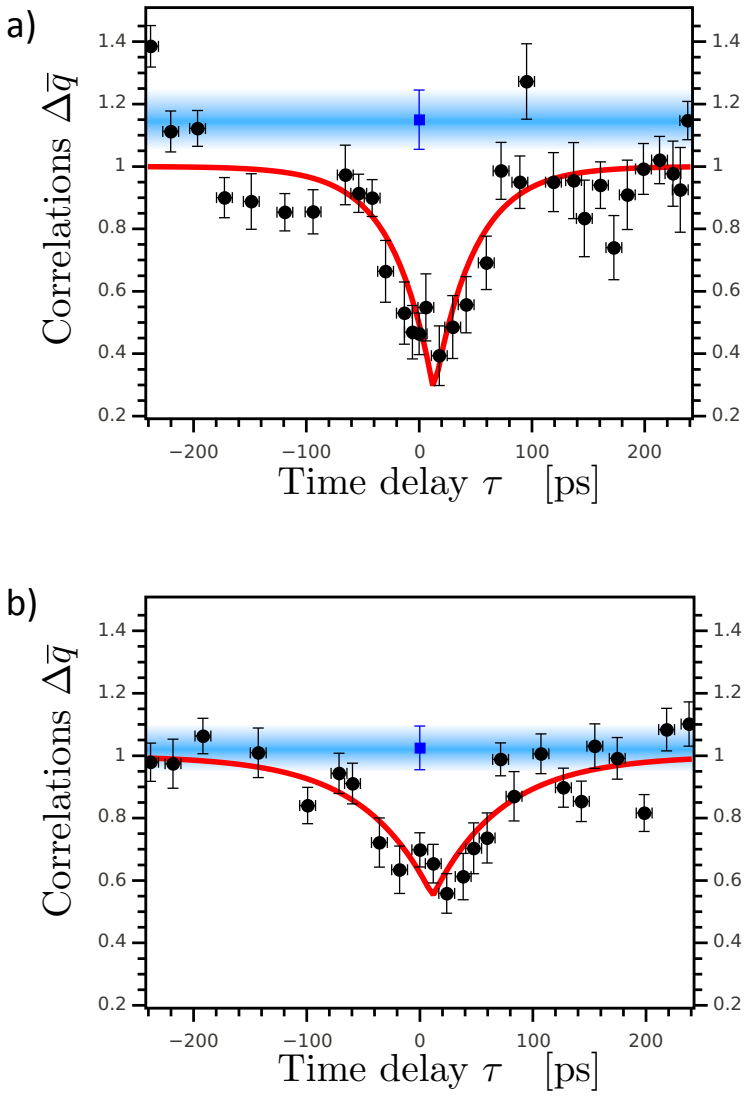

FIGURE 5.6: **Hong-Ou-Mandel correlations in two configurations** – HOM correlations as a function of time delay between sources τ, in two different configurations: a) opened dot $D_1 = D_2 = 1$; b) reduced transmission $D_1 = D_2 \simeq 0.4$. In both cases, the HOM dip is observed for $\tau \simeq 0$. Exponential (red line) fits are used to extract the width τ_e and amplitude of the peak γ. The sum of the HBT contribution of each source is pictured by the blue point at ($\tau = 0$) and with blur giving the standard deviation. The agreement is very good in the lower panel, and falls at less than two times (error $\lesssim 15\%$) of the standard deviation in the upper graph.

In these measurements, the normalization was obtained by dividing the experimental data points by the value of the measured noise on the plateau. This value should be consistent with the summed HBT contributions of both sources. It has been measured, by simply turning off alternatively one of the two sources, and the results are presented in blue on Fig.5.6, with a blur symbolizing the error bar on this measurement. The agreement is very good for the lower panel ($D_1 = D_2 = 0.4$), with the HBT contributions exactly aligned with the plateau of the HOM correlation. For the upper panel, the agreement is not as good ($\lesssim 15\%$), but not unrealistic due to relatively large error bars.

Wavepacket model A first analysis, based on the wavepacket model, can be proposed. Since the excitation is provided by the square wave generator, the emitted wavepackets are supposedly exponential. Besides, they should also be identical: as they contain one electron or hole, and the escape time τ_e is approximately the same ($D_1 = D_2$), so that both the amplitude and decay time of the exponential wave-packet are similar. Under these hypotheses, we have shown that $\Delta\overline{q}(\tau)$ is in theory of the form:

$$\Delta\overline{q}(\tau) \quad = \quad 1 - e^{-|\tau|/\tau_e} \tag{5.18}$$

Taking into account some reduced visibility γ, and a small discrepancy τ_0 in the evaluation of zero-time delay, a fit is realized using the function:

$$\Delta\overline{q}(\tau) = 1 - \gamma e^{-|\tau-\tau_0|/\tau_e} \tag{5.19}$$

It gives access to both the visibility γ and an estimation of the width of the wavepacket τ_e. We obtain the fits pictured by red solid lines in Fig.5.6, with fitting parameters summarized in the following table 5.1.

a) $D_1 = D_2 = 1$	b) $D_1 = D_2 = 0.4$
$\gamma = 0.72 \pm 0.05$	$\gamma = 0.45 \pm 0.05$
$\tau_e = 36 \pm 6$ ps	$\tau_e = 62 \pm 15$ ps
$\tau_0 = 13 \pm 4$ ps	$\tau_0 = 11 \pm 6$ ps

TABLE 5.1: **Summary of fitting parameters** – Fitting by the exponential function of Eq.(5.19), we evaluate the visibility γ, the wavepacket width τ_e and the residual discrepancy τ_0 on the evaluation of time delay. For $D_1 = D_2 = 1$, we observe a rather good visibility $\gamma = 0.72$ for a short wavepacket of $\tau_e = 36$ ps, while for $D_1 = D_2 = 0.4$, visibility is reduced to $\gamma = 0.45$ for a longer wavepacket of $\tau_e = 62$ ps.

5.3.1.1 Conclusions of this analysis

Several conclusions can be drawn from the preceding remarks.

First of all, the quality of our synchronization protocol is assessed by the values of $\tau_0 \simeq 11 \pm 4$ ps that are relatively small, and in agreement with the expected precision of our calibration. However, both values are similar, and could be the result of a slight deviation, not understood, rather than an inaccuracy in the calibration.

Then, even though the SNR of our measurements is limited, the so-called Hong-Ou-Mandel dips are clearly observed in both cases. The visibilities of respectively $\gamma = 0.72 \pm 0.05$ and $\gamma = 0.45 \pm 0.05$ are correct, but not excellent. Several factors, listed below, could be taken into account. Some of them can be easily ruled out, others will be examined later (section 5.3.2):

- *Phase noise of the generator:* the RF excitation can be a first source of loss of visibility. Indeed, some residual jitter can exist on the RF generator's clock, so that the amount of time between two wavepackets is not exactly $T/2$ and quasiparticles are emitted by both sources with a small fluctuating time-delay. Using a fast digital oscilloscope, we have measured the jitter, which is on the order of $1 - 2$ ps. This effect can be modeled as averaging the HOM signal on a 2 ps time-window: it causes a loss of 2% in the visibility, which is consequently not sufficient to explain our data.

- *Fluctuations and drifts on gate voltages $V_{g,i}$:* As V_g is coupled electrostatically to the position of the levels $\phi_{0,i}$, a jitter or a drift on the gate voltages $V_{g,i}$ could lead to averaging over different values of $\phi_{0,i}$, that is supposedly set to $\phi_{0,i} = 0$. This aspect is reviewed in section 5.3.2 using Floquet simulations.

- *Partial indistinguishability of sources:* Even though calibrations have shown that level spacings $\Delta_1 \simeq \Delta_2 \simeq 1.4$ K and transmission $D_1 \simeq D_2$, small discrepancies (below 10%) can still be present. The overlap of the generated wavepackets could then be reduced. Floquet simulations (section 5.3.2) enable to probe these effects.

- *Decoherence due to interactions:* As seen in Chapter 4, co-propagating edge channels are coupled via Coulomb interaction, leading to decoherence of electronic wavepackets as propagation takes place between the source and the QPC. We briefly examine the relevance of decoherence in section 5.3.2.4

Finally, we observe a variation of τ_e when $D_1 = D_2$ is varied. In the first case ($D_1 = D_2 = 1$), $\tau_e = 36 \pm 6$ ps while in the second ($D_1 = D_2 = 0.4$), we find $\tau_e = 62 \pm 15$ ps. This variation is in qualitative agreement with the fact that decreasing the transmission of the dots increases the escape time. Knowing $\Delta_1 = \Delta_2 \simeq 1.4$ K, predictions of $\tau_e = \frac{h}{\Delta_i}(\frac{1}{D_i} - \frac{1}{2})$ can be realized and yield $\tau_1 = \tau_2 = 17$ ps and $\tau_1 = \tau_2 = 69$ ps respectively. The prediction differs quite drastically in the case of the opened $D_1 = D_2 = 1$. This

discrepancy can be explained by the non-ideal character of the excitation square voltage. Indeed, we have already gathered strong evidences that the square signal only contains in fact roughly a limited number of harmonics. Concerning the HOM experiment , the major consequence is the limited rise time τ_r of the drive signal that in the end limits the temporal width of the wavepacket to $\tau_e \gtrsim \tau_r$. τ_r can be evaluated from the specifications of the source, $\tau_r \simeq 30$ ps, and has been verified on a fast digital oscilloscope, thus giving a reasonable explanation to the discrepancy between prediction and measure of τ_e.

This general analysis has yielded interesting results that enable to interpret the Hong-Ou-Mandel experiment. We then complete our analysis with the help of Floquet scattering theory that will in the end unveil interesting interference effect between hole and electrons that have no optical counterpart.

5.3.2 Floquet scattering model and finite-temperature regime

Contrary to the HBT experiment, most features of HOM correlations can be simply understood in the wavepacket model. Nevertheless, the effect of temperature T_{el} can not be easily taken into account in this picture and it is known to affect strongly HBT correlations. As a consequence, in this section, we first model our experiment as accurately as possible with the help of Floquet scattering theory. In particular we explore parameters such as the aforementioned electronic temperature T_{el} but also the number of harmonics in the drives $V_{exc,i}$, or slight discrepancies between D_1, D_2 or Δ_1, Δ_2.

5.3.2.1 Hong-Ou-Mandel correlations in the Floquet formalism

We have seen in Eq.(5.2) how Hong-Ou-Mandel correlations could be expressed in terms of the coherence functions, whose translation in Floquet formalism has been obtained in chapter 2, in Eq.(2.23). If we introduce a Floquet matrix V_m for source 2, the combination of these equations finally yields:

$$\begin{aligned}\Delta\overline{Q} &= \frac{2e^2}{h}\sum_p \int d\epsilon \left(f_\mu(\epsilon) - f_\mu(\epsilon - \frac{p}{2}\hbar\Omega)\right) \\ &\times \left(\Big|\sum_m U_m^*(\epsilon + \frac{m}{2}\hbar\Omega)V_{p-m}(\epsilon + \frac{m}{2}\hbar\Omega)\Big|^2\right. \\ &+ \left.\Big|\sum_m V_m^*(\epsilon + \frac{m}{2}\hbar\Omega)U_{p-m}(\epsilon + \frac{m}{2}\hbar\Omega)\Big|\right)^2 \end{aligned} \tag{5.20}$$

Though Eq.(5.20) emphasizes the symmetry between roles of sources 1 and 2, the structure of Eq.(5.3) is not easily distinguished as the HBT contribution do not appear clearly.

However, if one takes $V_m(\epsilon) = \delta_{m,0}$ as if source 2 was a lead at equilibrium, one recovers the HBT expression of Eq.(3.38).

This expression predicts perfect antibunching for identical emission condition. Indeed, if $\forall m, U_m = V_m$, Eq.(5.20) identifies with autocorrelations of the source $\Delta\overline{S}(\omega = 0)$ (Eq.(2.67)) that is known to be zero, so that $\Delta\overline{q} = 0$. It is difficult however to derive the analytical form of $\Delta\overline{q}(\tau)$ when the delay τ is varied. For identical desynchronized sources, it is possible to show that $V_m(\epsilon) = U_m(\epsilon)e^{-im\Omega\tau}$ so that one can understand that all terms appearing in summations in Eq.(5.20) progressively get out of phase when τ increases. We have been able to simulate the expected correlations $\Delta\overline{q}$ and to compare them with our results.

5.3.2.2 Modeling of the experiment in the Floquet scattering theory

As in the HBT experiment, average current measurement have enabled to calibrate the electronic temperature $T_{el} = 90 \pm 10$ mK, the level spacings $\Delta_1 \simeq \Delta_2 \simeq 1.4$ K, as well as transmissions evaluated at $D_1 = D_2 = 1$ and $D_1 = D_2 \simeq 0.4$. Comparison between simulations and results are presented in figure 5.7, and discussed below. As discussed above, Floquet scattering theory predicts perfect anti-bunching which is not observed in our experiment. To take into account a reduced visibility, we applied a correcting factor γ on the HOM two-particle interferences. The plotted quantity is then:

$$\Delta\overline{q}(\tau) \quad = \quad 1 - \gamma(1 - \Delta\overline{q}_{Fl}(\tau)) \tag{5.21}$$

where $\Delta\overline{q}_{Fl}(\tau)$ is the results from Floquet theory simulations, and γ is chosen in agreement with above exponential fits. Please note that γ is the only free parameter, as all the others have been obtained during calibration stage. We applied $\gamma = 0.7$ in the first graph (opened dot $D_1 = D_2 = 1$) and $\gamma = 0.5$ for the second ($D_1 = D_2 \simeq 0.4$). Moreover, the square wave is reproduced with a finite number of harmonics: either two odd harmonics (red curves) or three (blue curves).

The results are quite convincing and a good agreement is obtained for a choice of 2 or 3 harmonics. In the upper panel, simulations with two harmonics give better results. In the lower panel, three harmonics yield surprisingly longer wavepackets that are in better agreement with our observations. As already mentioned, with a driving frequency of $f = 2.1$ GHz, this corresponds to a bandwidth of at least 6.3 GHz.

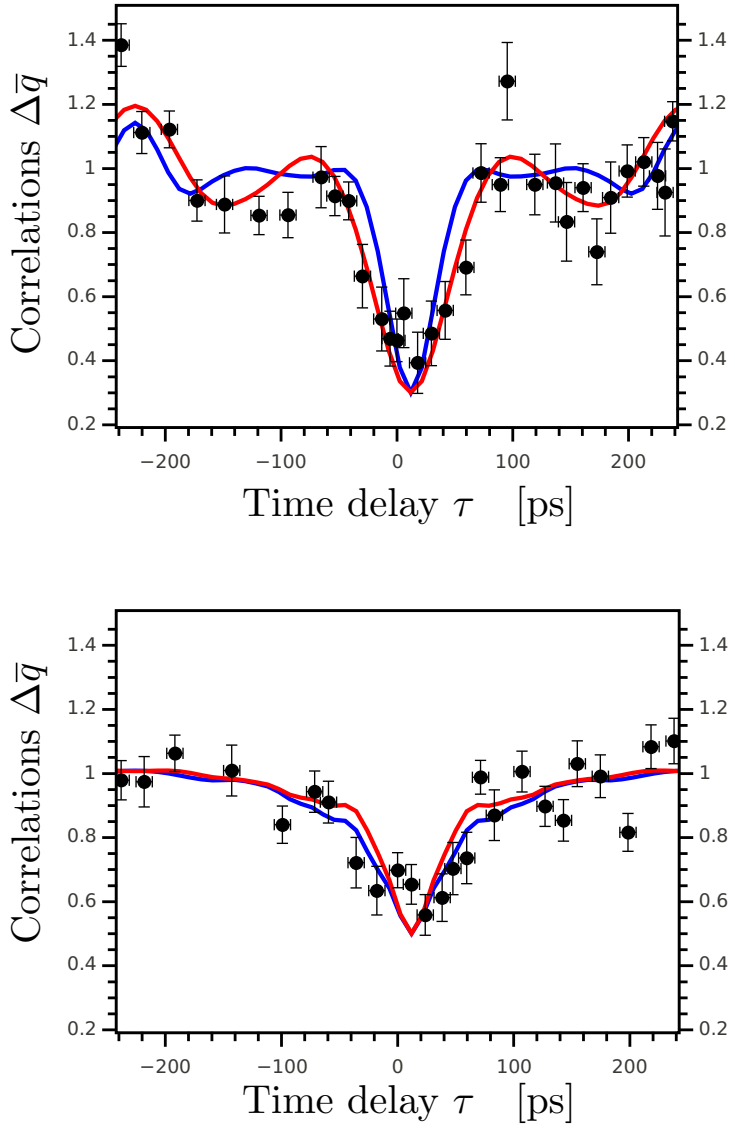

FIGURE 5.7: **Comparison between experimental results and simulations of Floquet scattering matrix formalism** – Experimental data (black dots) are compared to simulations from Floquet scattering theory, with a square drive containing two (red curves) or three (blue curves) odd harmonics. A correcting factor γ in agreement with the gaussian and exponential fits is applied to take into account a reduced visibility in the HOM dip. The upper panel ($D_1 = D_2 = 1$) shows a good agreement with a two-harmonic signal, while in the lower panel ($D_1 = D_2 = 0.4$), better concordance is found for 3 harmonics.

5.3.2.3 Visibilities from Floquet simulations

The parameters characterizing each source can be independently chosen enabling to probe the effects of deviations on transmissions D_i, level spacings Δ_i and phases $\phi_{0,i}$.

Numerical tests have revealed that D_i, Δ_i and excitation drives $V_{exc,i}$ have relatively low impacts on the visibility. For deviations of 10% of these three parameters, loss of

visibilities are on the order of 15%, and on the order of 5% when only one parameter exhibits a mismatch. This is in fact expected: the precise shape of wavepackets are indeed modified, but the global properties (average energy of emission $\pm\Delta_i/2$, energy width $D_i\Delta_i$) are only slightly modified so that the overlap is not considerably altered, visibilities remain close to unity, $\gamma \simeq 1$.

The situation is a bit different when tuning the positions of the levels in the dot $\phi_{0,i}$. Keeping levels in $\phi_{0,1} = 0$ in source 1, we have investigated the visibilities when $\phi_{0,2}$ is changed. At $D_1 = D_2 = 1$, visibility remains perfect, as the density of states in the dot is constant (since the dot is fully opened) so that Floquet simulations are necessarily $\phi_{0,i}$-independent in that case. On the contrary, for $D_1 = D_2 = 0.4$, reduction toward $\gamma \simeq 0.65$ are predicted for relatively low values of $\phi_{0,2} = \pi/8$. The fluctuations of the voltage sources (*Yokogawa 7651*) that deliver $V_{g,i}$ are too low to explain such large values of $\phi_{0,2}$. However drifts or jumps in gate voltages have sometimes be observed, which could lead to observing such a loss in contrast. Though the value of $\phi_{0,i}$ is regularly verified and adjusted if necessary, this argument could explain the reduced visibility of the curve at $D_1 = D_2 = 0.4$, with respect to $D_1 = D_2 = 1$ where the change of $\phi_{0,i}$ is irrelevant.

Finally, this study may give a reasonable answer to the difference in visibilities between both HOM dips, but does not explain the overall limited contrast of these graphs. Though some relevant ingredients might be missing, it could also be a first sign of decoherence of the electronic wavepackets attributed to interactions between the different edge channels, that we briefly analyze in the next paragraph.

5.3.2.4 Decoherence effects

Though a detailed study of decoherence is out of reach, it is possible to present a very simple model that enables to extract a characteristic time over which decoherence takes place. Following Degiovanni *et al.* [47], we suppose that, due to decoherence mechanisms that we do not describe in detail, the coherence functions $\Delta\mathcal{G}^{(e/h)}$ and HOM correlations $\Delta\overline{Q}_{HOM}$ are modified in the following manner:

$$\Delta\mathcal{G}^{(e/h)}(t,t') \longrightarrow \Delta\mathcal{G}^{(e/h)}(t,t')\mathcal{D}(t-t') \tag{5.22}$$

$$\Delta\overline{Q}_{HOM} = -8e^2 f \,\mathrm{Re}\left[\int dtdt'\, \varphi_1(t)\varphi_2^*(t)\varphi_1^*(t')\varphi_2(t')\mathcal{D}^2(t-t')\right] \tag{5.23}$$

where $\mathcal{D}(t-t')$ is a decoherence factor that varies over a typical scale τ_c being the coherence time. When $\tau_c \gg \tau_e$, $\mathcal{D}(t-t') \simeq 1$ so that decoherence effects are negligible. On the contrary, when $\tau_c \ll \tau_e$, $\mathcal{D}(t-t') \simeq \tau_c\,\delta(t-t')$: coherences in $\Delta\mathcal{G}^{(e/h)}(t,t')$ are

suppressed and only the stationary part $t = t'$ subsists. Then, the electronic state is completely determined by the occupation numbers.

In this limit, it is possible to show that for identical wavepackets $\varphi_1 = \varphi_2$, decoherence is responsible for a loss of visibility, with to first order $\gamma \simeq \tau_c/2\tau_e$. From our measurement, we can then extract a typical coherence time of $\tau_c \simeq 50 - 60$ ps. Further measurements with enhanced resolution are required to understand accurately the deep origin of loss of contrast. However, this simple model emphasizes the necessity to produce short wavepackets (on the order of a few tens of picoseconds) to be able to observe Hong-Ou-Mandel interferences.

In the next section, we analyze a peculiar feature of the electronic Hong-Ou-Mandel experiment, that relies on the existence of two types of carriers and that has consequently no counterpart in conventional quantum optics.

5.3.3 Electron-hole HOM interferometry

So far, our analysis has demonstrated a deep analogy with its optics analog. Due to their respective statistics, bosons and fermions differ on the sign of the HBT correlations (positive cross-correlations for bosons, negative for fermions, see 3.1.3.1). When two particles collide on a beamsplitter, the HOM effect tends to reduce the absolute value of the cross-correlations so that a dip is observed in both situations, and graphs of Fig.5.1 b) and Fig.5.7 look very similar.

Nevertheless, we have seen the physics of electronic devices was enriched by the presence of both interactions and two types of charge carriers (electron/hole). In this HOM experiment, this rises the question of the interest of electron/hole collisions. Though our data are not fully conclusive due to limited accuracy, we discuss this new way of investigation that has no photonic counterpart. At first sight, such an experiment can not work: in Eq.(5.7) electron and hole wavepackets do not overlap so that no HOM effect is expected. However, Floquet scattering theory exhibits in Fig.5.7 (upper panel) unexpected features for $\tau = \pm T/2$ when the electronic excitations are synchronized with holes: $\Delta\overline{q} > 1$ in strong contradiction with previsions from the wavepacket model.

As a matter of fact, this behavior originates from finite temperature effects, that were not discussed in previous sections. In Eq.(5.7), the electronic wavepacket have non-zero components only for positive energies ($\epsilon > 0$) since there are in fact no unoccupied levels below the Fermi level ($\epsilon_F = 0$) when $T_{el} = 0$. On the contrary, at finite temperature, the electron wavepacket can actually spread below the Fermi level as there are, at a

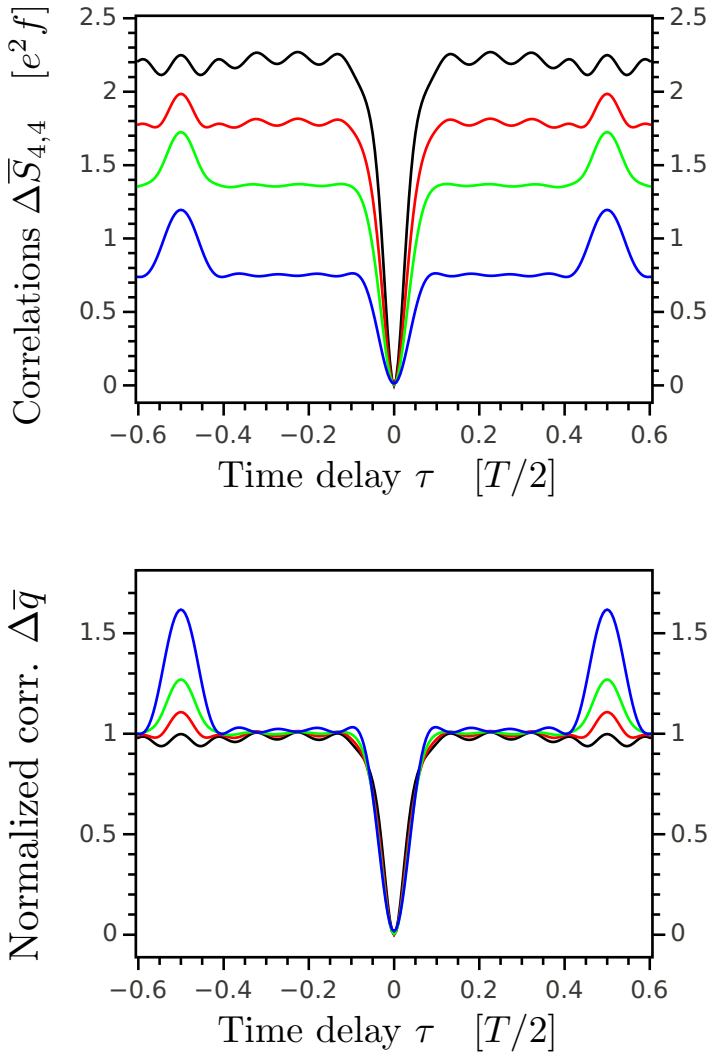

FIGURE 5.8: **Electron/hole interferometry**– As electronic temperature is increased, partial interference between electrons and hole appear when synchronizing an electron from source 1 with a hole from source 2, i.e. for a delay $\tau \simeq \pm T/2$. Temperatures are respectively $T_{el} = 0$ K (black curves), $T_{el} = 90$ mK (red), $T_{el} = 200$ mK (green), $T_{el} = 500$ mK (blue). *Upper panel:* Non-normalized correlations $\Delta\overline{S}_{4,4}$ for $T = 1/2$ are plotted. The HBT contribution of both sources decreases with temperature, so that the value of the plateau (typically for $\tau \simeq \pm T/4$) decreases. However, peaks start to appear as temperature increases around $\tau \simeq \pm T/2$. *Lower panel:* When normalizing the total correlations $\Delta\overline{S}_{4,4}$ by the HBT contribution, we observe that the relative part of the electron/hole interference peak increases in $\Delta\overline{q}$, as the overlap mediated by the Fermi distribution rises.

given energy ϵ, a fraction $1 - f(\epsilon)$ of empty levels. At the same time, a hole wavepacket can spread over positive energies, so that electron and hole wavefunctions can partially overlap when $T_{el} \neq 0$. Quite surprisingly, the overlap is then reinforced as temperature increases.

Moreover, this effect should be more perceptible for wavepackets emitted at low energies.

This gives an explanation for the fact that our measurements and simulations do not seem to exhibit any particular feature in the case of high-energy excitations obtained for $D_1 = D_2 = 0.4$, while e/h correlations may be observed for low-energy quasiparticles ($D_1 = D_2 = 1$).

In fact, one can actually evaluate the HOM correlations at finite temperature in the wavepacket model (see appendix A), and find [146]:

$$\Delta\overline{Q}_{HOM} = 8e^2 f \left| \int d\epsilon\, \varphi_1(\epsilon)\varphi_2^*(\epsilon) f_{\mu=0}(\epsilon)\big(1 - f_{\mu=0}(\epsilon)\big) \right|^2 \tag{5.24}$$

It is important here to notice that the sign of $\Delta\overline{Q}_{HOM}$ has changed, so that $\Delta\overline{Q} \geq \Delta\overline{Q}_{HBT,1} + \Delta\overline{Q}_{HBT,2}$. At first sight, this result is very surprising: the HOM noise is larger than the noise obtaining by partitioning independently both excitations. However, we have to take into account that these HBT contributions are crucially reduced by antibunching with thermal excitations when $T_{el} \neq 0$. In Fig.5.8, numerical simulations of correlations $\Delta\overline{Q}$ and normalized correlations $\Delta\overline{q}$ are presented for different temperatures. They tend to prove that in fact $\Delta\overline{Q}$ is always limited by the zero temperature HBT contribution, so that we have the following inequalities, that hold for e/h collisions:

$$\sum_{i=1,2} \Delta\overline{Q}_{HBT,i}(T_{el}) \leq \Delta\overline{Q} \leq \sum_{i=1,2} \Delta\overline{Q}_{HBT,i}(T_{el} = 0) \tag{5.25}$$

This paragraph has revealed unexpected features of the HOM correlations that can only occur at finite temperature. Besides, they also supply arguments to discuss the issue of Coulomb interactions that could lead to similar effects,

5.3.4 Discarding Coulomb repulsion effects

One major objection that one may rise on the presented results lies in the fact that the zero-delay HOM dip could be explained by interactions effects. Indeed, if electrons strongly repel each other when colliding on the central QPC, they will in most cases exit in two different outputs, and the HOM correlations will look similar to our experimental results.

A way to discard the effects of interactions is to take advantage of electron/hole interferences. On Fig.5.9, schematics of electron/hole two particle interference are presented, in the non-interacting and strongly interacting cases. As mentioned earlier, statistics and interactions have the same effect on electron/electron collisions (Fig.5.9, panel a) and b)). The situation is different for electron/hole collisions. First, strongly interacting electron and hole should mimic a bunching effect as they would exit in the same output,

either 3 or 4. Interference of electron and hole are difficult to picture in full generality as they rely on finite temperature effects, but in the limit $T_{el} = 0$ they simply do not feel each other (the wavepackets do not overlap) and are partitioned independently.

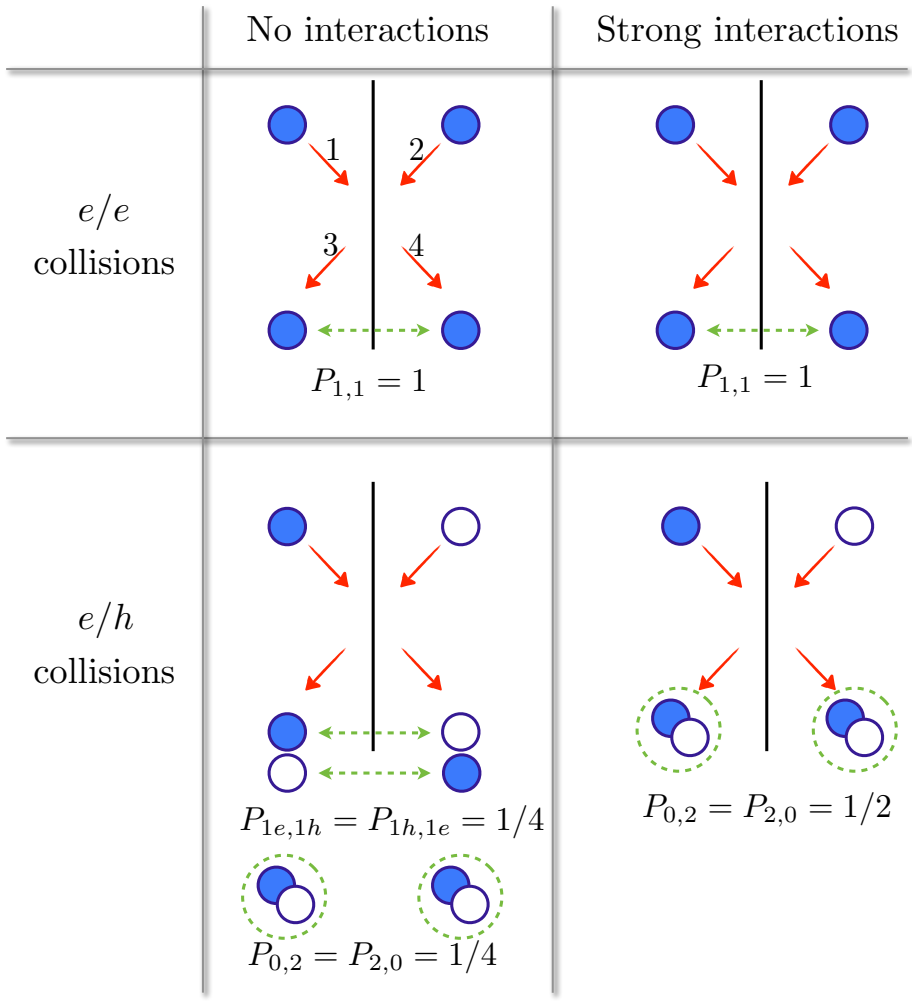

	no interactions	strong interactions
e/e	$P_{1,1} = 1$	$P_{1,1} = 1$
e/h	$P_{1e,1h} = P_{1h,1e} = P_{2,0} = P_{0,2} = 1/4$	$P_{2,0} = P_{0,2} = 1/2$

FIGURE 5.9: **Effects of interactions on Hong-Ou-Mandel correlations** – Collisions on a beamsplitter are schematized in four different case: e/e or e/h collisions with or without interactions. The motion of particles is symbolized by red arrows, from inputs 1 and 2 to outputs 3 and 4. Each possible output corresponds to green dashes (arrow or circle), and the corresponding probability is detailed, and recalled in a table. Only e/h collisions enable to distinguish interference effects from strong interactions.

In this simple model that disregards the presence of thermal excitations, the probabilities of the different possible outputs can first be computed. Then, the charge correlations can be derived, similarly to the classical partitioning model of section 3.1.3. In the HBT

experiment, a single electron/hole has an equal probability of going out in output 3 or 4, i.e. $P_{10} = P_{01} = 1/2$. Additionally, the possible outcomes of the HOM collision experiment are summarized in Fig.5.9, consistently with previous discussion.

Then, one can compute the charge correlations in one of the two outputs 3 or 4 as in section 3.1.3. To simulate the HBT contribution of the two sources, we double the HBT contribution of one electron being partitioned.

$$Q_4 \quad = \quad e(N_{e,4} - N_{h,4}) \tag{5.26}$$

Since there is only one output possible in the case of e/e collisions (see Fig.5.9), the process is noiseless, so that $\langle \delta Q_4^2 \rangle = 0$. For electron and hole "bunching" due to strong interactions, the process is also noiseless and $\langle \delta Q_4^2 \rangle = 0$, as the charge exiting in the outputs is always zero. In the last case, electron and hole are partitioned independently. The fluctuations are then obtained by doubling the HBT fluctuations of one source. From the results of section 3.1.3, we obtain that, for a transmission $T = 1/2$: $\langle \delta Q_4^2 \rangle = 2\,T(1-T)e^2 = \frac{e^2}{2}$.

In the end, we can translate these charge fluctuations into spectral density of noise by the relation $\overline{S}_{4,4} = 2f\langle \delta Q_4^2 \rangle$. This analysis shows that strong interactions and interferences can not be distinguished easily by scrutinizing only e/e collisions, but that we can instead make use of e/h correlations. In the presence of strong interactions, our measurement should show the appearance of three dips in $\tau = 0$ (e/e collisions) and $\tau = \pm\frac{T}{2}$ (e/h collisions). This is not observed so that we can discard the interactions in this experiment. This analysis validates our approach in terms of "interference" instead of "collisions".

Conclusion to chapter 5

In this chapter, we have studied an electronic analog of the Hong-Ou-Mandel experiment, in which two synchronized sources emit mono-electronic excitations that can interfere on a beamsplitter. Varying the time-delay τ between the arrivals of both excitations, we observe a reduction (up to 60%) of the output correlations around $\tau = 0$, as a signature of the two-particle Hong-Ou-Mandel interference. It demonstrates the (partial) indistinguishability of the excitations produced by the two independent sources. The width of the Hong-Ou-Mandel dip is controlled by the length of the emitted wavepackets, that can be tuned by changing the transmission of the quantum dot. A detailed analysis, combining both Floquet scattering model and a wavepacket model has been carried out, and the possible interplay of strong interactions has been discarded.

At the same time, our analysis has shown how the underlying physics was enriched by the presence of two types of excitations, electrons and holes. Although the energy distribution of these excitations do not overlap, a novel partial interference effect can occur for a non-zero electronic temperature $T_{el} \neq 0$. Contrary to electron/electron collisions, a peak in the HOM correlations is then observed.

After the Hanbury-Brown & Twiss experiment, this constitutes a new assessment of the validity of the quantum optics approach in quantum Hall edge channels. It provides a way to probe in more details the properties of the emitted wavepackets and could reveal interesting results on the consequences of interactions as propagation takes place in the edge channels.

Chapter 6

Conclusion

6.1 Summary and conclusion

In this manuscript, we have scrutinized the realization of single to few electrons experiments in quantum Hall edge devices. By means of quantum optics language, our setups aim at proposing benchmarks experiments to address the problem of an elementary particle among the surrounding thermal excitations of the Fermi sea. The investigation was carried out under two angles, quite different in the approach but closely related, and relies on the ability to trigger the emission of single charges offered by a driven mesoscopic capacitor.

6.1.1 Electron quantum optics in quantum Hall edge channels

The first approach consists in developing analogs of quantum optics experiments by manipulating triggered wavepackets. The analogy spreads both on the experimental side, with devices mimicking optics elements, and on the theoretical side, with the use of coherence functions to analyse the results. It follows pioneering experiments [1–3] by bringing them down to the single electron scale.

In a first experiment (chapter 3), we have reproduced the seminal Hanbury-Brown & Twiss experiment and studied the partitioning of triggered electron/hole pairs by measurements of current correlations. As explained by a classical model, it offers a way to count the total number of quasiparticles emitted by our single electron/hole source, information that can not be accessed easily without partitioning. However, this counting is profoundly modified by the presence of thermal excitations that naturally exist in the Fermi sea of the 2DEG. Indeed, quantum two-particle interferences between emitted quasiparticles and indistinguishable counterparts in the Fermi sea occur and reduce the Hanbury-Brown & Twiss signal. This effect has been used to probe the energy distribution of the particles produced by the source, as it actually measures the overlap between the wavefunction of these particles and the Fermi equilibrium distribution. Then, we have been able to give strong evidence that the generated energy distribution can be tuned by the choice of parameters such as the excitation (sine or square waves) or transmission of the quantum dot. For example, a square wave in the ideal single charge emission regime has a tendency to generate high energy quasiparticles, while a sine wave and an opened dot produce low-energy excitations.

In a second experiment (chapter 5), we have investigated the interference between monoelectronic excitations emitted by two independent sources, thus reproducing the Hong-Ou-Mandel scheme. When the excitations are synchronized so that they reach the QPC at the same time, a reduction of the Hong-Ou-Mandel correlations has been recorded,

proving the (partial) indistinguishability of the two quasiparticles. When the time-delay between the excitations is varied, the HOM interference is modulated and controlled by the temporal width of the wavepacket. By measuring the HOM correlations for two different choices of parameters, we have observed a modification of the width of the so-called Hong-Ou-Mandel dip reflecting a change in the escape time of the source.

These two studies have provided very interesting results on our single electron/hole source, and confirmed the validity of this "quantum optics" approach. However, as such, it completely ignores Coulomb interactions which are known to be quite pronounced, and which start to appear as the accuracy of our measurements is improved.

6.1.2 Channel-resolved microwave measurements of inter-channel interactions

The second approach (chapter 4) tends to correct the lack of knowledge on interactions. We take advantage of our mesoscopic capacitor to induce sinusoidal edge-magnetoplasmons in the outer channel of $\nu = 2$. The current that appears in the inner edge channel thus results entirely from capacitive coupling between both edge channels and yields information on it. Using a QPC and varying the drive frequency (instead of the propagation length), we have been able to prove that the interactions were responsible for the appearance of new collective eigenmodes with different velocities. We have established (with a 10% accuracy) that the fast one is a charge mode, while the slow one is neutral, in agreement with a strong coupling picture. Furthermore, we have extracted from our measurements the dispersion relation of the slow neutral mode, the velocity of the slow spin mode (in a low-frequency limit) and the bare Fermi velocity without inter/intra-channel interaction. A careful study has proved the existence of a finite range in the interaction, and our data are in reasonable agreement with a long-range model, in which the range is on the order of the propagation length.

6.1.3 Complementarity and generality of our approaches

These two approaches are actually very complementary in the study of quantum Hall edge devices. Channel-resolved experiments in the microwave domain gives access to properties of interactions at a very fundamental level, that can be studied in the framework of (chiral) Luttinger liquid theory. They shed new light on these phenomena, known to be responsible for decoherence and relaxation in quantum Hall edge channels and more specifically in electron quantum optics experiments. As such they constitute a necessary and complementary step in the understanding of electron quantum optics experiments, which are first established by assuming that interactions play a negligible

role. Spectacular results have been obtained by neglecting interactions. However, the more sophisticated the correlations measurements, the more tangible interactions. In particular, first results on the Hong-Ou-Mandel experiment tend to demonstrate that decoherence occur and is responsible for a reduced visibility. In a near future, improved experimental resolution in the HOM and spectroscopy/tomography experiments should give a very accurate way of probing interactions.

Besides, the generality of these methods has to be stressed. Radio-frequency measurements have already been widely used to study the propagation of edge magnetoplasmons [72–74, 77–81]. More recently, channel-resolved spectroscopy experiments have been performed [49–51]. The method detailed in this manuscript unifies those two domains and opens the way to more advanced studies of inter-edge channel relaxation.

The quantum optics protocols detailed in this manuscript have also a relatively broad domain of application as they can be in principles applied to any type of electron source: lorentzian Levitov pulses [38–40], single electron pumps [27, 33–36], etc. Besides, one can imagine in a near future the development of spin-resolved electron quantum optics. Such experiments could naturally be implemented in quantum Hall edge channels [147, 148] or in the recently developed helical edge channels [149, 150] of 2D topological insulators.

6.2 Future developments

To conclude, we briefly review future experiments that are under current development in our group. They will be under the responsibility of V. Freulon, PhD student, supervised by G. Fève, B. Plaçais and J.-M. Berroir.

Spectroscopy and tomography protocols The obvious next step is to implement the spectroscopy protocol [46] detailed in section 3.4. In the purpose of considerably improving the signal-to-noise ratio, the dilution fridge will be equipped with cold amplifiers developed in LPN Marcoussis by our long-time collaborator Y. Jin and the group of F. Pierre. All ingredients would then be gathered to launch this new experiment, that should give deep insights on the effects of interactions, as propagation occurs in the edge channels. Besides, new techniques initiated by the group of F. Pierre [50] could help to diminish the influence of interactions while working at filling factors $\nu \geq 2$. The idea is to create loops by closing the inner channel on itself along the outer edge channel's path: thus an energy gap appears in the inner channel, on a scale $E_g \sim v/L$, so that energy exchanges are frozen in this energy window. The effects of interactions between channels could then be tuned, and directly probed in current correlations.

The tomography protocol seems currently a bit further ahead. High-frequency harmonics are difficult to produce and the detection scheme has to be modified. However, this perspective could be facilitated by new theoretical developments. For example, our collaborators in Lyon, supervised by P. Degiovanni have obtained first results on a generalization of Wigner functions [128, 134, 151] to electronic systems, that makes the analysis of tomography easier: non-classical behavior can for example be clearly identified. Moreover, the tomography protocol relies on a two-dimensional Fourier analysis, that could be in fact replaced by a wavelet picture. Lorentzian pulses could then be interesting candidates for such wavelets.

Neutral modes Aside from these experiments, the group wishes to pursue the study of interactions in quantum Hall systems. On a dedicated sample, one can first imagine longer propagation length. With the same bandwidth, several charge oscillations could then be recorded. One particular goal would be to study the characteristics of neutral modes appearing in the fractional Hall regime ($\nu = 4/3$ for example) and that are currently under investigation using other techniques [152–155].

Appendix A

Coherence functions: complements and formulary

In this appendix, we review some aspects of the general theoretical framework of this work. First we give details on the wavepacket model and derive in particular the coherence functions of a mono-electronic wavepacket at both zero and finite temperature. Then we list up useful definitions and formulas related to coherence functions. Finally we recall the links between coherence functions and Floquet scattering theory.

A.1 Wavepacket above the Fermi sea

A.1.1 Coherence function at $T_{el} = 0$

The quantum state is obtained by creating the electron above the Fermi sea, so that the state reads:

$$|\varphi_e\rangle = \int dt\, \varphi_e(t)\psi^\dagger(t)|F_\mu\rangle \tag{A.1}$$

The normalization is set by the relation:

$$\langle\varphi_e|\varphi_e\rangle = \int dtdt'\, \varphi_e^*(t)\varphi_e(t')\langle\psi(t)\psi^\dagger(t')\rangle_\mu \tag{A.2}$$

$$= \int d\epsilon\, |\varphi_e(\epsilon)|^2(1-f(\epsilon)) = 1 \tag{A.3}$$

that reduces to $\int_0^\infty d\epsilon\, |\varphi_e(\epsilon)|^2 = 1$ at zero temperature.

The main difficulty in the calculation of $\mathcal{G}^{(e)}$ lies in the quantum average over the state $|\varphi_e\rangle$. The previous equation shows how to relate this to an average over $|F_\mu\rangle$ where one

can then use Wick's theorem :

$$\begin{aligned}
\mathcal{G}^{(e)}(t,t') &= \langle\varphi_e|\psi^\dagger(t')\psi(t)|\varphi_e\rangle && \text{(A.4)}\\
&= \int dt_1\, dt_1'\, \varphi_e^*(t_1')\varphi_e(t_1)\langle\psi(t_1')\psi^\dagger(t')\psi(t)\psi^\dagger(t_1)\rangle_\mu \\
&= \int dt_1\, dt_1'\, \varphi_e^*(t_1')\varphi_e(t_1)\langle\psi(t_1')\psi^\dagger(t')\rangle_\mu\langle\psi(t)\psi^\dagger(t_1)\rangle_\mu \\
&\quad +\langle\psi^\dagger(t')\psi(t)\rangle_\mu \int dt_1\, dt_1'\, \varphi_e^*(t_1')\varphi_e(t_1)\langle\psi(t_1')\psi^\dagger(t_1')\rangle_\mu && \text{(A.5)}
\end{aligned}$$

We consider here the case of the single-shot emission of an electronic excitation at rather high energies: we assume that the particle is represented by a wavepacket φ_e such that in the energy domain $\varphi_e(\epsilon) = \int dt\, e^{i\epsilon t/\hbar}\varphi_e(t)$ is concentrated around an energy $\epsilon_e \gg kT_{el}$. Thus, the expression of $\mathcal{G}^{(e)}(t,t')$ can be greatly simplified. Making use of Eqs.(A.17) and (A.18), the first term is transformed as follows:

$$\begin{aligned}
&\int dt_1\, dt_1'\, \varphi_e^*(t_1')\varphi_e(t_1)\langle\psi(t_1')\psi^\dagger(t')\rangle_\mu\langle\psi(t)\psi^\dagger(t_1)\rangle_\mu \\
&= \left(\int dt_1 d\epsilon d\epsilon_1\, \varphi_e(\epsilon_1)\big(1-f_\mu(\epsilon)\big)e^{-i\epsilon_1 t_1/\hbar}e^{i\epsilon(t_1-t)/\hbar}\right) \\
&\quad \times\left(\int dt_1' d\epsilon' d\epsilon_1'\, \varphi_e^*(\epsilon_1')\big(1-f_\mu(\epsilon')\big)e^{-i\epsilon_1' t_1'/\hbar}e^{i\epsilon'(t_1'-t')/\hbar}\right) \\
&= \left(\int d\epsilon d\epsilon_1\, \varphi_e(\epsilon_1)\big(1-f_\mu(\epsilon)\big)\delta(\epsilon-\epsilon_1)e^{-i\epsilon t/\hbar}\right) \\
&\quad \times\left(\int d\epsilon' d\epsilon_1'\, \varphi_e^*(\epsilon_1')\big(1-f_\mu(\epsilon')\big)\delta(\epsilon'-\epsilon_1')e^{-i\epsilon' t'/\hbar}\right) && \text{(A.6)}\\
&\simeq \varphi_e^*(t')\varphi_e(t) && \text{(A.7)}
\end{aligned}$$

The keypoint is the small overlap of $f_\mu(\epsilon)$ with $\varphi_e(\epsilon)$: $\int d\epsilon\, \varphi_e(\epsilon)f_\mu(\epsilon) \simeq 0$. The second term can also be simplified using the normalization condition (Eq.(A.2)) and the coherence function of an ideal one-shot electron source finally reads:

$$\begin{aligned}
\mathcal{G}^{(e/h)}(t,t') &= \mathcal{G}_\mu^{(e/h)}(t-t') + \varphi_e^*(t')\varphi_e(t) && \text{(A.8)}\\
\Delta\mathcal{G}^{(e/h)}(t,t') &= \varphi_e^*(t')\varphi_e(t) && \text{(A.9)}
\end{aligned}$$

A.1.2 Coherence function at $T_{el} \neq 0$

Calculations can easily be performed at finite temperature as well in the wavepacket model for a finite temperature. The results presented here justify the calculations of section 5.3.3.

Using Wick's theorem, the second term is here again simplified via the normalization condition. Please note that it is now written $\int d\epsilon\, |\varphi_e(\epsilon)|^2(1-f(\epsilon)) = 1$. The first term

is slightly modified as $\int d\epsilon\, \varphi_e(\epsilon) f_\mu(\epsilon) \neq 0$. Starting from Eq.(A.6), we see that if we introduce $\tilde{\varphi}_e(\epsilon) = \varphi_e(\epsilon)\big(1 - f_\mu(\epsilon)\big)$, we easily get:

$$\mathcal{G}^{(e/h)}(t,t') = \mathcal{G}_\mu^{(e/h)}(t-t') + \tilde{\varphi}_e^*(t')\tilde{\varphi}_e(t) \tag{A.10}$$

$$\Delta\mathcal{G}^{(e/h)}(t,t') = \tilde{\varphi}_e^*(t')\tilde{\varphi}_e(t) \tag{A.11}$$

The coherence function keeps the same form at finite temperature, though it has to be written using a modified wavefunction $\tilde{\varphi}_e$.

A.2 Coherence functions: formulary

Definitions

$$\{\hat{b}(t), \hat{b}^\dagger(t')\} = \delta(t-t') \tag{A.12}$$

$$\mathcal{G}^{(e)}(t,t') = \langle \hat{b}^\dagger(t')\hat{b}(t)\rangle \tag{A.13}$$

$$\mathcal{G}^{(h)}(t,t') = \langle \hat{b}(t')\hat{b}^\dagger(t)\rangle \tag{A.14}$$

$$\mathcal{G}^{(e/h)}(t,t') = \sum_n e^{-i\Omega n\bar{t}}\mathcal{G}_n^{(e/h)}(\tau) \tag{A.15}$$

$$\mathcal{G}_n^{(e/h)}(\tau) = \int d\epsilon\, e^{i\epsilon\tau/\hbar}\mathcal{G}_n^{(e/h)}(\epsilon) \tag{A.16}$$

Coherence functions of the Fermi sea

$$\mathcal{G}_\mu^{(e)}(t-t') = \int \frac{d\epsilon}{h} f_\mu(\epsilon) e^{i\epsilon(t'-t)/\hbar} \tag{A.17}$$

$$\mathcal{G}_\mu^{(h)}(t-t') = \int \frac{d\epsilon}{h} (1 - f_\mu(\epsilon)) e^{i\epsilon(t-t')/\hbar} \tag{A.18}$$

e/h relations

$$\mathcal{G}^{(e/h)}(t,t') = \mathcal{G}^{(e/h)^*}(t',t) \tag{A.19}$$

$$\mathcal{G}^{(e)}(t,t') + \mathcal{G}^{(h)}(t',t) = \delta(\tau) \tag{A.20}$$

$$\mathcal{G}_n^{(e)}(\tau) + \mathcal{G}_n^{(h)}(-\tau) = \delta(\tau)\delta_{n,0} \tag{A.21}$$

$$\Delta\mathcal{G}_n^{(e)}(\tau) + \Delta\mathcal{G}_n^{(h)}(-\tau) = 0 \tag{A.22}$$

$$\mathcal{G}_n^{(e)}(\tau) = \mathcal{G}_{-n}^{(e)^*}(-\tau) \tag{A.23}$$

$$\mathcal{G}_n^{(e)}(\epsilon) + \mathcal{G}_n^{(h)}(-\epsilon) = \delta_{n,0} \tag{A.24}$$

$$\Delta\mathcal{G}_n^{(e)}(\epsilon) + \Delta\mathcal{G}_n^{(h)}(-\epsilon) = 0 \tag{A.25}$$

$$\mathcal{G}_n^{(e)}(\epsilon) = \mathcal{G}_{-n}^{(e)\,*}(\epsilon) \tag{A.26}$$

Useful relation

$$\langle \hat{b}^\dagger(\epsilon')\hat{b}(\epsilon)\rangle = \frac{1}{h}\int dt dt'\, e^{\frac{i}{\hbar}(\epsilon t - \epsilon' t')}\langle \hat{b}^\dagger(t')\hat{b}(t)\rangle \tag{A.27}$$

$$= \sum_n \mathcal{G}_n^{(e)}\Big(\frac{\epsilon+\epsilon'}{2}\Big)\delta(\epsilon' - \epsilon + n\hbar\Omega) \tag{A.28}$$

A.3 Floquet scattering theory: formulary

Definitions and unitarity

$$\hat{b}(t_2) = \int dt_1\; U(t_2,t_1)\hat{a}(t_1) \tag{A.29}$$

$$U(t',t) = \sum_m U_m(\tau)e^{-im\Omega\bar{t}} \tag{A.30}$$

$$U(\epsilon',\epsilon) = \int dt' dt\, U(t',t)e^{\frac{i}{\hbar}(\epsilon' t' - \epsilon t)} \tag{A.31}$$

$$\hat{b}(\epsilon') = \int d\epsilon\; U(\epsilon',\epsilon)\hat{a}(\epsilon) \tag{A.32}$$

$$\hat{b}(\epsilon) = \int \frac{dt}{\sqrt{h}} e^{i\epsilon t/\hbar}\hat{b}(t) \tag{A.33}$$

$$U(\epsilon',\epsilon) = \sum_m U_m(\epsilon' - \frac{m}{2}\hbar\Omega)\delta(\epsilon' - \epsilon - m\hbar\Omega) \tag{A.34}$$

$$\hat{b}(\epsilon') = \sum_m U_m(\epsilon' - \frac{m}{2}\hbar\Omega)\hat{a}(\epsilon' - m\hbar\Omega) \tag{A.35}$$

$$\sum_m U_m^*(\epsilon)U_{m+n}(\epsilon + \frac{n}{2}\hbar\Omega) = \delta_{n,0} \quad \text{(Unitarity)} \tag{A.36}$$

Coherence functions in Floquet formalism

$$\mathcal{G}^{(e)}(t,t') = \int dt_1 dt_1'\, U(t',t_1')U^*(t,t_1)\,\mathcal{G}_\mu^{(e)}(t_1 - t_1') \tag{A.37}$$

$$\mathcal{G}_n^{(e)}(\epsilon) = \sum_m U_m^*(\epsilon)U_{m+n}(\epsilon + \frac{n}{2}\hbar\Omega)f_\mu(\epsilon - \frac{m}{2}\hbar\Omega)) \tag{A.38}$$

Appendix B

Semi-classical heuristic model

In this appendix, we give details on the probabilistic model of the source, first introduced by A. Mahé in his thesis [83] before generalization and analytical treatment by Albert *et al.* [115]. This model supplies a formula for the noise of a single charge emitter that can then be compared with Floquet scattering theory and experimental data.

B.1 Rules of single particle emission

First, we detail the construction of the semi-classical model of the source, based on a few probabilistic rules:

- One level only is considered in the dot. The charge in the dot can only take two values, 1 or 0.
- Inside the dot, the electron performs turn in a time τ_0. After each turn, the electron has a probability b to escape.
- Each half-period of the square drive is divided into N turns, $T/2 = N\tau_0$. Emissions of electron can only occur if the charge is 1 in the dot, and only one emission process is permitted during one half-period.
- After the end of the first of the half-period, the second half-period is described with symmetric rules concerning the absorption of electrons: absorptions can only take place if the dot is empty, with a limit of one absorption per half-period.

These simples rules can be simulated easily as demonstrated in the following section. Nonetheless, it is important to understand the limits of this model beforehand, even though most of them are quite obvious. First, this description only applies for a square

voltage, for which emission and absorption are clearly triggered by the sudden shifts of potential. Moreover, this incompressible time increment τ_0 render this model null when a time-scale reaches τ_0. This can be the case for $D \to 1$, for which $\tau_e \sim \tau_0$. Last, this model does not take into account the presence of the Fermi sea: no temperature can be simply attributed to the particle reservoir that provides electrons and holes to empty of fill the dot.

B.2 Instantaneous current and average current

The previous probabilistic rules can be simulated easily with pseudo-random number generators. The successive emission/absorption of holes gives rise to an AC current $I(t)$, pictured on Fig.B.1. A peak (resp. a dip) occur whenever an electron is emitted (resp. absorbed). The emission rules ensure that every absorption is followed by an emission and vice-versa, as observed on Fig.B.1 (left panels). Averaging $I(t)$ over a large amount of periods yields the average current $< I(t) >$, displaying exponentially decaying currents (right panels of Fig.B.1).

These predictions can then be compared with the experimental results of section 2.2.2.2. The decay time τ_e is in good agreement (for $b < 0.3$, see following remark) with the formula $\tau_e = \tau_0(\frac{1}{b} - \frac{1}{2})$ so that we can identify $b = D, \tau_0 = h/\Delta$. The transferred charge per half-period Q_t can also be computed from the previous model and corroborates the formula $Q_t = e \tanh(\frac{1}{4f\tau_e})$.

For small values of b (Fig.B.1, panel a, with $b = 0.025$), some emission/absorption events are missed, $\tau_e \gg T/2$ and the computed transferred charge is $Q_t = 0.56\,e$. For intermediate values of b, (Fig.B.1 b, $b = 0.1$), all charge transfers are observed ($Q_t = 0.99\,e$), but the emission can occur at anytime in the dedicated half-period, with $\tau_e \sim T/2$ For large values of b (Fig.B.1 c, $b = 0.3$), each emission/absorption occur immediately after the beginning of the dedicated half-period, this corresponds to a short escape time τ_e as compared to the half-period $T/2$.

B.3 Current autocorrelations

This heuristic model enables to generate sequences of emission/absorption processes, with probabilistic rules that seem to reproduce accurately experimental observation on the average current. Statistical studies of the generated currents $I(t)$ can be pursued beyond average current: following the precursory work of A. Mahé [83], we here present the main features of the current correlations of this peculiar single charge emitter. This

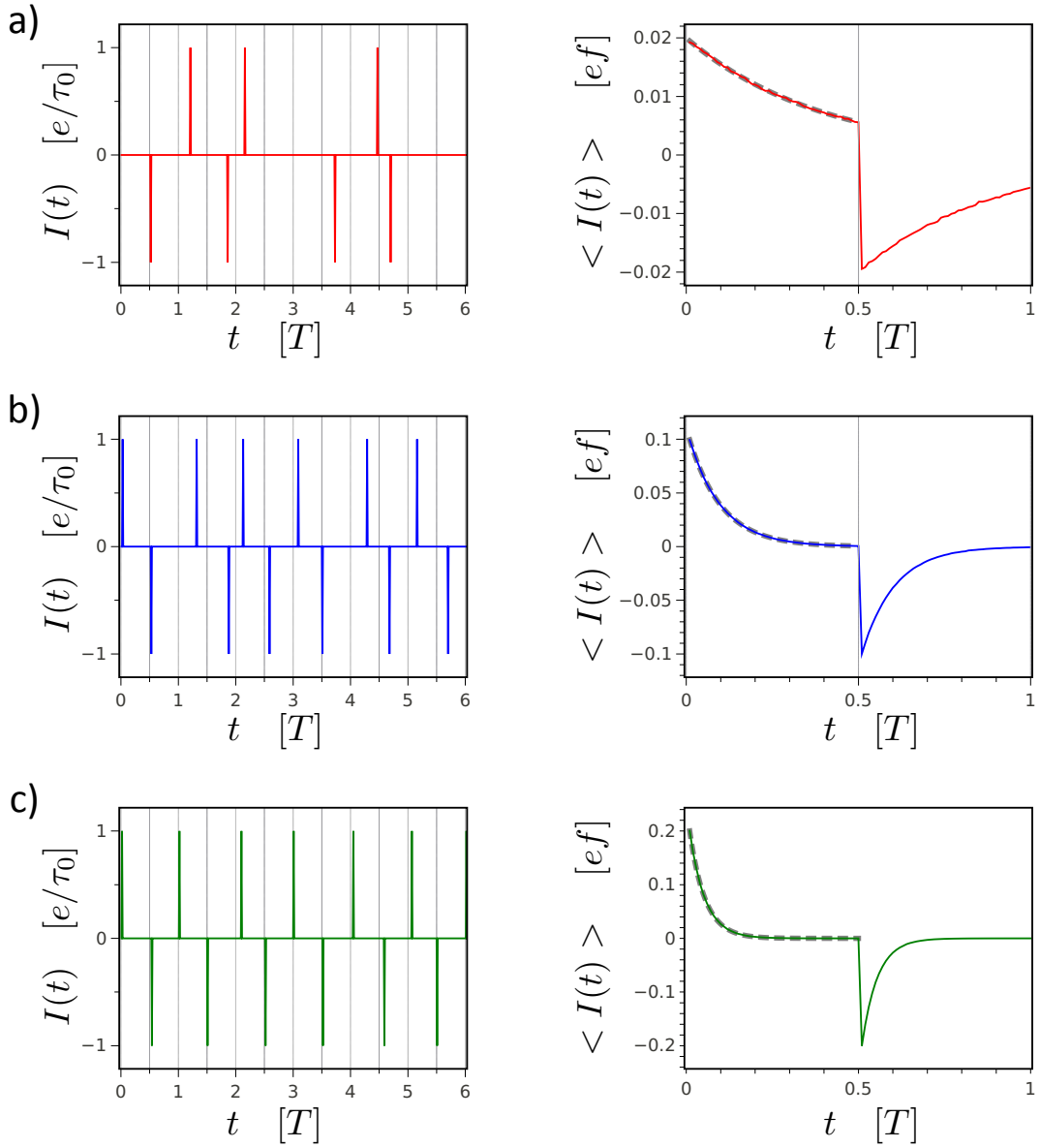

FIGURE B.1: **Current and average current, computed from the heuristic model** – For different values of p, instantaneous current (6 periods) and average current (1 period, averaged over 10^6 periods) are presented. In grey dashed line, an exponential fit shows a perfect agreement with simulations.The parameters are: $T = 100\tau_0$, with $p = 0.025$ (panel a), $p = 0.1$ (b), and $p = 0.3$ (c)

helps to reveal the physical meaning of previous Floquet calculations. Besides, M. Albert *et al.* have realized a comprehensive study of fluctuations in this semi-classical, including the computation of the full counting statistics [115], but their results are not described in this manuscript.

B.3.1 Computation of the noise

We compute the noise from Eq.(2.51), by replacing the quantum average $\langle \cdots \rangle$ by a classical ensemble average $< \cdots >$. Two contributions, defined hereinafter, are calculated separately:

$$C(\tau) = \overline{< \delta I(t')\delta I(t) >}^{\bar{t}} \tag{B.1}$$

$$= \overline{< I(t')I(t) >}^{\bar{t}} - \overline{< I(t') >< I(t) >}^{\bar{t}} \tag{B.2}$$

$$= C_1(\tau) - C_2(\tau) \tag{B.3}$$

Depending on the escape probability $b = D$, the correlators C_1 and C_2 vary, but it is possible to understand each of these contributions and build up an interpretation of the fluctuations of the single charge emitter. We emphasize however the fact that thermal fluctuations are not contained in this description since the thermodynamics of the Fermi sea is not pictured. Consequently, the noise predicted is directly equal to the excess noise:

$$\Delta\overline{S}(\omega) = \overline{S}(\omega) = \int d\omega\, C(\tau) e^{i\omega\tau} \tag{B.4}$$

The correlator C_1 is the average of the correlation of instantaneous currents $I(t)$, $I(t')$. Since only one charge (at most) is emitted during one half-period, for small non-zero τ, $I(t+\tau) = 0$ if $I(t) \neq 0$ (and vice-versa) so that $C_1(\tau)$ is reduced to a Dirac peak in $\tau = 0$ for small values of τ. The amplitude of this peak is directly proportional to the transferred charge Q_t as $C_1(\tau = 0)$ directly counts the average number of charges in the current. This Dirac peak is a very important feature in this reasoning: it is the signature of single particle emission. Any additional charge would spoil this very clear signature in the correlations. For larger τ, close to multiples of $T/2$, one emitted electron will be correlated with the preceding and following electrons/holes, giving a series of negative contributions (e/h correlations) alternating with positive contributions (e/e correlations). Each contribution is a peak or dip of width τ_e, reflecting the uncertainty on the position of the following/preceding electron/hole.

The correlator C_2 is the average over $\bar{t}$ of the product of the average currents $< I(t) >$ and $< I(t') >$. Consequently, it consists of an alternate series of peaks and dips of width τ_e and period T. In the long time regime, charges emitted by the source are not correlated, and C_1 and C_2 compensate: $C_1(\tau) = C_2(\tau) \Leftrightarrow C(\tau) = 0$. The scale on which these correlations are lost depends on the escape time τ_e.

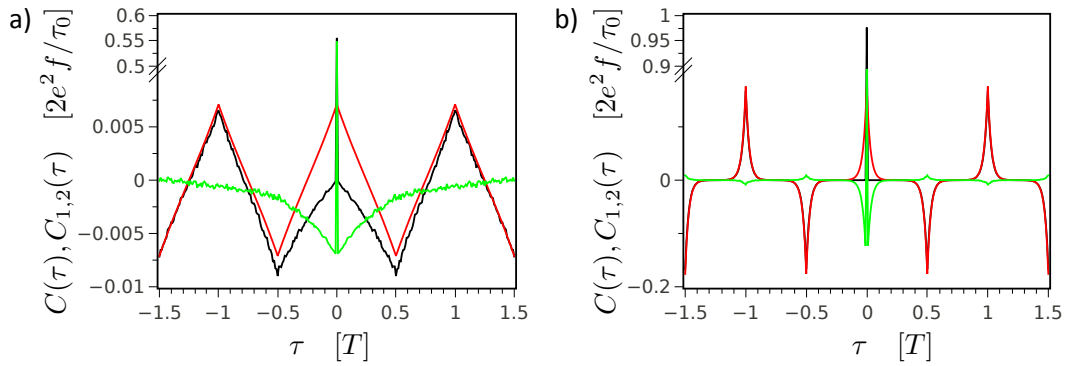

FIGURE B.2: **Autocorrelations, computed from the heuristic model** – For different values of p, contributions $C_1(\tau) = \overline{< I(t')I(t) >}^{\bar{t}}$ (black), $C_2(\tau) = \overline{< I(t') >< I(t) >}^{\bar{t}}$ (red) and $C = C_1 - C_2$ (green) are presented. In panel a), $p = 0.025$, corresponding to shot noise regime. In panel b), $p = 0.3$, corresponding to phase noise regime. The difference in the amplitude of the Dirac peak at $\tau = 0$ reflects the fact that $Q_t \ll 1$ in panel a) (low transmission) while $Q_t \simeq 1$ in panel b) (higher transmission). In the meantime, the escape time τ_e is longer in a) than in b) so that the decay is faster in b).

B.3.2 Shot noise regime

For small escape probabilities, the escape time τ_e becomes comparable or larger than the half-period $T/2$, and some emission events do not occur (Fig.B.1, panel a). Consequently, for small τ, C_2 presents a very wide peak, with a very small amplitude. C_1 being a Dirac peak, $C(\tau) \simeq 0$ for $\tau \neq 0$, and the noise power spectrum is white, except around $\omega = 0$. We thus recover a shot-noise regime. Neglecting C_2, and writing $C_1(\tau) = 2e^2 f \frac{Q_t}{e}\delta(\tau)$, with $Q_t \simeq \frac{e}{4f\tau_e}$ we get a simple expression for $\overline{S}$ in this regime:

$$\overline{S}_{shot}(\omega) \quad = \quad \frac{e^2}{\tau_e} = 4e^2 f \times P \tag{B.5}$$

where $P = Q_t/e$ is the probability of charge emission. This expression is similar to the usual shot noise $\overline{S} = 2eI$ with $I = 2ef \times P$.

B.3.3 Phase noise regime

For large probabilities $b = D$ we recover the phase noise limit of a perfect single charge emitter: if b is large enough so that all charges escape, $P = 1$ and shot noise vanishes. Then, thus average current is written $< I(t) >= e/\tau_e\, e^{-t/\tau_e}$ (in the first half-period). With this expression, $\overline{S}$ is calculated:

$$\overline{S}_{phase}(\omega) \quad = \quad 4e^2 f^2 \frac{\omega^2 \tau_e^2}{1 + \omega^2 \tau_e^2} \tag{B.6}$$

As already mentioned, when all charges are emitted, a residual finite noise is still present, stemming from the fundamental uncertainty on the emission time, here given by the escape time τ_e.

B.3.4 Analytic formula

M. Albert *et al.* [115] have obtained an analytic formula for the current autocorrelations, valid for all values of b. The heuristic rules detailed in section B.1 can be translated into a master equation (on the charge in the dot) that can be solved. One then obtains the noise power spectral density that interpolates between shot noise and phase noise regimes:

$$\overline{S}(\omega) = 4e^2 f \tanh\left(\frac{1}{4f\tau_e}\right)\frac{\omega^2\tau_e^2}{1+\omega^2\tau_e^2} \quad \text{(B.7)}$$

$$= \frac{Q_t}{e}\frac{\omega^2\tau_e^2}{1+\omega^2\tau_e^2} \quad \text{(B.8)}$$

$$= \frac{1}{4e^2 f}\overline{S}_{shot}(\omega)\overline{S}_{phase}(\omega) \quad \text{(B.9)}$$

Appendix C

Interactions and bosonization at $\nu = 2$

In this appendix, we present rudiments of bosonization theory. It enables to derive the equations of motion of bosonic fields representing edge magneto-plasmons. Both short and long range models can then be properly introduced.

C.1 Coulomb interactions and bosonization

C.1.1 Equation of motion of the chiral bosonic fields

Focusing on the $\nu = 2$ case, the Hamiltonian for the two edge channels coupled through Coulomb interaction can be written as:

$$H = H_0 + H_{int} \tag{C.1}$$

$$H_0 = -i\hbar \sum_\alpha v_\alpha \int dx\, \Psi^\dagger_\alpha(x) \partial_x \Psi_\alpha(x) \tag{C.2}$$

$$H_{int} = \frac{1}{2} \sum_{\alpha\beta} \int dx dy\, U_{\alpha\beta}(x,y) \rho_\alpha(x) \rho_\beta(y) \tag{C.3}$$

where $\Psi_\alpha(x)$ is the field operator in channel $\alpha = 1, 2$ and $\rho_\alpha(x) = e\Psi^\dagger_\alpha(x)\Psi_\alpha(x)$ the charge density. H_0 is the free Hamiltonian from which we deduce the free evolution described in section 4.4.1 and where we assumed that the velocity v_α could be different in each channel. H_{int} describes both the intra-channel Coulomb interaction for $\alpha = \beta$ and the inter-channel Coulomb interaction for $\alpha \neq \beta$.

This problem can be solved by relating the density along each edge to the derivative of a bosonic field, $\rho_\alpha(x) = -\frac{e}{\sqrt{\pi}}\partial_x\phi_\alpha(x)$ [156, 157]. Using the equation of charge conservation, the electrical current in edge α can also be related to the bosonic field by: $i_\alpha(x,t) = \frac{e}{\sqrt{\pi}}\partial_t\phi_\alpha(x,t)$.

The Hamiltonian can be rewritten in term of the bosonic field [1]:

$$H = \hbar\sum_\alpha v_\alpha \int dx\,(\partial_x\phi_\alpha(x))^2 + \frac{e^2}{2\pi}\sum_{\alpha\beta}\int dxdy\,\partial_x\phi_\alpha(x)U_{\alpha\beta}(x,y)\partial_x\phi_\beta(y), \quad \text{(C.4)}$$

giving the following equation of motion:

$$(\partial_t + v_F\partial_x)\phi_\alpha(x,t) = \frac{e\sqrt{\pi}}{h}u_\alpha(x,t) \quad \text{(C.5)}$$

$$u_\alpha(x,t) = \sum_{\beta=1,2}\int dy\,U_{\alpha\beta}(x,y)\rho_\alpha(y,t) \quad \text{(C.6)}$$

$u_\alpha(x,t)$ is the potential in edge α which depends on the charge densities in each edges through the long range potential $U_{\alpha\beta}(x,y)$.

C.1.2 Short range interactions

We will consider two case, in the first one, the potential is short range, $U_{\alpha\beta}(x,y) = U_{\alpha\beta}\,\delta(x-y)$. The second case will describe an heuristic long range potential, where the potential is taken as uniform, that is $U_{\alpha\beta}(x,y)$ does not depend on x and y. Both cases can be understood by a model of capacitive coupling between the edges. In the first case, $u_\alpha(x,t)$ can be related to the charge densities at the same position through the inverse capacitance matrix $\mathcal{C}^{-1}$:

$$u_\alpha(x,t) = \sum_\beta \mathcal{C}^{-1}_{\alpha\beta}\rho_\beta(x,t) \quad \text{(C.7)}$$

$$\mathcal{C}^{-1}_{\alpha\alpha} = U_{\alpha\alpha} \geq 0 \qquad \mathcal{C}^{-1}_{\alpha\beta} = U_{\alpha\beta} \quad \text{(C.8)}$$

$$\mathcal{C} = \begin{pmatrix} \mathcal{C}_{11} & -\mathcal{C} \\ -\mathcal{C} & \mathcal{C}_{22} \end{pmatrix} \quad \text{(C.9)}$$

where $\mathcal{C}_{\alpha\beta}$ is the geometrical capacitance matrix per unit length describing Coulomb interactions in edges 1 and 2, see Fig.4.15.

[1] This Hamiltonian only contains the energy associated with the density fluctuations and not the one associated with the background charge (also called zero modes).

C.1.3 Long range model

In the heuristic long range model, the potential of the edge channels is assumed to be uniform, $u_\alpha(x,t) = u_\alpha(t)$ and related to the total charges inside the wires, $Q_\alpha(t) = \int dx\, \rho_\alpha(x,t)$ by the total capacitance matrix $C_{\alpha\beta}$:

$$u_\alpha(t) = \sum_\beta C^{-1}_{\alpha\beta} Q_\beta(t) \tag{C.10}$$

Calculations can then be performed in a similar way.

C.2 Complements

C.2.1 Dissipation in the short-range regime

As for the long-range interaction, dissipation can be added in the zero-range model (section 4.4.2.1). Adding the term γ in the same manner in the equation of motion directly leads to a modified scattering matrix:

$$\boldsymbol{\mathcal{S}}_{EMP}(\omega, l) = e^{i(\omega + i\gamma(\omega))l\boldsymbol{\mathcal{V}}^{-1}} \tag{C.11}$$

$$\boldsymbol{\mathcal{V}} = v_F \mathbb{I} + \frac{e^2}{h}\boldsymbol{\mathcal{C}}^{-1} \tag{C.12}$$

$$S_{21} = \frac{1 - \exp(i\frac{\omega l}{v_n^0}(1 + i\omega\tau_r))}{2} \tag{C.13}$$

Once again we obtain $S_{21} \to 1/2$. However no quantitative agreement can be obtained with this description: the additional term γ does not modify the fact that no ω-dependence appears in the velocity.

C.2.2 Links between short and long range models

To find the link between short and long range models, it is natural to proceed as follows: the short-range picture is seen as the succession of N copies of the long range model, on a length δl such that $\delta l \to 0, N \to \infty$ keeping $N\delta l = l$ constant. Chirality suppresses possible effects of multiples-wave interferences between all these copies, acting like single scatterers. We thus expect a relation of the type:

$$\boldsymbol{\mathcal{S}}^{\text{short}}_{EMP}(\omega, l) = \lim_{\substack{N\to\infty \\ \delta l \to 0}} \left[\boldsymbol{\mathcal{S}}^{\text{long}}_{EMP}(\omega, \delta l)\right]^N \tag{C.14}$$

$\delta\tau$ and $\delta\tau_0$ are both proportional to δl, so that $\frac{\delta\tau_0}{d\tau} = \frac{\tau_0}{\tau}$ is constant and $\delta\tilde{\tau} \propto \delta l$ when $\delta l \to 0$. Besides, in the limit $\delta l \to 0$,

$$S_{21} \simeq -i\omega\tilde{\tau} \quad \text{with } \delta\tilde{\tau} = \frac{\delta\tau_0}{2 + \delta\tau_0/\delta\tau} = \frac{\delta\tau_0}{2 + \tau_0/\tau} \tag{C.15}$$

$$\boldsymbol{\mathcal{S}}^{\text{long}}_{EMP}(\omega, \delta l) \simeq \begin{pmatrix} 1 + i\omega\delta\tilde{\tau} & -i\omega\delta\tilde{\tau} \\ -i\omega\delta\tilde{\tau} & 1 + i\omega\delta\tilde{\tau} \end{pmatrix} \tag{C.16}$$

$$\simeq \mathbb{I} + i\omega\delta\tilde{\tau}(\mathbb{I} - \sigma_x) \tag{C.17}$$

where σ_x is the Pauli matrix. Thus, we obtain:

$$\boldsymbol{\mathcal{S}}^{\text{short}}_{EMP}(\omega, l) = \lim_{\substack{N\to\infty \\ \delta l\to 0}} \left(\mathbb{I} + i\omega\delta\tilde{\tau}\,(\mathbb{I} - \sigma_x)\right)^N \tag{C.18}$$

$$= e^{i\omega\tilde{\tau}(\mathbb{I}-\sigma_x)} \tag{C.19}$$

$$\boldsymbol{\mathcal{S}}^{\text{short}}_{EMP}(\omega, l) = e^{i\omega\tilde{\tau}} \begin{pmatrix} \cos\omega\tilde{\tau} & -i\sin\omega\tilde{\tau} \\ -i\sin\omega\tilde{\tau} & \cos\omega\tilde{\tau} \end{pmatrix} \tag{C.20}$$

We then set $\frac{2}{v} = \frac{1}{v_n} - \frac{1}{v_\rho} \simeq \frac{1}{v_n} = \frac{\tilde{\tau}}{l}$ so that the matrix finally writes

$$\boldsymbol{\mathcal{S}}^{\text{short}}_{EMP}(\omega, x) = e^{i\frac{\omega x}{v}} \begin{pmatrix} \cos\frac{\omega x}{v} & -i\sin\frac{\omega x}{v} \\ -i\sin\frac{\omega x}{v} & \cos\frac{\omega x}{v} \end{pmatrix} \tag{C.21}$$

This matrix is then identical to the short-range scattering matrix obtained in chapter 4, 4.4.2.1.

C.2.3 Coupling between regions before and after the Quantum Point Contact

One parasitic effect that may completely ruin previous analyses is the existence of a long-range coupling between regions before and after the central QPC that isolates inner and outer channels before readout in ohmic contact 1. Since our experimental observations do not corroborate a picture of short-range interactions, it is of great interest to analyse whether long-range interactions couples this two regions.

We have then try to evaluate quantitatively this coupling. To this end, a fourth measurement configuration is used: the QPC is set to pinch-off, and the excitation is set on a second source, placed symmetrically with respect to the second QPC (see Fig.C.1). In an ideal setup, no current is to be measured in ohmic contact 1, since the QPC is pinched. However, if regions situated before and after QPC are capacitively coupled,

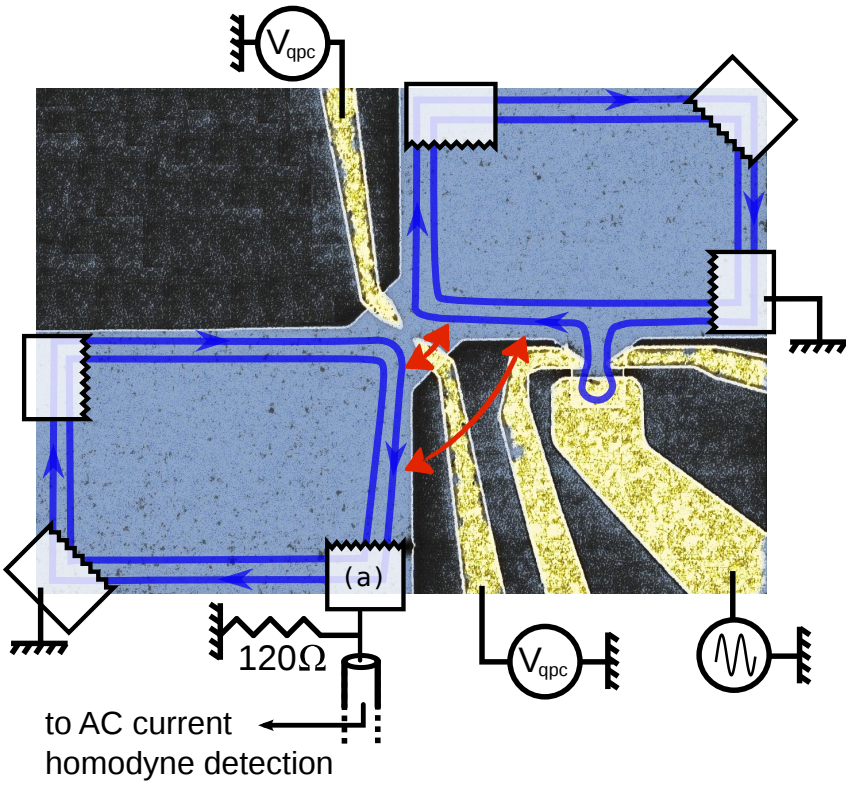

FIGURE C.1: **Configuration to evaluate coupling before/after QPC** – The driven source is in the measured in the transmitted path (with respect to central QPC) in this reverse configuration. Thus, when the QPC is pinched, no current should be measured in contact (a). Recording the small non-zero current in this contact helps to evaluate the parasitic coupling between regions placed before and after the QPC, symbolized by red arrows.

We model the results with a law comparable to an RC-circuit : $S_{par} \simeq -i\omega\tau_{par}$. Our measurements show that the coupling between excitation/propagation region, and the region after the QPC are coupled with a time constant $\tau_{par} = 5.5$ ps, which corresponds to circa $\tilde{\tau}/6$. This relatively weak parasitic effect is then ignored in our analysis.

Appendix D

Complements on experimental setup

D.1 Summary of configurations of the custom homodyne detection.

f (GHz)	Couplers	Source	Filters on reference	Filters on signal	Amplifiers
0.7–2.2	0.5–7 GHz	Pulse	0.5–2 GHz 1870+	1800+ DC–850 MHz	0.1–4 GHz
0.9–2.2	0.5–7 GHz	Pulse	0.5–2 GHz	1800+ DC–850 MHz	0.1–4 GHz
2–4	2–18 GHz	P & S	3800+	3800+	0.1–4 GHz
2.6–6	2–18 GHz	P & S	6000+	6000+	0.1–4 GHz
4–9	2–18 GHz	Sine			4–8 GHz
7–13	2–18 GHz	Sine			8–12 GHz

Sine :	Sine wave-generator Anritsu 3692C
Pulse :	Pulse wave-generator Anritsu 1810A
LNA 0.1–4 GHz :	Miteq JS2-00100400-10-10A
LNA 4–8 GHz :	Miteq AFS-040000800-07-10P-4
LNA 8–12 GHz :	Miteq AMF-4F-12001800-13-10P
Hybrid couplers 0.5–7 GHz :	Krytar 3005070
Hybrid couplers 2–18 GHz :	M/A-COM 2032-6371-00
Filters DC-850 MHz :	Mini-Circuits VLP-11
Filters 1800+ :	Mini-Circuits VLF-6000+
Filters 3800+ :	Mini-Circuits VLF-3800+
Filters 6000+ :	Mini-Circuits VLF-1800+
Filters 0.5–2 GHz :	Micro-Tronics BPM50604

List of Figures

Bibliography

[1] R. Schuster, E. Buks, M. Heiblum, D. Mahalu, V. Umansky, and Hadas Shtrikman. Phase measurement in a quantum dot via a double-slit interference experiment. *Nature*, 385(6615):417–420, January 1997. ISSN 0028-0836. doi: 10.1038/385417a0. URL http://www.nature.com/doifinder/10.1038/385417a0.

[2] Y. Ji, Y. Chung, D. Sprinzak, M. Heiblum, D. Mahalu, and H. Shtrikman. An Electronic Mach-Zehnder Interferometer. *Nature*, 422(6930):415–8, 2003. URL http://www.nature.com/nature/journal/v422/n6930/abs/nature01503.html.

[3] M. Henny, S. Oberholzer, C. Strunk, T. Heinzel, K. Ensslin, M. Holland, and C. Schönenberger. The Fermionic Hanbury Brown and Twiss Experiment. *Science*, 284(5412):296, April 1999. ISSN 00368075. doi: 10.1126/science.284.5412.296. URL http://www.sciencemag.org/content/284/5412/296.abstract.

[4] R. Glauber. The Quantum Theory of Optical Coherence. *Physical Review*, 130 (6):2529–2539, June 1963. URL http://prola.aps.org/abstract/PR/v130/i6/p2529_1.

[5] Th. Martin and R. Landauer. Wave-packet approach to noise in multichannel mesoscopic systems. *Physical Review B*, 45(4):1742–1755, January 1992. URL http://prb.aps.org/abstract/PRB/v45/i4/p1742_1.

[6] G. Fève. *Quantification du courant alternatif : la boîte quantique comme source d'électrons uniques subnanoseconde*. PhD thesis, Université Pierre et Marie Curie 6, 2006. URL http://tel.archives-ouvertes.fr/tel-00119589.

[7] C. Rössler, S. Baer, E. de Wiljes, P-L Ardelt, T. Ihn, K. Ensslin, C. Reichl, and W. Wegscheider. Transport properties of clean quantum point contacts. *New Journal of Physics*, 13(11):113006, November 2011. ISSN 1367-2630. doi: 10.1088/1367-2630/13/11/113006. URL http://iopscience.iop.org/1367-2630/13/11/113006.

[8] A.T. Hatke, M.A. Zudov, L.N. Pfeiffer, and K.W. West. Shubnikov de Haas oscillations in GaAs quantum wells in tilted magnetic fields. *Physical Review B*,

85(24):241305, June 2012. ISSN 1098-0121. doi: 10.1103/PhysRevB.85.241305. URL http://prb.aps.org/abstract/PRB/v85/i24/e241305.

[9] X. Lin, C. Dillard, and MA Kastner. Measurements of quasi-particle tunneling in the nu= 5/2 fractional quantum Hall state. *Physical Review B*, 85(16):165321, 2012. URL http://prb.aps.org/abstract/PRB/v85/i16/e165321.

[10] C. Dillard, X. Lin, and MA Kastner. Breakdown of the integer and fractional quantum Hall states in a quantum point contact. *arXiv:1204.5712*, April 2012. URL http://arxiv.org/abs/1204.5712.

[11] D. Yoshioka. *The quantum Hall effect*. Springer-Verlag Berlin and Heidelberg GmbH & Co., 2002. ISBN 978-3540431152. URL http://pdfserv.aip.org/PHTOAD/vol_40/iss_3/93_1.pdf.

[12] M. Büttiker. Absence of backscattering in the quantum Hall effect in multiprobe conductors. *Physical Review B*, 38(14):9375–9389, November 1988. URL http://prb.aps.org/abstract/PRB/v38/i14/p9375_1.

[13] P. Roulleau, F. Portier, P. Roche, A. Cavanna, G. Faini, U. Gennser, and D. Mailly. Direct Measurement of the Coherence Length of Edge States in the Integer Quantum Hall Regime. *Physical Review Letters*, 100(12):126802, March 2008. URL http://prl.aps.org/abstract/PRL/v100/i12/e126802.

[14] M. Reznikov, M. Heiblum, Hadas Shtrikman, and D. Mahalu. Temporal Correlation of Electrons: Suppression of Shot Noise in a Ballistic Quantum Point Contact. *Physical Review Letters*, 75(18):3340–3343, October 1995. URL http://prl.aps.org/abstract/PRL/v75/i18/p3340_1.

[15] A. Kumar, L. Saminadayar, D. Glattli, Y. Jin, and B. Etienne. Experimental Test of the Quantum Shot Noise Reduction Theory. *Physical Review Letters*, 76 (15):2778–2781, April 1996. URL http://prl.aps.org/abstract/PRL/v76/i15/p2778_1.

[16] M. Büttiker. Quantized transmission of a saddle-point constriction. *Physical Review B*, 41(11):7906–7909, 1990. URL http://link.aps.org/doi/10.1103/PhysRevB.41.7906.

[17] B. van Wees, L. Kouwenhoven, H. van Houten, C. Beenakker, J. Mooij, C. Foxon, and J. Harris. Quantized conductance of magnetoelectric subbands in ballistic point contacts. *Physical Review B*, 38(5):3625–3627, August 1988. URL http://prb.aps.org/abstract/PRB/v38/i5/p3625_1.

[18] L. Litvin, H.-P. Tranitz, W. Wegscheider, and C. Strunk. Decoherence and single electron charging in an electronic Mach-Zehnder interferometer. *Physical Review B*, 75(3):033315, January 2007. URL `http://prb.aps.org/abstract/PRB/v75/i3/e033315`.

[19] E. Bieri, M. Weiss, O. Göktas, M. Hauser, C. Schönenberger, and S. Oberholzer. Finite-bias visibility dependence in an electronic Mach-Zehnder interferometer. *Physical Review B*, 79(24):245324, June 2009. URL `http://prb.aps.org/abstract/PRB/v79/i24/e245324`.

[20] S. Oberholzer, M. Henny, C. Strunk, C. Schönenberger, T. Heinzel, K. Ensslin, and M. Holland. The Hanbury Brown and Twiss experiment with fermions. *Physica E: Low-dimensional Systems and Nanostructures*, 6(1-4):314–317, 2000. URL `http://www.sciencedirect.com/science/article/pii/S1386947799001629`.

[21] H. Kiesel, A. Renz, and F. Hasselbach. Observation of Hanbury Brown-Twiss anticorrelations for free electrons. *Nature*, 418(6896):392–4, July 2002. ISSN 0028-0836. doi: 10.1038/nature00911. URL `http://www.nature.com/nature/journal/v418/n6896/full/nature00911.html`.

[22] C. K. Hong, Z. Y. Ou, and L. Mandel. Measurement of subpicosecond time intervals between two photons by interference. *Physical Review Letters*, 59(18):2044–2046, November 1987. ISSN 0031-9007. doi: 10.1103/PhysRevLett.59.2044. URL `http://prl.aps.org/abstract/PRL/v59/i18/p2044_1`.

[23] G. Fève, Pascal Degiovanni, and Th. Jolicoeur. Quantum detection of electronic flying qubits in the integer quantum Hall regime. *Physical Review B*, 77(3):035308, January 2008. URL `http://prb.aps.org/abstract/PRB/v77/i3/e035308`.

[24] S. Olkhovskaya, J. Splettstoesser, M. Moskalets, and M. Büttiker. Shot Noise of a Mesoscopic Two-Particle Collider. *Physical Review Letters*, 101(16):1–4, October 2008. ISSN 0031-9007. doi: 10.1103/PhysRevLett.101.166802. URL `http://link.aps.org/doi/10.1103/PhysRevLett.101.166802`.

[25] I. Neder, N. Ofek, Y. Chung, M. Heiblum, D. Mahalu, and V. Umansky. Interference between two indistinguishable electrons from independent sources. *Nature*, 448(7151):333–337, 2007. URL `http://dx.doi.org/10.1038/nature05955`.

[26] S. Hermelin, S. Takada, M. Yamamoto, S. Tarucha, A.D. Wieck, L. Saminadayar, C. Bäuerle, and T. Meunier. Electrons surfing on a sound wave as a platform for quantum optics with flying electrons. *Nature*, 477(7365):25, July 2011. URL `http://www.nature.com/nature/journal/v477/n7365/abs/nature10416.html`.

[27] S.P. Giblin, M. Kataoka, J.D. Fletcher, P. See, T.J.B.M. Janssen, J.P. Griffiths, G.A.C. Jones, I. Farrer, and D.A. Ritchie. Towards a quantum representation of the ampere using single electron pumps. *Nature communications*, 3:930, January 2012. ISSN 2041-1723. doi: 10.1038/ncomms1935. URL http://www.nature.com/ncomms/journal/v3/n7/abs/ncomms1935.html.

[28] J.M. Shilton, V.I. Talyanskii, M. Pepper, D.A. Ritchie, J.E.F. Frost, C.J.B. Ford, C.G. Smith, and G.A.C. Jones. High-frequency single-electron transport in a quasi-one-dimensional GaAs channel induced by surface acoustic waves. *Journal of Physics: Condensed Matter*, 8(38):L531, 1996. URL http://stacks.iop.org/0953-8984/8/i=38/a=001.

[29] V. Talyanskii, J. Shilton, M. Pepper, C. Smith, C. Ford, E. Linfield, D. Ritchie, and G. Jones. Single-electron transport in a one-dimensional channel by high-frequency surface acoustic waves. *Physical Review B*, 56(23):15180–15184, December 1997. URL http://prb.aps.org/abstract/PRB/v56/i23/p15180_1.

[30] J. Cunningham, V. Talyanskii, J. Shilton, M. Pepper, M. Simmons, and D. Ritchie. Single-electron acoustic charge transport by two counterpropagating surface acoustic wave beams. *Physical Review B*, 60(7):4850–4855, August 1999. URL http://prb.aps.org/abstract/PRB/v60/i7/p4850_1.

[31] A. Robinson and V. Talyanskii. Shot Noise in the Current of a Surface Acoustic-Wave-Driven Single-Electron Pump. *Physical Review Letters*, 95(24):247202, December 2005. URL http://prl.aps.org/abstract/PRL/v95/i24/e247202.

[32] R.P.G. McNeil, M. Kataoka, and C.J.B. Ford. On-demand single-electron transfer between distant quantum dots. *Nature*, 477(7365):439–442, 2011. URL http://www.nature.com/nature/journal/v477/n7365/abs/nature10444.html.

[33] M.D. Blumenthal, B. Kaestner, L. Li, S. Giblin, T.J.B.M. Janssen, M. Pepper, D. Anderson, G. Jones, and D A Ritchie. Gigahertz quantized charge pumping. *Nature Physics*, 3(5):343–347, April 2007. ISSN 1745-2473. doi: 10.1038/nphys582. URL http://www.nature.com/doifinder/10.1038/nphys582.

[34] N. Maire, F. Hohls, B. Kaestner, K. Pierz, H. W. Schumacher, and R. J. Haug. Noise measurement of a quantized charge pump. *Applied Physics Letters*, 92 (8):082112, February 2008. URL http://link.aip.org/link/APPLAB/v92/i8/p082112/s1/html.

[35] F. Battista and P. Samuelsson. Proposal for nonlocal electron-hole turnstile in the quantum Hall regime. *Physical Review B*, 83(12):125324, March 2011. ISSN

1098-0121. doi: 10.1103/PhysRevB.83.125324. URL http://link.aps.org/doi/10.1103/PhysRevB.83.125324.

[36] S.P. Giblin, S.J. Wright, J.D. Fletcher, M. Kataoka, M. Pepper, T.J.B.M. Janssen, D.A. Ritchie, C.A. Nicoll, D. Anderson, and G.A.C. Jones. An accurate high-speed single-electron quantum dot pump. *New Journal of Physics*, 12(7):073013, July 2010. URL http://stacks.iop.org/1367-2630/12/i=7/a=073013.

[37] J.P. Pekola, O.-P. Saira, V.F. Maisi, A. Kemppinen, M. Möttönen, Y.A. Pashkin, and D.V. Averin. Single-electron current sources: towards a refined definition of ampere. *arXiv:1208.4030*, August 2012. URL http://arxiv.org/abs/1208.4030.

[38] L.S. Levitov, H.-W. Lee, and G.B. Lesovik. Electron Counting Statistics and Coherent States of Electric Current. *Journal of Mathematical Physics*, 37(10):43, 1996. URL http://jmp.aip.org/resource/1/jmapaq/v37/i10/p4845_s1.

[39] J. Keeling, I. Klich, and L. Levitov. Minimal Excitation States of Electrons in One-Dimensional Wires. *Physical Review Letters*, 97(11):116403, September 2006. ISSN 0031-9007. doi: 10.1103/PhysRevLett.97.116403. URL http://prl.aps.org/abstract/PRL/v97/i11/e116403.

[40] F. Hassler, B. Küng, G.B. Lesovik, and G. Blatter. Single-Particle Excitations Generated by Voltage Pulses. *AIP Conf. Proc.*, 1134:113, 2009. URL http://proceedings.aip.org/resource/2/apcpcs/1134/1/113_1.

[41] M. Büttiker, H. Thomas, and A. Prêtre. Mesoscopic capacitors. *Physics Letters A*, 180(4-5):364–369, September 1993. ISSN 03759601. doi: 10.1016/0375-9601(93)91193-9. URL http://dx.doi.org/10.1016/0375-9601(93)91193-9.

[42] G. Fève, A. Mahé, J.-M. Berroir, T. Kontos, B. Plaçais, D.C. Glattli, A. Cavanna, B. Etienne, and Y. Jin. An on-demand coherent single-electron source. *Science*, 316(5828):1169–72, May 2007. ISSN 1095-9203. doi: 10.1126/science.1141243. URL http://www.sciencemag.org/content/316/5828/1169.abstract.

[43] R. Loudon. *The Quantum Theory of Light*. Oxford University Press, 1983. ISBN 0-19-851155-8.

[44] C. Grenier. *Optique quantique électronique*. PhD thesis, Université de Lyon - Ecole Normale Supérieure de Lyon, June 2011. URL http://tel.archives-ouvertes.fr/tel-00617869.

[45] C. Grenier, R. Hervé, G. Fève, and P. Degiovanni. Electron quantum optics in quantum Hall edge channels. *Modern Physics Letters B*, 25(12n13):1053–1073,

May 2011. ISSN 0217-9849. doi: 10.1142/S0217984911026772. URL http://www.worldscientific.com/doi/abs/10.1142/S0217984911026772.

[46] C. Grenier, R. Hervé, E. Bocquillon, F.D. Parmentier, B. Plaçais, J.M. Berroir, G. Fève, and P. Degiovanni. Single-electron quantum tomography in quantum Hall edge channels. *New Journal of Physics*, 13(9):093007, September 2011. ISSN 1367-2630. doi: 10.1088/1367-2630/13/9/093007. URL http://stacks.iop.org/1367-2630/13/i=9/a=093007.

[47] P. Degiovanni, C. Grenier, and G. Fève. Decoherence and relaxation of single-electron excitations in quantum Hall edge channels. *Physical Review B*, 80(24): 241307, December 2009. ISSN 1098-0121. doi: 10.1103/PhysRevB.80.241307. URL http://prb.aps.org/abstract/PRB/v80/i24/e241307.

[48] P. Degiovanni, C. Grenier, G. Fève, C. Altimiras, H. Le Sueur, and F. Pierre. Plasmon scattering approach to energy exchange and high-frequency noise in ν=2 quantum Hall edge channels. *Physical Review B*, 81(12):121302, March 2010. ISSN 1098-0121. doi: 10.1103/PhysRevB.81.121302. URL http://prb.aps.org/abstract/PRB/v81/i12/e121302.

[49] C. Altimiras, H. Le Sueur, U. Gennser, A. Cavanna, D. Mailly, and F. Pierre. Non-equilibrium edge-channel spectroscopy in the integer quantum Hall regime. *Nature Physics*, 6(1):34–39, 2009. ISSN 1745-2473. URL http://www.nature.com/nphys/journal/vaop/ncurrent/full/nphys1429.html.

[50] C. Altimiras, H. Le Sueur, U. Gennser, A. Cavanna, D. Mailly, and F Pierre. Tuning Energy Relaxation along Quantum Hall Channels. *Physical Review Letters*, 105(22):226804, 2010. URL http://link.aps.org/doi/10.1103/PhysRevLett.105.226804.

[51] H. Le Sueur, C. Altimiras, U. Gennser, A. Cavanna, D. Mailly, and F. Pierre. Energy relaxation in the integer quantum Hall regime. *Physical Review Letters*, 105 (5):056803, 2010. URL http://prl.aps.org/abstract/PRL/v105/i5/e056803.

[52] P.-A. Huynh, F. Portier, H. le Sueur, G. Faini, U. Gennser, D. Mailly, F. Pierre, W. Wegscheider, and P. Roche. Quantum coherence engineering in the integer quantum Hall regime. *Physical Review Letters*, 108(25):4, February 2012. doi: 10.1103/PhysRevLett.108.256802. URL http://prl.aps.org/abstract/PRL/v108/i25/e256802.

[53] H. C. Lee and S. R. E. Yang. Spin-charge separation in Quantum Hall Liquids. *Physical Review B*, 56(24):R15529–R15532, 1997. URL http://prb.aps.org/abstract/PRB/v56/i24/pR15529_1.

[54] K.-V. Pham, M. Gabay, and P. Lederer. Fractional excitations in the Luttinger liquid. *Physical Review B*, 61(24):16397–16422, June 2000. ISSN 0163-1829. doi: 10.1103/PhysRevB.61.16397. URL `http://link.aps.org/doi/10.1103/PhysRevB.61.16397`.

[55] E.V. Sukhorukov and V.V. Cheianov. Resonant dephasing in the electronic Mach-Zehnder interferometer. *Physical Review Letters*, 99(15):156801, 2007. URL `http://link.aps.org/doi/10.1103/PhysRevLett.99.156801`.

[56] E. Berg, Y. Oreg, E.-A. Kim, and F. von Oppen. Fractional Charges on an Integer Quantum Hall Edge. *Physical Review Letters*, 102(23):1–4, June 2009. ISSN 0031-9007. doi: 10.1103/PhysRevLett.102.236402. URL `http://link.aps.org/doi/10.1103/PhysRevLett.102.236402`.

[57] S. Oberholzer, E. Bieri, C. Schönenberger, M. Giovannini, and J. Faist. Positive Cross Correlations in a Normal-Conducting Fermionic Beam Splitter. *Physical Review Letters*, 96(4):046804, February 2006. ISSN 0031-9007. doi: 10.1103/PhysRevLett.96.046804. URL `http://link.aps.org/doi/10.1103/PhysRevLett.96.046804`.

[58] P. Roulleau, F. Portier, P. Roche, A. Cavanna, G. Faini, U. Gennser, and D. Mailly. Noise Dephasing in Edge States of the Integer Quantum Hall Regime. *Physical Review Letters*, 101(18):186803, October 2008. ISSN 0031-9007. doi: 10.1103/PhysRevLett.101.186803. URL `http://prl.aps.org/abstract/PRL/v101/i18/e186803`.

[59] I.P. Levkivskyi and E.V. Sukhorukov. Dephasing in the electronic Mach-Zehnder interferometer at filling factor ν=2. *Physical Review B*, 78(4):14, July 2008. ISSN 1098-0121. doi: 10.1103/PhysRevB.78.045322. URL `http://link.aps.org/doi/10.1103/PhysRevB.78.045322`.

[60] A.M. Lunde, S.E. Nigg, and M. Büttiker. Interaction-induced edge channel equilibration. *Physical Review B*, 81(4):10, January 2010. ISSN 1098-0121. doi: 10.1103/PhysRevB.81.041311. URL `http://link.aps.org/doi/10.1103/PhysRevB.81.041311`.

[61] D.L. Kovrizhin and J.T. Chalker. Equilibration of integer quantum Hall edge states. *Physical Review B*, 84(8):085105, September 2011. URL `http://prb.aps.org/abstract/PRB/v84/i8/e085105`.

[62] D.L. Kovrizhin and J.T. Chalker. Relaxation in driven integer quantum Hall edge states. *Physical Review Letters*, 109(10):106403, 2012. URL `http://link.aps.org/doi/10.1103/PhysRevLett.109.106403`.

[63] I.P. Levkivskyi and E.V. Sukhorukov. Energy relaxation at quantum Hall edge. *Physical Review B*, 85(7):075309, 2012. URL http://prb.aps.org/abstract/PRB/v85/i7/e075309.

[64] I. Neder, M. Heiblum, Y. Levinson, D. Mahalu, and V. Umansky. Unexpected Behavior in a Two-Path Electron Interferometer. *Physical Review Letters*, 96(1): 016804, January 2006. doi: 10.1103/PhysRevLett.96.016804. URL http://link.aps.org/doi/10.1103/PhysRevLett.96.016804.

[65] P. Roulleau, F. Portier, D. Glattli, P. Roche, A. Cavanna, G. Faini, U. Gennser, and D. Mailly. Finite bias visibility of the electronic Mach-Zehnder interferometer. *Physical Review B*, 76(16):161309, October 2007. URL http://prb.aps.org/abstract/PRB/v76/i16/e161309.

[66] I.P. Levkivskyi and E.V. Sukhorukov. Noise-induced phase transition in the electronic Mach-Zehnder interferometer. *Physical Review Letters*, 103(3):4, March 2009. URL http://prl.aps.org/abstract/PRL/v103/i3/e036801.

[67] P. Roulleau, F. Portier, P. Roche, A. Cavanna, G. Faini, U. Gennser, and D. Mailly. Tuning Decoherence with a Voltage Probe. *Physical Review Letters*, 102(23): 236802, June 2009. ISSN 0031-9007. doi: 10.1103/PhysRevLett.102.236802. URL http://prl.aps.org/abstract/PRL/v102/i23/e236802.

[68] P.-A. Huynh. *Amélioration de la cohérence quantique dans le régime d'effet Hall quantique entier*. PhD thesis, Université Paris Sud - Paris XI, February 2012. URL http://tel.archives-ouvertes.fr/tel-00683582.

[69] O.M. Auslaender, H. Steinberg, A. Yacoby, Y. Tserkovnyak, B.I. Halperin, K.W. Baldwin, L.N. Pfeiffer, and K.W. West. Spin-charge separation and localization in one dimension. *Science*, 308(5718):88–92, April 2005. ISSN 1095-9203. doi: 10.1126/science.1107821. URL http://www.sciencemag.org/content/308/5718/88.abstract.

[70] H. Steinberg, G. Barak, A. Yacoby, L.N. Pfeiffer, K.W. West, B.I. Halperin, and K. Le Hur. Charge fractionalization in quantum wires. *Nature Physics*, 4(2): 116–119, December 2007. ISSN 1745-2473. doi: 10.1038/nphys810. URL http://www.nature.com/nphys/journal/vaop/ncurrent/full/nphys810.html.

[71] Y. Jompol, C.J.B. Ford, J.P. Griffiths, I. Farrer, G.A.C. Jones, D. Anderson, D.A. Ritchie, T.W. Silk, and A.J. Schofield. Probing spin-charge separation in a Tomonaga-Luttinger liquid. *Science*, 325(5940):597–601, July 2009. ISSN 1095-9203. doi: 10.1126/science.1171769. URL http://www.sciencemag.org/content/325/5940/597.short.

[72] R.C. Ashoori, H.L. Stormer, and L.N. Pfeiffer. Edge magnetoplasmons in the time domain. *Physical Review B*, 45(7):3894–3897, 1992. URL `http://prb.aps.org/abstract/PRB/v45/i7/p3894_1`.

[73] N. Zhitenev, R. Haug, K. Klitzing, and K. Eberl. Time-resolved measurements of transport in edge channels. *Physical Review Letters*, 71(14):2292–2295, October 1993. ISSN 0031-9007. doi: 10.1103/PhysRevLett.71.2292. URL `http://prl.aps.org/abstract/PRL/v71/i14/p2292_1`.

[74] G. Sukhodub, F. Hohls, and R. Haug. Observation of an Interedge Magnetoplasmon Mode in a Degenerate Two-Dimensional Electron Gas. *Physical Review Letters*, 93(19):2–5, November 2004. ISSN 0031-9007. doi: 10.1103/PhysRevLett.93.196801. URL `http://link.aps.org/doi/10.1103/PhysRevLett.93.196801`.

[75] H. Kamata, T. Ota, K. Muraki, and T. Fujisawa. Voltage-controlled group velocity of edge magnetoplasmon in the quantum Hall regime. *Physical Review B*, 81(8):085329, 2010. URL `http://prb.aps.org/abstract/PRB/v81/i8/e085329`.

[76] N. Kumada, H. Kamata, and T. Fujisawa. Edge magnetoplasmon transport in gated and ungated quantum Hall systems. *Physical Review B*, 84(4):1–6, July 2011. ISSN 1098-0121. doi: 10.1103/PhysRevB.84.045314. URL `http://link.aps.org/doi/10.1103/PhysRevB.84.045314`.

[77] D.C. Glattli, E. Andrei, G. Deville, J. Poitrenaud, and F. Williams. Dynamical Hall Effect in a Two-Dimensional Classical Plasma. *Physical Review Letters*, 54(15):1710–1713, April 1985. ISSN 0031-9007. doi: 10.1103/PhysRevLett.54.1710. URL `http://prl.aps.org/abstract/PRL/v54/i15/p1710_1`.

[78] J. Gabelli, G. Fève, T. Kontos, J.-M. Berroir, B. Plaçais, D.C. Glattli, B. Etienne, Y. Jin, and M. Büttiker. Relaxation time of a chiral quantum RL circuit. *Physical Review Letters*, 98(16):166806, 2007. URL `http://link.aps.org/doi/10.1103/PhysRevLett.98.166806`.

[79] V. Talyanskii, A. Polisski, D. Arnone, M. Pepper, C. Smith, D. Ritchie, J. Frost, and G. Jones. Spectroscopy of a two-dimensional electron gas in the quantum-Hall-effect regime by use of low-frequency edge magnetoplasmons. *Physical Review B*, 46(19):12427–12432, November 1992. ISSN 0163-1829. doi: 10.1103/PhysRevB.46.12427. URL `http://prb.aps.org/abstract/PRB/v46/i19/p12427_1`.

[80] M. Hashisaka, K. Washio, H. Kamata, K. Muraki, and T. Fujisawa. Distributed electrochemical capacitance evidenced in high-frequency admittance measurements on a quantum Hall device. *Physical Review B*, 85(15):155424, April 2012.

ISSN 1098-0121. doi: 10.1103/PhysRevB.85.155424. URL http://prb.aps.org/abstract/PRB/v85/i15/e155424.

[81] I. Petkovic, F.I.B. Williams, K. Bennaceur, F. Portier, P. Roche, and D. C. Glattli. Chiral magneto-plasmons on the quantum Hall edge in graphene. *arXiv:1206.2940*, June 2012. URL http://arxiv.org/abs/1206.2940.

[82] J. Gabelli. *Mise en évidence de la cohérence quantique des conducteurs en régime dynamique*. PhD thesis, Université Pierre et Marie Curie Paris 6, 2006. URL http://tel.archives-ouvertes.fr/tel-00011619.

[83] A. Mahé. *Bruit de charge d'une source d'électrons uniques subnanoseconde*. PhD thesis, Université Pierre et Marie Curie - Paris 6, 2009. URL http://tel.archives-ouvertes.fr/tel-00440198.

[84] F.D. Parmentier. *Short-Time Hanbury Brown & Twiss correlations of single-electron beams*. PhD thesis, Université Pierre et Marie Curie, 2010. URL http://tel.archives-ouvertes.fr/tel-00556458.

[85] L.-H. Reydellet, P. Roche, D. C. Glattli, B. Etienne, and Y. Jin. Quantum partition noise of photo-created electron-hole pairs. *Physical Review Letters*, 90(17):176803, 2003. URL http://prl.aps.org/abstract/PRL/v90/i17/e176803.

[86] M.L. Polianski, P. Samuelsson, and M. Buttiker. Shot noise of photon-excited electron-hole pairs in open quantum dots. *Physical Review B*, 55(3):4, 2005. URL http://arxiv.org/abs/cond-mat/0507336.

[87] V. Rychkov, M. Polianski, and M. Büttiker. Photon-assisted electron-hole shot noise in multiterminal conductors. *Physical Review B*, 72(15):155326, October 2005. ISSN 1098-0121. doi: 10.1103/PhysRevB.72.155326. URL http://prb.aps.org/abstract/PRB/v72/i15/e155326.

[88] M. Vanević, Y.V. Nazarov, and W. Belzig. Elementary Events of Electron Transfer in a Voltage-Driven Quantum Point Contact. *Physical Review Letters*, 99(7):4, August 2007. ISSN 0031-9007. doi: 10.1103/PhysRevLett.99.076601. URL http://link.aps.org/doi/10.1103/PhysRevLett.99.076601.

[89] M. Vanević, Y.V. Nazarov, and W. Belzig. Elementary charge-transfer processes in mesoscopic conductors. *Physical Review B*, 78(24):1–14, December 2008. ISSN 1098-0121. doi: 10.1103/PhysRevB.78.245308. URL http://link.aps.org/doi/10.1103/PhysRevB.78.245308.

[90] M. Moskalets and M. Büttiker. Time-resolved noise of adiabatic quantum pumps. *Physical Review B*, 75(3):035315, January 2007. URL http://prb.aps.org/abstract/PRB/v75/i3/e035315.

[91] F.D. Parmentier, E. Bocquillon, J.-M. Berroir, D. Glattli, B. Plaçais, G. Fève, M. Albert, C. Flindt, and M. Büttiker. Current noise spectrum of a single-particle emitter: Theory and experiment. *Physical Review B*, 85(16):17, April 2012. ISSN 1098-0121. doi: 10.1103/PhysRevB.85.165438. URL `http://link.aps.org/doi/10.1103/PhysRevB.85.165438`.

[92] M. Moskalets. Floquet scattering theory of quantum pumps. *Physical Review B*, 66 (20):205320, 2002. URL `http://prb.aps.org/abstract/PRB/v66/i20/e205320`.

[93] J. Keeling, A. Shytov, and L. Levitov. Coherent Particle Transfer in an On-Demand Single-Electron Source. *Physical Review Letters*, 101(19):1–4, November 2008. ISSN 0031-9007. doi: 10.1103/PhysRevLett.101.196404. URL `http://link.aps.org/doi/10.1103/PhysRevLett.101.196404`.

[94] T. Jonckheere, T. Stoll, J. Rech, and T Martin. Real-time simulation of finite-frequency noise from a single-electron emitter. *Physical Review B*, 85(4):045321, November 2012. URL `http://prb.aps.org/abstract/PRB/v85/i4/e045321`.

[95] A. Mahé, F.D. Parmentier, E. Bocquillon, J.-M. Berroir, D.C. Glattli, T. Kontos, B. Plaçais, G. Fève, A. Cavanna, and Y. Jin. Current correlations of an on-demand single-electron emitter. *Physical Review B*, 82(20):201309, April 2010. URL `http://link.aps.org/abstract/PRB/v82/e201309/`.

[96] E. Bocquillon, F. Parmentier, C. Grenier, J.-M. Berroir, P. Degiovanni, D. Glattli, B. Plaçais, A. Cavanna, Y. Jin, and G. Fève. Electron Quantum Optics: Partitioning Electrons One by One. *Physical Review Letters*, 108(19): 5, May 2012. ISSN 0031-9007. doi: 10.1103/PhysRevLett.108.196803. URL `http://link.aps.org/doi/10.1103/PhysRevLett.108.196803`.

[97] T. Taniguchi and M. Büttiker. Friedel phases and phases of transmission amplitudes in quantum scattering systems. *Physical Review B*, 60(19):13814–13823, November 1999. ISSN 0163-1829. doi: 10.1103/PhysRevB.60.13814. URL `http://link.aps.org/doi/10.1103/PhysRevB.60.13814`.

[98] S. Nigg and M. Büttiker. Quantum to classical transition of the charge relaxation resistance of a mesoscopic capacitor. *Physical Review B*, 77(8):085312, 2008. URL `http://link.aps.org/doi/10.1103/PhysRevB.77.085312`.

[99] C. Mora and K. Le Hur. Universal resistances of the quantum resistance-capacitance circuit. *Nature Physics*, 6(9):697–701, June 2010. URL `http://dx.doi.org/10.1038/nphys1690`.

[100] J. Splettstoesser, M. Governale, J. König, and M. Büttiker. Charge and spin dynamics in interacting quantum dots. *Physical Review B*, 81(16):5, April 2010.

ISSN 1098-0121. doi: 10.1103/PhysRevB.81.165318. URL http://link.aps.org/doi/10.1103/PhysRevB.81.165318.

[101] Y. Hamamoto, T. Jonckheere, T. Kato, and T. Martin. Quantum phase transition of dynamical resistance in a mesoscopic capacitor. *Journal of Physics: Conference Series*, 334:012033, July 2011. URL http://iopscience.iop.org/1742-6596/334/1/012033.

[102] L. Debora Contreras-Pulido, Janine Splettstoesser, Michele Governale, Jürgen König, and Markus Büttiker. Time scales in the dynamics of an interacting quantum dot. *Physical Review B*, 85(7):075301, November 2011. URL http://prb.aps.org/abstract/PRB/v85/i7/e075301.

[103] M. Filippone, K. Le Hur, and C. Mora. Giant Charge Relaxation Resistance in the Anderson Model. *Physical Review Letters*, 107(17):176601, 2011. URL http://link.aps.org/doi/10.1103/PhysRevLett.107.176601.

[104] M. Lee, R. Lopez, M.S. Choi, T. Jonckheere, and T. Martin. Effect of many-body correlations on mesoscopic charge relaxation. *Physical Review B*, 83(20):201304, January 2011. URL http://prb.aps.org/abstract/PRB/v83/i20/e201304.

[105] M. Filippone and C. Mora. Fermi liquid approach to the quantum RC circuit: Renormalization group analysis of the Anderson and Coulomb blockade models. *Physical Review B*, 86(12):125311, May 2012. URL http://prb.aps.org/abstract/PRB/v86/i12/e125311.

[106] A. Mahé, F.D. Parmentier, A. Cavanna, T. Kontos, B. Etienne, Y. Jin, and D.C. Glattli. Subnanosecond single electron source in the time-domain. *Journal of Low Temperature Physics*, 153(5-6):339–349, 2008. URL http://www.springerlink.com/index/U2U5V631R2705775.pdf.

[107] J. Gabelli, G. Fève, J.-M. Berroir, B. Plaçais, A. Cavanna, B. Etienne, Y. Jin, and D.C. Glattli. Violation of Kirchhoff's laws for a coherent RC circuit. *Science*, 313 (5786):499–502, July 2006. ISSN 1095-9203. doi: 10.1126/science.1126940. URL http://www.sciencemag.org/cgi/content/abstract/313/5786/499.

[108] F. Lefloch, C. Hoffmann, M. Sanquer, and D. Quirion. Doubled Full Shot Noise in Quantum Coherent Superconductor-Semiconductor Junctions. *Physical Review Letters*, 90(6), February 2003. ISSN 0031-9007. doi: 10.1103/PhysRevLett.90.067002. URL http://prl.aps.org/abstract/PRL/v90/i6/e067002.

[109] R. Danneau, F. Wu, M. Craciun, S. Russo, M. Tomi, J. Salmilehto, A. Morpurgo, and P. Hakonen. Shot Noise in Ballistic Graphene. *Physical Review Letters*, 100

(19):1–4, May 2008. ISSN 0031-9007. doi: 10.1103/PhysRevLett.100.196802. URL http://link.aps.org/doi/10.1103/PhysRevLett.100.196802.

[110] E. Zakka-Bajjani, J. Dufouleur, N. Coulombel, P. Roche, D.C. Glattli, and F. Portier. Experimental determination of the statistics of photons emitted by a tunnel junction. *Physical review letters*, 104(20):206802, May 2010. ISSN 1079-7114. URL http://link.aps.org/doi/10.1103/PhysRevLett.104.215501.

[111] C. Emary, C. Pöltl, A. Carmele, and J. Kabuss. Bunching and antibunching in electronic transport. *Physical Review B*, 85(16):165417, 2012. URL http://prb.aps.org/abstract/PRB/v85/i16/e165417.

[112] C. Beenakker and H. Schomerus. Counting Statistics of Photons Produced by Electronic Shot Noise. *Physical Review Letters*, 86(4):700–703, January 2001. ISSN 0031-9007. doi: 10.1103/PhysRevLett.86.700. URL http://link.aps.org/doi/10.1103/PhysRevLett.86.700.

[113] C. Beenakker and H. Schomerus. Antibunched Photons Emitted by a Quantum Point Contact out of Equilibrium. *Physical Review Letters*, 93(9):4, August 2004. ISSN 0031-9007. doi: 10.1103/PhysRevLett.93.096801. URL http://link.aps.org/doi/10.1103/PhysRevLett.93.096801.

[114] F.D. Parmentier, A. Mahé, A. Denis, J.-M. Berroir, D.C. Glattli, B. Plaçais, and G. Fève. A high sensitivity ultralow temperature RF conductance and noise measurement setup. *The Review of scientific instruments*, 82(1):013904, January 2011. ISSN 1089-7623. doi: 10.1063/1.3518945. URL http://link.aip.org/link/doi/10.1063/1.3518945/html.

[115] M. Albert, C. Flindt, and M. Büttiker. Accuracy of the quantum capacitor as a single-electron source. *Physical Review B*, 82(4):41407, 2010. URL http://arxiv.org/pdf/1004.4510.

[116] M. Albert, C. Flindt, and M. Büttiker. Distributions of Waiting Times of Dynamic Single-Electron Emitters. *Physical Review Letters*, 107(8):086805, August 2011. ISSN 0031-9007. doi: 10.1103/PhysRevLett.107.086805. URL http://link.aps.org/doi/10.1103/PhysRevLett.107.086805.

[117] M. Albert, C. Flindt, and M. Büttiker. Noise and Counting Statistics of a Single Electron Emitter: Theory. February 2011. URL http://arxiv.org/abs/1102.2343.

[118] G. Lesovik and L. Levitov. Noise in an ac biased junction: Nonstationary Aharonov-Bohm effect. *Physical Review Letters*, 72(4):538–541, January 1994.

ISSN 0031-9007. doi: 10.1103/PhysRevLett.72.538. URL http://prl.aps.org/abstract/PRL/v72/i4/p538_1.

[119] M. Pedersen and M. Büttiker. Scattering theory of photon-assisted electron transport. *Physical Review B*, 58(19):12993–13006, November 1998. ISSN 0163-1829. doi: 10.1103/PhysRevB.58.12993. URL http://link.aps.org/doi/10.1103/PhysRevB.58.12993.

[120] R. Hanbury-Brown and R.Q. Twiss. A Test of a New Type of Stellar Interferometer on Sirius. *Nature*, 178(4541):1046–1048, November 1956. ISSN 0028-0836. doi: 10.1038/1781046a0. URL http://www.nature.com/nature/journal/v178/n4541/pdf/1781046a0.pdf.

[121] R. Hanbury-Brown and R.Q. Twiss. Correlation between Photons in two Coherent Beams of Light. *Nature*, 177(4497):27–29, January 1956. ISSN 0028-0836. doi: 10.1038/177027a0. URL http://www.nature.com/nature/journal/v177/n4497/pdf/177027a0.pdf.

[122] W.D. Oliver, J. Kim, R.C. Liu, and Y. Yamamoto. Hanbury Brown and Twiss-type experiment with electrons. *Science*, 284(5412):299–301, April 1999. ISSN 00368075. doi: 10.1126/science.284.5412.299. URL http://www.sciencemag.org/content/284/5412/299.abstracthttp://www.sciencemag.org/content/284/5412/299.short.

[123] J. Gabelli, L.-H. Reydellet, G. Fève, J.-M. Berroir, B. Plaçais, P. Roche, and D.C. Glattli. Hanbury-Brown Twiss correlations to probe the population statistics of GHz photons emitted by conductors. *Physical Review Letters*, 93(5):056801, 2004. URL http://prl.aps.org/abstract/PRL/v93/i5/e056801.

[124] T. Jeltes, J.M. McNamara, W. Hogervorst, W. Vassen, V. Krachmalnicoff, M. Schellekens, A. Perrin, H. Chang, D. Boiron, A. Aspect, and C. Westbrook. Comparison of the Hanbury Brown-Twiss effect for bosons and fermions. *Nature*, 445(7126):402–405, 2006. URL http://www.nature.com/nature/journal/v445/n7126/full/nature05513.html.

[125] Y. Bromberg, Y. Lahini, E. Small, and Y. Silberberg. Hanbury Brown and Twiss interferometry with interacting photons. *Nature Photonics*, 4(October):721–726, 2010. ISSN 17494885. doi: 10.1038/NPHOTON.2010.195. URL http://dx.doi.org/10.1038/nphoton.2010.195.

[126] T. Rejec and Y. Meir. Magnetic impurity formation in quantum point contacts. *Nature*, 442(7105):7, 2006. URL http://www.nature.com/nature/journal/v442/n7105/abs/nature05054.html.

[127] G. Haack, M. Moskalets, J. Splettstoesser, and M. Büttiker. Coherence of single-electron sources from Mach-Zehnder interferometry. *Physical Review B*, 84(8): 081303, 2011. URL http://prb.aps.org/abstract/PRB/v84/i8/e081303.

[128] D. Smithey, M. Beck, M. Raymer, and A. Faridani. Measurement of the Wigner distribution and the density matrix of a light mode using optical homodyne tomography: Application to squeezed states and the vacuum. *Physical Review Letters*, 70 (9):1244–1247, March 1993. ISSN 0031-9007. doi: 10.1103/PhysRevLett.70.1244. URL http://prl.aps.org/abstract/PRL/v70/i9/p1244_1.

[129] P. Bertet, A. Auffeves, P. Maioli, S. Osnaghi, T. Meunier, M. Brune, J.-M. Raimond, and S. Haroche. Direct Measurement of the Wigner Function of a One-Photon Fock State in a Cavity. *Physical Review Letters*, 89(20):200402, October 2002. ISSN 0031-9007. doi: 10.1103/PhysRevLett.89.200402. URL http://link.aps.org/doi/10.1103/PhysRevLett.89.200402.

[130] A. Ourjoumtsev, R. Tualle-Brouri, and P. Grangier. Quantum homodyne tomography of a two-photon Fock state. *Physical Review Letters*, 96(21):213601, 2006. URL http://prl.aps.org/abstract/PRL/v96/i21/e213601.

[131] C. Eichler, D. Bozyigit, C. Lang, L. Steffen, J. Fink, and A. Wallraff. Experimental Tomographic State Reconstruction of Itinerant Microwave Photons. *Physical Review Letters*, 106(22):220503, November 2011. URL http://prl.aps.org/abstract/PRL/v106/i22/e220503.

[132] C. Eichler, D. Bozyigit, C. Lang, M. Baur, L. Steffen, J. Fink, S. Filipp, and A. Wallraff. Observation of Two-Mode Squeezing in the Microwave Frequency Domain. *Physical Review Letters*, 107(11):4, September 2011. ISSN 0031-9007. doi: 10.1103/PhysRevLett.107.113601. URL http://link.aps.org/doi/10.1103/PhysRevLett.107.113601.

[133] F. Mallet, M. Castellanos-Beltran, H. Ku, S. Glancy, E. Knill, K. Irwin, G. Hilton, L. Vale, and K. Lehnert. Quantum State Tomography of an Itinerant Squeezed Microwave Field. *Physical Review Letters*, 106(22):220502, June 2011. ISSN 0031-9007. doi: 10.1103/PhysRevLett.106.220502. URL http://prl.aps.org/abstract/PRL/v106/i22/e220502.

[134] S. Deléglise, I. Dotsenko, C. Sayrin, J. Bernu, M. Brune, J.-M. Raimond, and S. Haroche. Reconstruction of non-classical cavity field states with snapshots of their decoherence. *Nature*, 455(7212):510–4, September 2008. ISSN 1476-4687. doi: 10.1038/nature07288. URL http://www.nature.com/nature/journal/v455/n7212/full/nature07288.html.

[135] M. Horsdal, M. Rypestø l, H. Hansson, and J.M. Leinaas. Charge Fractionalization on Quantum Hall Edges. *Physical Review B*, 84(11):115313, 2011. URL http://prb.aps.org/abstract/PRB/v84/i11/e115313.

[136] M. Büttiker, A. Prêtre, and H. Thomas. Dynamic conductance and the scattering matrix of small conductors. *Physical Review Letters*, 70(26):4114–4117, June 1993. ISSN 0031-9007. doi: 10.1103/PhysRevLett.70.4114. URL http://prl.aps.org/abstract/PRL/v70/i26/p4114_1.

[137] T. Christen and M. Büttiker. Low-frequency admittance of quantized Hall conductors. *Physical Review B*, 53(4):2064–2072, January 1996. ISSN 0163-1829. doi: 10.1103/PhysRevB.53.2064. URL http://link.aps.org/doi/10.1103/PhysRevB.53.2064.

[138] D. Chklovskii, B. Shklovskii, and L. Glazman. Electrostatics of edge channels. *Physical Review B*, 46(7):4026–4034, August 1992. ISSN 0163-1829. doi: 10.1103/PhysRevB.46.4026. URL http://prb.aps.org/abstract/PRB/v46/i7/p4026_1.

[139] I.L. Aleiner and L.I. Glazman. Novel edge excitations of two-dimensional electron liquid in a magnetic field. *Physical Review Letters*, 72(18):2935–2938, 1994. ISSN 10797114. doi: 10.1103/PhysRevLett.72.2935. URL http://link.aps.org/doi/10.1103/PhysRevLett.72.2935.

[140] J.H. Han and D.J. Thouless. Dynamics of compressible edge and bosonization. *Physical Review B*, 55(4):7, 1996. URL http://prb.aps.org/abstract/PRB/v55/i4/pR1926_1.

[141] G. Ernst, R.J. Haug, and J. Kuhl. Acoustic edge modes of the degenerate two-dimensional electron gas studied by time-resolved magnetotransport measurements. *Physical Review Letters*, 77(20):4245–4248, 1996. URL http://link.aps.org/doi/10.1103/PhysRevLett.77.4245.

[142] C. Santori, D. Fattal, J. Vučković, G.S. Solomon, and Y. Yamamoto. Indistinguishable photons from a single-photon device. *Nature*, 419(6907):594–597, October 2002. ISSN 0028-0836. doi: 10.1038/nature01086. URL http://dx.doi.org/10.1038/nature01086.

[143] E.B. Flagg, A. Muller, S.V. Polyakov, A. Ling, A. Migdall, and G.S. Solomon. Interference of Single Photons from Two Separate Semiconductor Quantum Dots. *Physical Review Letters*, 104(13):4, April 2010. ISSN 0031-9007. doi: 10.1103/PhysRevLett.104.137401. URL http://link.aps.org/doi/10.1103/PhysRevLett.104.137401.

[144] J. Beugnon, M.P.A. Jones, J. Dingjan, B. Darquié, G. Messin, A. Browaeys, and P. Grangier. Quantum interference between two single photons emitted by independently trapped atoms. *Nature*, 440(7085):779–82, April 2006. ISSN 1476-4687. doi: 10.1038/nature04628. URL `http://www.nature.com/nature/journal/v440/n7085/full/nature04628.html`.

[145] P. Maunz and D.L. Moehring. Quantum interference of photon pairs from two remote trapped atomic ions. *Nature Physics*, 3:538–541, August 2007. URL `http://www.nature.com/nphys/journal/v3/n8/full/nphys644.html`.

[146] T. Jonckheere, J. Rech, C. Wahl, and T. Martin. Electron and hole Hong-Ou-Mandel interferometry. *Physical Review B*, 86(12):125425, September 2012. ISSN 1098-0121. doi: 10.1103/PhysRevB.86.125425. URL `http://prb.aps.org/abstract/PRB/v86/i12/e125425`.

[147] B. Karmakar, D. Venturelli, L. Chirolli, F. Taddei, V. Giovannetti, R. Fazio, S. Roddaro, G. Biasiol, L. Sorba, V. Pellegrini, and F. Beltram. Controlled Coupling of Spin-Resolved Quantum Hall Edge States. *Physical Review Letters*, 107 (23):9, November 2011. ISSN 0031-9007. doi: 10.1103/PhysRevLett.107.236804. URL `http://prl.aps.org/abstract/PRL/v107/i23/e236804`.

[148] L. Chirolli, D. Venturelli, F. Taddei, R. Fazio, and V. Giovannetti. Proposal for a Datta-Das transistor in the quantum Hall regime. *Physical Review B*, 85 (15):6, April 2012. ISSN 1098-0121. doi: 10.1103/PhysRevB.85.155317. URL `http://link.aps.org/doi/10.1103/PhysRevB.85.155317`.

[149] A. Roth, C. Brüne, H. Buhmann, L.W. Molenkamp, J. Maciejko, X.-L. Qi, and S.-C. Zhang. Nonlocal transport in the quantum spin Hall state. *Science*, 325 (5938):294–7, July 2009. ISSN 1095-9203. doi: 10.1126/science.1174736. URL `http://www.sciencemag.org/content/325/5938/294.abstract`.

[150] C. Brüne, A. Roth, H. Buhmann, E.M. Hankiewicz, L.W. Molenkamp, J. Maciejko, X.-L. Qi, and S.-C. Zhang. Spin polarization of the quantum spin Hall edge states. *Nature Physics*, 8(6):485–490, May 2012. ISSN 1745-2473. doi: 10.1038/nphys2322. URL `http://www.nature.com/doifinder/10.1038/nphys2322`.

[151] S. Haroche and J.-M. Raimond. *Exploring the Quantum: Atoms, Cavities, and Photons*. Oxford University Press, 2006. ISBN 9780198509141. URL `http://ukcatalogue.oup.com/`.

[152] S. Takei and B. Rosenow. Neutral mode heat transport and fractional quantum Hall shot noise. *Physical Review B*, 84(23):235316, December 2010. URL `http://prb.aps.org/abstract/PRB/v84/i23/e235316`.

[153] C. Altimiras, H. le Sueur, U. Gennser, A. Anthore, A. Cavanna, D. Mailly, and F. Pierre. Chargeless Heat Transport in the Fractional Quantum Hall Regime. *Physical Review Letters*, 109(2):5, July 2012. ISSN 0031-9007. doi: 10.1103/PhysRevLett.109.026803. URL http://link.aps.org/doi/10.1103/PhysRevLett.109.026803.

[154] Y. Gross, M. Dolev, M. Heiblum, Vl. Umansky, and D. Mahalu. Upstream Neutral Modes in the Fractional Quantum Hall Effect Regime: Heat Waves or Coherent Dipoles. *Physical Review Letters*, 108(22):226801, May 2012. ISSN 0031-9007. doi: 10.1103/PhysRevLett.108.226801. URL http://prl.aps.org/abstract/PRL/v108/i22/e226801.

[155] V. Venkatachalam, S. Hart, L.N. Pfeiffer, K. West, and A. Yacoby. Local thermometry of neutral modes on the quantum Hall edge. *Nature Physics*, 8 (9):676–681, August 2012. ISSN 1745-2473. doi: 10.1038/nphys2384. URL http://www.nature.com/doifinder/10.1038/nphys2384.

[156] J. von Delft and H. Schoeller. Bosonization for beginners refermionization for experts. *Annalen der Physik*, 7(4):225–305, November 1998. ISSN 0003-3804. URL http://arxiv.org/pdf/cond-mat/9805275.pdf.

[157] T. Giamarchi. *Quantum Physics in One Dimension*. Oxford University Press, 2003. ISBN 0-19-852500-1.

Résumé : Cette thèse est consacrée à la manipulation d'excitations mono-électroniques dans un conducteur quantique balistique, par l'implémentation d'expériences d'optique quantique électronique avec la résolution d'une charge élémentaire. Une capacité mésoscopique produit à la demande des excitations monoélectroniques dans le canal de bord externe de l'effet Hall quantique.

Nous mesurons les fluctuations de courant après partitionnement des excitations sur une lame séparatrice électronique, dans un analogue de l'expérience de Hanbury-Brown & Twiss, afin de révéler les excitations neutres (paires électron/trou) qui peuvent accompagner la charge produite. Les excitations thermiques dans la mer de Fermi sont alors responsables d'interférences à deux particules qui permettent d'obtenir des informations sur la distribution en énergie des quasiparticules émises par la source. A l'aide de deux sources indépendantes et synchronisées, nous générons deux quasi-particules indiscernables, qui interfèrent sur une lame séparatrice dans un analogue de l'expérience de Hong-Ou-Mandel. La visibilité de ce phénomène est possiblement limité par la décohérence des paquets d'ondes électroniques par interaction avec l'environnement, notamment les autres canaux de bords. En mesurant le couplage capacitif entre deux canaux de bords co-propageant, nous caractérisons les effets de l'interaction coulombienne et mettons en évidence un mode neutre de propagation. Ces expériences constituent les premières implémentations d'expériences d'optique quantique électronique avec des charges uniques, et permettent d'envisager des expériences plus complexes comme la tomographie d'un paquet d'onde mono-électronique.
Mots clés : physique mésoscopique, optique quantique électronique, effet Hall quantique, dynamique électronique cohérente subnanoseconde, source d'électrons uniques, fluctuations de courant.

Abstract : This thesis is devoted to the implementation of quantum optics experiments in a ballistic quantum conductor, with single charge resolution. A mesoscopic capacitor produces on-demand single-electron excitations in the outermost edge channel of quantum Hall effect.

We measure current fluctuations after partitioning of excitations on an electronic beamsplitter, in analogy with the Hanbury-Brown & Twiss experiment, so as to unveil neutral excitations (electron/holes pairs) that can accompany the emission of the charge. Thermal excitations in the Fermi sea are then responsible for two-particle interferences that yield information on the energy distribution of the generated quasiparticles. Using two independent and synchronized sources, we generate two indistinguishable quasiparticles that interfere on a beamsplitter as in the Hong-Ou-Mandel experiment. The visibility of this phenomenon could be limited by decoherence of the wavepackets due to interactions with the environment and especially with other co-propagating edge channels. By measuring the capacitive coupling between two co-propagating edge channels, we characterize the effects of Coulomb interaction on propagation and highlight a neutral mode of propagation.

These experiments constitute the first implementations of electron quantum optics experiments with single charges. They pave the way to more complex experiments such as the tomography of a mono-electronic wavepacket.
Keywords : mesoscopic physics, electron quantum optics, quantum Hall effect, subnanosecond coherent electron dynamics, single electron source, current fluctuations.